國立臺灣大學工學院土木工程學系

碩士論文

Department of Civil Engineering
College of Engineering
National Taiwan University
Master's Thesis

海底邊坡在地震作用下的數值模擬分析

Numerical Simulation of Submarine Slope under Seismic Loading

張永詮

Yung-Chuan Chang

指導教授：郭安妮 博士

Advisor: Annie On-Lei Kwok, Ph.D.

中華民國 114 年 7 月

July, 2025

doi:10.6342/NTU202503752

致謝

轉眼間兩年的碩士學程即將結束，在台大土研的兩年我學習到非常多的專業知識，以及體會到大地組在課程和做研究上的強度和扎實性，首先感謝郭老師的指導讓我能完成一份正式的學術論文，老師非常有耐心的教導我以及指引研究的方向以及給我很好的建議，同時我也學到很多制式和工具的使用，讓我為來具備更好的工作條件。感謝大地組 R12 的同學們，在同一間研究室裡使我們有深厚的感情和友誼，大家一起修課、寫很難的作業、準備考試、做研究的過程至今歷歷在目，有大家的幫忙和鼓勵才能讓我順利完成碩士學位。感謝郭門好兄弟大元跟辛哥還有半個郭門的李昌，雖然大家都覺得郭門的很廢，但我們一起拿了全國浮式基礎競賽優等，還蹭了老師很多餐，能說是過得最滋潤的一群，最後口試也順利通過沒有被噴（除了我），希望各位未來一切順利。課餘之時也很感謝籃球幫 Gino、津津、An、蔡哥、晟祐，還有週四排球幫阿汪、俞姊、筱丰、丫佑，週五羽球幫澄毓、昕儀、彥翔、婉潔，以及國粹研究團詒茹、Gino、An、婉潔，課餘時間有大家的陪伴非常的開心跟放鬆。研究方面我要特別感謝邊坡大師溫靖瑀海歸碩士和數值的神煥神仙，沒有他們我的數值造詣將會低非常多，有句話是這麼說的：「模型給他就收斂，大家都愛煥神仙」，只要心中有供煥神，靈感一下就來了，真的非常感謝他們的幫忙。感謝徐律師，儘管在阿里媽媽有個慘案，但不知不覺你已經陪伴了我整個碩二，我們互相扶持、一起出遊、傾聽對方、互相陪伴這一年的每一天，讓我的人生有重大的改變，技師考試上榜、讓我變成 j 人、讓我體驗世界之大，點點滴滴都非常謝謝妳。最後要感謝我的家人，不管是課業、生活、玩樂等等他們永遠都非常支持我的決定，並默默地幫助著我，家人永遠都會關心我的生活狀況，我可以衣食無憂的從這裡畢業最大的功臣就是他們，我希望未來我可以帶者這份專業能力，讓他們過上衣食無憂的好日子。

doi:10.6342/NTU202503752

摘要

近年來，隨著全球對能源需求的提升與可再生能源技術的快速進展，海洋資源的開發活動愈發活躍，特別是在石油與天然氣開採以及離岸風電等領域。這些工程設施多建置於大陸棚及其邊緣區域，而這些區域常伴隨著地質條件複雜的海底邊坡。海底邊坡若因天然或人為因素發生破壞，不僅會對離岸風力機基礎、油氣輸送管線與其他設施造成嚴重損壞，進而導致工程延誤與重大經濟損失，更會因海底修復工作的困難度高及環境危險性強，使得災後復原作業代價昂貴且耗時。因此，深入瞭解海底邊坡的破壞機制，並建立可靠的破壞模式與分析方法，對於海洋工程設施的風險管理與設計安全性而言具有相當關鍵的意義。

本研究採用有限元素軟體 ABAQUS 對海底邊坡進行穩定性分析。首先，在靜態條件下，針對不同坡度的海底邊坡幾何，利用強度折減法（Strength Reduction Method）計算其安全係數。分析中同時進行總應力分析（Total Stress Analysis, TSA）與有效應力分析（Effective Stress Analysis, ESA），以探討不同分析方法對安全係數結果的影響，並與陸域飽和土坡之行為進行對比，了解海水與孔壓對於邊坡穩定性的潛在影響。此外，為模擬地震條件下海底邊坡的動態行為，本研究進一步於 ABAQUS 中進行動態分析，並引入地震加速度歷時作為輸入地震。分析中特別考慮地震動的振幅大小與頻率組成等特性，藉此評估其對邊坡反應的影響。材料行為方面，使用簡化非線性運動硬化模型（Simplified Nonlinear Kinematic Hardening, SNKH Model），以模擬土壤於反覆剪應變歷程下之非線性與循環硬化特性。最後探討在不同地震歷史、材料強度、地盤種類下邊坡位移及剪應變情形，以及地震動放大比分析（Ground Motion Amplification Ratio, GMAR），結果顯示 GMAR 並不與坡角、地盤種類、地震最大加速度有絕對關係，而是和地震主頻大小、土壤強度參數等等有密切關係，說明邊坡因低頻率地震產生的共振效應是動態分析中導致地震動放大和破壞的主因，本研究最後進一步與陸地彈性邊坡比較其地震動放大效應，發現絕大部分 GMAR 值皆小於陸地彈性邊坡，說明邊坡產生塑性破壞的能量耗散使得地震波無法有效轉換成地表加速度。

關鍵字：海底邊坡、ABAQUS、強度折減法、動態分析、地盤反應分析、非線性動態模型、地震動放大比

doi:10.6342/NTU202503752

Abstract

In recent years, the development of offshore resources such as oil and wind energy has become increasingly active. However, submarine slope failures can severely impact the construction and operation of offshore infrastructure such as wind turbine foundations and pipelines, resulting in substantial losses. Moreover, the repair of submarine facilities is extremely challenging, not only due to high costs but also because personnel are exposed to hazardous working environments. Therefore, understanding the failure mechanisms of submarine slopes and conducting failure analyses are critically important.

In this study, stability analyses of submarine slope were conducted using the ABAQUS software. Factors of safety for submarine slope with various slope angles under static condition were computed using the strength reduction method. Total stress analysis (TSA) and effective stress analysis (ESA) were carried out to compare the factors of safety corresponding to saturated slopes on land.

For the evaluation of seismic submarine slope stability, dynamic analyses were performed in ABAQUS. Effects of ground motion characteristics (such as amplitude, frequency content) on the seismic behavior of submarine slope were studied. Nonlinear material model (Simplified Nonlinear Kinematic Hardening, SNKH Model) is used to simulate the nonlinear and cyclic behavior of soils under repeated shear loading. The study examines displacement, shear strain, and ground motion amplification ratio (GMAR) under various seismic inputs, soil strengths, and bedrock types. Results indicate that GMAR is more influenced by the dominant frequency and soil strength than by slope angle, ground type, or PGA, highlighting resonance from low-frequency earthquakes as a key factor in amplification and failure. Compared to elastic land slopes, this study shows lower GMAR due to energy dissipation from plastic deformation.

doi:10.6342/NTU202503752

Key words：Submarine Slope, ABAQUS, Strength Reduction Method, Dynamic Analysis, Ground Response Analysis, SNKH model, Ground Motion Amplification Ratio

doi:10.6342/NTU202503752

TABLE OF CONTENTS

doi:10.6342/NTU202503752

doi:10.6342/NTU202503752

doi:10.6342/NTU202503752

List of Figures

doi:10.6342/NTU202503752

doi:10.6342/NTU202503752

doi:10.6342/NTU202503752

doi:10.6342/NTU202503752

doi:10.6342/NTU202503752

doi:10.6342/NTU202503752

doi:10.6342/NTU202503752

doi:10.6342/NTU202503752

doi:10.6342/NTU202503752

List of Tables

doi:10.6342/NTU202503752

doi:10.6342/NTU202503752

Chapter 1 Introduction

1.1 Motivation

The growing demand for offshore infrastructure, such as wind farms, pipelines, and coastal facilities, has made the stability of submarine slopes a critical issue in geotechnical engineering. Failure of these slopes could result in underwater landslides, damage to infrastructure, and severe environmental consequences. Ensuring slope stability is thus essential for the safety and sustainability of offshore development. Compared to slopes on land, which have been extensively studied and are supported by a long history of research, submarine slope stability remains less understood. The unique conditions of underwater environments, including pore water pressures, complex sediment layering, and dynamic loading from waves and currents, present additional challenges. Conventional analysis methods developed for terrestrial slopes often fail to capture these factors adequately. Recent studies have begun addressing submarine slope stability, but standardized analysis approaches specifically designed for marine conditions are still lacking. Simplified assumptions may overlook key behaviors like strain softening, soil anisotropy, or cyclic loading effects. These gaps highlight the need for refined modeling techniques that can reliably predict submarine slope performance. This research is motivated by the necessity to improve understanding of submarine slope failure mechanisms and develop reliable analysis methods. Through advanced numerical modeling and parameter studies, this study seeks to contribute practical insights that support safer offshore infrastructure design and risk mitigation.

doi:10.6342/NTU202503752

1.2 Research Method

In this study, a two-dimensional plane strain finite element model is developed to simulate the failure behavior of submarine slopes under seismic loading. The model aims to represent the realistic boundary conditions and mechanical behavior of underwater slopes as accurately as possible. Both total and effective stress analyses are conducted to capture the variation in slope response. Dynamic loading is applied in the form of earthquake time histories, and cyclic degradation of shear strength parameters is considered to reflect material weakening under repeated shaking. The numerical software ABAQUS is employed in to evaluate the factor of safety (FS) and observe potential failure surfaces. A series of parametric studies is performed by varying key soil parameters and loading conditions to examine how different scenarios influence the slope's failure pattern and stability. This simulation includes assessments of displacement, plastic strain development, and stress distribution to provide insight into both the initiation and progression of failure. The outcomes of total and effective stress analyses are compared, and the influence of dynamic degradation on the critical FS is discussed in detail.

doi:10.6342/NTU202503752

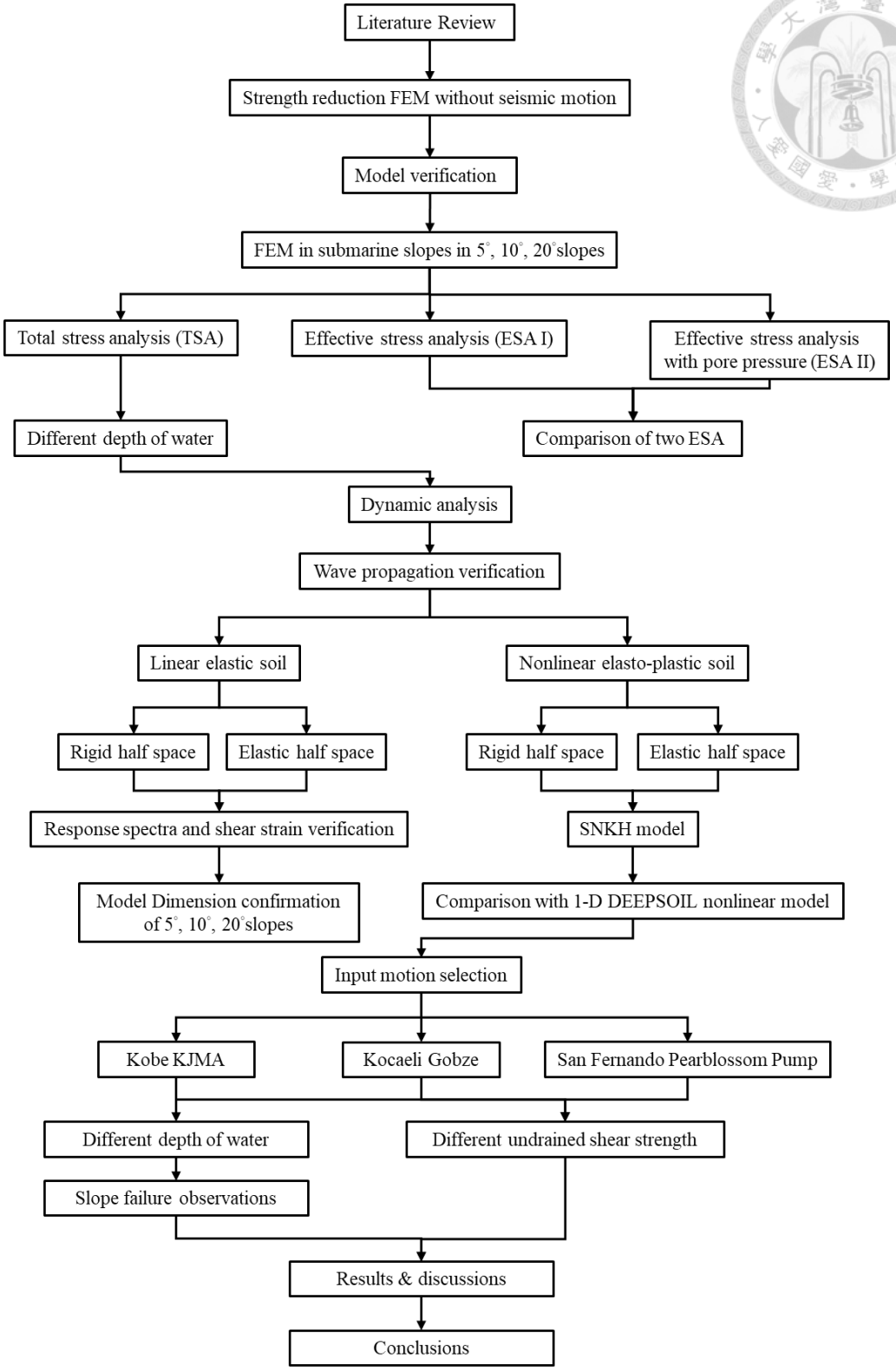

Figure1.1 The flowchart of this study

doi:10.6342/NTU202503752

1.3 Thesis Organization

This thesis is divided into five main chapters. Chapter 1 presents the research background, motivation, objectives, and an overview of the research structure. Chapter 2 provides a comprehensive literature review on the characteristics of submarine slopes in the Taiwan Strait, the differences between onshore and offshore slope stability, cyclic softening of clay, and the numerical modeling approaches used in previous studies, including the implementation of infinite boundary elements. Chapter 3 describes the methodology used in this study. It includes the verification of the numerical model based on the strength reduction method and the development of 2D plane strain slope models in ABAQUS. Simulations are conducted for various slope angles and water depths under both total and effective stress conditions. Additionally, dynamic analysis is performed using the explicit method with seismic input motion, incorporating Rayleigh damping and infinite boundary conditions to minimize wave reflection effects. Chapter 4 presents the simulation results and analysis. including comparisons of reduction factors from static analyses under various slope angles, seawater depths, and analytical methods; a comparison of shear strains between the one-dimensional nonlinear model and the two-dimensional slope model in dynamic analysis, and evaluations of displacement, shear strain, and ground motion amplification ratio under different earthquake records, undrained shear strengths, and slope angles. Finally, the onset and duration of permanent slope deformation are identified based on the evolution of plastic shear strain. Chapter 5 summarizes the key findings of the research and provides practical recommendations for submarine slope stability assessment and further studies.

doi:10.6342/NTU202503752

Chapter 2 Literature Review

2.1 Information of The Taiwan Strait

The Taiwan Strait, located between the southeastern coast of China and Taiwan, serves as a key conduit connecting the East China Sea to the South China Sea. The strait is characterized by relatively shallow waters, with most areas exhibiting depths of less than 100 meters. It is bordered by major river systems such as the Yangtze River and the Pearl River, which contribute significant sediment loads into the strait annually.

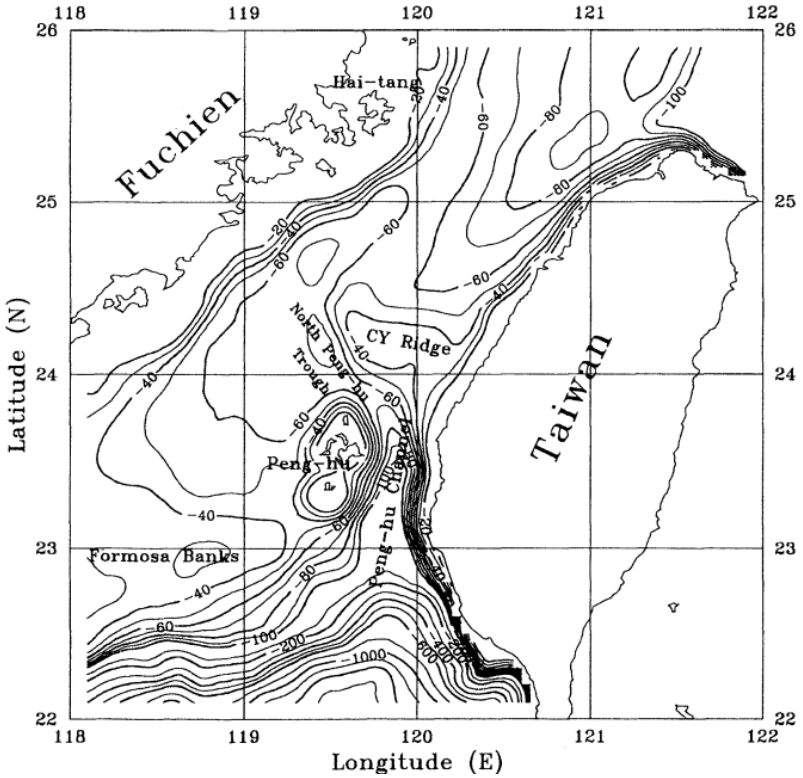

Figure 2.1 Depth contour of The Taiwan Strait in meters (Wang and Chern, 1992)

doi:10.6342/NTU202503752

2.1.1 Topography and Soil properties

Shen et al. (2021) investigated the composition and provenance of sand deposits in the Taiwan Strait. They conducted framework petrography and heavy mineral analyses to identify the characteristics of sand sources and sedimentary mechanisms. In addition, they plotted several cross-sectional profiles of the Taiwan Strait (Figure 2.2), which reveal the formation of submarine slopes resulting from the deposition of sands and minerals transported by rivers from Taiwan.

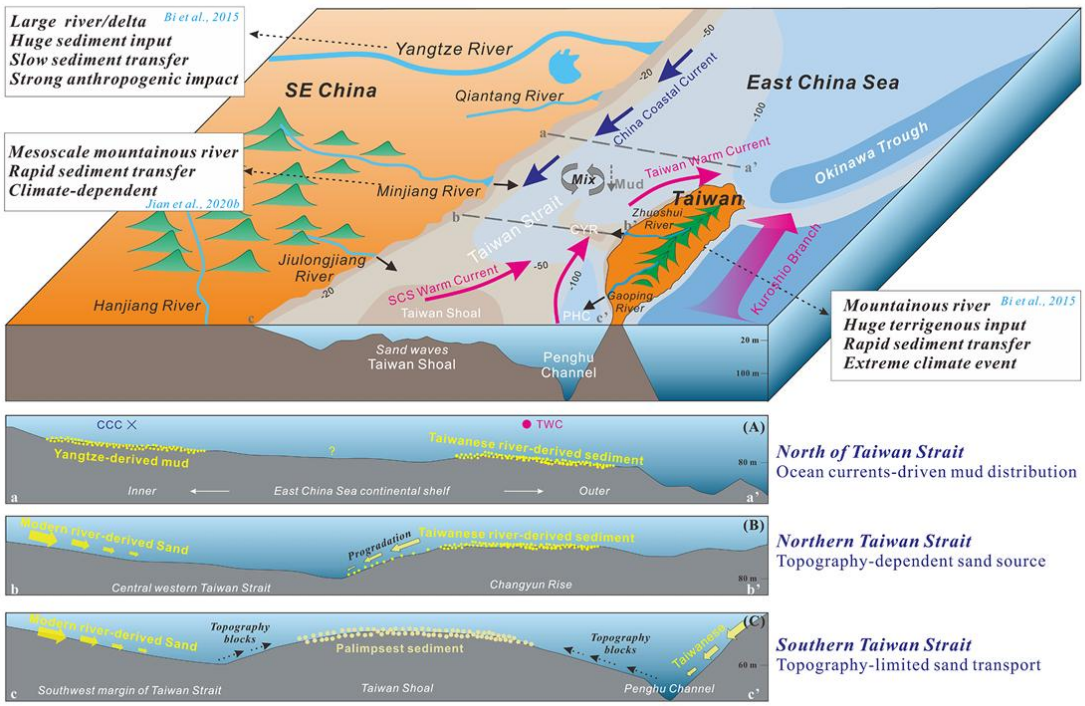

Figure 2.2 Model illustrating the sediment source-to-sink system across the East China Sea continental shelf and the Taiwan Strait, with the simplified submarine topography. (Shen et al., 2021)

doi:10.6342/NTU202503752

The borehole information was obtained from Taiwan Power Company (2018). As illustrated in Figure 2.3, borehole BH04 is situated offshore along the western coast of Taiwan. Details of the borehole are provided in Figure 2.4. For soil layers where the undrained shear strength is not reported, it indicates a non-cohesive soil type. Values enclosed in parentheses denote the average undrained shear strength.

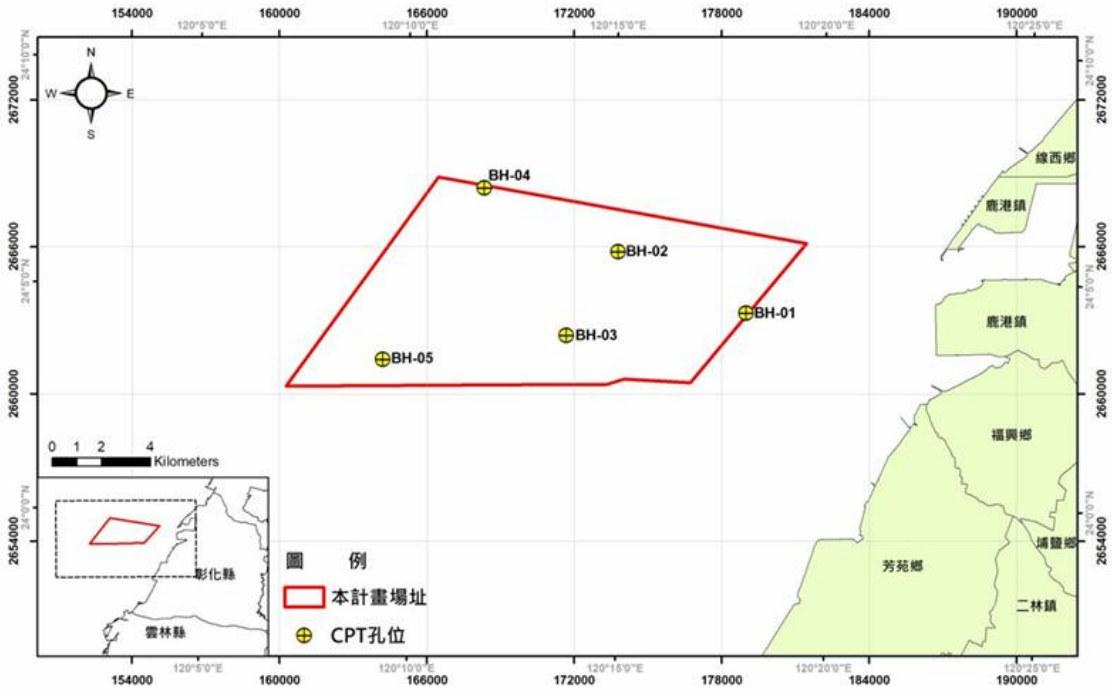

Figure 2.3 Borehole location of the offshore wind power generation project phase II (Taiwan Power Company, 2018)

doi:10.6342/NTU202503752

Layer	Depth Elevation (meters)		Thickness	Soil Description	Relative Density	Friction Angle	Undrained Shear Strength	Submerged Unit Weight	Shear wave velocity	Shear Modulus	Young's Modulus
No.	From	To	(meters)		Dr(Ave.) (%)	ϕ'(Ave.) (Degrees)	Su(Ave.) (kPa)	γ'(Ave.) (kN/m^3)	Vs(Ave.) (m/s)	G_0(Ave.) (MPa)	E_0(Ave.) (MPa)
II	0	12	12	軟弱至堅實黏土	-	-	6.9~145.8 (45.1)	4.8	88.6	13.0	33.9
	-42.3	-54.3									
	12	19.6	7.6	中等堅實至堅實黏土與中等緊密砂互層	44.4	30.0	33.5~353.7 (97.5)	7.3	162.8	47.9	124.6
	-54.3	-61.9									
	19.6	24.9	5.3	緊密粉土	47.1	30.0	67.4~447.6 (244.2)	7.0	184.6	59.3	154.3
	-61.9	-67.2									
	24.9	27.7	2.8	堅實至極堅實黏土	-	-	36.2~356.1 (101.4)	7.6	189.6	66.1	171.8
	-67.2	-70									
	27.7	35.5	7.8	中等緊密砂間夾緊密粉土及黏土	51.3	32.2[b]	-	8.3	228.3	98.1	255.1
	-70	-77.8									
	35.5	38.2	2.7	堅實至極堅實黏土	-	-	45.7~169.4 (96.0)	8.0	217.1	86.5	225.0
	-77.8	-80.5									
	38.2	39.7	1.5	疏鬆砂	40.5	30.0	-	9.0	258.5	129.4	336.5
	-80.5	-82									
	39.7	42.9	3.2	堅實至極堅實黏土	-	-	47.8~500.1 (122.3)	8.0	230.9	98.3	255.6
	-82	-85.2									

Figure 2.4 Information of BH04 borehole (Taiwan Power Company, 2018)

2.2 Introduction of Submarine Slope

Submarine slopes are inclined surfaces found on the seafloor, typically occurring along continental margins, island flanks, submarine ridges, and seamounts. These slopes are formed through various geological processes, including sediment accumulation, tectonic activity, erosion, and mass wasting events such as landslides. The gradient of submarine slopes can vary widely, from gentle inclines of a few degrees to steep escarpments exceeding 30 degrees.

When failure occurs, massive mass of soil movement can cause severe damage to subsea cables, pipelines, foundations, and other infrastructure buried on the seafloor. Such events not only result in significant losses but also pose major challenges to repair and reconstruction. Currently, there are no well-established techniques for reinforcing or remediating submarine slopes. Therefore, studying the failure behavior of submarine slopes and predicting potential failure zones is critically important for offshore engineering.

doi:10.6342/NTU202503752

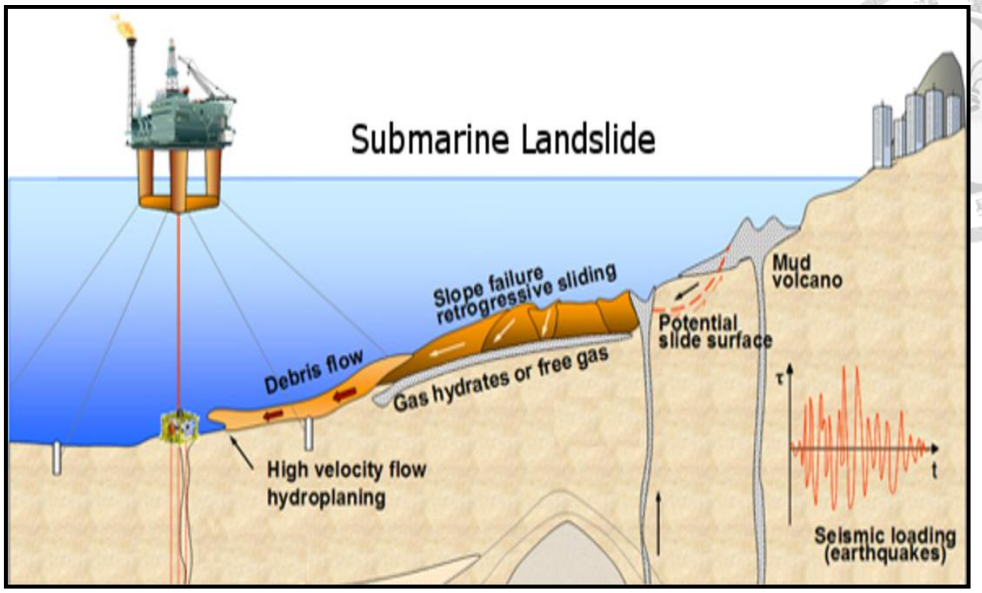

Figure 2.5 Submarine landslide as a major geohazard (Ma, 2015)

2.2.1 Observations of on-Land Slope Failure Mechanisms

Fellenius (1927) and Taylor (1937) performed mass procedure (Figure 2.6) in numerical simulation to establish the failure mechanisms, failure surfaces, and stability number "*m*" (eq. 2.1) for saturated purely cohesive (ϕ = 0°) slopes on land (Figure 2.7), where c_d is the mobilized undrained shear strength (full mobilization : $c_d = c_u$ in $\mathrm{kN/m^2}$); γ is the saturated unit weight of clay in $\mathrm{kN/m^2}$, and H is the height of the slope.

$$m = \frac{c_d}{\gamma H} \tag{2.1}$$

By Steward et al. (2011) the failure surfaces can be classified into three types: toe circle, slope circle, and midpoint circle (Figure 2.8). The types of failure arc are influenced by the slope height ratio "*D*" and the slope angle "β". Additionally, Fellenius (1927) and Taylor (1937) identified a relationship, denoted as ratio "*n*" (Figure 2.9), between the failure surface and the toe of the slope when the failure surface reaches the lower slope. As *D* increases and β decreases, the value of *n* increases, tending toward

doi:10.6342/NTU202503752

large-scale sliding represented by the midpoint circle failure. Conversely, when D decreases and β increases, n becomes smaller, indicating a failure mode more similar to the toe circle failure.

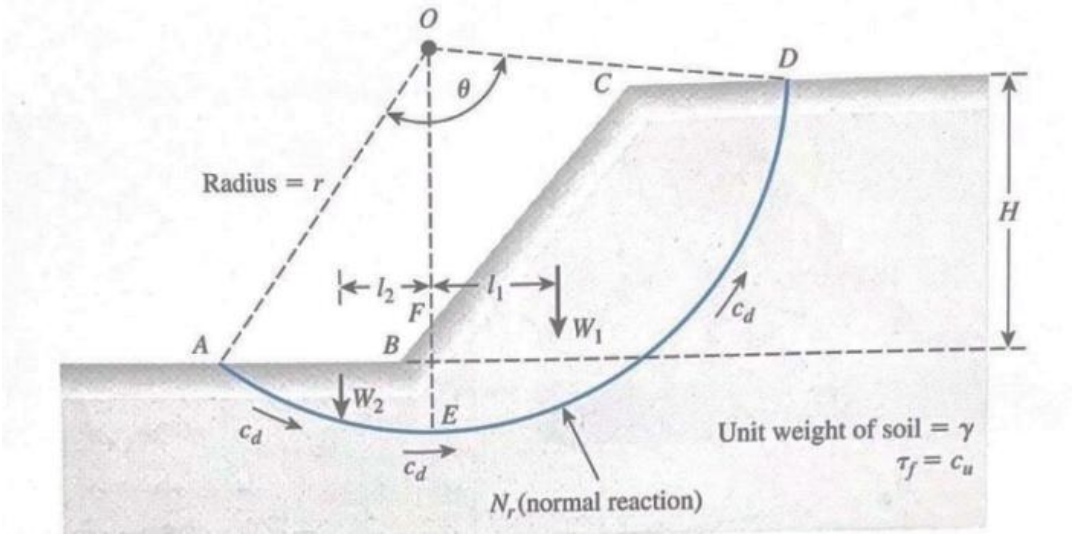

Figure 2.6 Stability analysis of homogeneous saturated clay slope (images obtained from Das, 2011)

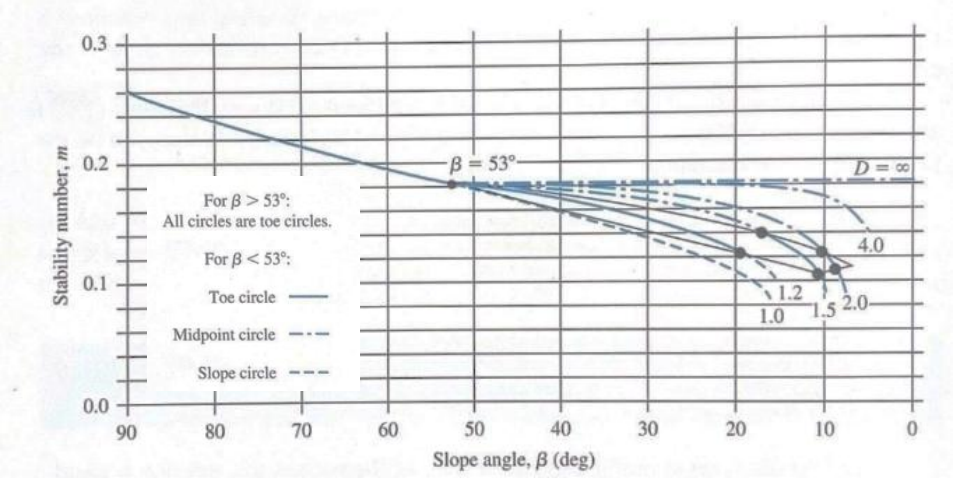

Figure 2.7 Stability analysis of homogeneous saturated clay slope (images obtained from Das, 2011)

doi:10.6342/NTU202503752

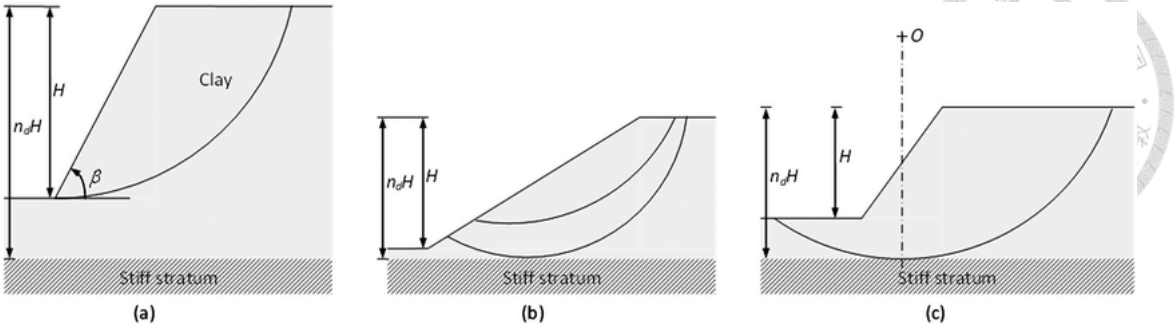

Figure 2.8 Slip circles (a) toe circle; (b) slope circle; (c) midpoint circle (Steward et al., 2011).

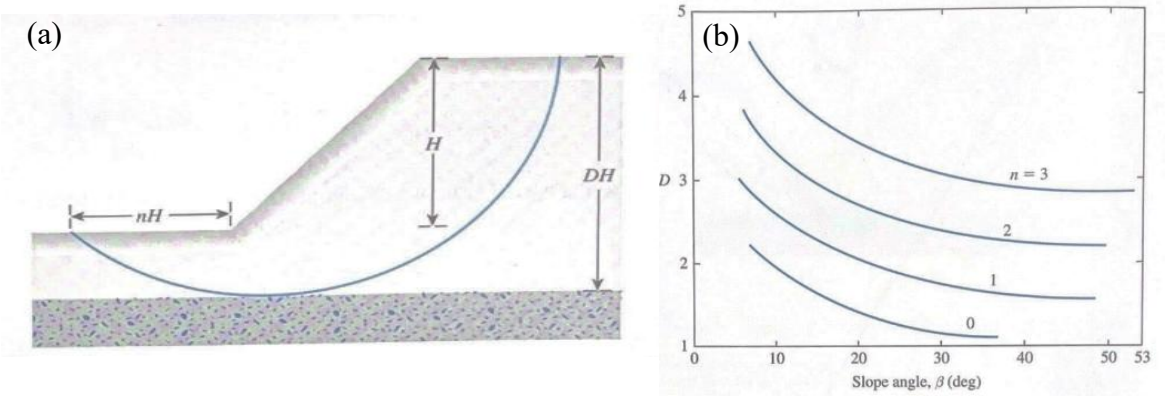

Figure 2.9 (a) Definition of parameters for midpoint circle type of failure; (b) location of midpoint circle (images obtained from Das, 2011).

2.2.2 Distribution of Failure Trigger Mechanisms of Submarine Slope

There are numerous causes of submarine slope failures. Compared to slopes on land, submarine slopes are affected by unique factors such as seawater infiltration, soil relative density, and wave erosion—conditions not typically encountered on land. Moreover, due to the challenges in underwater observation, the causes of many failures remain uncertain. Hance (2003) compiled a total of 544 submarine slope failure cases, among which only 366 had identifiable causes. Of all the cases, as many as 225 failures were attributed to "earthquakes and faulting," accounting for 41% of the total—the highest among all

doi:10.6342/NTU202503752

identified triggering mechanisms. This statistic highlights the necessity and importance of conducting dynamic analyses.

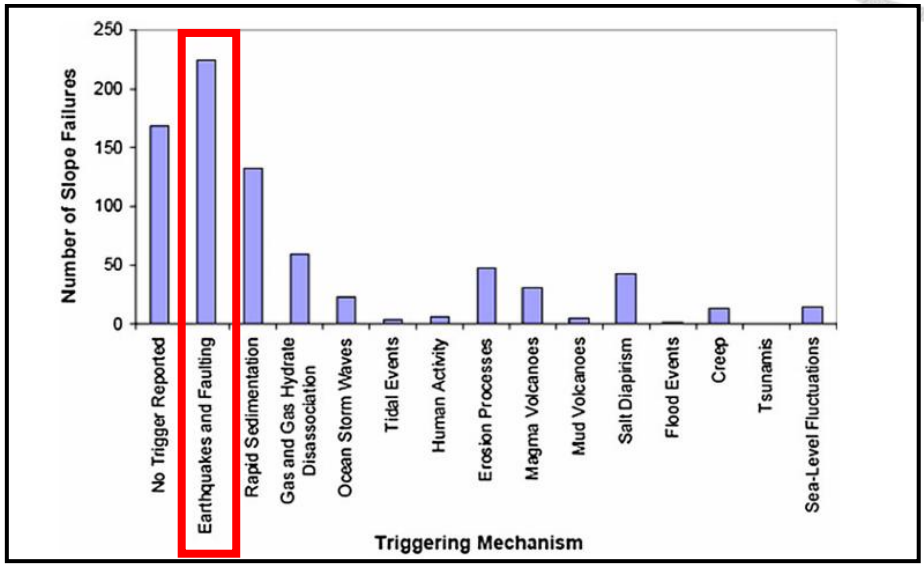

Figure 2.10 Distribution of triggering mechanisms of submarine slope (Hance, 2003).

2.2.3 Stability Evaluation in Limit Equilibrium Method

Denlinger and Iverson (1990) derived the factor of safety formula under effective stress equilibrium, the Coulomb failure criterion and infinite boundary conditions. First of all, the gradient of total head *h* in fluid seepage system should be defined as

$$h = \frac{p}{\gamma_w} + E \tag{2.2}$$

where *p* is the pore water pressure height, *E* is the elevation above the horizontal datum we defined, and γ_w is the unit weight of the pore water. In submarine cases, it's convenient to use sea level as the horizontal reference, with *E* representing depth below sea level (Figure 2.11). If the pore pressure *p* is caused only by the weight of seawater above and there's no seepage, then the hydraulic head *h* will be zero everywhere. This

doi:10.6342/NTU202503752

condition isn't possible in an infinite slope on land unless the slope is flat or there's no groundwater.

The static effective pressure equilibrium can be written in Equation 2.3 referring to the control volume in Figure 2.12

$$\frac{\partial \sigma_{ij}}{\partial x_j} = \rho_t g_i - \frac{\partial p}{\partial x_i} \tag{2.3}$$

where σ_{ij} is the effective stress tensor, with compressive normal stresses taken as positive. The variables x_i and x_j denote general spatial coordinates, and *i* and *j* refer to orthogonal directions (e.g., *x*, *y*, or *z*). ρ_t represents the bulk density of the sediment–water mixture, and g_i is a component of gravitational acceleration. It's important to note that pore pressure gradients are considered part of the body forces in this static equilibrium equation. As long as the control volume is in infinity boundary, the stress gradients tangential to the slope are zero, so the initial condition can be written in Equation 2.4.

$$\frac{\partial \sigma_{ij}}{\partial x} = 0 \qquad \frac{\partial \sigma_{ij}}{\partial z} = 0 \tag{2.4}$$

By Equation. 2.3 and 2.4, the equilibrium Equations reduce to Equation. 2.5 a and 2.5 b, noted that the water pressure *p* is written in terms of water head *h*.

$$\frac{\partial \sigma_{yy}}{\partial y} = (\gamma_t - \gamma_w)\cos\theta - \gamma_w \frac{\partial h}{\partial y} \tag{2.5 a}$$

$$\frac{\partial \sigma_{yx}}{\partial y} = (\gamma_t - \gamma_w)\sin\theta - \gamma_w \frac{\partial h}{\partial x} \tag{2.5 b}$$

doi:10.6342/NTU202503752

where γ_t is the total unit weight of the saturated soil, γ_w is the unit weight of the fluid, σ_{yy} is the effective normal stress in y direction, σ_{yx} is the shear stress in x direction referring to Figure 2.12, and θ is the slope angle.

$$-\cos\theta = \frac{\partial E}{\partial y} \tag{2.6 a}$$

$$-\sin\theta = \frac{\partial E}{\partial x} \tag{2.6 b}$$

$$\gamma_w \frac{\partial h}{\partial y} = \frac{\partial p}{\partial y} - \gamma_w \frac{\partial E}{\partial y} \tag{2.7 a}$$

$$\gamma_w \frac{\partial h}{\partial x} = \frac{\partial p}{\partial x} - \gamma_w \frac{\partial E}{\partial x} \tag{2.7 b}$$

In order to build a relationship between the head gradient and the pressure gradient, Equation. 2.6 and 2.7 are derived by Equation. 2.5, which is more convenient to describe different cases of groundwater level. In submarine slope cases, slopes subject to steady seepage, and pore pressure is constant. If we define pore pressure equal to zero along the slope surface, the boundary conditions along the slope surface are written in Equation. 2.8 and 2.9, pore pressure is also constant along any planes parallel to the slope surface.

$$\frac{\partial p}{\partial x} = 0 \; ; \; \frac{\partial p}{\partial z} = 0 \; ; \; p = 0 \;\; (\text{at y} = 0) \tag{2.8}$$

$$\frac{\partial h}{\partial x} = 0 \; ; \; \frac{\partial h}{\partial z} = 0 \; ; \; h = 0 \;\; (\text{at y} = 0) \tag{2.9}$$

Then combining the equilibrium expressions with the Coulomb failure criterion to find the limit strength of the slope, the failure criterion can be written in Equation. 2.10. We should integrate Equation 2.5 a and b to get the effective stresses. When Equation. 2.11 and 2.12 are computed, we can substitute the effective stresses into Equation. 2.10 to obtain the limit shear strength of the soil. Finally, the factor of safety of submarine slopes

doi:10.6342/NTU202503752

under limit equilibrium method can be presented in Equation. 2.13, which y_f is the depth from the surface to the failure plane.

$$\left|\sigma_{yx}\right| = \sigma_{yy}\tan\phi + c \tag{2.10}$$

$$\sigma_{yy}(y) = \int_0^y \left[(\gamma_t - \gamma_w)\cos\theta - \gamma_w \frac{\partial h}{\partial y} \right] dy \tag{2.11}$$

$$\sigma_{yx}(y) = \int_0^y \left[(\gamma_t - \gamma_w)\sin\theta - \gamma_w \frac{\partial h}{\partial x} \right] dy \tag{2.12}$$

$$FS = \frac{c + \left[(\gamma_t - \gamma_w) y_f \cos\theta - \gamma_w h(y_f) \right] \tan\phi}{(\gamma_t - \gamma_w) y_f \sin\theta} \tag{2.13}$$

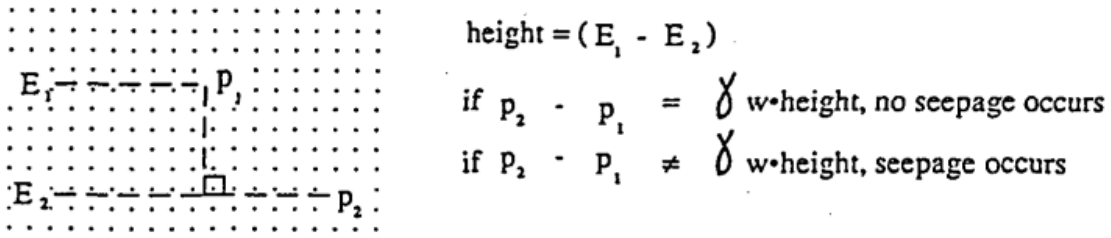

Figure 2.11 Differences in hydraulic head based on elevation *E* and pore pressure *p* (Denlinger and Iverson, 1990).

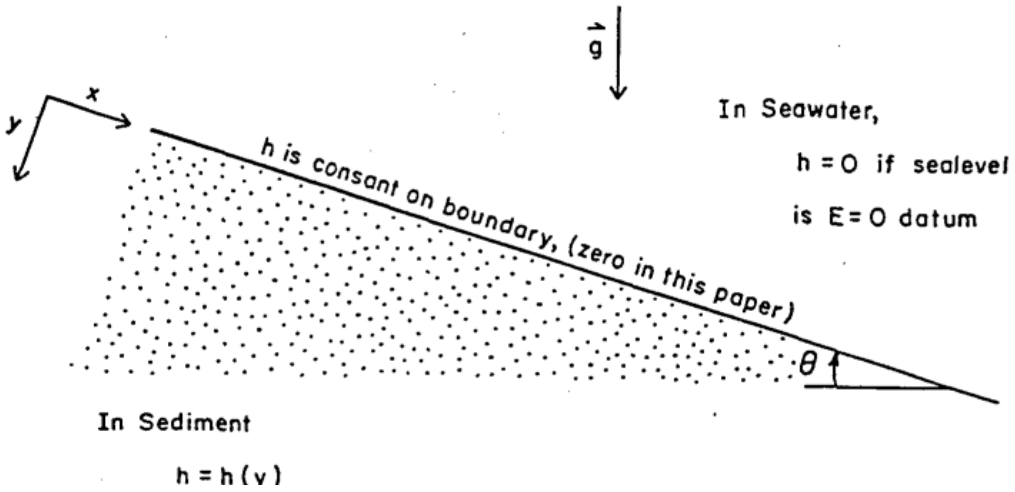

Figure 2.12 The coordinate system and the boundary conditions (Denlinger and Iverson ,1990).

doi:10.6342/NTU202503752

2.2.4 Stability Evaluation in Finite Element Method

Rodríguez-Ochoa et. al (2015) performed finite element method on static slope stability evaluations and 1-D and 2-D non-linear dynamic analyses, they estimated the factor of safety with the strength reduction factor $\sum$Msf in PLAXIS 2D. The definition of $\sum$Msf is shown in Equation. 2.14. The strength of soil is gradually decreased until the failure surface appears, at that time or step, the reduction factor can be viewed as the factor of safety (PLAXIS, 2012).

$$\sum \text{Msf} = \tan(\varphi'_{\text{input}}) / \tan(\varphi'_{\text{reduced}}) = c'_{\text{input}} / c'_{\text{reduced}} \quad (2.14)$$

The initial conditions (pore pressure) in the model were set according to the method proposed by Rodríguez-Ochoa et al. (2015). Since the slope is located on the seafloor, the lateral and bottom boundaries are considered impermeable, and no seepage is assumed. Therefore, only the surface of the slope is subjected to hydrostatic pressure corresponding to the water depth, simulating the confining pressure exerted by the seawater. The slope material is assumed to be fully saturated (S = 100%). Regarding the material properties, the study utilized soil data from borehole AP-16 in the Gulf of Mexico. The undrained shear strength (s_u) of the soil was obtained using the SHANSEP method. Comparisons between triaxial and direct shear test results show that the su value of the clay increases linearly with depth.

doi:10.6342/NTU202503752

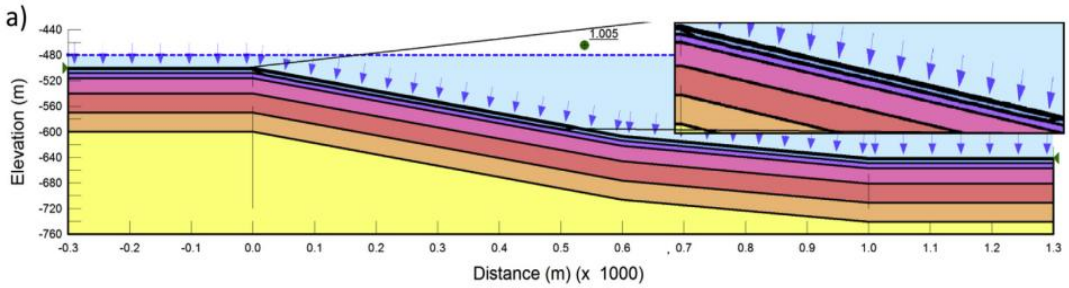

Figure 2.13 Hydrostatic pressure corresponding to the water depth

(Rodríguez-Ochoa et. al, 2015)

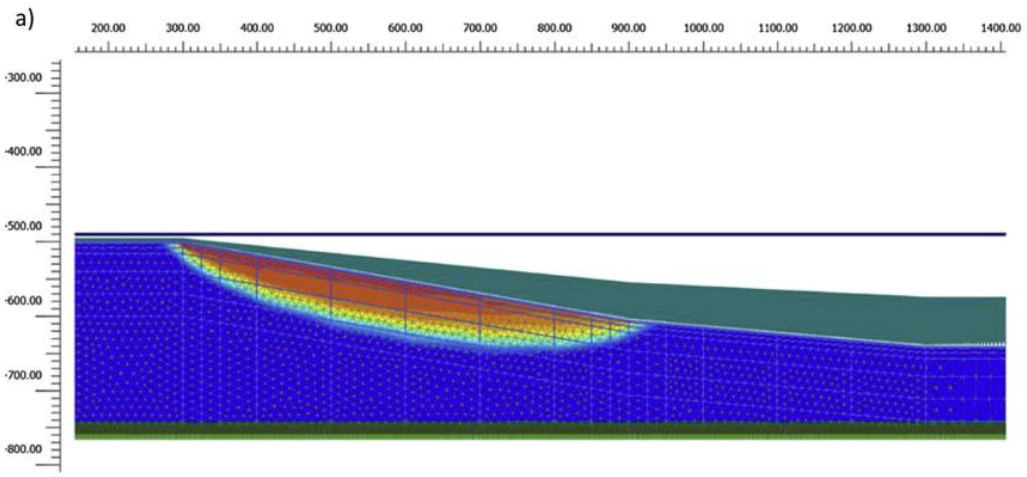

Figure 2.14 Numerical model in PLAXIS 2D (Rodríguez-Ochoa et. al, 2015)

doi:10.6342/NTU202503752

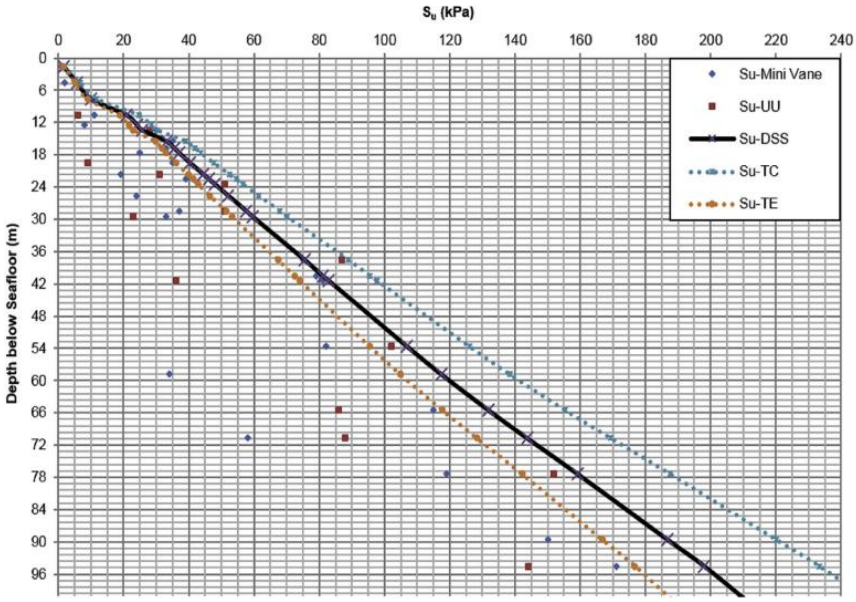

Figure 2.15 Undrained shear strength data from offshore testing

(Rodríguez-Ochoa et. al, 2015)

2.2.5 Stability Evaluation under Seismic Loading

Nian et al. (2019) derived the factor of safety formulas by limit equilibrium method under seismic motion. They assumed that the submarine slope strip is simplified to a rigid body owing to the undrained state to the short acting time of earthquake motions. The seismic coefficients k_h and k_v are adopted in the expression of seismic loading, under the quasi-static bidirectional seismic loads, there are four types of force combinations shown in Figure 2.16. By resolving the bidirectional seismic forces into components parallel and perpendicular to the slope surface, a set of Equations is developed for evaluating the safety factor of slopes composed of multiple soil layers.

Case (1): Where the horizontal seismic force acts outward from the slope and the vertical seismic force acts upward (in case (1) of Figure 2.16), the corresponding safety factor formula is expressed as Equation 2.15.

doi:10.6342/NTU202503752

$$FS = \frac{\tau_f}{\tau} = \frac{s_u(h) + 0.5k_v \cdot \sin 2\beta \cdot \int_0^h \gamma(h)dh}{0.5k_v \cdot \sin 2\beta \cdot \int_0^h \gamma'(h)dh + k_h \cdot \cos^2 \beta \cdot \int_0^h \gamma(h)dh} \quad (2.15)$$

Case (2): Where the horizontal seismic force acts outward from the slope and the vertical seismic force acts downward (in case (2) of Figure 2.16), the corresponding safety factor formula is expressed as Equation 2.16.

$$FS = \frac{\tau_f}{\tau} = \frac{s_u(h)}{0.5 \cdot \sin 2\beta \cdot \int_0^h \gamma'(h)dh + 0.5k_v \cdot \sin 2\beta \cdot \int_0^h \gamma(h)dh + k_h \cdot \cos^2 \beta \cdot \int_0^h \gamma(h)dh} \quad (2.16)$$

Case (3): Where the horizontal seismic force acts inward from the slope and the vertical seismic force acts upward (in case (3) of Figure 2.16), the corresponding safety factor formula is expressed as Equation 2.17.

$$FS = \frac{\tau_f}{\tau} = \frac{s_u(h) + k_h \cdot 0.5\sin 2\beta \cdot \int_0^h \gamma(h)dh + k_v \cdot \cos^2 \beta \cdot \int_0^h \gamma(h)dh}{0.5 \cdot \sin 2\beta \cdot \int_0^h \gamma'(h)dh} \quad (2.17)$$

Case (4): Where the horizontal seismic force acts inward from the slope and the vertical seismic force acts downward (in case (4) of Figure 2.16), the corresponding safety factor formula is expressed as Equation 2.18.

$$FS = \frac{\tau_f}{\tau} = \frac{s_u(h) + k_h \cdot \cos^2 \beta \cdot \int_0^h \gamma(h)dh}{0.5 \cdot \sin 2\beta \cdot \int_0^h \gamma'(h)dh + 0.5k_v \cdot \sin 2\beta \cdot \int_0^h \gamma(h)dh} \quad (2.18)$$

doi:10.6342/NTU202503752

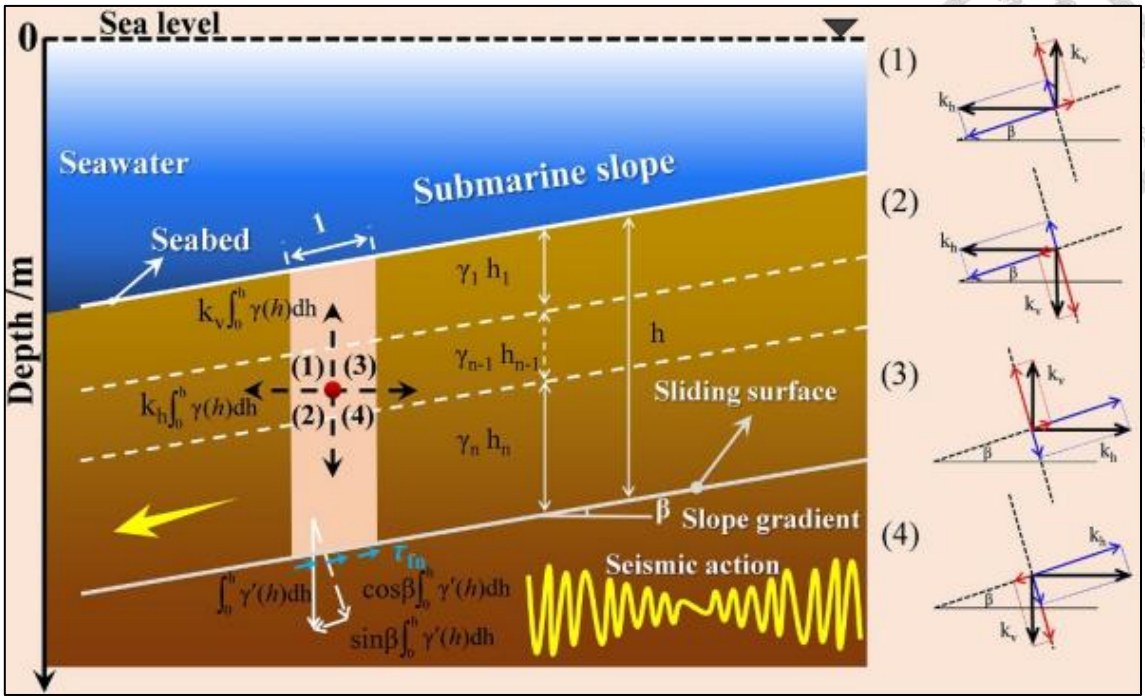

Figure 2.16 Stress analysis of a submarine slope under bidirectional seismic actions.

(Nian et al., 2019)

2.3 Dynamic Soil Properties

2.3.1 Cyclic Softening of Soil

When saturated clay is subjected to cyclic loading, the buildup of excess pore water pressure leads to a progressive reduction in both stiffness and strength. At the initial loading cycle (N=1), the shear modulus reaches its peak, representing the maximum shear resistance of the soil. As the number of cycles increases, the shear modulus steadily declines, as illustrated in Figure 2.17. Tsai et al. (2014) introduced a simplified strain-based approach to evaluate the degradation of saturated clay under cyclic conditions, offering an alternative to conventional stress-based liquefaction assessment methods.

According to their findings, the degree of strength degradation is influenced by the overconsolidation ratio (OCR) and the plasticity index (PI). Specifically, OCR governs the fitting parameters s and r, while PI shapes the overall degradation curve (see Figure

doi:10.6342/NTU202503752

2.18). During cyclic softening, clay exhibits both a loss of stiffness and a reduction in strength. For clay materials, the modulus degradation index is equivalent to the stress softening index, as defined in Equation 2.29.

$$\delta_c = \delta_\tau = N_c^{-s(\gamma-\gamma_t)^r} \tag{2.29}$$

In this Equation, γ_t is the threshold strain. When the existing shear strain surpasses this critical threshold, the clay begins to exhibit cyclic softening behavior. The assessment procedure is conducted in the following steps:

1. Determine the values of M_w and PGA through suitable seismic hazard analyses.
2. Estimate the maximum shear modulus $G_{\max}$ by using Equation 2.30.

$$\mathrm{G}_{\max} = \rho \times V_s^2 \tag{2.30}$$

3. Evaluate how the product γ_{eff} changes with depth by applying Equation 2.31, where G_{eff} is the effective shear modulus, σ_0 is the total stress at depth z, r_d is the stress reduction factor.

$$\gamma_{eff}\left(\frac{G_{eff}}{G_{\max}}\right) = 0.65 \times \left(\frac{a_{\max}}{g \times G_{\max}}\right)\sigma_0 \times r_d \tag{2.31}$$

4. Apply Equation 2.29 for the calculation, using the values of *s* and *r* provided in Table 2.1, and setting the value of γ to 0.03%.

5. Finally, use Equation 2.34 to calculate the equivalent number of loading cycles, where t where, $c_0 = 3.43$, $c_1 = 0.352$, $c_2 = 0.402$, $c_3 = 0.798$, $c_4 = 1.72$, and $c_5 = 1.50$. Set the parameter *b* to 1, and determine and according to Equations 2.32 and 2.33. Note that is defined as the spectral ratio between the 1.0-second $S_a(1)$ and 0.2-second spectral accelerations $S_a(0.2)$.

doi:10.6342/NTU202503752

$$T_s = \frac{4Z}{V_s} \tag{2.32}$$

$$S_1 = \frac{S_a(1)}{S_a(0.2)} \tag{2.33}$$

$$\ln N_c = \ln\left[\frac{\exp\left(c_0 + c_1 \ln PGA + c_2 \ln S_1 + c_3 M_w + c_4 \ln b + c_5 b T_s\right) + 0.5}{0.65^{\frac{1}{b}}}\right] \tag{2.34}$$

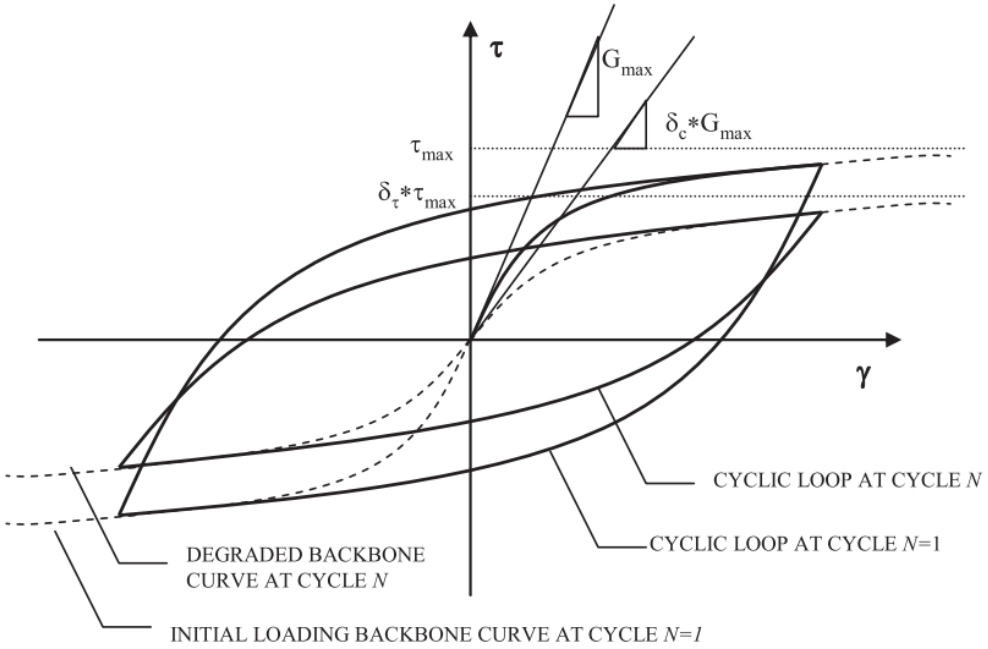

Figure 2.17 Decreasing in stiffness due to cyclic loading (Tsai et al., 2014)

doi:10.6342/NTU202503752

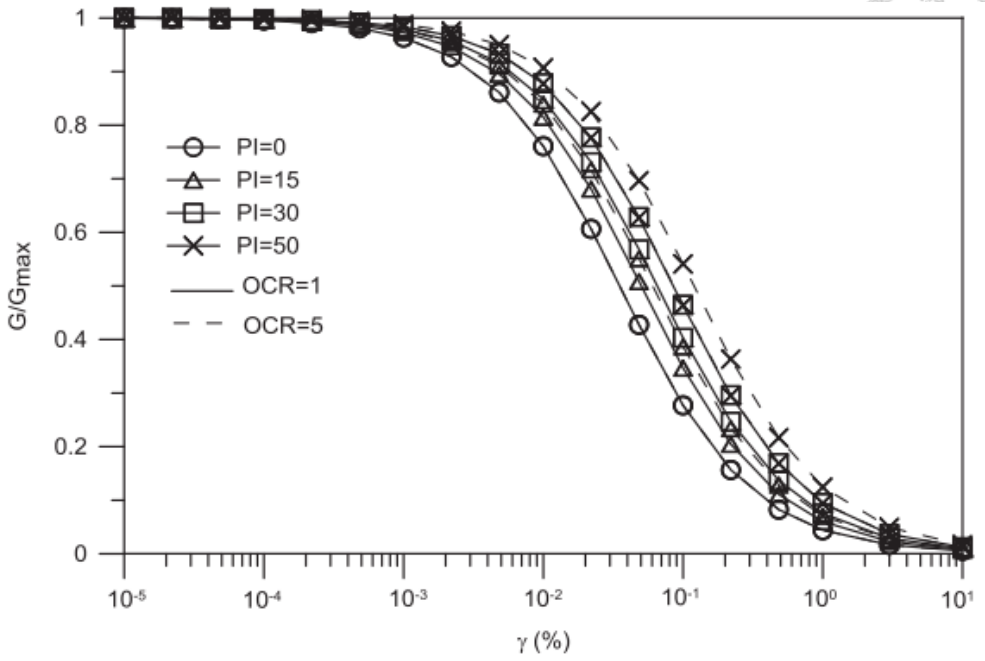

Figure 2.18 Modulus reduction curve in different PI and OCR (Tsai et al., 2014)

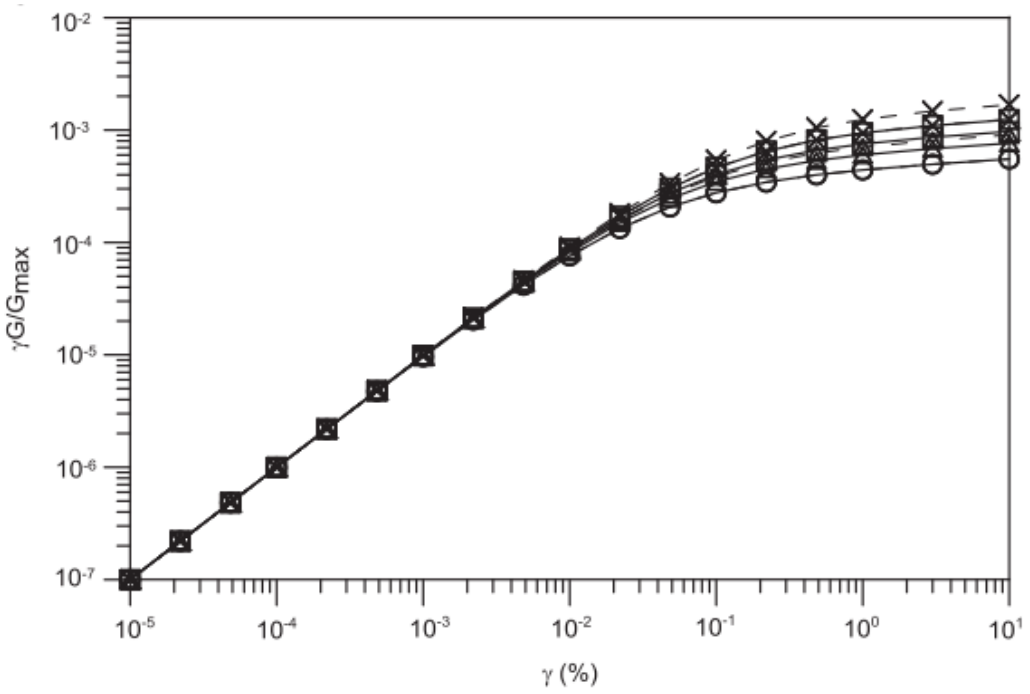

Figure 2.19 Shear modulus reduction curve (Tsai et al., 2014)

doi:10.6342/NTU202503752

Table 2.1 Model parameters of cyclic softening (Tsai et al., 2014)

OCR	s	r
1	0.075	0.495
1.4	0.064	0.520
2	0.054	0.480
4	0.042	0.423

2.3.2 Simplified Nonlinear Kinematic Hardening Model

The nonlinear kinematic hardening (NKH) model has been widely adopted for simulating soil behavior in dynamic analyses using ABAQUS. According to Ngo et al. (2021), a simplified version of this model—referred to as the Simplified Nonlinear Kinematic Hardening (SNKH) model—was employed. This model incorporates the von Mises yield criterion and introduces a back stress (α) to govern the translation of the yield surface. The corresponding yield condition is defined in Equation 2.35, where σ_0 is the initial yield stress at zero plastic strain. The increment of back stress is in Equation 2.36.

$$F = f(\sigma - \alpha) - \sigma_0 = 0 \tag{2.35}$$

$$\dot{\alpha} = C_1 \frac{1}{\sigma_0}(\sigma - \alpha)\varepsilon^{pl} - \gamma_1 \alpha \varepsilon^{pl} \tag{2.36}$$

In this model, ε^{pl} denotes the increment of equivalent plastic strain. To implement the SNKH model, three key parameters are required: the initial yield stress (σ_0), the initial kinematic hardening modulus (C_1, which is typically taken as the Young's modulus E), and the rate at which the kinematic hardening modulus decreases (γ_1). These parameters can be approximated by assuming that the stress at a large plastic strain reaches the

doi:10.6342/NTU202503752

ultimate yield stress (σ_y) of the soil. The yield stress σ_0 itself can be estimated from the soil's strength properties, such as cohesion (c) and friction angle (ϕ). When it's under undrained condition of clay, the σ_y can be defined by $\sigma_y = \sqrt{3} S_u$. The initial yield stress σ_0 is commonly taken as a proportion (λ) of the maximum yield stress, using the relation $\sigma_0 = \lambda \cdot \sigma_y$. Based on this assumption, the γ_1 parameter can be computed in Equation 2.37. Typically, the λ value is ranging from 0.1~0.3 for soil, by this model the G / G_{max} can be fit by the parameters. The mean average error (MAE) was employed to quantify the discrepancy between the predicted model response and the target curve, where A_m and A_t are the G / G_{max} values obtained from the SNKH model and target curve, respectively. Figure 2.20 G / G_{max} and damping curves obtained from RCTs and the SNKH model for (a) silica sand; (b) mixture soil; and (c) Toyoura sand; and (d) MAE value for three soils. (Ngo et al., 2021)shows the fitting curves between the target G / G_{max} and damping curves and the SNKH model's.

Yang (2024) used ABAQUS to simulate the shear modulus reduction curve based on the SNKH model in a one-dimensional soil column. The curve of clay with a plasticity index (PI) of 30% from the study by Vucetic and Dobry (1991) was adopted as the target curve for verification. Yang (2024) simplified the soil parameters of borehole BH-04 based on the geotechnical investigation report from the Taipower Company Offshore Wind Farm Phase II Project. The simplified soil parameters are listed in Table 2.2. The SNKH model setup in ABAQUS is illustrated in Figure 2.21, which requires inputs including the yield stress at zero plastic strain, the initial kinematic hardening modulus C1 (namely Young's modulus), and the parameter gamma. Yang (2024) set gamma = 0.15

doi:10.6342/NTU202503752

and the undrained shear strength s_u = 101.4 kPa. Based on the previously described calculation method, the yield stress σ_0, σ_y can be obtained. The resulting parameters are summarized in Table 2.3. Figure 2.23 shows the shear strain history of the soil after inputting the Northridge earthquake record (first 12 seconds), with a maximum shear strain of 1%. Figure 2.24 presents the final comparison results with the shear modulus reduction curve from Vucetic and Dobry (1991). It can be observed that, aside from slight discrepancies at low strain levels, the high strain values are accurately matched. This validates both the implementation and feasibility of the SNKH model in ABAQUS.

$$\gamma_1 = C_1 / (\sigma_y - \sigma_0) \tag{2.37}$$

$$MAE = \sum |A_m - A_t| \tag{2.38}$$

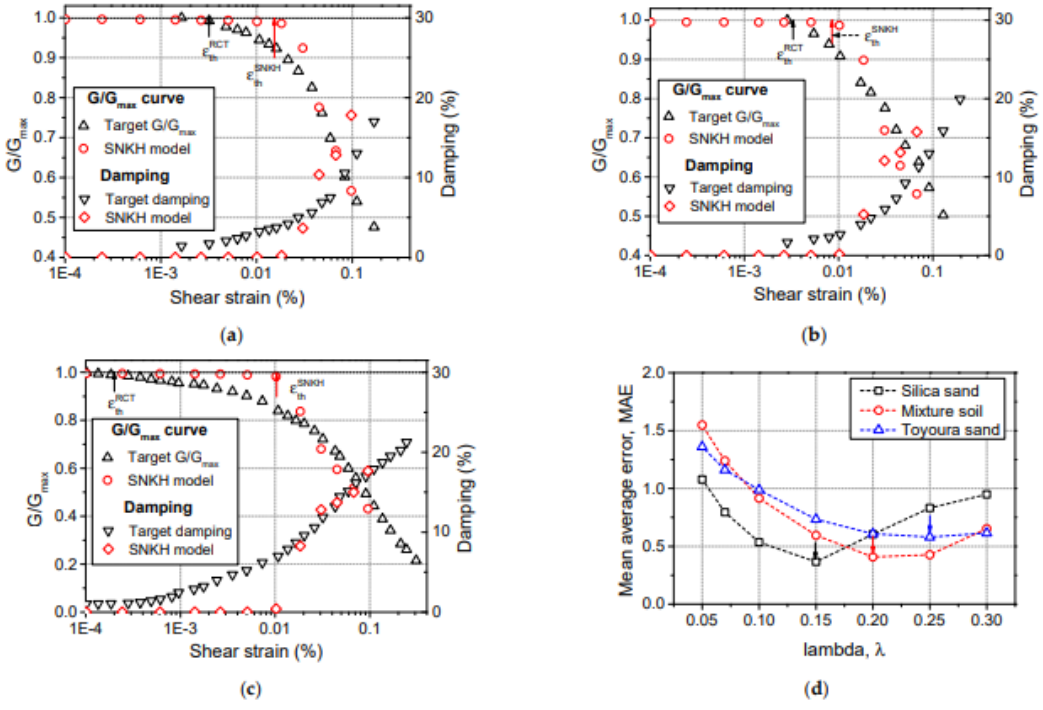

Figure 2.20 G / G_{max} and damping curves obtained from RCTs and the SNKH model for (a) silica sand; (b) mixture soil; and (c) Toyoura sand; and (d) MAE value for three soils. (Ngo et al., 2021)

doi:10.6342/NTU202503752

Table 2.2 The simplified soil parameters of the Taipower Company Offshore Wind Farm Phase II Project. (Yang, 2024)

Depth (m)	Density (kg/m^3)	S_u (kPa)	Yield stress (kPa)	E (MPa)	V_s (m/s)	G (MPa)
0~30m	1775.33	101.4	175.456	171.8	189.6	66.1

Table 2.3 Parameters of SNKH model in ABAQUS element test. (Yang, 2024)

σ_y (Pa)	λ (0.1-0.3)	$\sigma\|_0$ (Pa)	C (Pa)	γ_{kh}
175629.952	0.15	26344.493	171800000	1150.82

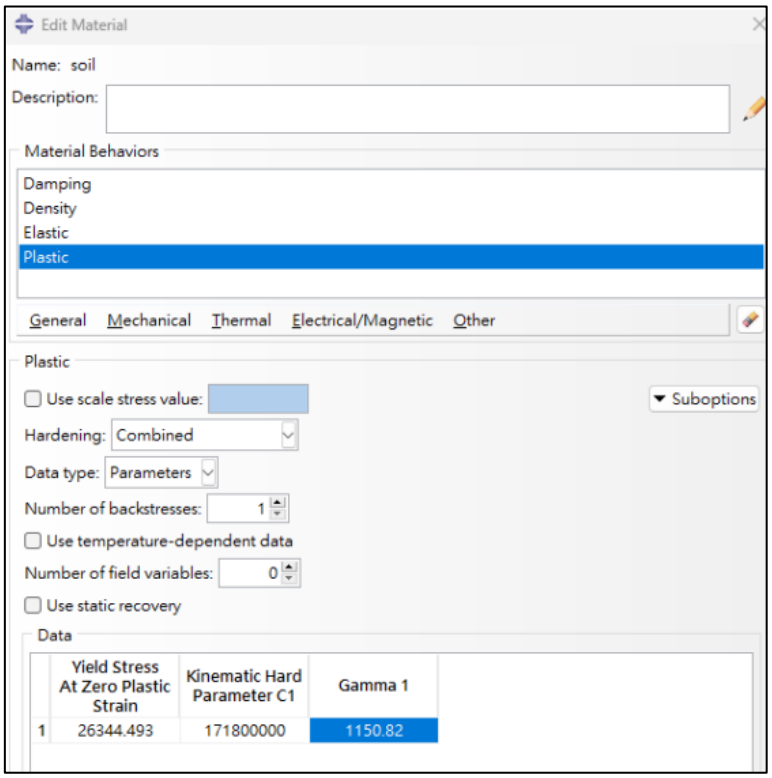

Figure 2.21 SNKH model setup in ABAQUS GUI. (Yang, 2024)

doi:10.6342/NTU202503752

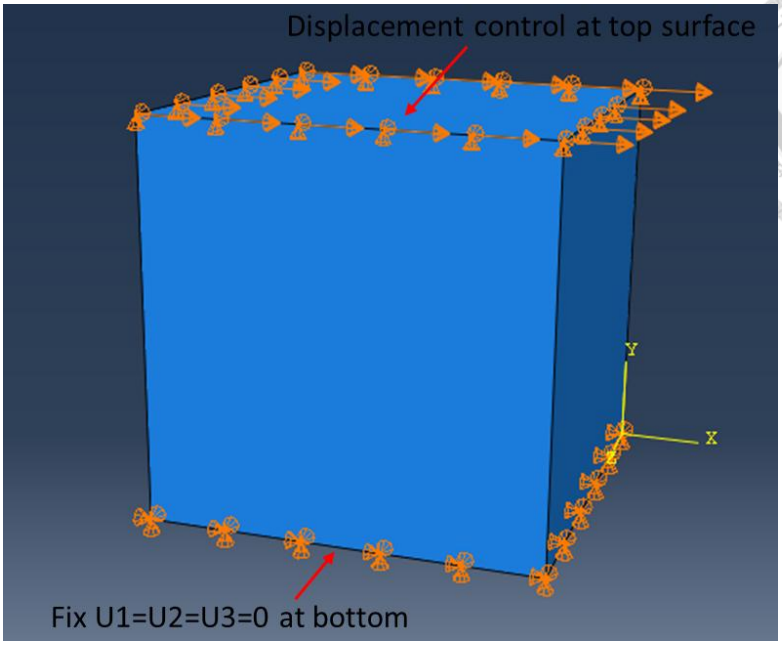

Figure 2.22 Testing soil element (Yang, 2024)

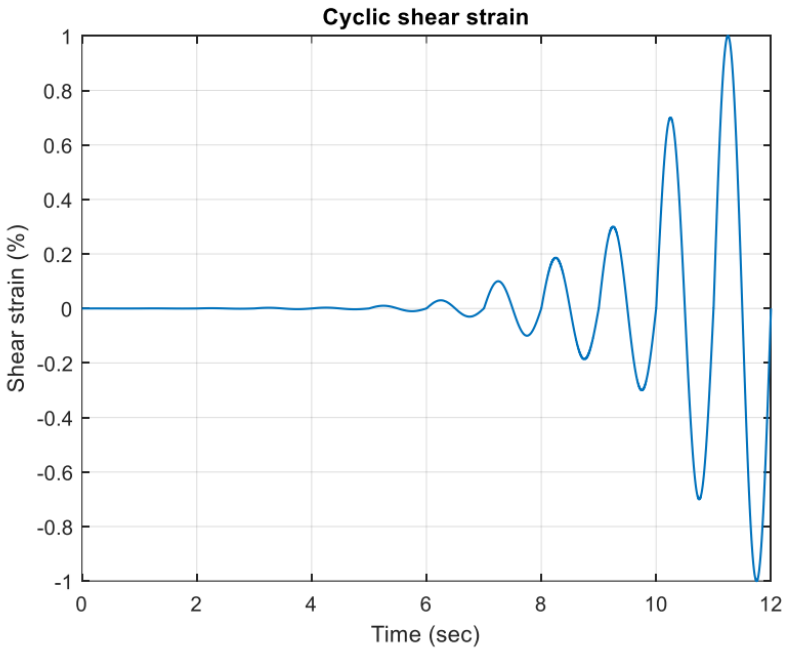

Figure 2.23 Input motion for the element test (Yang, 2024)

doi:10.6342/NTU202503752

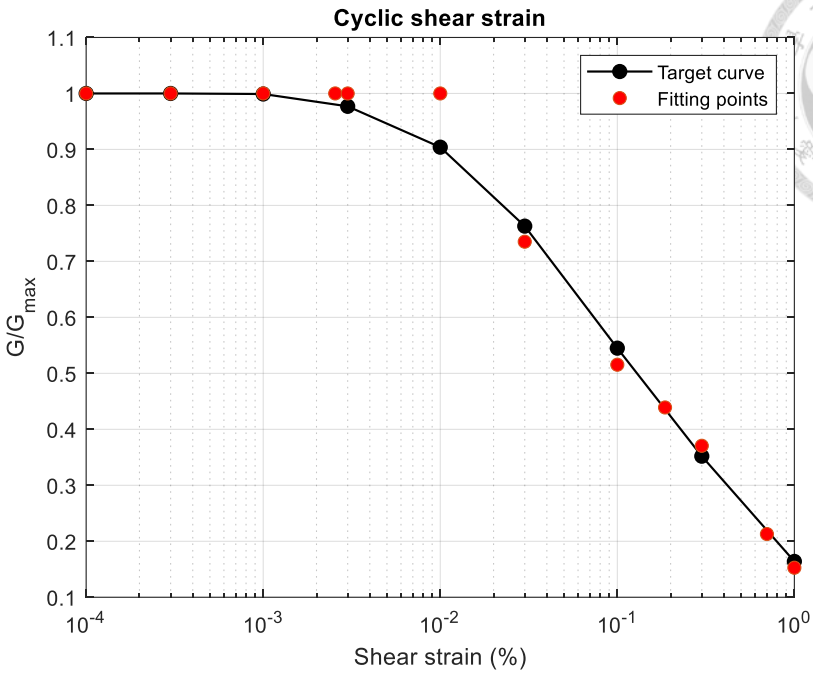

Figure 2.24 Comparison between the G / G_{max} obtained from the SNKH model and the target curve. (Yang, 2024)

2.4 Numerical Modeling

2.4.1 Infinite Element Boundary

In order to minimize seismic wave reflections along the lateral boundaries of the slope, this study employed the infinite boundary condition feature in ABAQUS. In numerical modeling of wave propagation problems, reflections from model boundaries can lead to inaccurate simulation results, particularly in dynamic analyses involving seismic loading. To address this issue, ABAQUS provides an infinite boundary formulation, which effectively absorbs outgoing waves and simulates the behavior of an unbounded domain (ABAQUS, 2006). The naming of the infinite element boundary is shown in Figure 2.25, it only supports linear and continuum analyses such as plane stress, plane strain, three-dimensional, and axisymmetric infinite elements.

doi:10.6342/NTU202503752

When defining infinite elements in ABAQUS, it is crucial that the first face of the element is the one attached to the finite element mesh. For explicit dynamic analyses, infinite element nodes that are not located on the first face are treated differently compared to other types of analysis. These nodes are positioned outward, in the infinite direction, away from the finite element domain. In explicit simulations, the precise placement of these distant nodes is irrelevant, and no loads or boundary conditions should be applied to them. In contrast, in other types of analyses, the position of these outer nodes is significant, as they are included in the formulation of the element and can be referenced for load and boundary condition definitions.

Except in explicit procedures, the fundamental concept for modeling the infinite domain involves associating each element edge extending to infinity with an origin point known as the "pole." For example, in the case of a point load acting on a half-space boundary, the pole is located at the load application point. To maintain consistency with this formulation, the second node along each infinite edge must be positioned at twice the distance from the pole compared to the corresponding boundary node connecting the finite and infinite elements. Illustrations of this requirement are shown in Figure 2.26 (a)-(c).

Additionally, it is essential to arrange these second nodes properly to prevent element edges from overlapping or crossing (Figure 2.26-d), which would result in non-unique mappings. If such an issue occurs, ABAQUS will terminate the analysis and issue an error message.

doi:10.6342/NTU202503752

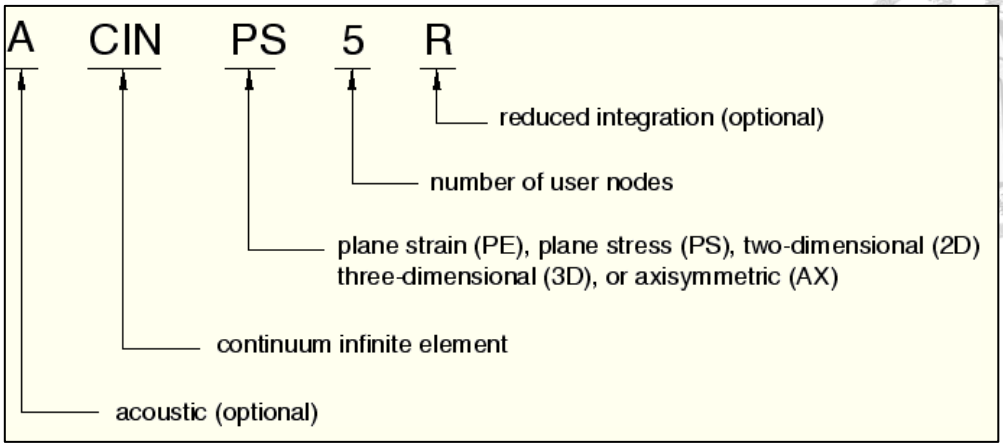

Figure 2.25 Naming of infinite elements (ABAQUS user's manual v6.6, 2024)

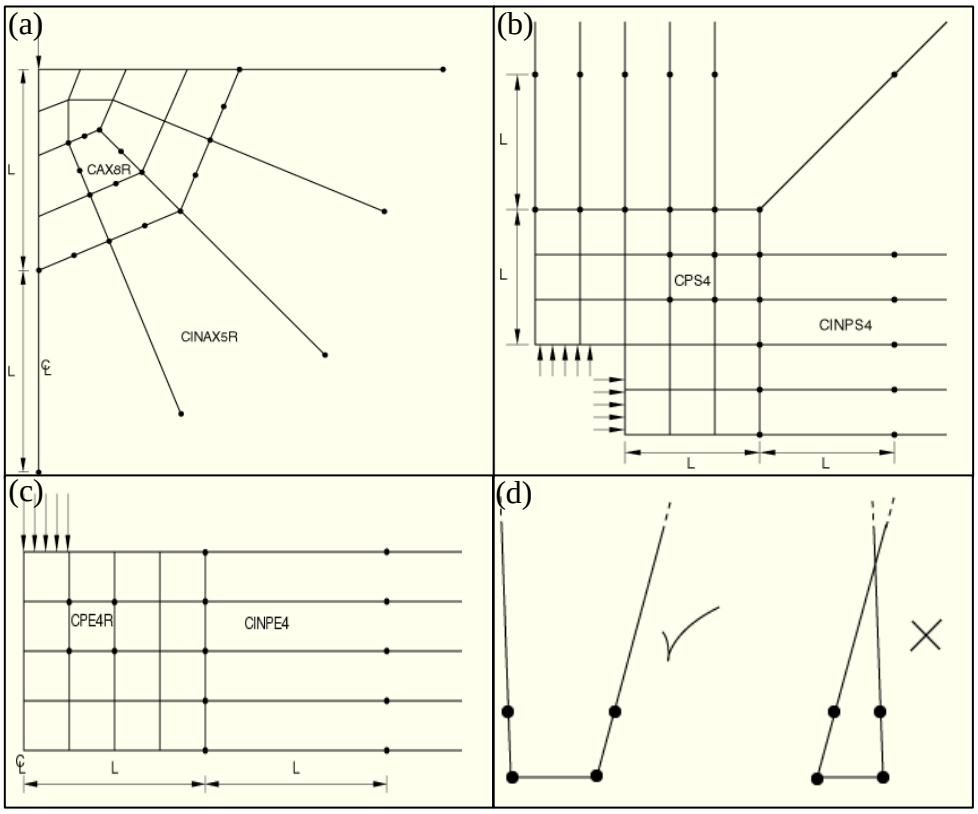

Figure 2.26 Examples of infinite elements setting and element edges in the infinite direction cannot cross over (a) Point load on elastic half-space. (b) Quarter plate with square hole. (c) Strip footing on infinitely extending layer of soil. (d) Examples of an acceptable and an unacceptable two-dimensional infinite element.

doi:10.6342/NTU202503752

2.4.2 Quiet Boundary on Elastic Half Space Simulation

Lysmer and Kuhlemeyer (1969) proposed a method where dashpots are installed independently along the boundary in both the normal and shear directions. These dashpots generate viscous tractions in response to motion, with the normal and shear components determined by Equations 2.35 and 2.36, where v_n and v_s are the normal and shear components of the velocity at the boundary ; ρ is the mass density and C_p, C_s are the p- and s-wave velocities.

$$t_n = -\rho C_p v_n \tag{2.35}$$

$$t_s = -\rho C_s v_s \tag{2.36}$$

These viscous effects can be incorporated directly into the Equations of motion at the boundary gridpoints. In ABAQUS, the normal and shear tractions, t_n and t_s , are computed and applied at each time step in the same manner as boundary loads. This method offers greater convenience compared to direct incorporation, and testing has confirmed its effectiveness. A potential concern with this implementation is numerical stability, since the viscous forces are based on velocities that lag by half a time step. Nonetheless, in practical analyses conducted so far, the use of non-reflecting boundaries has not necessitated any reduction in time step. Instead, timestep limitations are typically governed by the presence of small zones in the model.

In FLAC 3D 7.0 documentation (2024), the boundary condition setting of the viscous boundary is shown in Figure 2.27, the seismic waves propagate through the soil model and when they reach the boundary, the dashpot system will absorb the excess waves, which achieves the goal of simulating non-reflect scenario.

doi:10.6342/NTU202503752

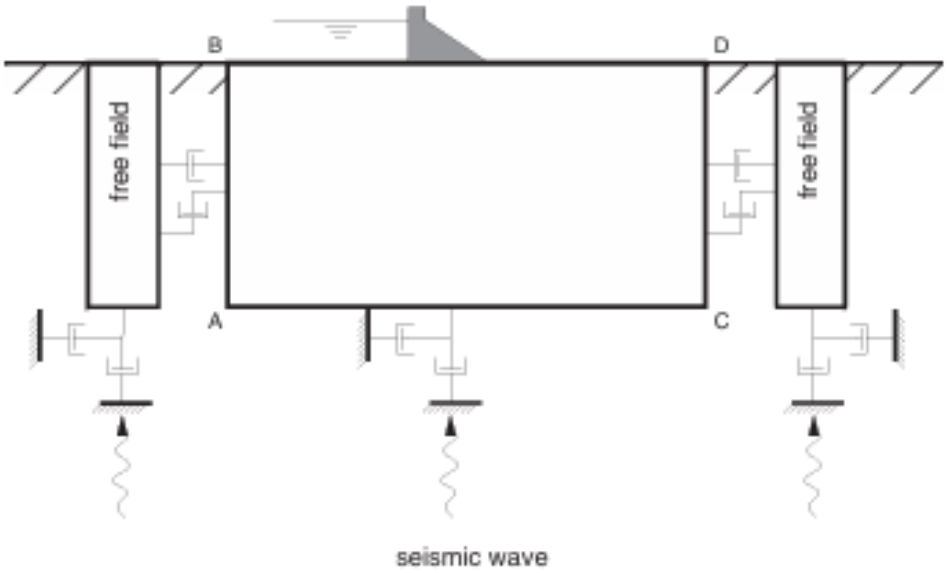

Figure 2.27 Model for seismic analysis of surface structures and free-field mesh.

(FLAC3D 7.0 documentation, 2024)

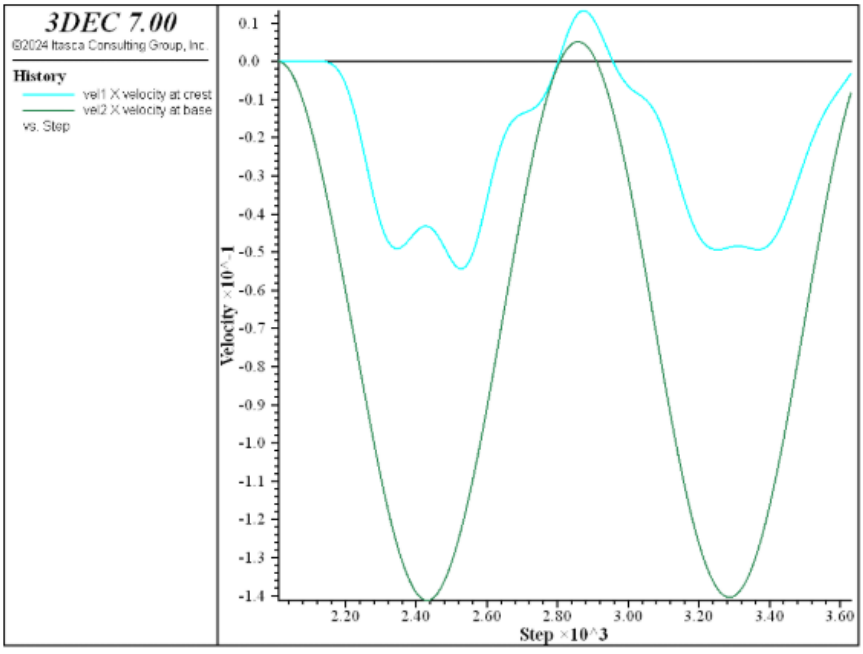

Figure 2.28 x-velocity histories at model base and dam crest using viscous boundaries.

(FLAC3D 7.0 documentation, 2024)

doi:10.6342/NTU202503752

Chapter 3 Methodology

3.1 ABAQUS Model Setting and Verification

According to section 2.2.1 in the literature review, a saturated clayey land slope was built to verify the model setting in ABAQUS. The problem in Section 2.2.1 is simplified to a single type of soil, and the base of the slope is assumed to be a rigid bedrock. The dimensions of the slope are not strictly specified; however, two factors must be carefully considered:

1. the slope angle β.

2. the ratio D between the total slope height and the height of the upper slope.

These two parameters influence both the failure mode of the slope and the calculation of the stability number m in Equation 2.1. Therefore, they must be controlled appropriately when constructing the model.

3.1.1 Model Geometry

The validation model is illustrated in Figure 3.1. The total slope width, upper platform width, and lower platform width are fixed at 150 m, 70 m, and 55 m, respectively. From this, the width of the sloped section B can be determined as $150 - 70 - 55 = 25$ m. Accordingly, the upper slope height H can be calculated using Equation 3.1.

$$H = L\tan\beta \tag{3.1}$$

In the analysis, we consider slopes with toe angles β of 20°, 30°, and 45°. Finally, the total slope height is determined by the ratio D, which is uniformly set as D=2 for all slope height calculations.

doi:10.6342/NTU202503752

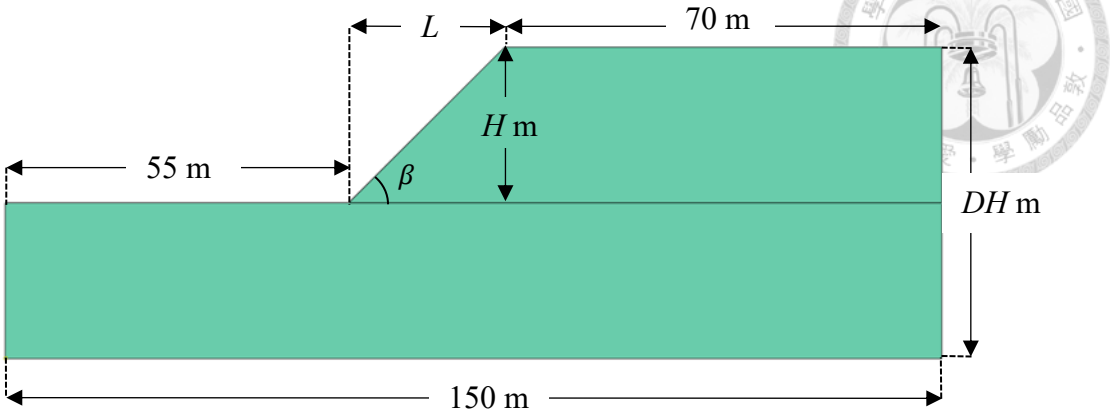

Figure 3.1 Model geometry of the clayey saturated land slope

3.1.2 Material

The soil parameters are listed in Table 3.1. Since the material is saturated clay under undrained conditions, the analysis is conducted using total stress parameters (s_u = 30 kPa; $\varphi = 0°$). According to the recommendations of NEHRP (2004), the Young's modulus for clay is taken as 100 MPa, Poisson's ratio as 0.45, and the total unit weight as 20 kN/m^3, which is typical for saturated clay.

Table 3.1 Soil parameters

Type	Shear strength			E (MPa)	μ	γ_{sat} (kN/m^3)
	S_u (kPa)	φ (°)	ψ (°)			
Clay	30	0	0	100	0.45	20

3.1.3 Element Type and Mesh

Since this study is conducted using a two-dimensional analysis, the z-direction is considered to extend infinitely. The CPE4R element (four-node plane strain element) is selected for the analysis. A structured mesh is adopted. In finite element analysis, a finer mesh leads to more accurate results; however, computational efficiency must also be considered. Therefore, a mesh size of 1 m × 1 m is used.

doi:10.6342/NTU202503752

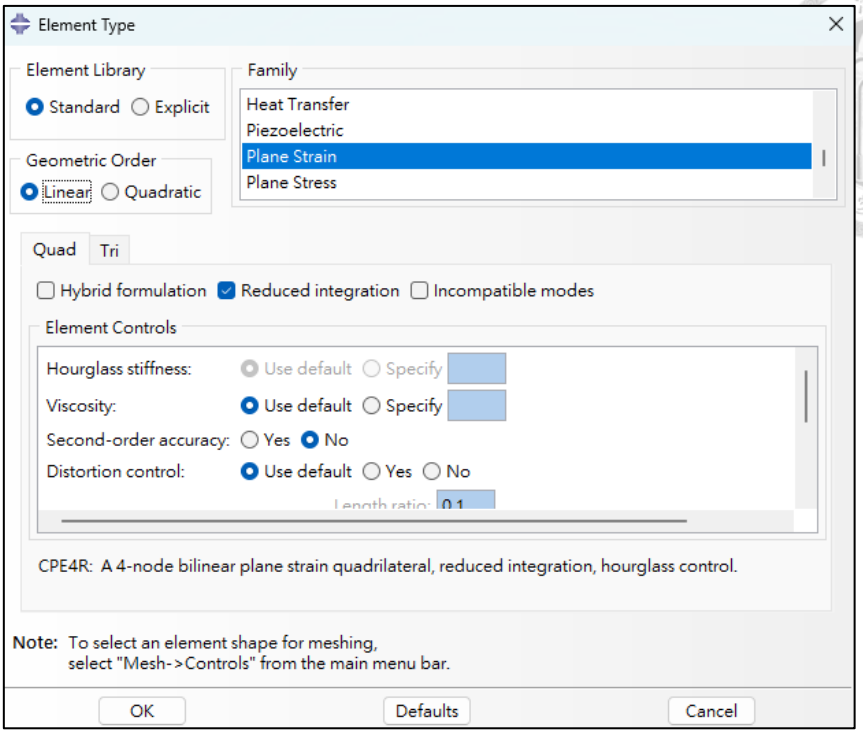

Figure 3.2 Element type CPE4R is used in the analysis

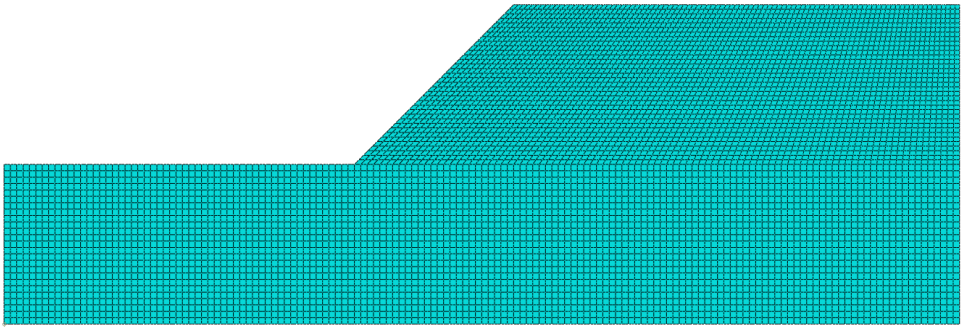

Figure 3.3 The slope model after meshing

3.1.3 Boundary Conditions and Loads

According to the slope modeling example in the ABAQUS User's Manual v6.6 (2024), the boundary and initial conditions of the slope are set as shown in Figure 3.4. Rollers are applied on both sides of the slope to restrain horizontal (x-direction) displacements, while the bottom is modeled as a pin support. These boundary conditions

doi:10.6342/NTU202503752

ensure that no unrealistic displacements or rotations occur during the geostatic stress initialization and strength reduction process. Gravity is also applied to the model, with an acceleration of 9.81 m/s².

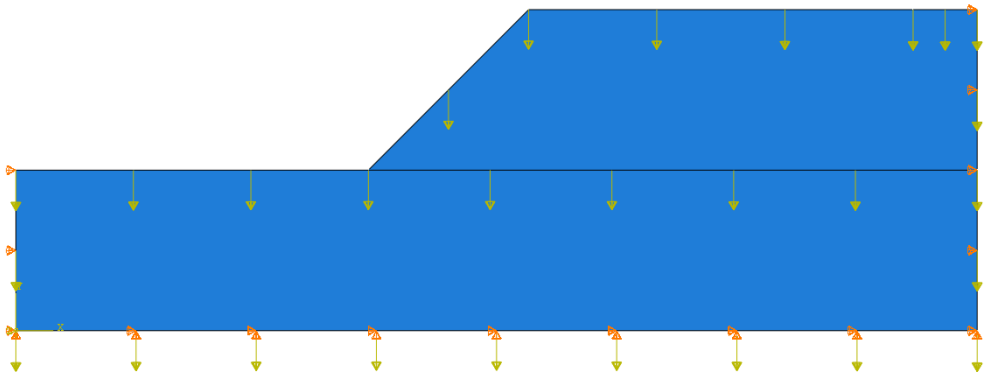

Figure 3.4 Boundary conditions and gravity load are applied in the analysis

3.1.4 Verification

According to Section 2.2.4 on the strength reduction method using finite element analysis, in this step we continuously reduce the undrained shear strength s_u to observe the failure behavior of the slope. When a sudden, large displacement or shear strain occurs, we define the corresponding strength at that moment as the model's ultimate resistance to sliding. Based on Figure 2.7, the stability number m can be determined according to the slope angle $\beta$and the ratio D. The obtained value of m is then substituted into Equation 2.1 to calculate the mobilized undrained shear strength c_d. Subsequently, the factor of safety for each of the three cases can be calculated using Equation 3.2, assuming an initial undrained shear strength of 30 kPa. The relevant parameters and computed results are summarized in Table 3.2. The strength reduction parameters and corresponding results from the ABAQUS finite element analysis are presented in Table 3.3. The factor of safety in this analysis was calculated according to the methodology described in Equation 2.14. A comparison of the factors of safety obtained using the traditional limit equilibrium

doi:10.6342/NTU202503752

methods by Fellenius (1927) and Taylor (1937) with those derived from the strength reduction finite element method in ABAQUS is shown in Figure 3.5. The results demonstrate a high level of agreement, indicating that the modeling parameters adopted in ABAQUS—including model dimensions, boundary conditions, and mesh types—are appropriate. This validates the model setup and provides a reliable basis for the subsequent analyses of submarine slope stability.

$$\text{FS} = \frac{c_u}{c_d} \tag{3.2}$$

Table 3.2 Factor of safety calculation by Fellenius (1927) and Taylor (1937)

β (°)	m	c_d (kPa)	c_u (kPa)	FS
20	0.160	29.118	30	1.030
30	0.177	51.095	30	0.587
45	0.180	90.000	30	0.333

Table 3.3 Factor of safety calculation by ABAQUS strength reduction method.

β (°)	$c_{reduced}$ (kPa)	c_u (kPa)	FS
20	31.080	30	1.036
30	18.660	30	0.622
45	9.960	30	0.332

doi:10.6342/NTU202503752

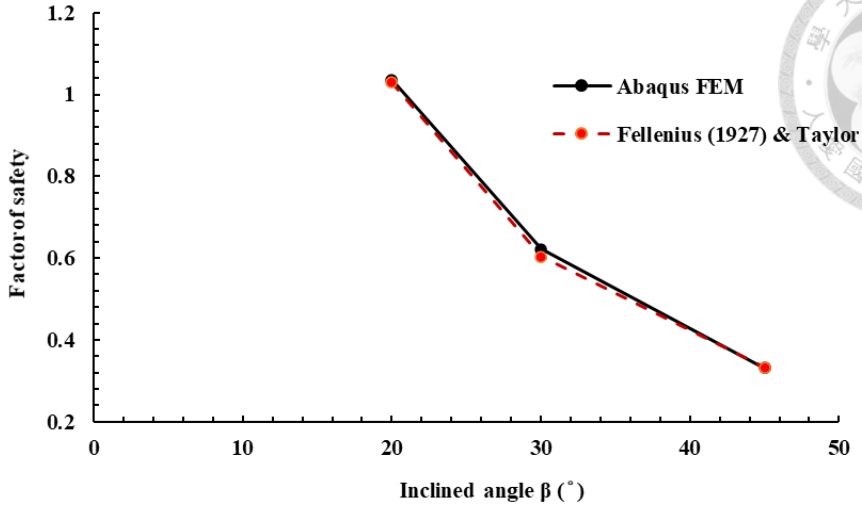

Figure 3.5 Factor of safety comparison varies in inclined angles.

3.2 Static Analyses of Submarine Slope under Numerical Simulation

After validating the ABAQUS model for a saturated land slope, we can proceed with the stability analysis of submarine slopes and compare the differences and trends among various slope angles, water depths, and analysis methods. Sections 3.2.1 to 3.2.3 will describe the initial condition settings for submarine slopes (initial stress field and pore water pressure field), the selection of slope angles, and the three analysis methods.

3.2.1 Initial Conditions

Since the current problem involves a submarine slope rather than a saturated slope on land, the initial conditions must be different. For example, the water pressure on the slope surface, the initial stress in the soil, and the pore water pressure within the soil all vary. Accurate definition of these initial conditions is essential to ensure that the submarine slope simulation is reasonable. Figure 3.6 illustrates the schematic of water pressure on the slope surface and the definition of seawater depth, respectively. Water pressure is simulated as a pressure load, and water depth is defined as the vertical distance

doi:10.6342/NTU202503752

from the sea surface to the lower slope platform. In addition, the definition of initial stress significantly influences the results of geostatic stress equilibrium. In Abaqus, initial stress can only be defined at two elevations within a given region (e.g., the slope surface and the bottom), and the stress field is interpolated between these two points based on the input values (see Figure 3.9Figure 3.9). Therefore, the slope region must be partitioned into several sections, with each partition assigned an approximately appropriate stress field. In our model, we divided the slope section into partitions every 5 meters horizontally, resulting in a total of 12 partitions including the left and right platforms (Figure 3.7).

In models considering pore water pressure, the soil's permeability coefficient *k*, degree of saturation *S*, and void ratio *e* must be defined, as these parameters influence the rate of water flow through the soil. However, in the static analysis of submarine slopes, based on the assumptions proposed by Denlinger and Iverson (1990), no seepage occurs along the slope boundaries, and the soil is assumed to be fully saturated (S = 100%). In this section, we set $k = 1.0 \times 10^{-5}$ m/s and $e = 0.8$. It should be noted that if k is set too low, it can lead to difficulties in achieving water pressure equilibrium.

Next, a linearly increasing water pressure boundary condition with depth, along with a predefined field, is applied to the entire slope region. The setup method is illustrated in Figure 3.11 to Figure 3.13. The calculation of water pressure u_{sea} follows Equation 3.1, where γ_w is the unit weight of seawater, typically ranging from 1.02 to 1.07 g/cm³. Here, we adopt a value of 1.024 g/cm³, g is the gravitational acceleration. H denotes the vertical distance from the sea surface to the bottom of the slope, while h represents the height of the lower slope platform. In the following sections, we will discuss how different seawater depths influence slope stability, with h fixed at 25 m.

doi:10.6342/NTU202503752

$$u_{sea} = \gamma_{sea} \times g \times (H - h) \tag{3.1}$$

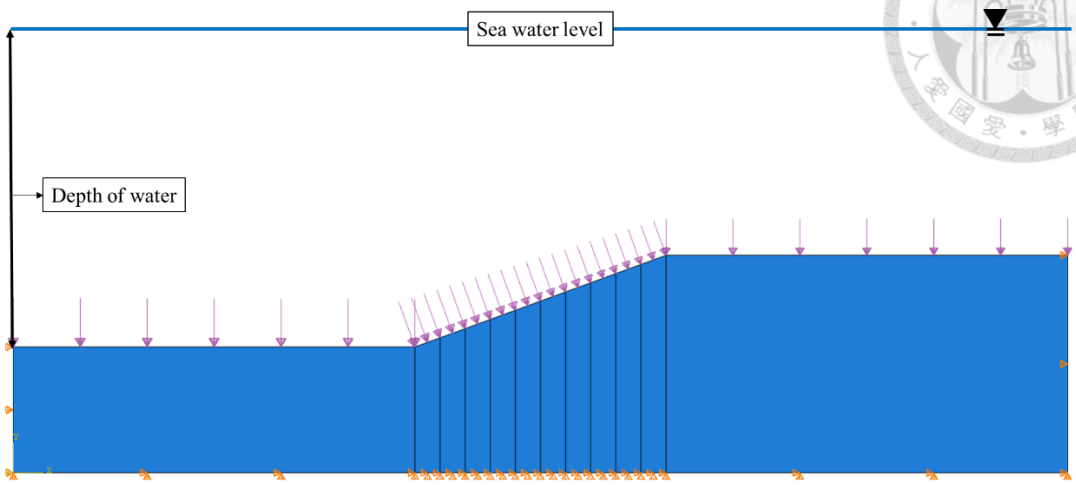

Figure 3.6 Water pressure illustration and definition of the sea water depth

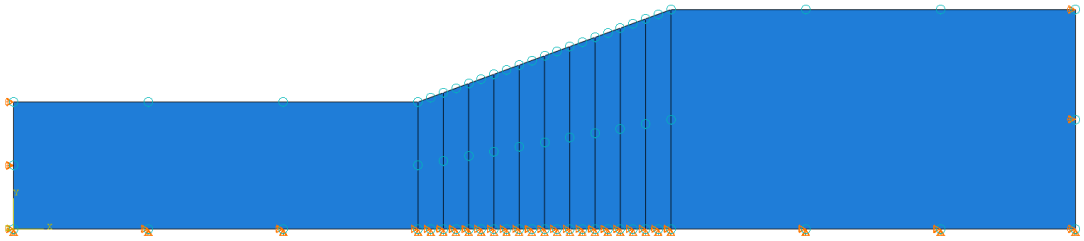

Figure 3.7 The slope is divided into 12 partitions.

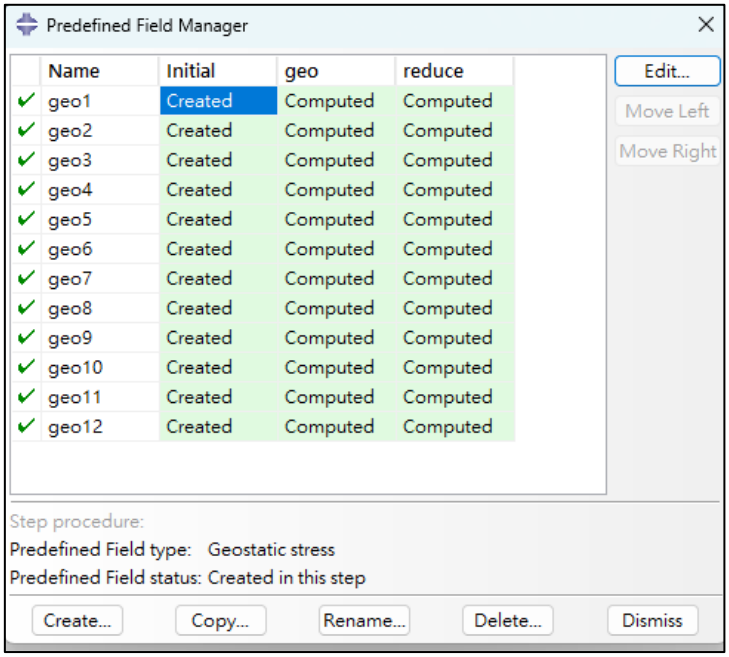

Figure 3.8 Geostatic stress setting in the predefined field manager.

doi:10.6342/NTU202503752

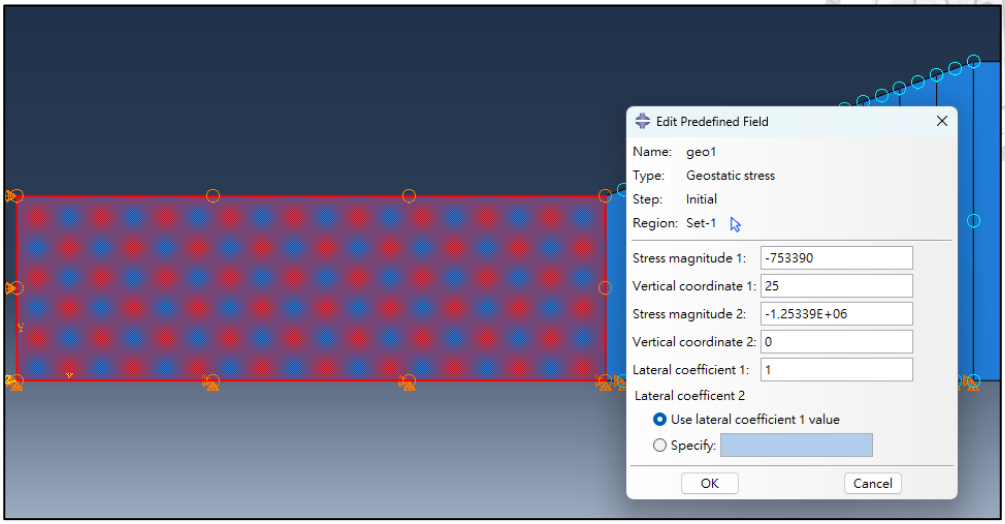

Figure 3.9 Each partition should be applied the initial stress at two different elevations.

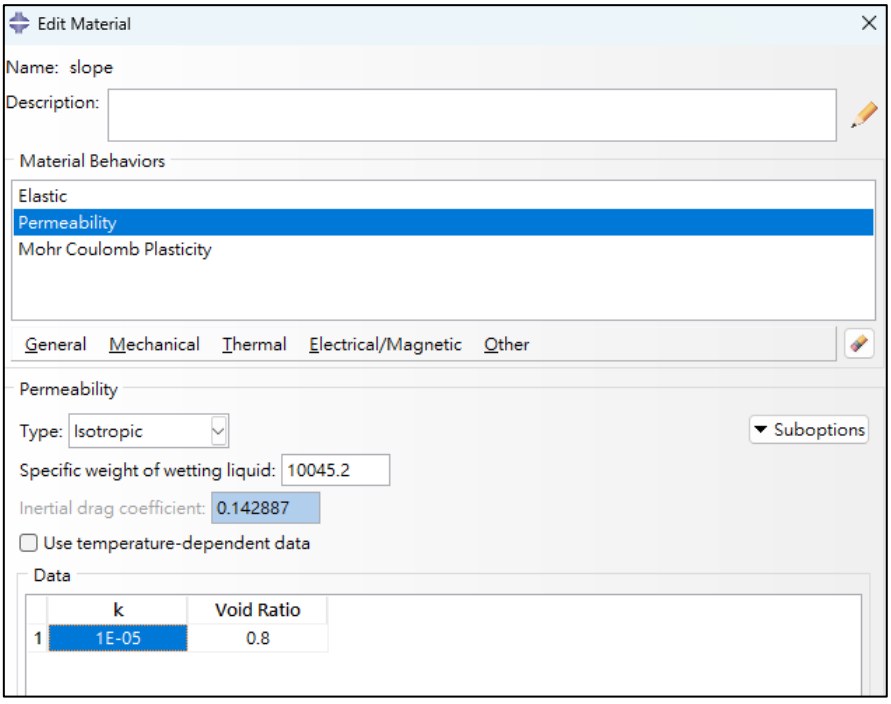

Figure 3.10 Permeability assignment in the soil material.

doi:10.6342/NTU202503752

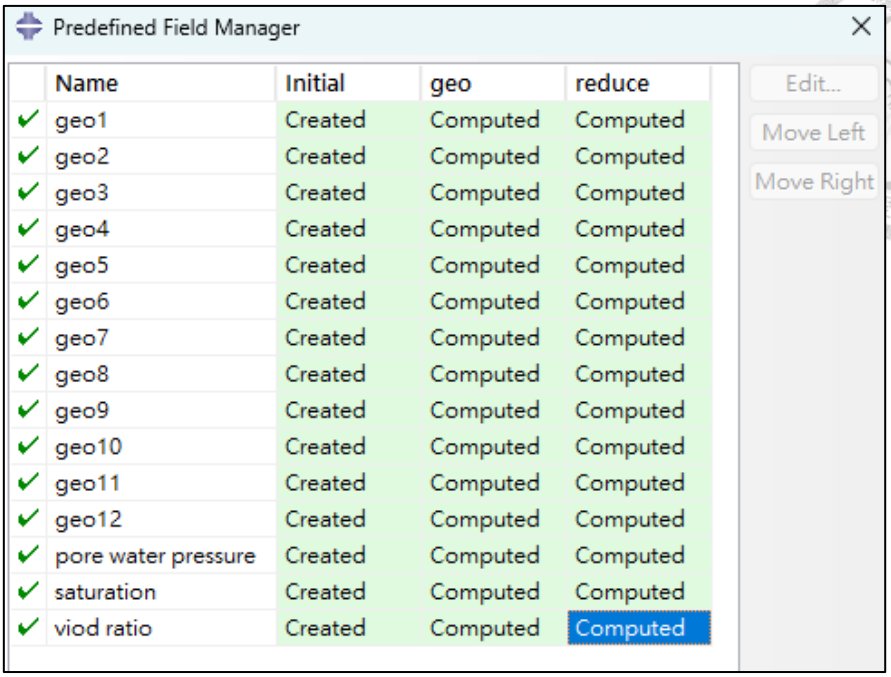

Figure 3.11 The pore pressure, saturation and void ratio initial values are set in the predefined field.

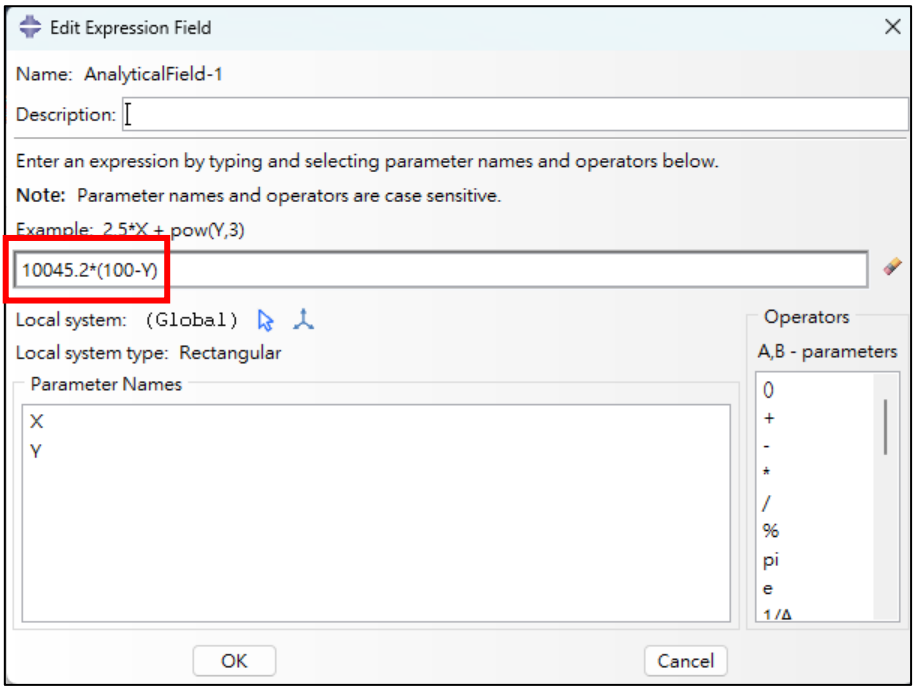

Figure 3.12 Pore pressure distribution calculation.

doi:10.6342/NTU202503752

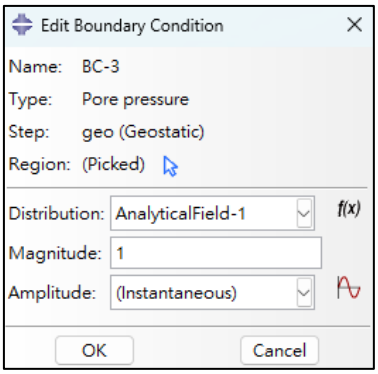

Figure 3.13 Pore pressure boundary condition setting.

3.2.2 Model Geometry of 5 Degree & 10 Degree & 20 Degree Slope

The geometric configuration of the model used for the static stability analysis of the submarine slope is shown in Figure 3.14 to Figure 3.16. Unlike the previous section, the slope angle of the submarine slope is significantly gentler than that of the terrestrial slope, typically ranging between 5° and 20°. To ensure that the failure arc can fully develop without being constrained by boundary effects, the model was widened—resulting in a total base width of 210 meters, with the slope region occupying 50 meters of this width. The height of the lower slope platform was fixed at 25 meters, and the height of the upper slope was then calculated based on the specified slope angle.

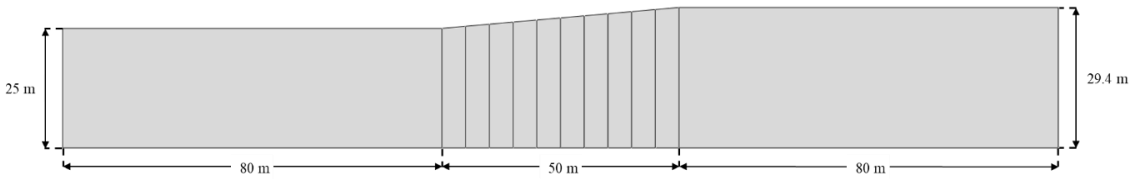

Figure 3.14 Model geometry and size of the 5-degree slope.

doi:10.6342/NTU202503752

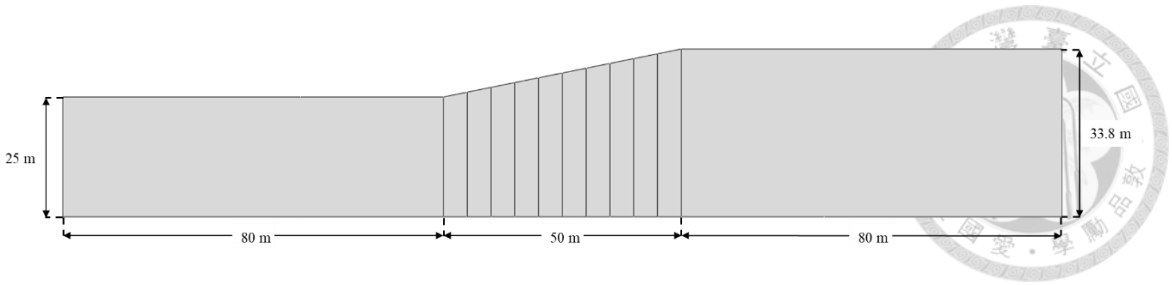

Figure 3.15 Model geometry and size of the 10-degree slope.

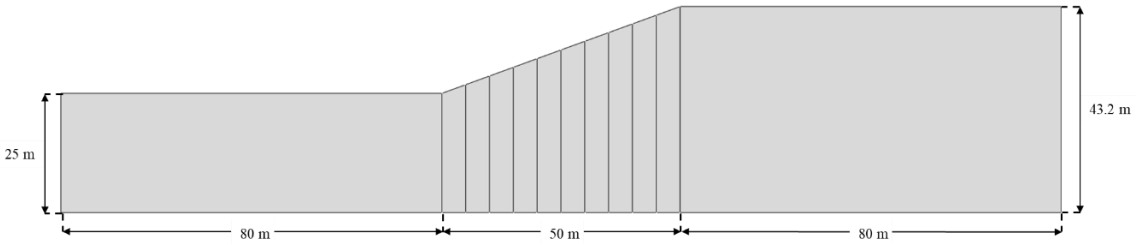

Figure 3.16 Model geometry and size of the 20-degree slope.

3.2.3 Total Stress & Effective Stress and Effective Stress with Pore Pressure Models

As discussed in the previous section, the initial stress conditions and the analysis method significantly affect the results of slope stability analysis. Total stress analysis and effective stress analysis yield different stress paths. In this section, we compare three different stress analysis approaches: total stress analysis, effective stress analysis, and effective stress analysis considering pore water pressure distribution. Two sets of soil strength parameters are incorporated to examine the influence on the safety factor distribution, depth and width of the failure surface, and other related failure characteristics. The stress computation methods are described in Equations 3.2 and 3.3, where σ_{total} is the total stress, σ' is the effective stress and u_{sea} is the water pressure calculated in Equation 3.1. The two soil strength parameters are listed in Table 3.4.

Theoretically, under conditions where no excess pore water pressure is generated, the results obtained from the effective stress model considering pore water pressure

doi:10.6342/NTU202503752

should be the same as those from the pure effective stress model. This is because, in ABAQUS, the effective stress is internally calculated by subtracting the input pore pressure from the input total stress. In the end, the results of these models will be demonstrated in section 4.2.1 to 4.2.4.

$$\sigma_{\text{total}} = \sigma' + u_{\text{sea}} \tag{3.2}$$

$$\sigma' = \gamma' \times g \times h \tag{3.3}$$

Table 3.4 Two different soil strength parameters

Total stress parameters			Effective stress parameters		
s_u (kPa)	φ (°)	ψ (°)	c' (kPa)	φ' (°)	ψ (°)
60	0	0	5	20	0.1

3.3 Earthquake Analysis

After discussing the static analysis, this section focuses on the dynamic analysis of the submarine slope. By introducing seismic velocity histories into the model, we simulate the slope's behavior under seismic loading. During this process, we used the one-dimensional wave propagation software DEEPSOIL to validate the wave propagation and reflection in ABAQUS for both rigid half-space and elastic half-space models under linear and nonlinear material. We also analyzed ground responses at different depths, shear strain histories, and more.

Due to the current lack of experimental studies on the seismic response of submarine slopes, we aimed to develop a reliable and evidence-based numerical simulation approach to investigate how factors such as incident wave angle, peak ground acceleration (PGA), earthquake magnitude, and frequency content affect the slope behavior.

doi:10.6342/NTU202503752

3.3.1 Infinite Element Boundary

According to Section 2.4.1, to prevent incorrect wave reflections at the model boundaries, the ABAQUS infinite boundary was adopted. However, the energy absorption performance of infinite elements is not entirely effective, and surplus energy reflection still occurs near the boundary regions. Therefore, in order to determine the minimum domain unaffected by boundary effects, we first constructed a 500 m × 20 m rectangular linear soil model, and applied 1-meter-thick infinite boundary zones on both sides of the model (Figure 3.17).

According to the ABAQUS User's Manual v6.6, the thickness of the infinite boundary is not critical; the key is that the energy must be swept outward. Thus, as shown in Figure 3.18 to Figure 3.20, the infinite boundary must be meshed using the sweep technique, with the sweep direction pointing away from the model, in this way, the infinite boundaries absorb excess energy or seismic waves successfully. The initial Mesh Type is set to AC2D4R (a 4-node linear 2D acoustic quadrilateral, reduced integration, with hourglass control). This element type is not the naming convention for infinite elements and must be manually modified in the generated input file. Following the naming convention in Section 2.4.1, we adopt CINPE4 as the correct designation for the infinite boundary element (Figure 3.21).

Figure 3.17 The 500m x 20m model (half size) with the infinite boundary.

doi:10.6342/NTU202503752

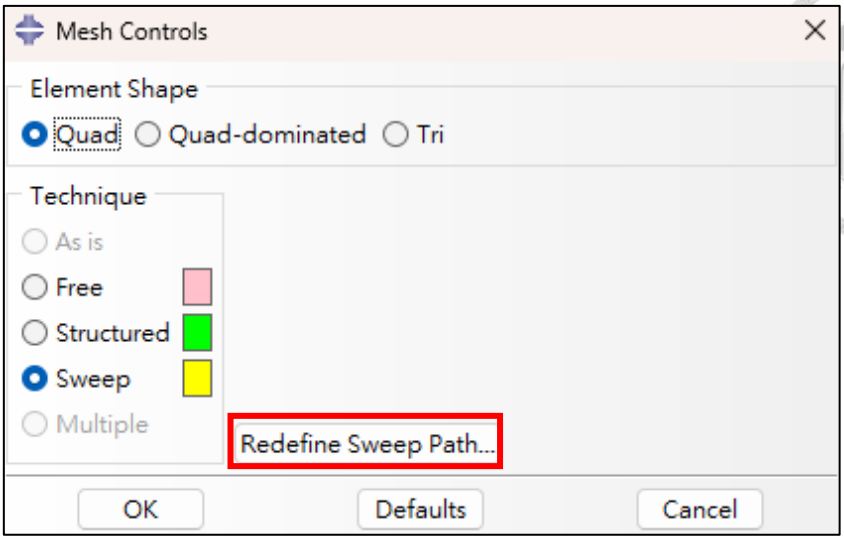

Figure 3.18 Assigning sweep mesh to the infinite element.

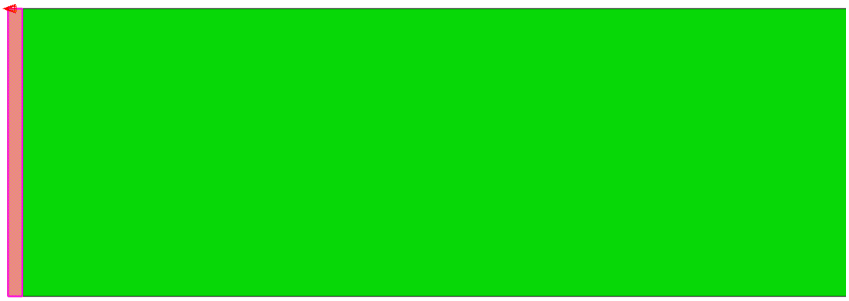

Figure 3.19 Defining sweep path pointing away from the model.

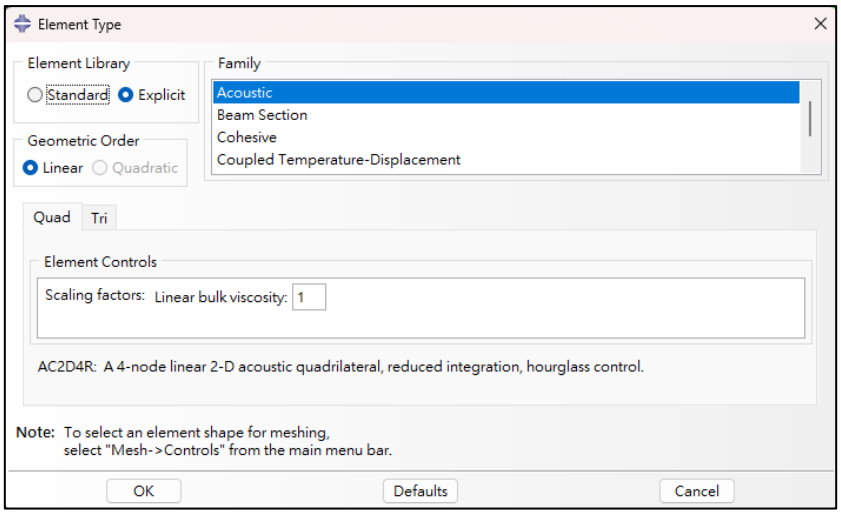

Figure 3.20 Infinite element type assignment in ABAQUS GUI.

doi:10.6342/NTU202503752

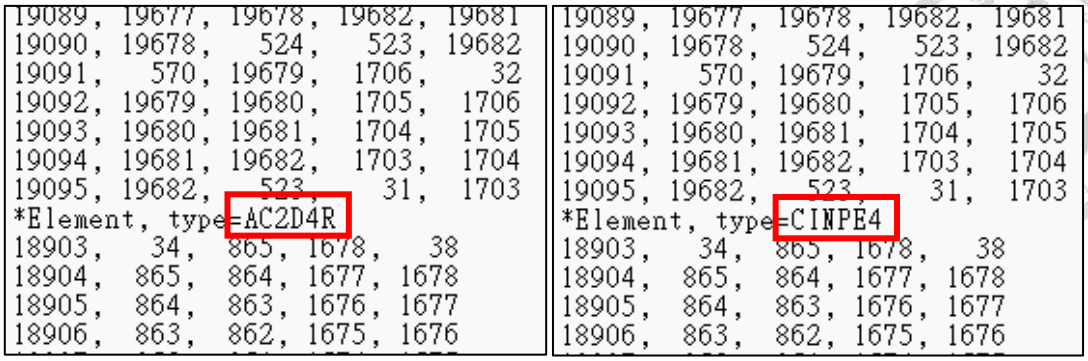

Figure 3.21 Changing the element type into CINPE4 in the model input file.

3.3.2 Ground Response Verification in Rigid Half Space

In this section, we continue with the model established in Section 3.3.1 to verify wave propagation. In the case of a rigid half-space, we employ dynamic explicit analysis. It is found that the initial stress state of the soil has a significant impact on wave propagation; therefore, a geostatic stress equilibrium must be performed first. The soil parameters used are listed in Table 3.5. In both section 3.3.2 and section 3.3.4, this elastic soil model is adopted. Structural damping is also considered, and the Rayleigh damping coefficients are calculated using Equations 3.4 and 3.5. The natural frequency calculation formula in Equation 3.7, after calculation, f_1 is 2.5 Hz, and the second natural frequency is five times the first, i.e., 12.5 Hz, with a damping ratio of 5%. After completing the geostatic analysis of the rectangular soil block, ABAQUS outputs an ODB file containing stress fields. All subsequent seismic analyses must import this file as the initial conditions. Next, we describe the boundary conditions and seismic loading method used in the dynamic step. As shown in Figure 3.23 (a), the encastre boundary conditions (U1 = U2 = U3 = UR1 = UR2 = UR3 = 0) are applied to the sides of the infinite boundary and at the interface between the soil and the infinite boundary. Locking all degrees of freedom ensures that stress fields do not leak out, preventing excessive deformation at the boundaries—a phenomenon commonly observed in inelastic models. Due to the energy-

doi:10.6342/NTU202503752

absorbing effect of the infinite boundary and the sufficiently large model width, the additional constraints do not affect the analysis results. At the bottom, U2 = 0 is imposed to simulate full reflection of waves reaching the base. The seismic input is applied as a boundary condition in the U1 direction (horizontal velocity history) at the model base. This study only considers seismic loading in the U1 direction. Importantly, no constraints should be applied to U1 at the bottom—otherwise, seismic waves will not be able to propagate into the model. The Northridge earthquake is selected for testing, and the input velocity time history is shown in Figure 3.24. Finally, we compared the response spectra and shear strain histories at different depths between ABAQUS and DEEPSOIL to validate this modeling approach. Additionally, to ensure that the model is sufficiently wide to avoid boundary effects, the response spectra at the top of the slope at varying distances from the lateral boundaries were also compared with DEEPSOIL results. This comparison was used to determine the final dimensions of the slope model for seismic analysis. The verification results will be presented in section 3.3.4.

$$\alpha = \frac{2\xi\omega_1\omega_2}{\omega_1+\omega_2} \tag{3.4}$$

$$\beta = \frac{2\xi}{\omega_1+\omega_2} \tag{3.5}$$

$$\omega = 2\pi f \tag{3.6}$$

$$f = \frac{V_s}{4H} \tag{3.7}$$

Table 3.5 Soil properties in earthquake analysis verification.

Soil Type	Structural Damping		E (MPa)	μ	Density (kg/m^3)	V_s (m/s)
	α	β				
Clay	1.309	0.00106	236	0.45	2000	200

doi:10.6342/NTU202503752

```
**
** STEP: eq
**
*INITIAL CONDITION,TYPE=STRESS,FILE=Job-geo-rigid.odb
*Step, name=eq, nlgeom=YES, inc=100000
*Dynamic
0.01,39.98,0.0003998
**
** BOUNDARY CONDITIONS
**
```

Figure 3.22 Applying geostatic stress initial conditions to the earthquake analysis.

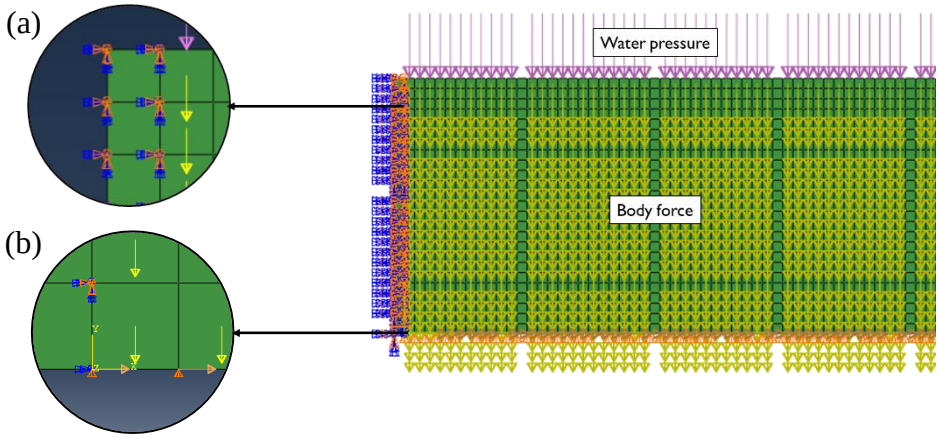

Figure 3.23 (a) Encastre boundary conditions along the interface between the soil and the infinite elements and the outside of the infinite elements. (b) The bottom boundary conditions U2=0 and the velocity history input of the earthquakes.

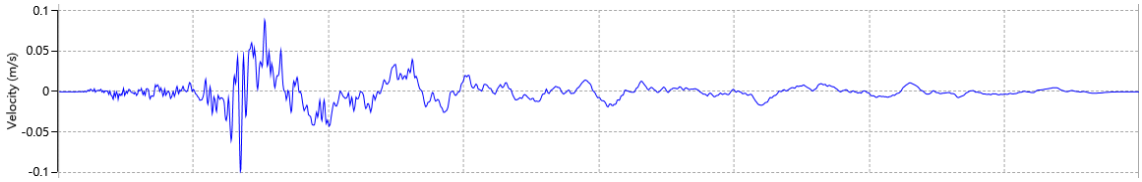

Figure 3.24 Input motion of the Northridge earthquake.

3.3.3 Ground Response Verification in Elastic Half Space

According to Section 2.4.2, in order to simulate an elastic half-space, we adopted the damping coefficient calculation method proposed by Lysmer and Kuhlemeyer (1969), combined with the viscous boundary simulation approach described in the FLAC 3D 7.0

doi:10.6342/NTU202503752

documentation (2024) to achieve energy absorption effects. In ABAQUS, a damping system can be established via the Interaction → Special option, which offers two types of configurations: “Connect two points” (as shown in the Figure), and “Connects points to ground”. Since the example in FLAC 3D connects the main model to the free-field boundary using dampers, we chose the two-point connection method (Figure 3.25). The free-field boundary consists of a 500 m × 1 m soil block with material properties identical to the test block. In the elastic half-space simulation, the seismic history is applied to the free-field boundary and transmitted into the main model through the dampers. Given that the seismic wave propagates in the 1-direction (x-direction), the damping effect was also applied in the same degree of freedom, as illustrated in Figure 3.26. Finally, the damping coefficient calculated using Equation 2.36 was input. The proper installation of the dampers can be viewed in the Interaction module. It is especially important to ensure that the nodes at the base of the slope and the corresponding nodes in the free-field are correctly paired (Figure 3.27).

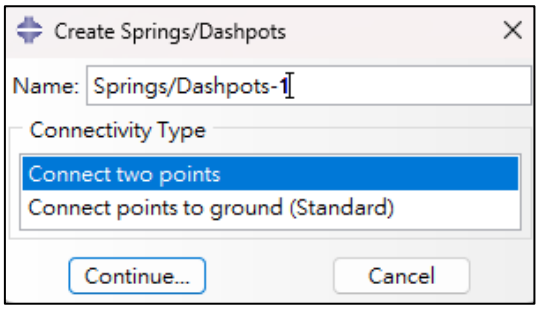

Figure 3.25 Two types of dashpots in ABAQUS.

doi:10.6342/NTU202503752

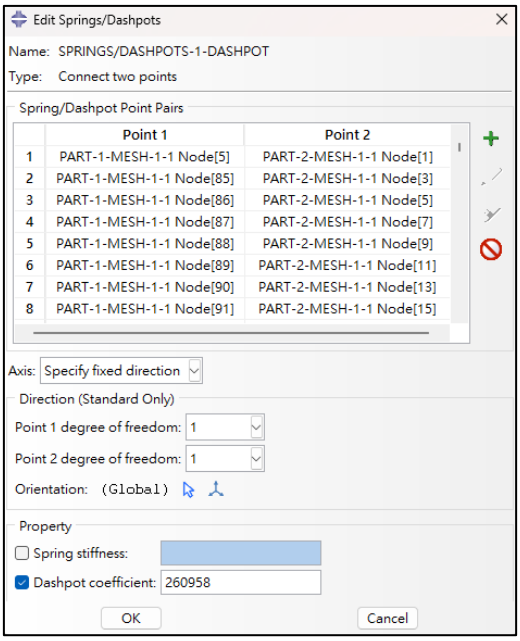

Figure 3.26 Setting of the x-direction dashpots.

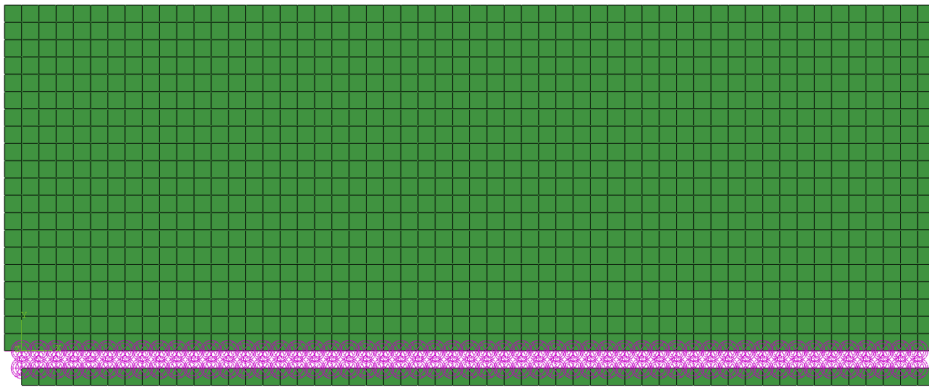

Figure 3.27 Dashpot system in elastic-half space simulation (pink part).

Since the damping system with fixed degrees of freedom (DASHPOT2 elements) can only be analyzed using ABAQUS/Standard, the seismic simulation must be performed using dynamic implicit analysis after completing the initial geostatic stress equilibrium. Implicit analysis is highly sensitive to the time increment, and therefore, a large initial time step cannot be assigned. Although the Northridge earthquake record outputs data every 0.02 seconds, testing has shown that the initial time increment must be set to less than 0.01 seconds to obtain accurate results (Figure 3.28). Next, the boundary

doi:10.6342/NTU202503752

conditions of the Elastic Half Space model are described. The two lateral sides of the soil block are defined as encastre (U1 = U2 = U3 = UR1 = UR2 = UR3 = 0), the same as in the rigid half-space model. During the geostatic step, the base of the slope and the free-field boundary are set to U1 = U2 = 0. In the seismic step, these boundaries are changed to U2 = 0, i.e., the x-direction restraint is released (as shown in Figure 3.29 and Figure 3.30), for the same reasons explained in Section 3.3.2.

The key difference from Section 3.3.2 lies in the input location of the seismic motion. In the elastic half space simulation, the seismic history must be applied to the nodes on the free-field boundary—either those connected to dampers or those at the base of the free-field boundary (Figure 3.31). If the seismic motions are applied directly at the slope base, seismic waves will enter the slope directly, rendering the dampers ineffective. Figure 3.32 compares the plastic strains at the top of a 500 m × 20 m soil block under three cases of seismic input locations, demonstrating that applying the earthquake motions at the slope base (Case 3) fails to activate the damping system. The verification results will be demonstrated in section 3.3.4, noticed that the elastic half space bedrock parameters are set to the same as the testing block in Figure 3.33.

doi:10.6342/NTU202503752

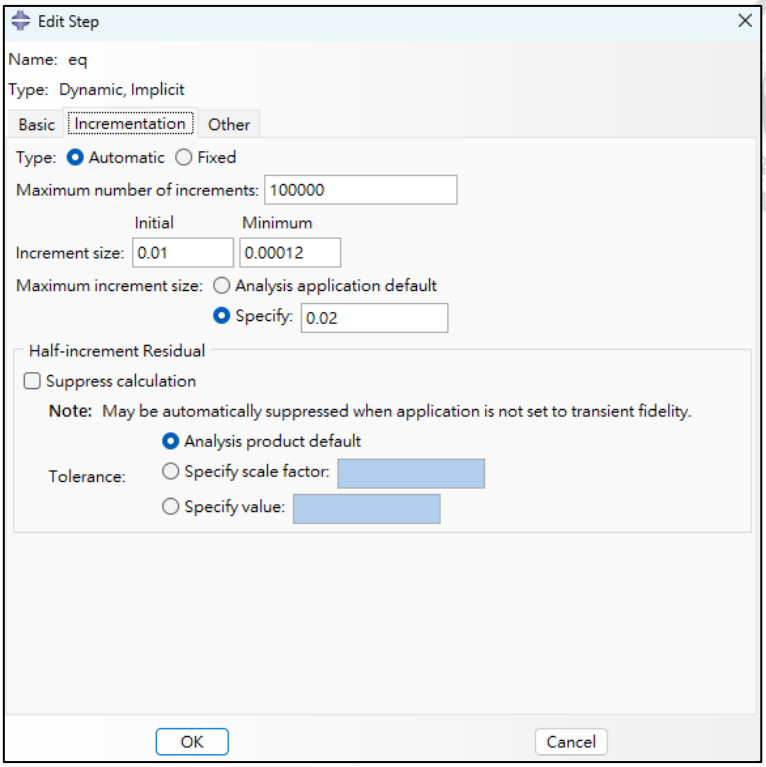

Figure 3.28 Initial time increment size is set to 0.01 second in dynamic implicit step.

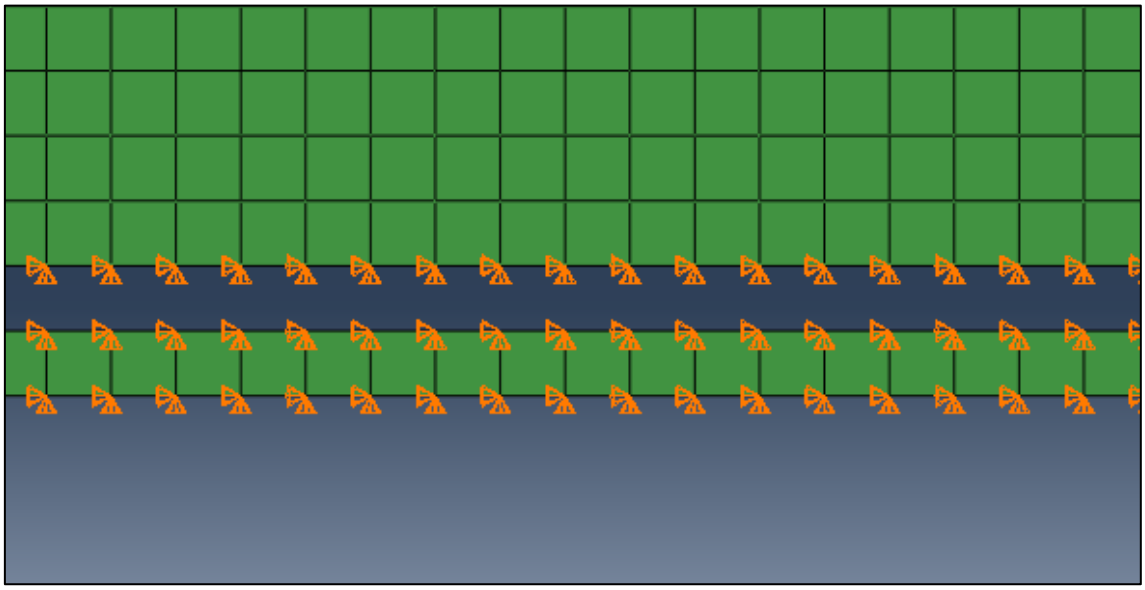

Figure 3.29 Boundary conditions of the slope base and the free field boundary in geostatic step.

doi:10.6342/NTU202503752

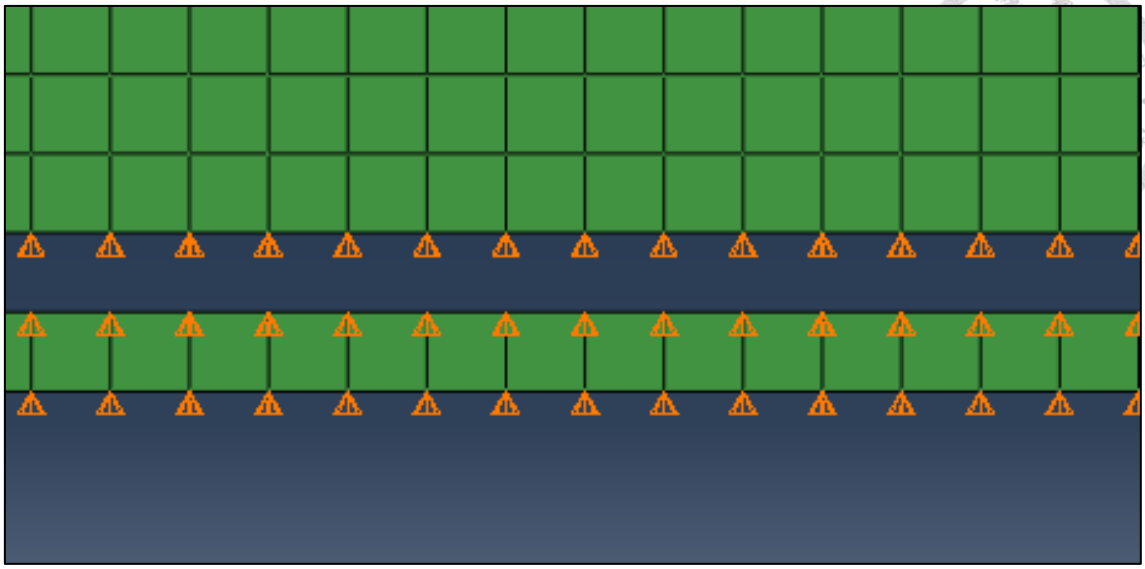

Figure 3.30 Boundary conditions of the slope base and the free field boundary in dynamic step.

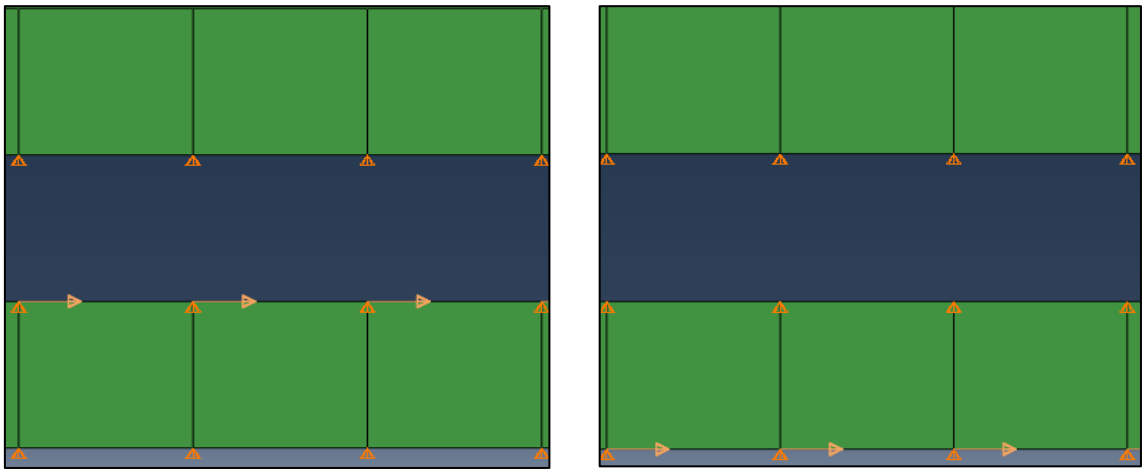

Figure 3.31 Seismic motions should be applied at the top or at the base of the free-field boundary.

doi:10.6342/NTU202503752

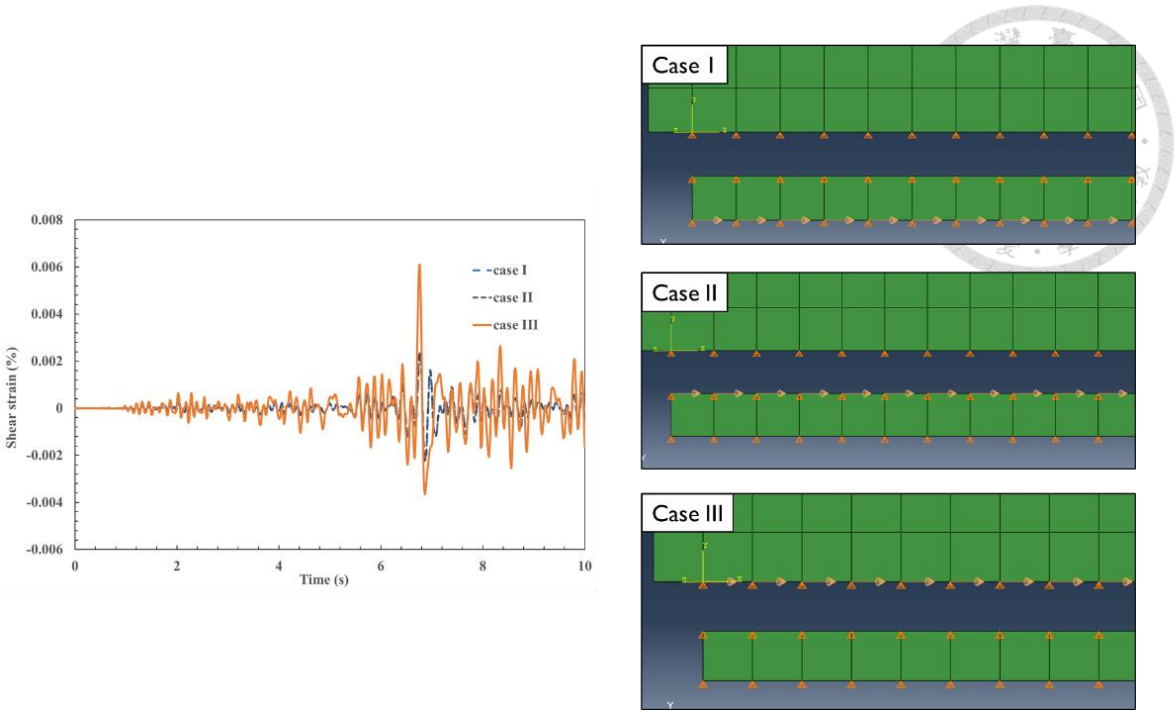

Figure 3.32 Shear strain history at the top of the testing block under three cases.

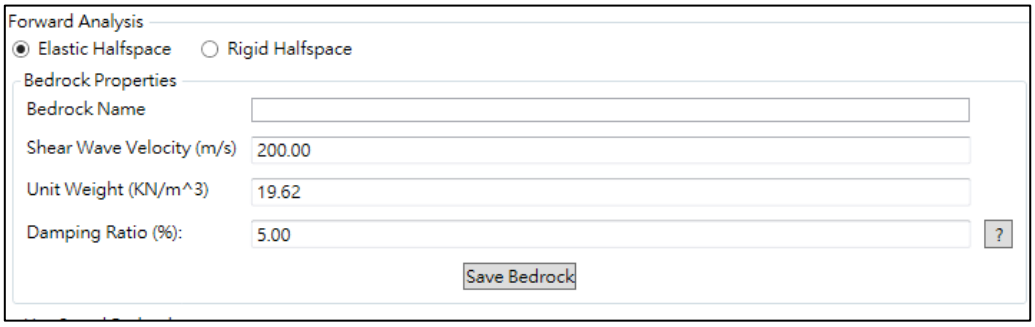

Figure 3.33 Elastic half space bedrock parameters in DEEPSOIL.

3.3.4 Model Dimensions for Seismic Slope Stability Analysis

Based on the simulation results presented in Sections 3.3.2 and 3.3.3, The 5% damped response spectra were extracted at various distances from the lateral model boundaries and compared with the results obtained from DEEPSOIL. The coordinate origin is shown in Figure 3.34. Specifically, acceleration spectra at x = 50 m, 100 m, 150 m, 200 m, and 250 m and y = 20 m were analyzed under both rigid and elastic half-space boundary conditions, as illustrated in Figures 3.35 and 3.36. The results indicate that, for

doi:10.6342/NTU202503752

the rigid half-space model, x must be greater than 200 m to obtain accurate acceleration spectra, whereas for the elastic half-space model, x must exceed 150 m.

To further validate the boundary effects, response spectra and plastic strain profiles were examined at various depths (y = 4 m, 8 m, 12 m, and 16 m) along the vertical sections at x = 200 m in both the rigid half-space model the elastic half-space model in Figure 3.35 to Figure 3.40. These results showed strong agreement with the DEEPSOIL simulations. Only after confirming this consistency can it be concluded that the slope crest and toe must be positioned at least 200 m away from the lateral boundaries to minimize the influence of boundary effects on the analysis results.

To ensure a conservative design, a platform extension of 250 m was adopted on both the upper and lower sides of the slope. The height of the lower platform was fixed at 25 m, while the height of the upper slope was determined based on the slope angle, following the same calculation method as described in Section 3.2.2. The width of the inclined slope region was also set to 50 m. As a result, the total width of the slope region was defined as 250 + 250 + 50 = 550 m. With the addition of 1 m thick infinite boundary zones on both lateral sides, the overall model width was set to 552 m. The slope angles considered in the analysis were the same as those used in Section 3.2.2, specifically 5°, 10°, and 20°. The geometric configuration of the slope models is illustrated in Figure 3.41 to Figure 3.43.

doi:10.6342/NTU202503752

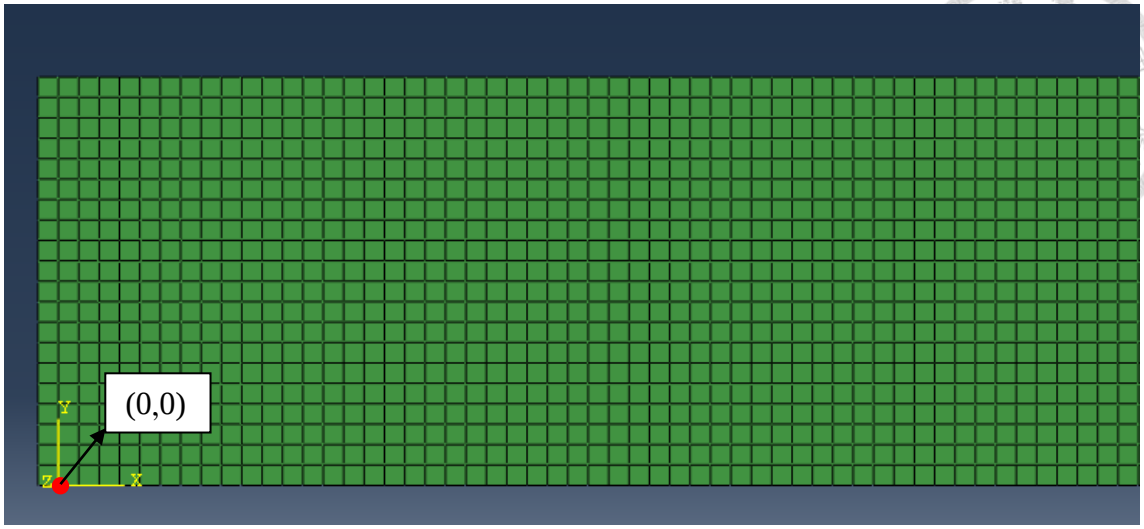

Figure 3.34 The origin of the 500 m x 20 m soil block.

doi:10.6342/NTU202503752

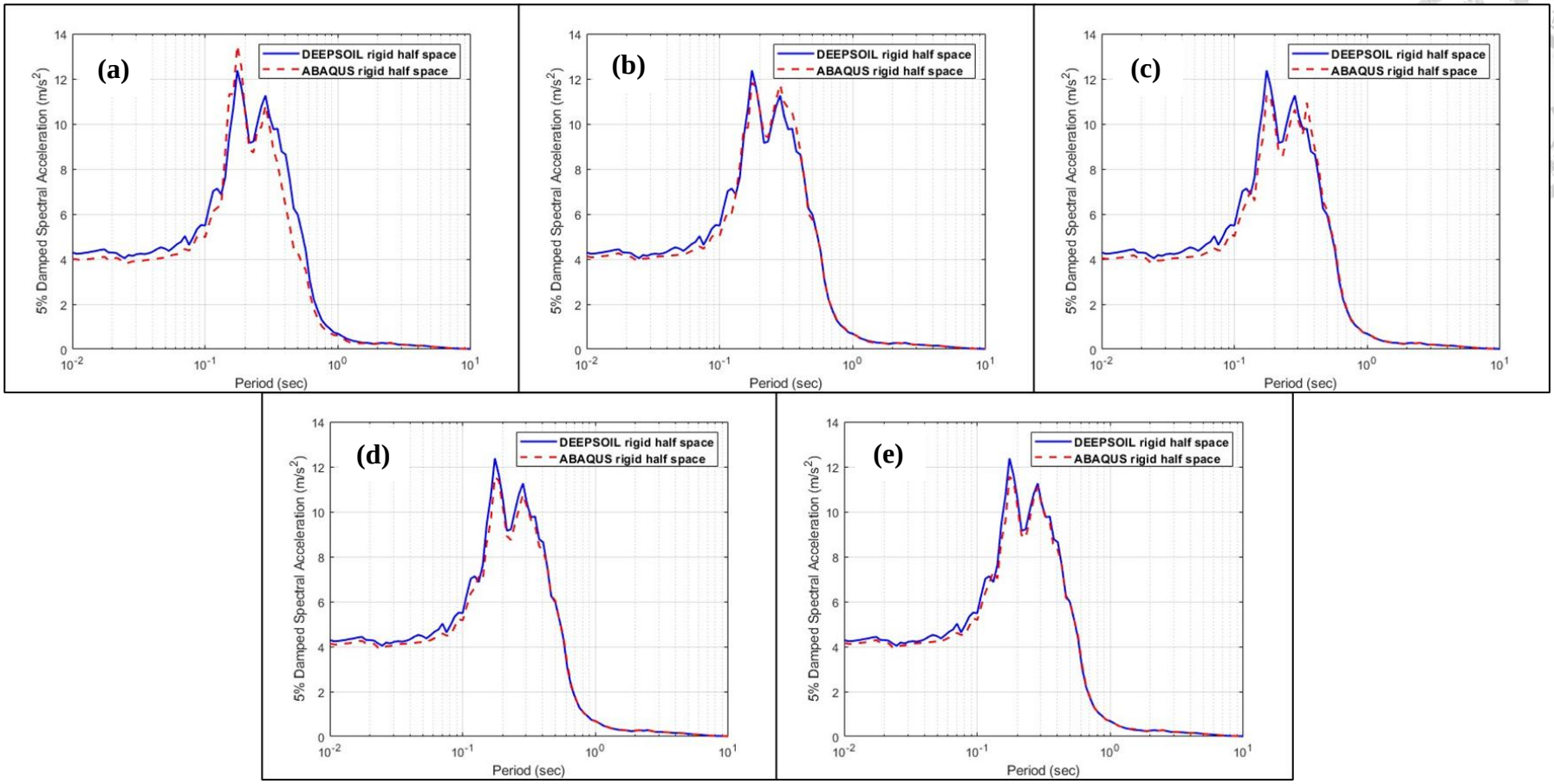

Figure 3.35 Response spectra comparison in rigid half space at y = 20 m and at (a) x = 50 m; (b) x = 100 m; (c) x = 150 m; (d) x = 200 m; (e) x = 250 m.

doi:10.6342/NTU202503752

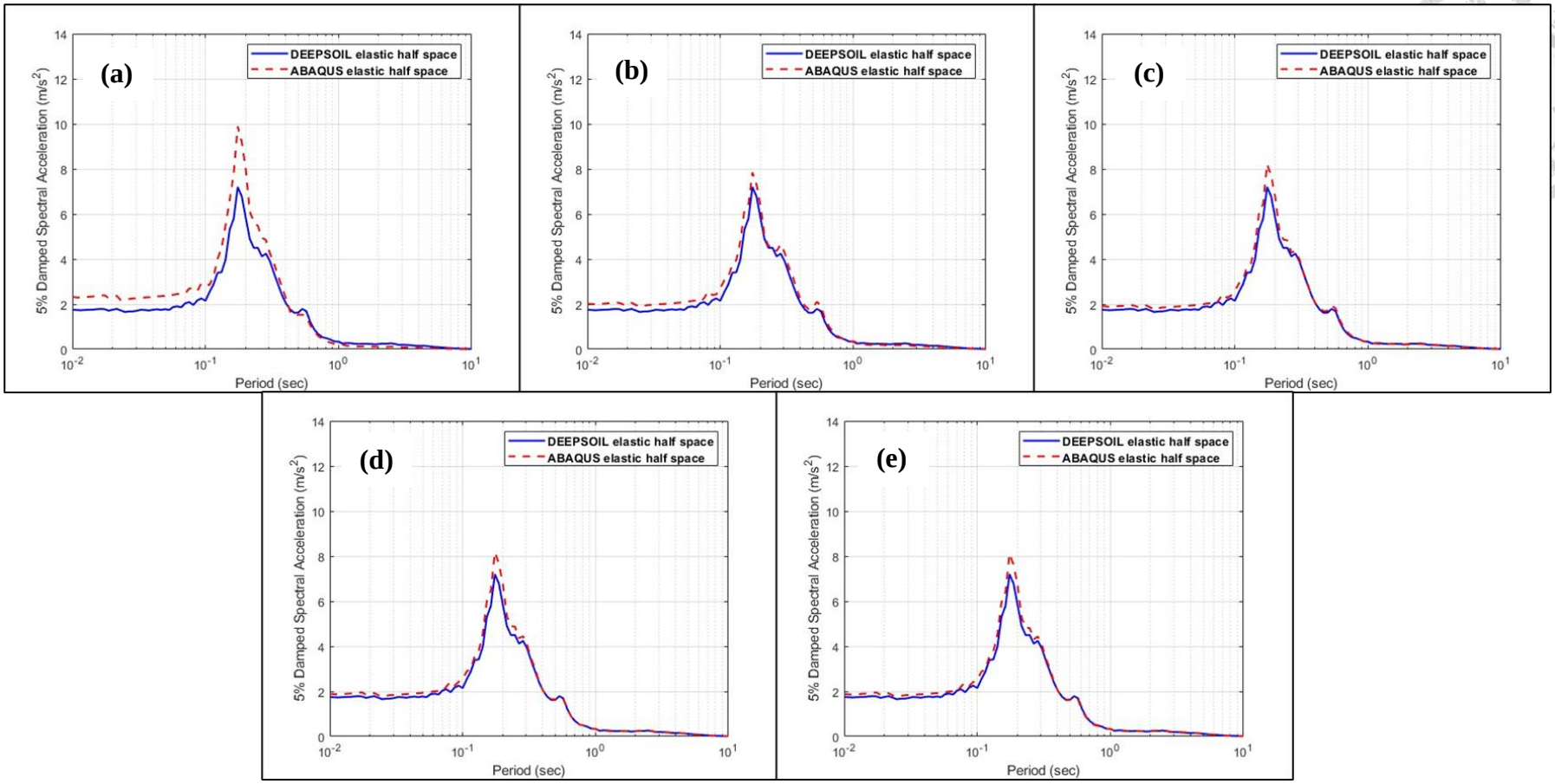

Figure 3.36 Response spectra comparison in elastic half space at y = 20 m and at (a) x = 50 m; (b) x = 100 m; (c) x = 150 m; (d) x = 200 m; (e) x = 250 m.

doi:10.6342/NTU202503752

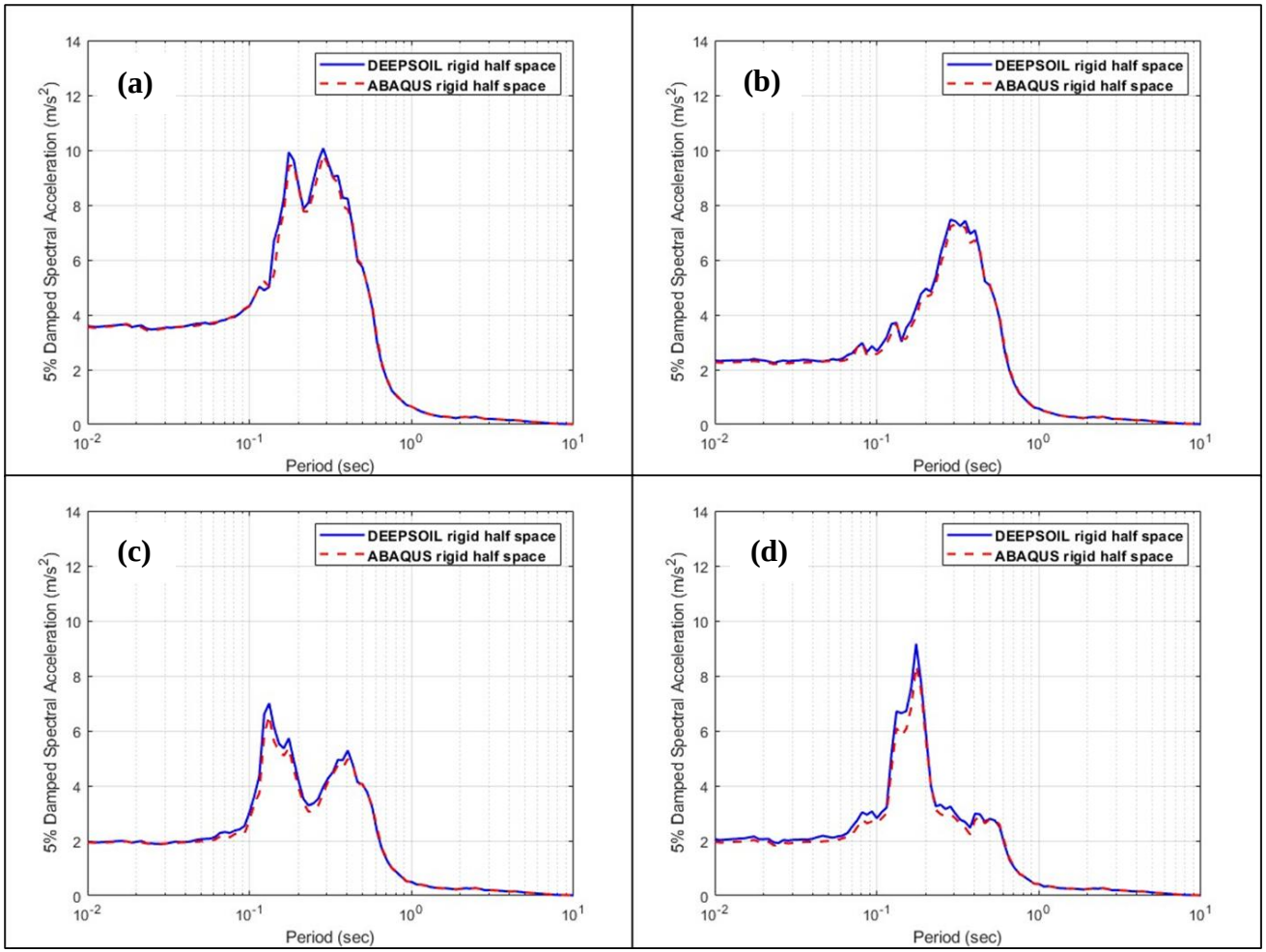

Figure 3.37 Response spectra comparison in rigid half space at x = 200 m and at (a) y = 16 m; (b) x = 12 m; (c) x = 8 m; (d) x = 4 m

doi:10.6342/NTU202503752

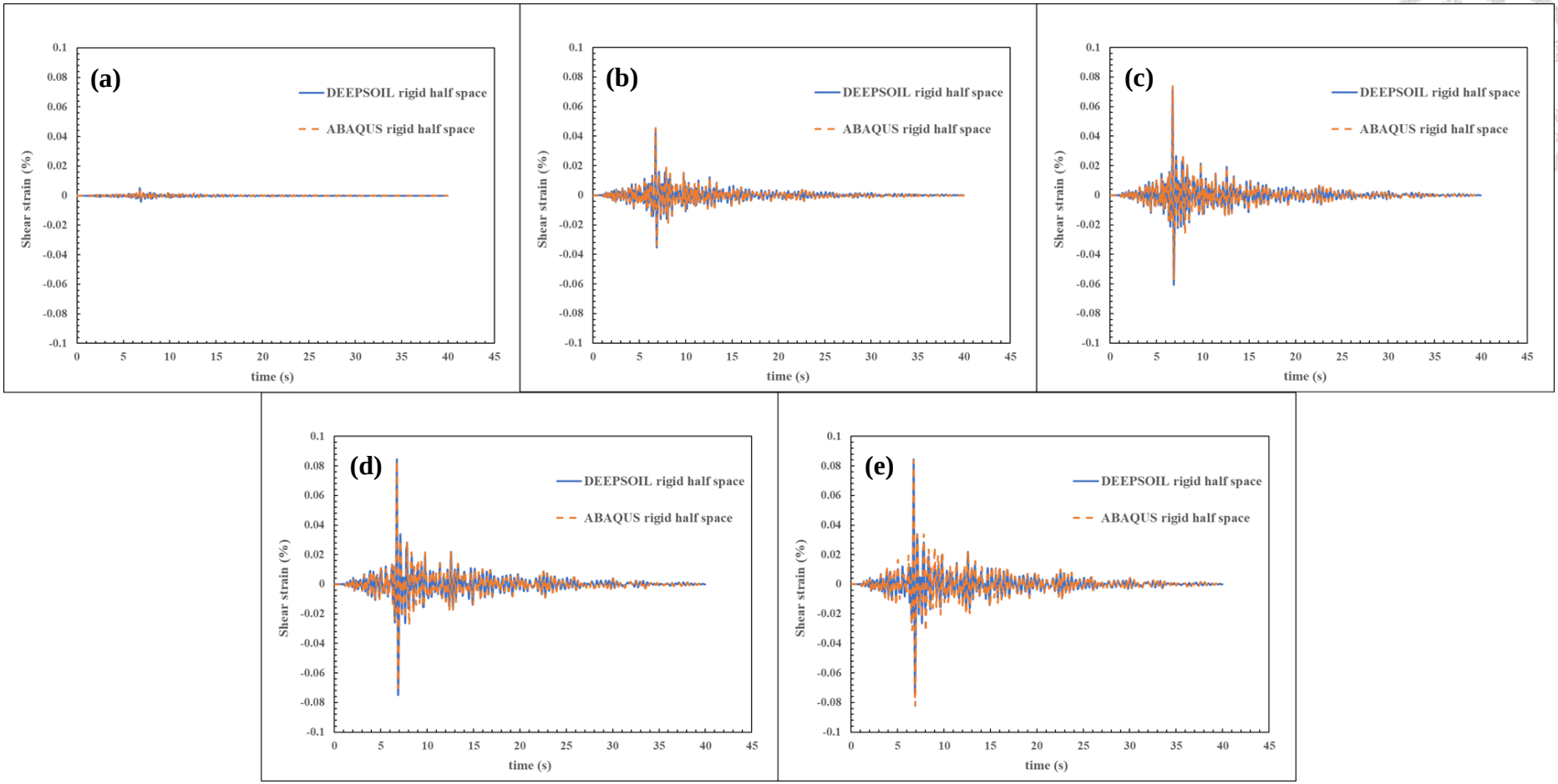

Figure 3.38 Shear strain comparison in rigid half space at x = 200 m and at (a) y = 20 m; (b) x = 16 m; (c) x = 12 m; (d) x = 8 m; (e) x = 4 m.

doi:10.6342/NTU202503752

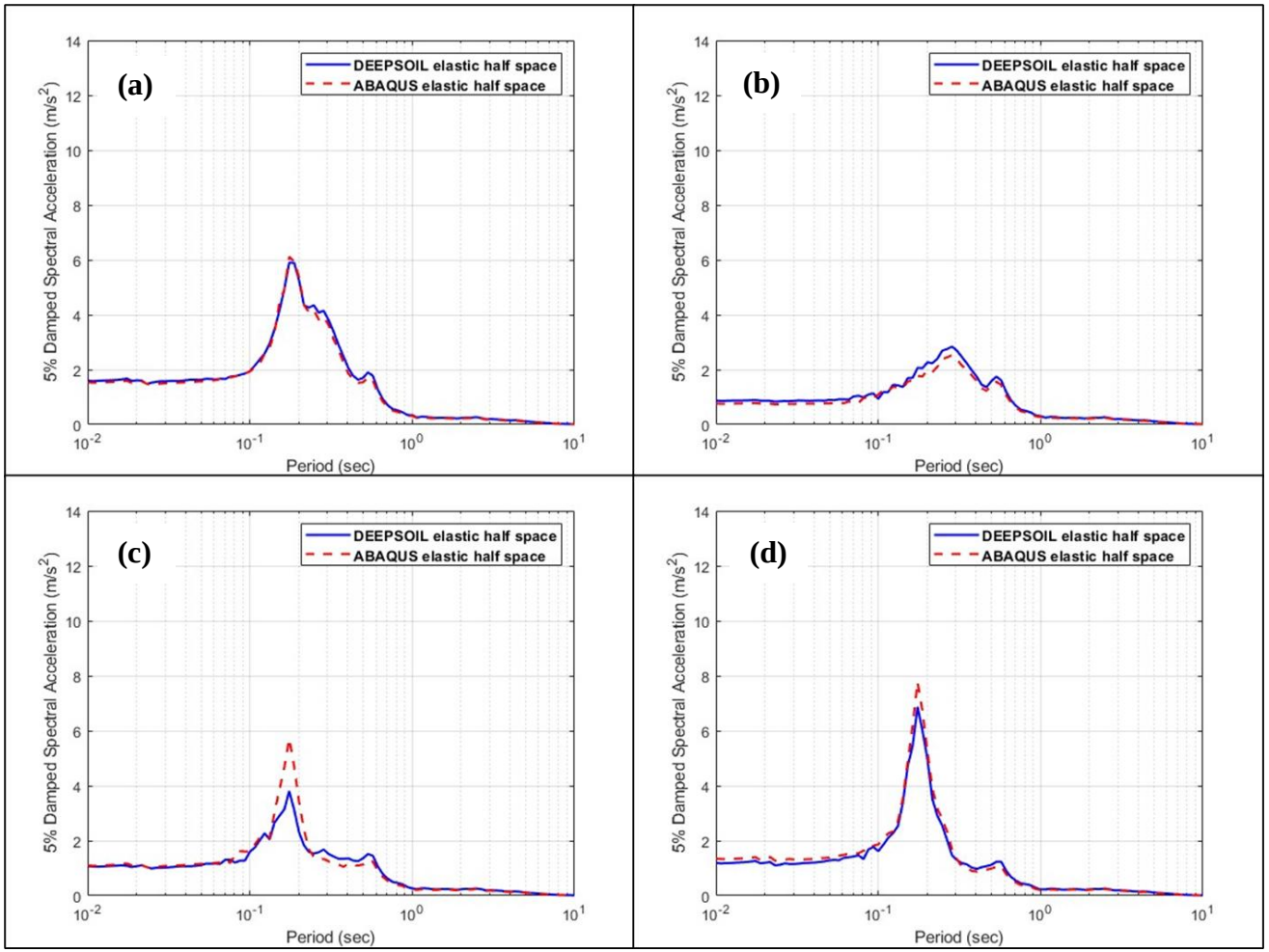

Figure 3.39 Response spectra comparison in elastic half space at x = 200 m and at (a) y = 16 m; (b) x = 12 m; (c) x = 8 m; (d) x = 4 m

doi:10.6342/NTU202503752

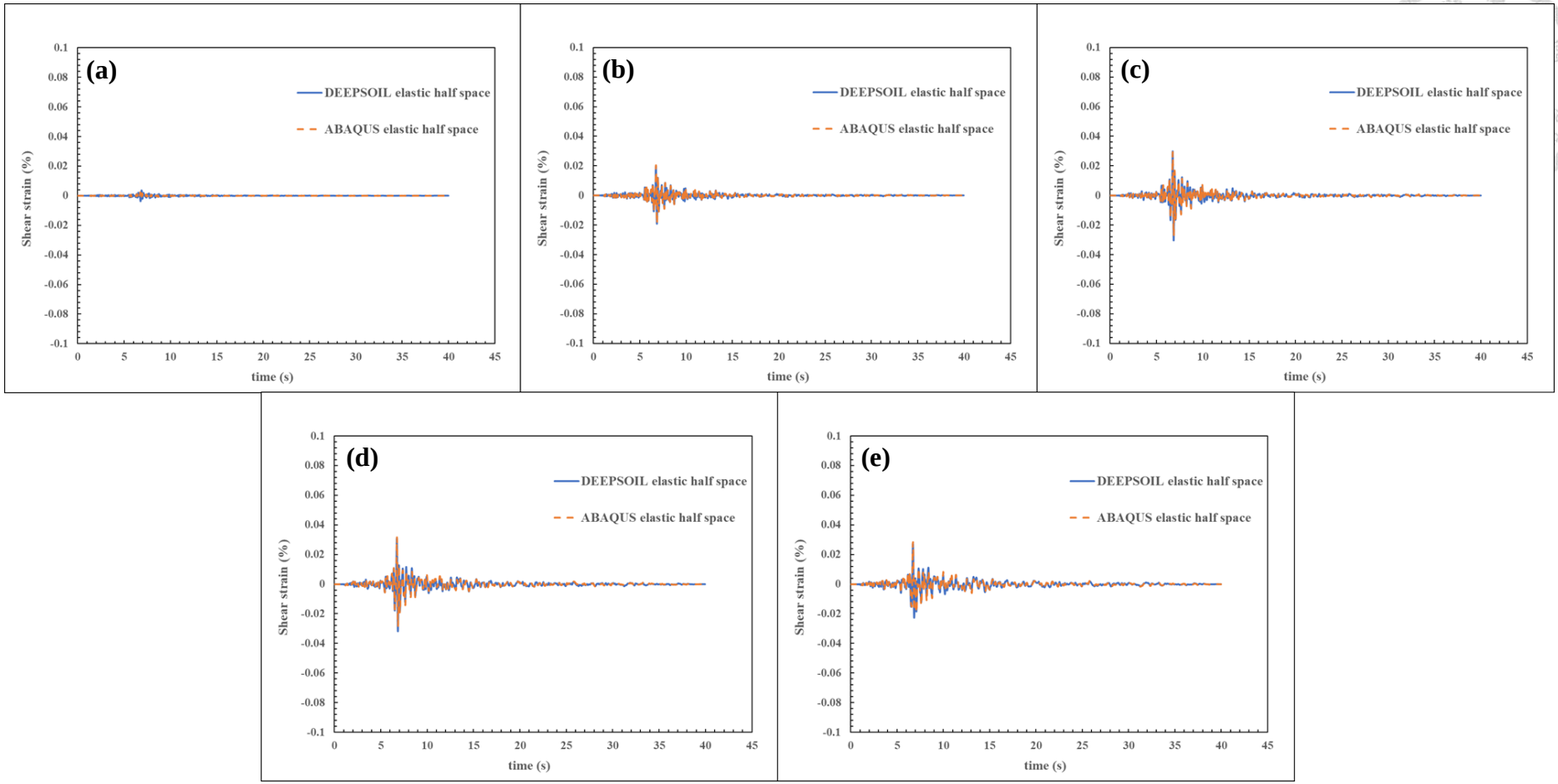

Figure 3.40 Shear strain comparison in elastic space at x = 200 m and at (a) y = 20 m; (b) x = 16 m; (c) x = 12 m; (d) x = 8 m; (e) x = 4 m.

doi:10.6342/NTU202503752

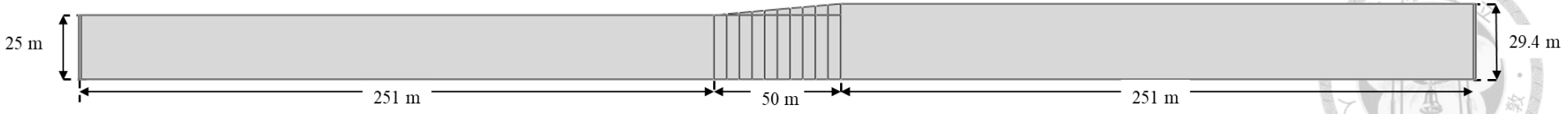

Figure 3.41 Model geometry and size of the 5-degree slope in earthquake analysis.

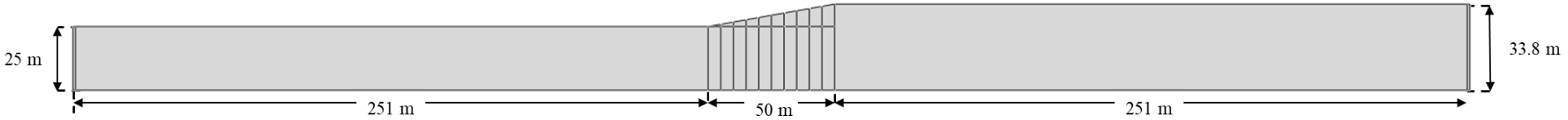

Figure 3.42 Model geometry and size of the 10-degree slope in earthquake analysis.

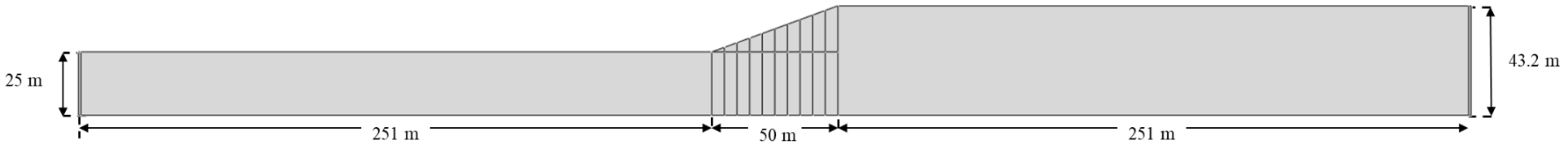

Figure 3.43 Model geometry and size of the 20-degree slope in earthquake analysis

doi:10.6342/NTU202503752

3.3.5 Nonlinear Material Model (SNKH Model)

Following the determination of the slope geometry and dimensions in the previous section, the nonlinear material model (SNKH model) will be incorporated into the seismic analysis to simulate the behavior of shear modulus reduction under earthquake loading. In addition, the nonlinear model in DEEPSOIL will be used to incorporate the shear modulus reduction curve proposed by Yang (2024), allowing for a comparison between the one-dimensional ground response from DEEPSOIL and the two-dimensional ground response from the ABAQUS model. In DEEPSOIL, users are allowed to define custom shear modulus reduction curves and input them into the software for analysis. As shown in the figure, the selected soil model and the hysteretic reloading/unloading formulation in DEEPSOIL are the MKZ model and Masing's rule, respectively. Yang (2024)'s results were first input into DEEPSOIL, after which the built-in curve fitting function was used. Since the actual damping ratios at various depths are not available, the fitting procedure selected was "Modulus Reduction Only." In this mode, DEEPSOIL disregards any user-defined damping ratio inputs and fits solely to the provided shear modulus reduction curve. The fitted results are illustrated in Figure 3.44 to Figure 3.47. These fitted parameters were then assigned to each soil layer as shown, completing the implementation of the shear modulus reduction curve into the nonlinear model.

Table 3.6 and Table 3.7 present the test parameters used for the nonlinear model. According to the borehole data from BH-04 of the Taipower Phase II project, as shown in Figure 2.4, the soil within the depth range of 0–12 meters exhibits the lowest undrained shear strength, with a value of 45.1 kPa. To ensure that the initial stress equilibrium of the slope remains stable and is not compromised by excessively low shear strength, the undrained shear strength for the test was conservatively assumed to be 40 kPa.

doi:10.6342/NTU202503752

Additionally, the slope angle was set to 20°, representing the steepest condition. This configuration—combining the minimum shear strength and maximum slope angle—constitutes the most critical case. If the numerical model remains stable during the verification process under these conditions, then other combinations involving lower slope angles and higher shear strengths are unlikely to pose any numerical issues. For the 20° slope case, a cross-section was extracted from each of the three zones: the upper platform, the slope section, and the lower platform (Figure 3.48). At each profile, response spectra and shear strain were output at various depths and subsequently compared with the results obtained from DEEPSOIL. In the DEEPSOIL configuration, soil column heights were set to 25 m (lower platform), 34 m (midpoint of the slope), and 43 m (upper platform), corresponding to the respective elevations in the numerical model. Both rigid and elastic half-space bedrock conditions were considered, resulting in a total of six verification cases. To reduce computation time, the input ground motion was limited to the first 12 seconds of the Northridge earthquake. The comparison results will be presented in section 4.2.1.

Table 3.6 Soil parameters.

Type	Structural Damping		E (MPa)	μ	Density (kg/m^3)	V_s (m/s)	s_u (kPa)
	α	β					
Clay	1.309	0.00106	236	0.45	2000	200	40

Table 3.7 Parameters of the SNKH model.

σ_y (Pa)	λ (0.1-0.3)	$\sigma\|_0$ (Pa)	C (MPa)	γ
69282.03	0.15	10392.305	236	4007.490

doi:10.6342/NTU202503752

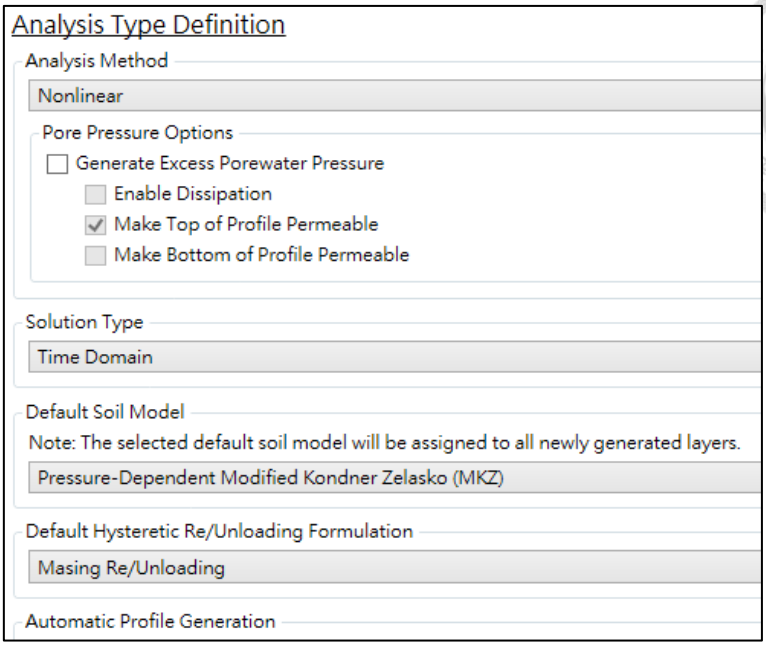

Figure 3.44 Nonlinear analysis method setting in DEEPSOIL.

Reference Curve

Sand | Clay | User Defined

Strain (%)	G/Gmax	Damping
0.0001	1	5
0.0005	1	5
0.001	1	5
0.0026	1	5
0.003	1	5
0.01	1	5
0.03	0.735	5
0.1	0.51	5
0.19	0.425	5
0.3	0.38	5
0.7	0.215	5
1	0.15	5

Number of Points: 12

Figure 3.45 Yang (2024)’s results were input into DEEPSOIL.

doi:10.6342/NTU202503752

Curve Fitting

Fitting Procedure: Modulus Reduction Only (MR) Fit

Parameter	Value
Dmin (%)	4.965
Ref. Strain (%)	0.2146
Ref. Stress (MPa)	0.18
Beta	1.485
s	0.87
b	0
d	0

Strain (%)	G/Gmax	Damping
0.0001	0.9981	5
0.0003	0.9951	5.058
0.001	0.9863	5.228
0.003	0.9651	5.642
0.01	0.9065	6.827
0.03	0.7886	9.454
0.1	0.5668	15.47
0.3	0.3347	24.34
0.7	0.194	32.22
1	0.15	35.42
3	0.06356	43.52
7	0.03145	47.79
10	0.02326	49.1

Use Fit

Figure 3.46 Fitting curve parameters.

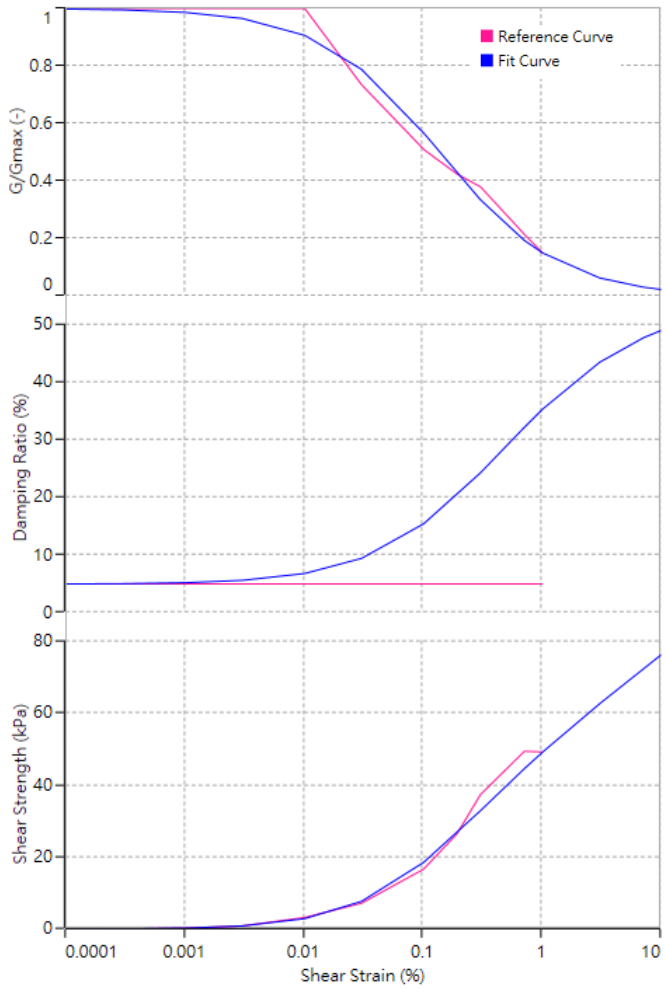

Figure 3.47 Plots of the reference curve and the fitting curve.

doi:10.6342/NTU202503752

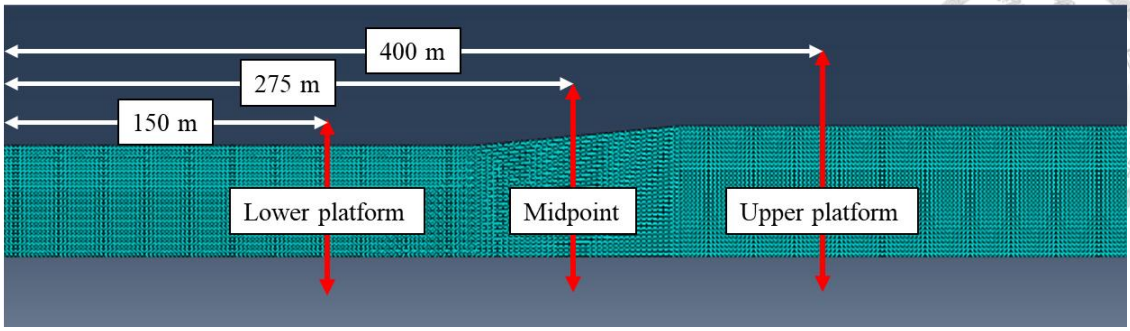

Figure 3.48 Three cross-sections for comparisons of 1-D and 2-D nonlinear models.

3.3.6 Modified Boundary Setting for Slopes with Elastic Half Space

In the elastic half-space configuration described in Section 3.3.3, a rectangular elastic soil block was used to verify whether the damping system was functioning correctly and to simulate the response spectra and shear strains under elastic half-space conditions. These results were then compared with those obtained from DEEPSOIL (Figure 3.36, Figure 3.39 and Figure 3.40). However, when this approach was applied to a nonlinear material slope model, the results were unsatisfactory. Figure 3.49 shows the shear strain histories at the midpoint of the slope for depths of y = 34 m, 30 m, 25 m, 15 m, and 5 m. It can be clearly observed that significant and unreasonable initial deformations occurred at the very beginning of the seismic loading, indicating the presence of an unknown external force disrupting the simulation of the elastic half-space condition. This issue was not identified in Section 3.3.3 because that section utilized a symmetric rectangular soil block, whereas in a slope, the stress fields in the upper and lower parts of the slope are inherently different. Figure 3.50 presents the x-direction stress contours at 0 and 0.4 seconds of the dynamic step. The results show that the x-direction stress field becomes horizontally distributed, indicating a "stress release" in the x-direction. Meanwhile, the y-direction stress field remains correct. The underlying cause is related to the change in boundary conditions: during the initial static stress equilibrium

doi:10.6342/NTU202503752

step, the slope base and free-field boundaries were constrained with U1 = U2 = 0. However, in the dynamic step, the U1 = 0 condition was removed to allow the input of x-direction velocity histories. This caused the original supporting forces to be released. Since dashpots possess no stiffness, they simply followed the displacement of the slope base after stress release, as shown in Figure 3.51. Despite this translation motion, the dampers still functioned effectively in energy dissipation. This is evident in Figure 3.49, where the range of simulated shear strains is comparable to that of the DEEPSOIL results, with the discrepancy being the presence of a rigid-body translation.

To address this issue, the horizontal reaction forces originally concentrated at the x-direction rollers at the base of the slope during the initial stress equilibrium step must be maintained throughout the dynamic step. To achieve this, the horizontal support reactions (RF1) obtained after completing the static stress initialization were extracted and subsequently applied as concentrated forces at each node along the base of the slope during the dynamic step, as illustrated in Figure 3.52. This approach prevents the occurrence of unreasonable deformations at the onset of seismic shaking. The shear strain results from the corrected model are shown in Figure 4.19 to 4.22. It is evident that there are no initial strains at t=0s, and the results generally agree with those from the DEEPSOIL analysis.

doi:10.6342/NTU202503752

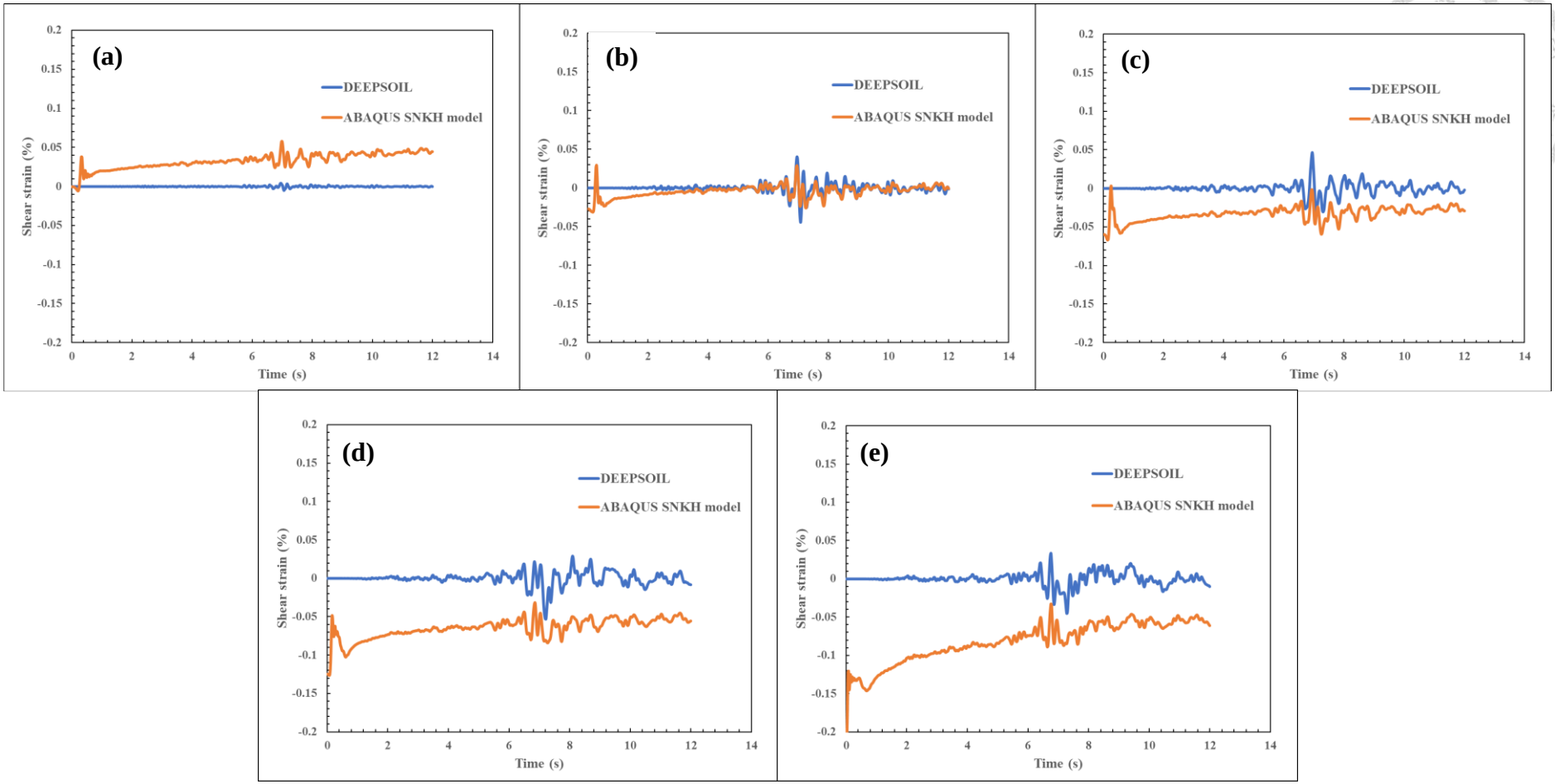

Figure 3.49 Shear strain comparison in elastic half space between DEEPSOIL nonlinear model and ABAQUS SNKH model in the middle of the slope at (a) y = 34; (b) y = 30; (c) y = 25; (d) y = 15m; (e) y = 5 m.

doi:10.6342/NTU202503752

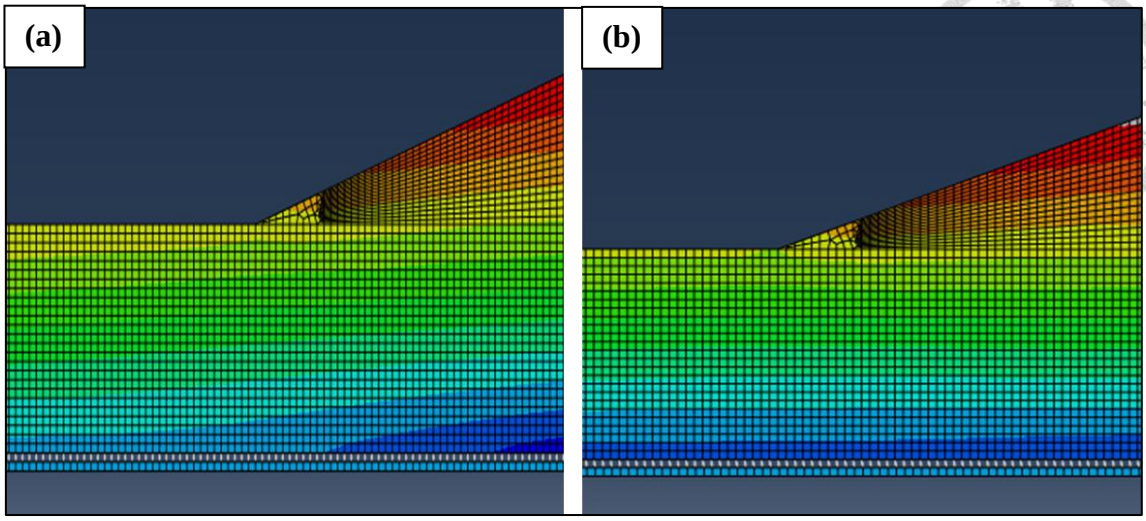

Figure 3.50 Stress fields of the x-component at (a) t = 0 s and (b) t = 0.4 s.

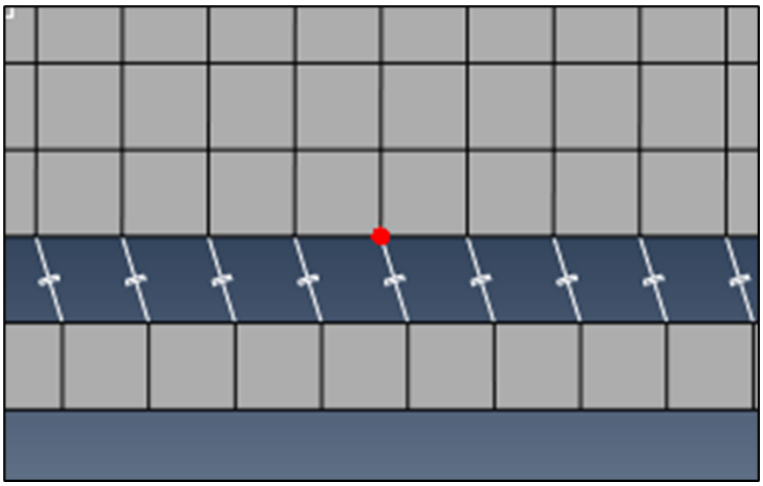

Figure 3.51 Dashpots simply followed the displacement of the slope base after stress release.

doi:10.6342/NTU202503752

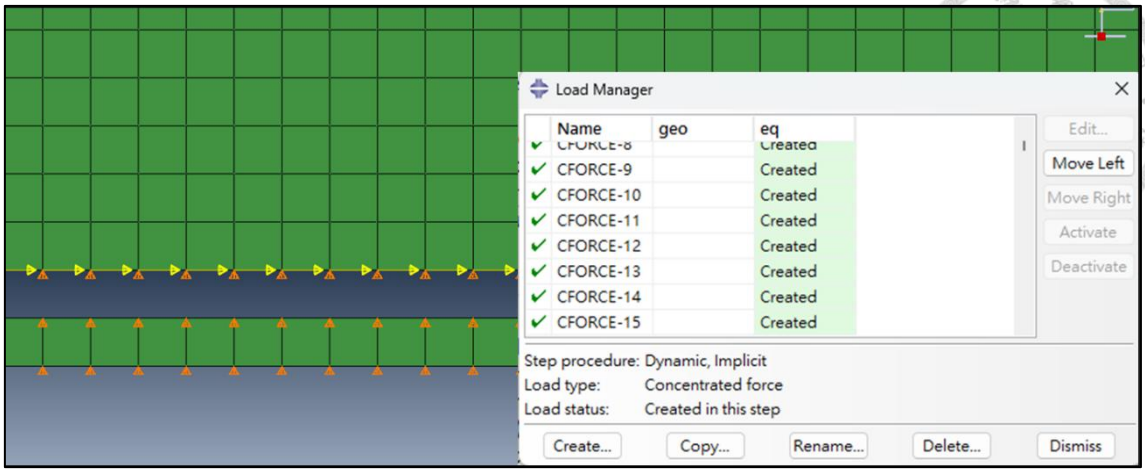

Figure 3.52 Adding the reaction forces at the base of the slope back in dynamic analysis.

3.3.7 Input Motions Information and Materials

This section introduces the ground motion records used in the seismic analyses, as summarized in Table 3.8. A total of three earthquake records were selected: the 1995 Kobe earthquake, the 1994 San Fernando earthquake, and the 1999 Kocaeli earthquake. For the Kobe earthquake, the KJMA station record was chosen due to its proximity to the fault, with a minimum rupture distance of only 0.96 km, allowing the simulation of near-fault effects on submarine slope response. In addition, the three earthquakes exhibit different mean periods, specifically 0.6577 seconds, 0.2187 seconds, and 1.0681 seconds, respectively. These differences in mean period reflect variations in the frequency content of each ground motion. A smaller mean period indicates that seismic energy is concentrated in the higher frequency range, while a larger mean period corresponds to energy concentration in the lower frequency range. The 5% damping acceleration response spectra and acceleration time histories for the three earthquakes are shown in Figure 3.53 to Figure 3.57.

doi:10.6342/NTU202503752

Based on the BH-04 borehole data from the Taipower Phase II project report, the soil parameters for the depth range of 0 to 27.7 meters are summarized in Table 3.9. Excluding the dense silty layer between depths of 19.6 and 24.9 meters, the undrained shear strength s_u of the remaining soils ranges from 45 kPa to 101 kPa. Therefore, two s_u values—40 kPa and 100 kPa—were selected for the analysis. The other soil parameters were calculated using a thickness-weighted average for each layer, with the results presented in Table 3.10 and Table 3.11. All seismic analyses in Chapter 4 were conducted using these parameter sets.

doi:10.6342/NTU202503752

Table 3.8 Information of the seismic motions.

Event	Station	Magnitude	PGA (g)	Rrup (km)	Duration (s)	Mean period (s)
Kobe	KJMA	6.9	0.63	0.96	50	0.6577
San Fernando	Pearblossom Pump	6.6	0.14	38.97	27	0.2187
Kocaeli	Gebze	7.5	0.14	10.92	28	1.0681

Table 3.9 BH-04 data (Taipower, 2018).

Layer	Depth (m)		Thickness (m)	s_u (Ave.) (kPa)	γ' (Ave.) (kN/m^3)	V_s (Ave.) (m/s)	G_0 (Ave.) (MPa)	E_0 (Ave.) (MPa)
No.	From	To						
1	0	12	12.0	45.1	4.8	88.6	13.0	33.9
	12	19.6	7.6	97.5	7.3	162.8	47.9	124.6
	19.6	24.9	5.3	244.2	7.0	184.6	59.3	154.3
	24.9	27.7	2.8	101.4	7.6	189.6	66.1	171.8

doi:10.6342/NTU202503752

Table 3.10 Soil parameters for seismic analysis where s_u = 40 kPa.

Depth (m)	s_u (Ave.) (kPa)	γ' (Ave.) (kN/m^3)	γ (Ave.) (kN/m^3)	V_s (Ave.) (m/s)	G_0 (Ave.) (MPa)	E_0 (Ave.) (MPa)	v
0~43.2	40	6.2	19.0	137.0	36.4	95.8	0.316

Table 3.11 Soil parameters for seismic analysis where s_u = 100 kPa.

Depth (m)	s_u (Ave.) (kPa)	γ' (Ave.) (kN/m^3)	γ (Ave.) (kN/m^3)	V_s (Ave.) (m/s)	G_0 (Ave.) (MPa)	E_0 (Ave.) (MPa)	v
0~43.2	100	6.2	19.0	137.0	36.4	95.8	0.316

doi:10.6342/NTU202503752

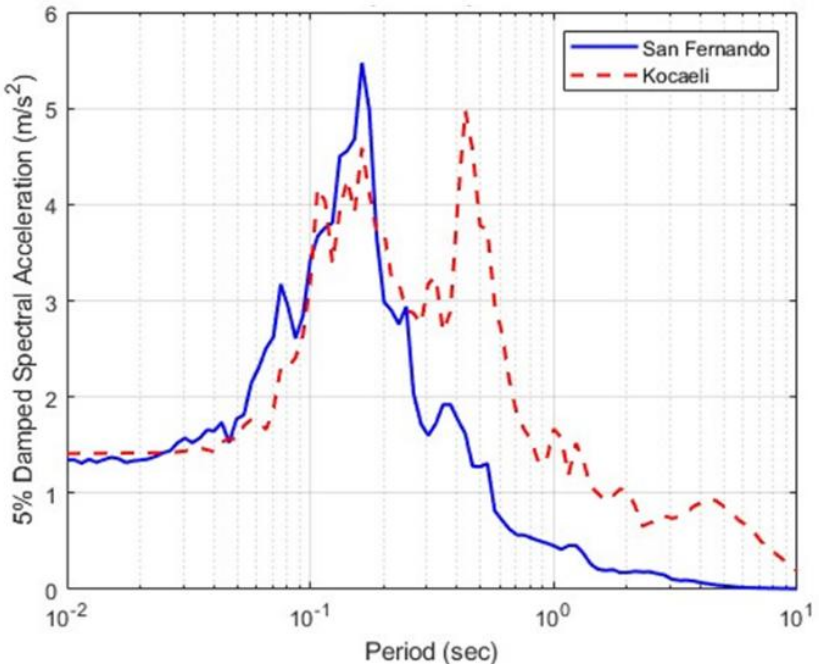

Figure 3.53 Response spectra of the San Fernando earthquake and the Kocaeli earthquake.

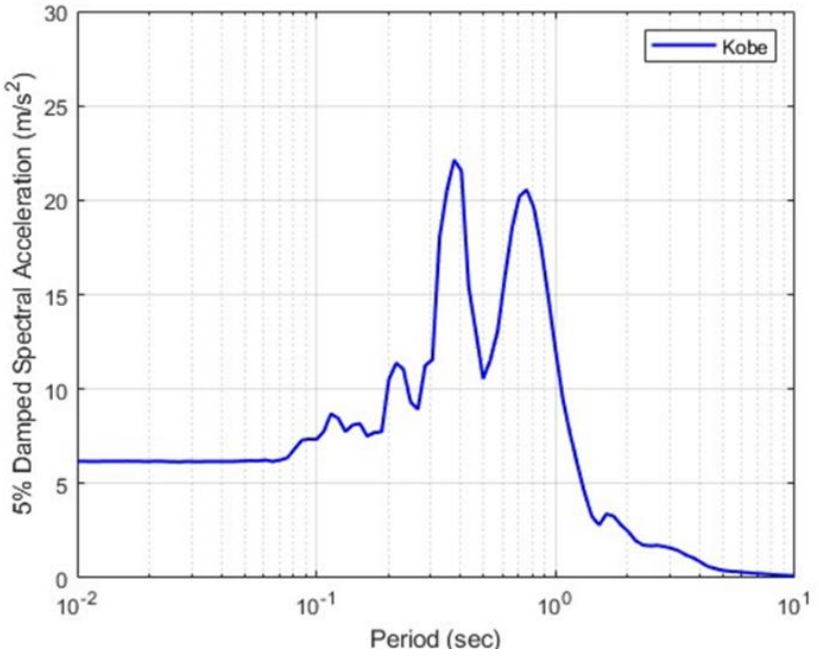

Figure 3.54 Response spectra of the Kobe earthquake.

doi:10.6342/NTU202503752

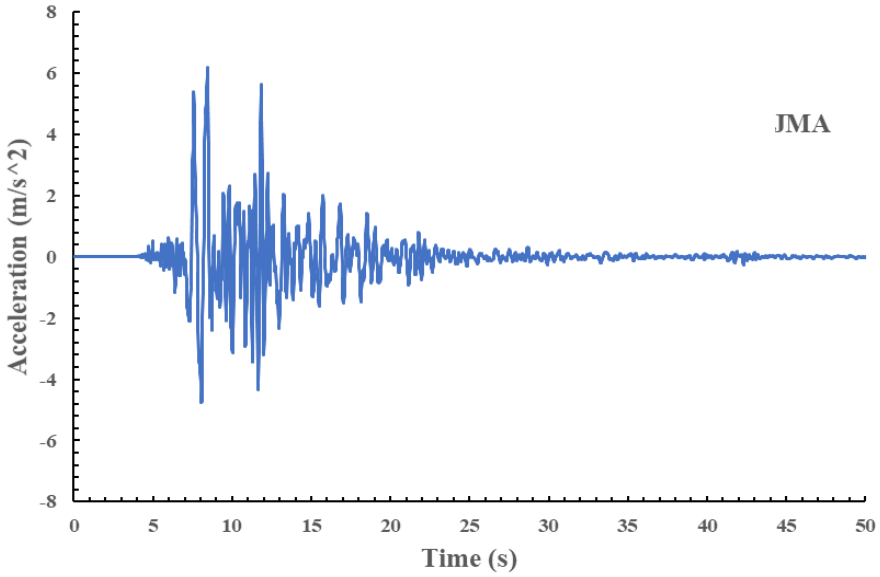

Figure 3.55 The acceleration time history of Kobe KJMA earthquake.

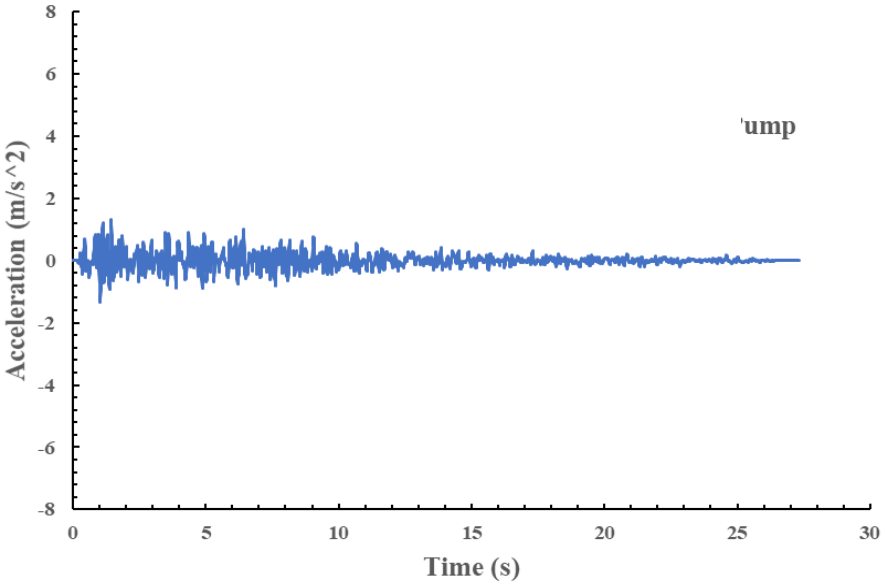

Figure 3.56 The acceleration time history of San Fernando Pearblossom Pump earthquake.

doi:10.6342/NTU202503752

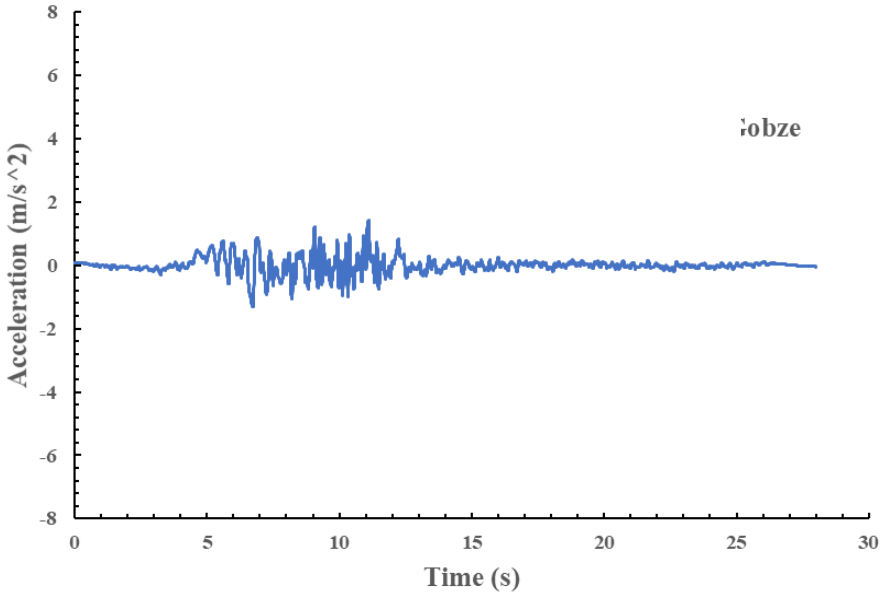

Figure 3.57 The acceleration time history of Kocaeli Gobze earthquake.

doi:10.6342/NTU202503752

Chapter 4 Simulation Results and Discussions

4.1 Stability Analysis of Strength Reduction Method

Sections 4.1.1 through 4.1.4 present the results of strength reduction static analyses for the submarine slope, including both total stress and effective stress analyses under various parameter settings. These sections also provide a discussion of the results and examine the trends in slope stability under different seawater depths.

4.1.1 Models with Total Stress Parameters

Based on Section 3.2, the results of the strength reduction analyses using three models—TSA, ESA (ESAI), and ESA with pore pressure (ESAII)—with total stress parameters from Table 3.4 are presented in Figure 4.1 to 4.4. Figure 4.1 to 4.3 show the relationship between the reduction factor and the horizontal displacement for slopes with three different angles. It is evident that once the reduction factor reaches a certain threshold, there is a sharp increase in displacement. This point of rapid displacement growth is defined as the failure moment. The displacement history at the point of maximum movement within the model is extracted for further analysis. In Figure 4.3, for the 20-degree slope, numerical instability occurs when the horizontal displacement reaches approximately 0.5 meters due to the steep slope angle, preventing further calculations. However, this does not affect the identification of the failure point. Figure 4.4 compares the reduction factors obtained from the three analysis methods across the different slope angles. It can be observed that the reduction factors derived under total stress conditions are nearly identical across all three methods. Figure 4.5 to 4.7 display the horizontal displacement contour plots at the moment of failure. In all cases, the failure surfaces extend to the bottom of the model, indicating large-scale sliding failures. This

doi:10.6342/NTU202503752

failure pattern occurs because the slope consists entirely of homogeneous cohesive soil, and once the shear strength falls below the critical value, a global sliding failure develops.

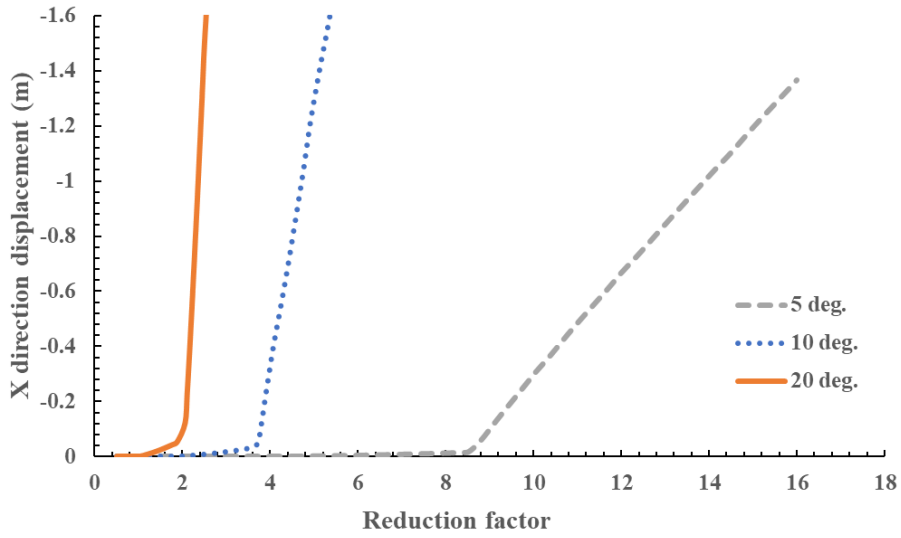

Figure 4.1 X-direction displacement vs. reduction factor by TSA with total stress parameters.

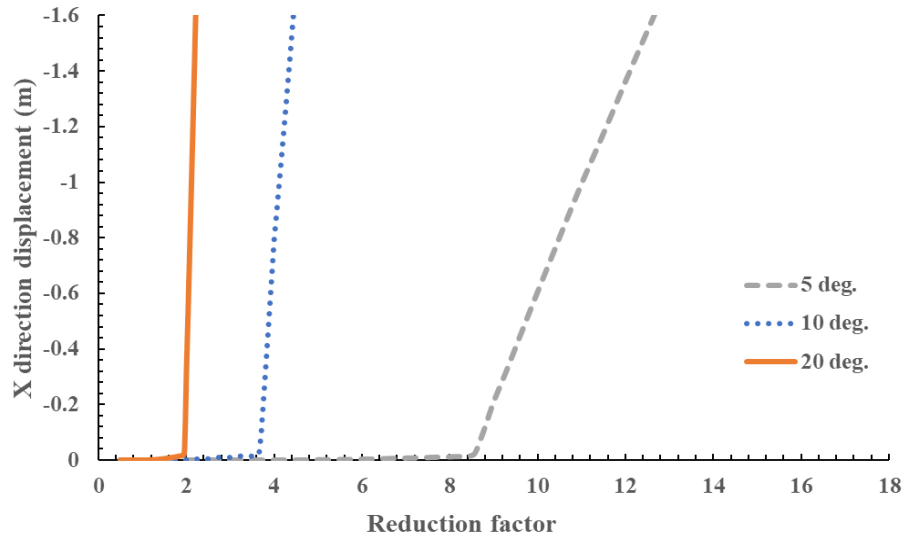

Figure 4.2 X-direction displacement vs. reduction factor by ESA(I) with total stress parameters.

doi:10.6342/NTU202503752

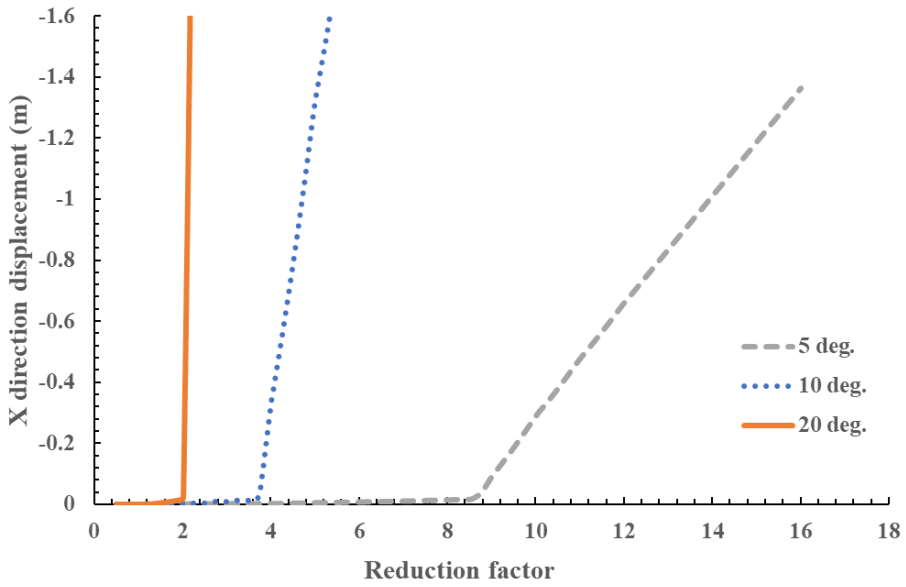

Figure 4.3 X-direction displacement vs. reduction factor by ESA(II) with total stress parameters.

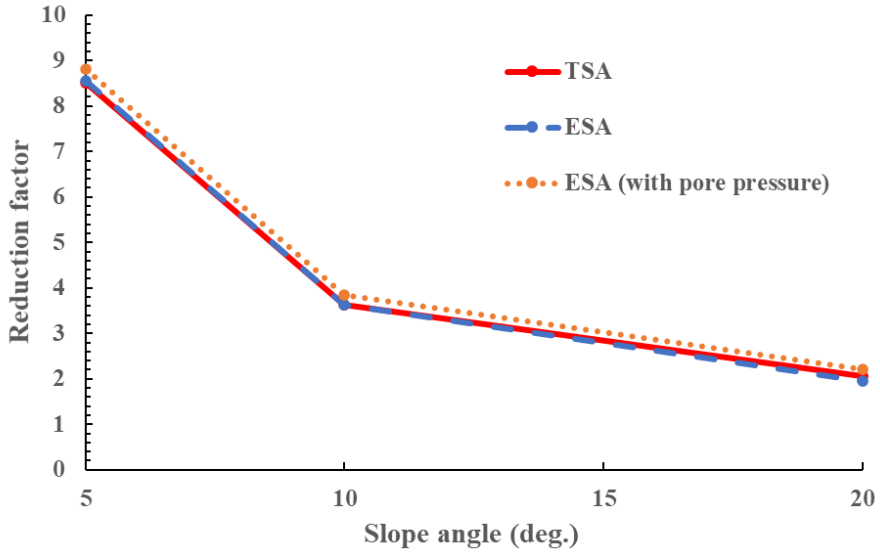

Figure 4.4 Slope angle vs. reduction factor in three analysis methods with total stress parameters.

doi:10.6342/NTU202503752

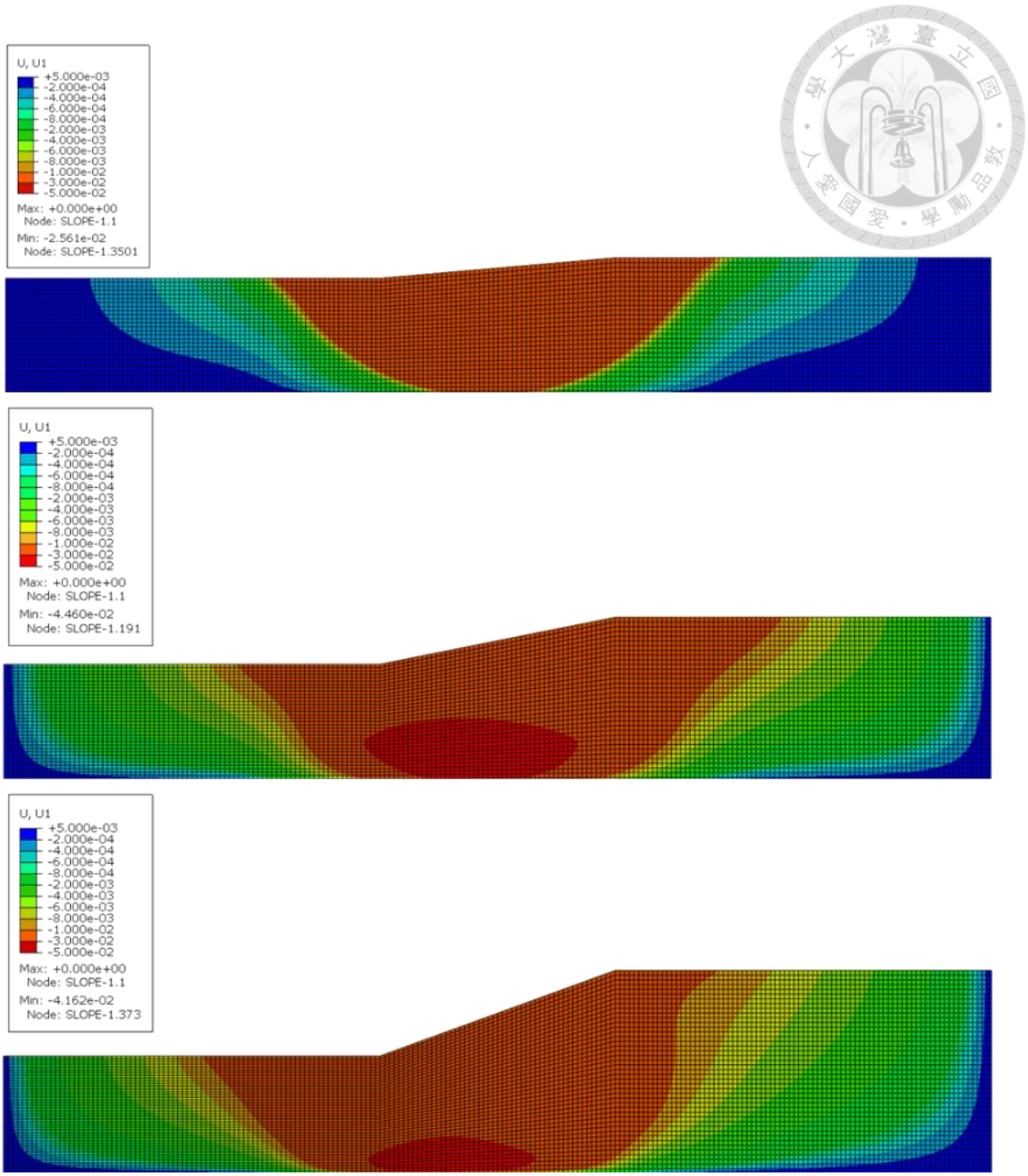

Figure 4.5 Contour plots of x-direction displacement in TSA models at failure state.

doi:10.6342/NTU202503752

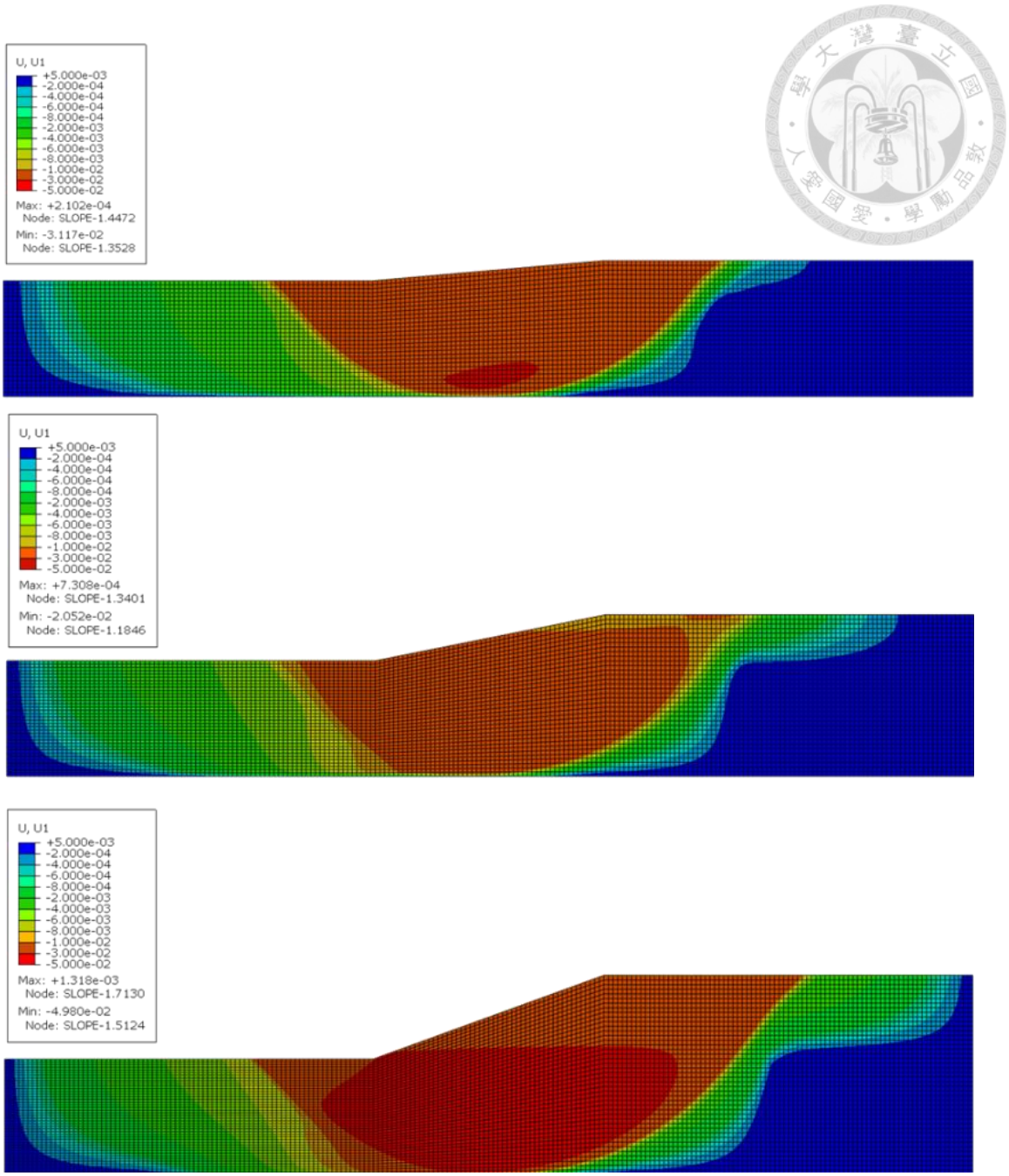

Figure 4.6 Contour plots of x-direction displacement in ESA(I) models at failure state.

doi:10.6342/NTU202503752

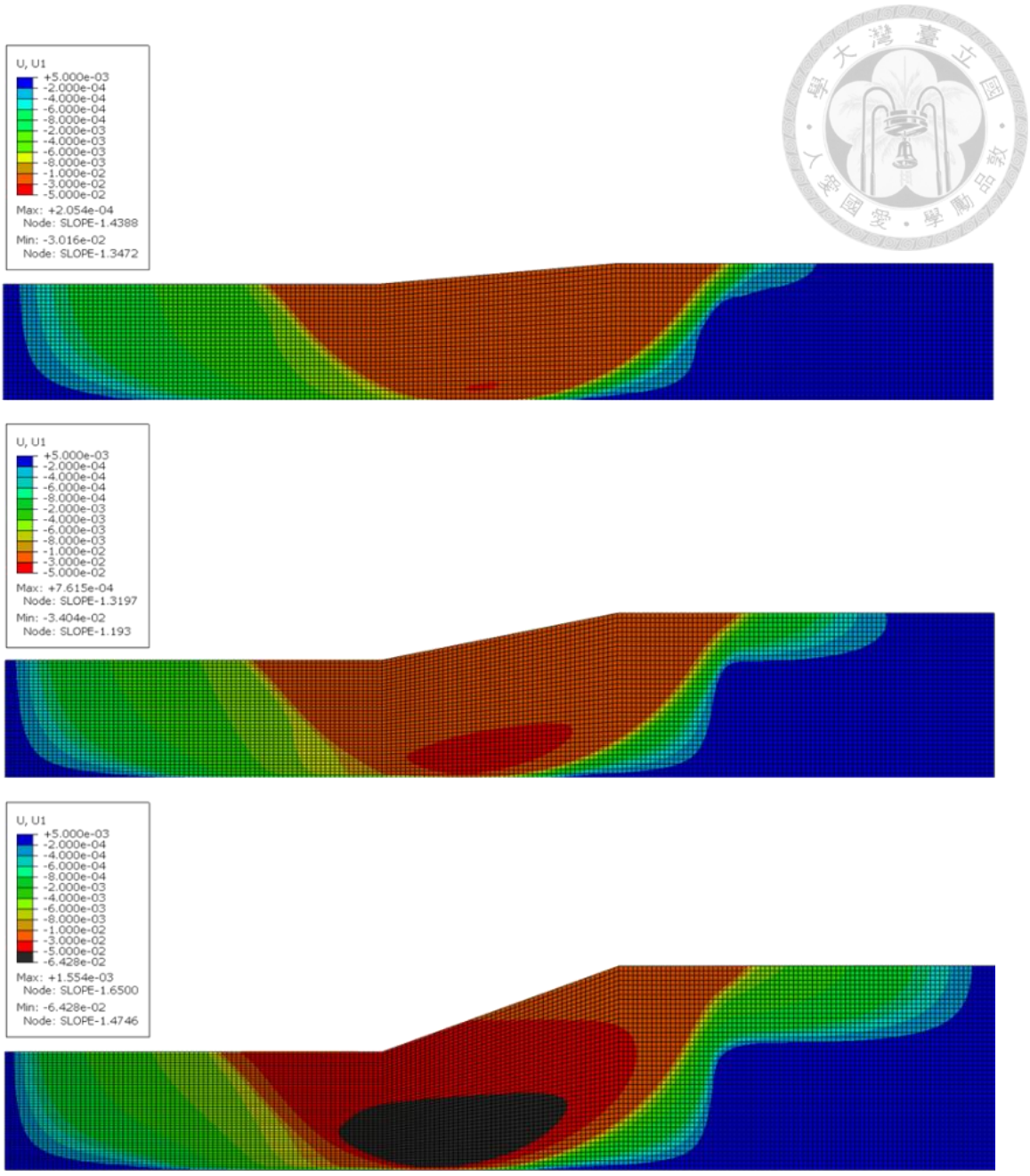

Figure 4.7 Contour plots of x-direction displacement in ESA(II) models at failure state.

4.1.2 Models with Effective Stress Parameters

This section discusses the strength reduction analysis results under effective stress parameters for the three analytical methods. As in the previous section, the displacement histories at the points of maximum displacement and their corresponding reduction factors are presented in Figure 4.8 to 4.10.Figure 4.11 shows the reduction factors for different slope angles under the same analysis method. Unlike the results using total stress

doi:10.6342/NTU202503752

parameters, the TSA model yields significantly higher factors of safety compared to the ESA models. This is because the initial confining stress in the total stress analysis is greater than in the effective stress analysis, due to the combined effect of self-weight and overlying seawater pressure. As a result, a larger deviatoric stress is required for the Mohr's circle to reach the failure envelope, thereby indicating a higher resistance to failure. In practice, however, total stress analyses should not be performed using effective stress parameters. Doing so leads to an inaccurate representation of stress conditions at failure. In this section, the parameters are treated purely as controlled variables for comparative purposes, and the results should not be interpreted as realistic factors of safety for submarine slopes. Apart from this, the two effective stress-based results (ESA and ESA with pore pressure) are nearly identical. Figure 4.12 to 4.14 show the displacement contour plots at the moment of failure. Compared to Section 4.1.1, the failure surfaces here do not extend to the base of the slope. Instead, they develop within a limited depth range, indicating shallow failures. This difference arises because, with increasing depth, the effective stress becomes higher, and according to the Mohr-Coulomb failure criterion, higher effective stress leads to greater shear strength. Consequently, failure initiates in the shallow layers where strength is lower, resulting in a different failure mechanism from that in Section 4.1.1. Additionally, in the ESA(II) model for the 20-degree slope, the original mesh had a poor aspect ratio in the slope region due to overly fine vertical divisions, which caused instability in the calculation of pore pressure and stress. Therefore, in Figure 4.14, the mesh size for the 20-degree slope is modified to 3 m × 3 m, allowing the failure point to be successfully identified.

doi:10.6342/NTU202503752

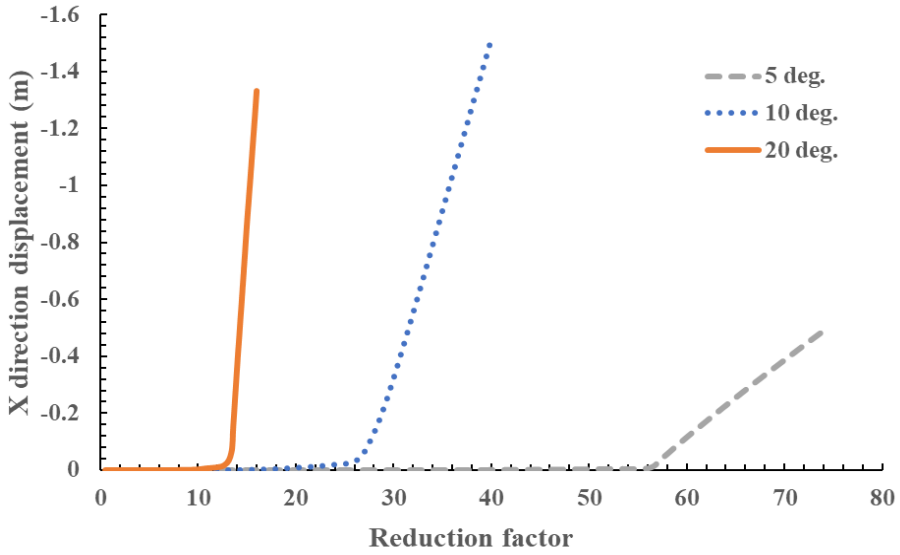

Figure 4.8 X-direction displacement vs. reduction factor by TSA with effective stress parameters.

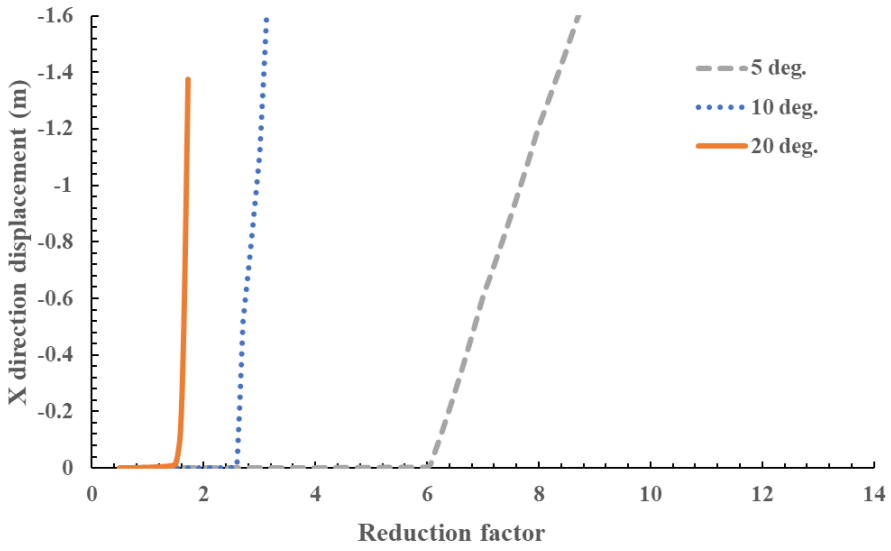

Figure 4.9 X-direction displacement vs. reduction factor by ESA(I) with effective stress parameters.

doi:10.6342/NTU202503752

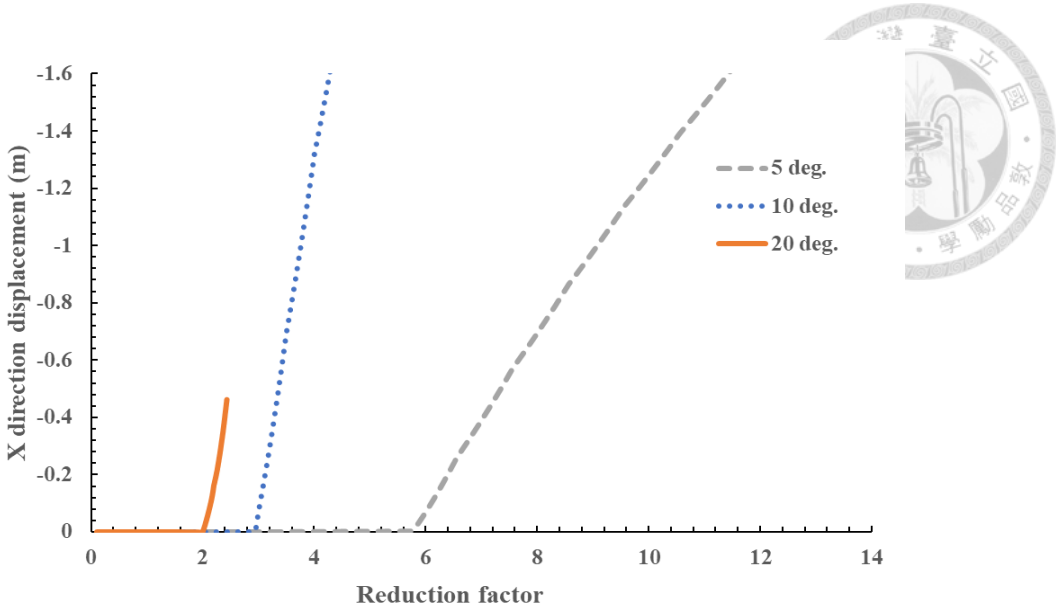

Figure 4.10 X-direction displacement vs. reduction factor by ESA(II) with effective stress parameters.

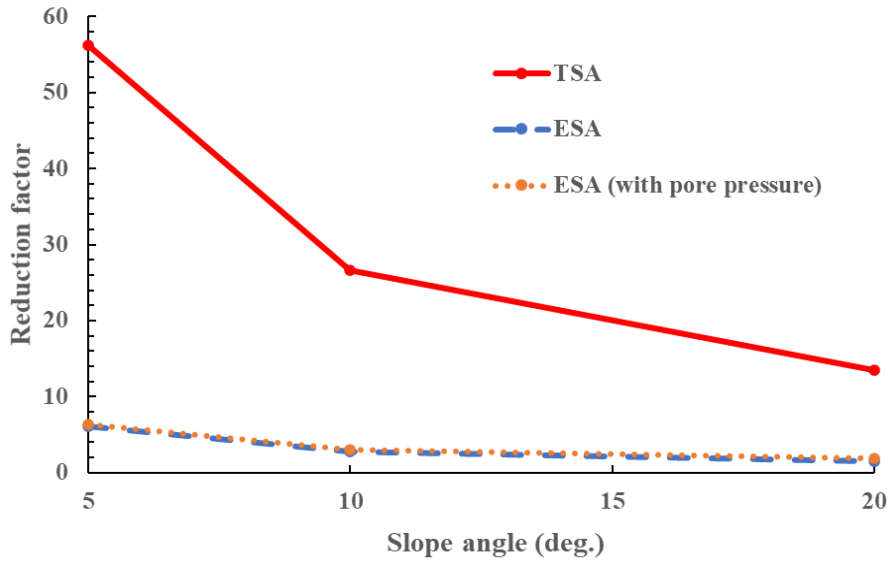

Figure 4.11 Slope angle vs. reduction factor in three analysis methods with effective stress parameters.

doi:10.6342/NTU202503752

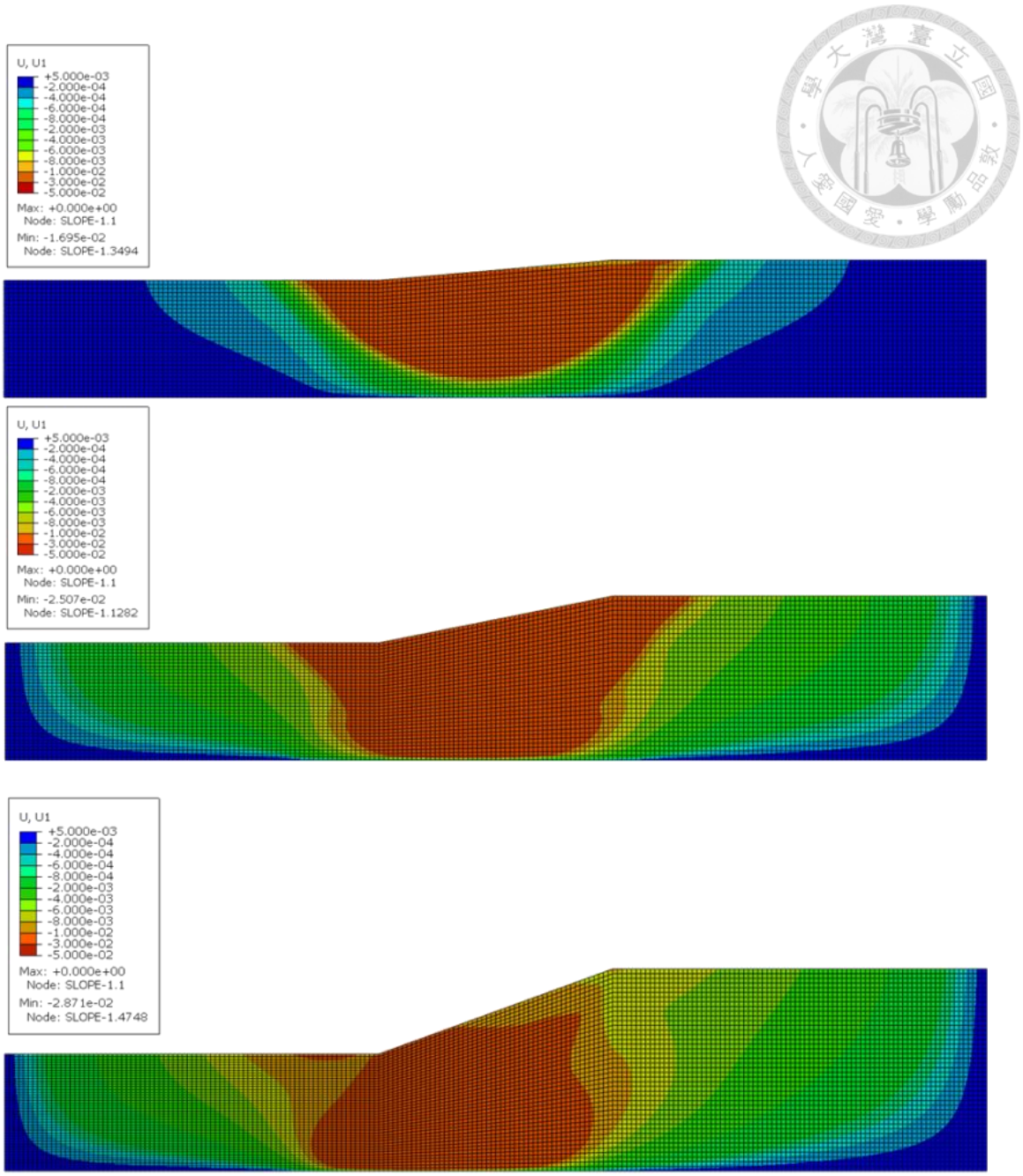

Figure 4.12 Contour plots of x-direction displacement in TSA models at failure state.

doi:10.6342/NTU202503752

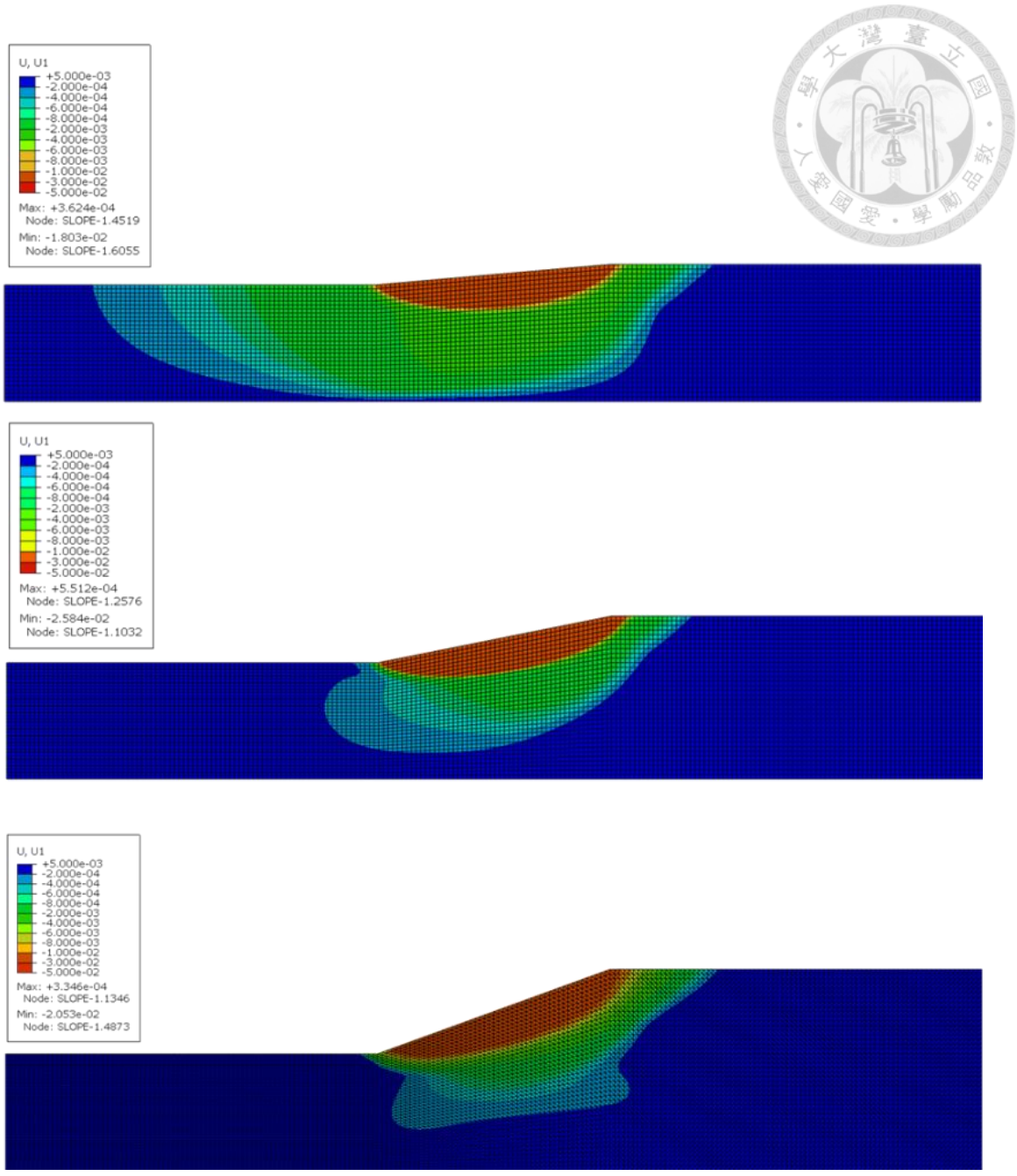

Figure 4.13 Contour plots of x-direction displacement in ESA(I) models at failure state.

doi:10.6342/NTU202503752

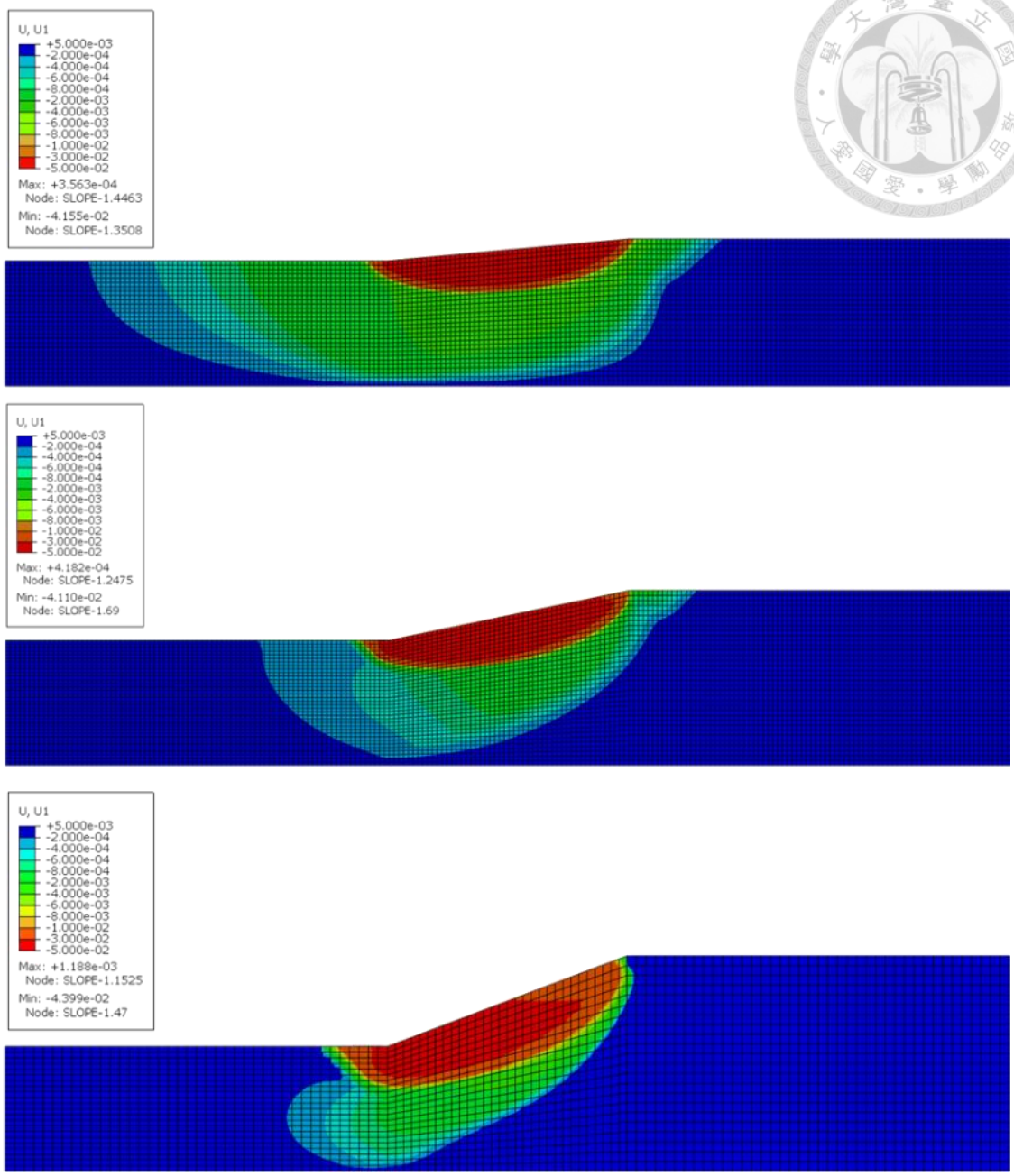

Figure 4.14 Contour plots of x-direction displacement in ESA(II) models at failure state.

4.1.3 Stability Analysis under Different Depths of Water

In total stress analysis, different seawater depths influence the initial stress state of the soil. To investigate this effect, we varied the water depth (depth of water = 10 m, 25 m, 50 m, 75 m, 175 m, and 275 m) and examined how the strength reduction factor changes. Figure 4.15 shows the variation of factors of safety derived from total stress parameters

doi:10.6342/NTU202503752

under different water depths. The case with "Depth of Water = 0" represents a saturated slope located on land. It can be observed that the reduction factors for submarine slopes are all higher than that of the land-based saturated slope. Notably, the highest reduction factor occurs at a water depth of 50 m, after which it gradually decreases as the depth increases. This result suggests that modeling seawater as a uniform surcharge acting on the slope surface can, in some cases, enhance stability compared to a slope on land. While the upper slope is subjected to water-induced destabilizing pressure, both the lower slope platform and the main slope body provide stabilizing forces and moments in the direction opposite to failure, thereby contributing to increased overall stability.

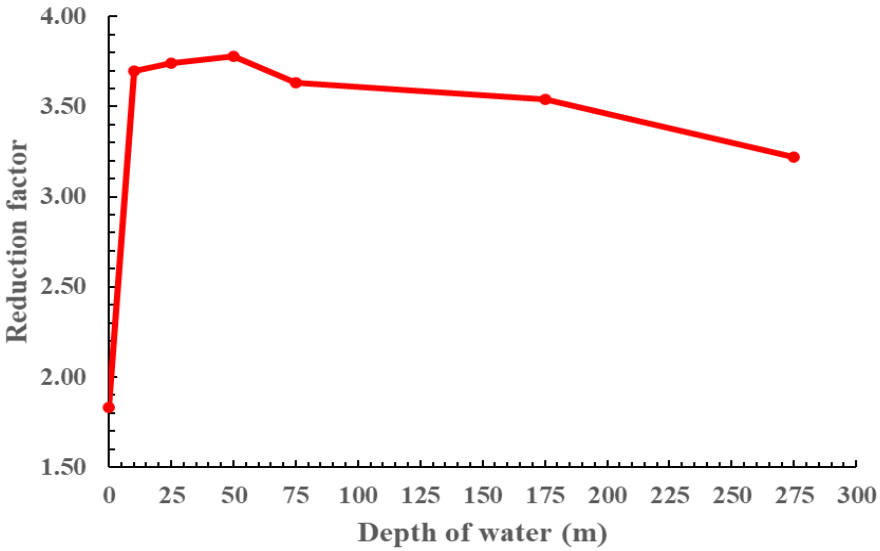

Figure 4.15 Reduction factor in TSA model with total stress parameters under different depth of water.

doi:10.6342/NTU202503752

4.1.4 Effect of Thickness of Foundation Soil on Slope Failure

In Section 4.1.1, it was observed that when using total stress parameters for analysis, the limited model thickness of 25 meters may cause the potential slip surface to be influenced by the model boundary, thereby affecting its development and the overall analysis results. To address this, the model was extended to a thickness of 125 meters (the lower platform). A 5-degree slope was used with total stress parameters to examine the development of the failure surface and compare the reduction factor with that of the original model. The x-direction displacement time history and displacement contours are shown in Figure 4.16 and Figure 4.17.

As shown in Figure 4.17, although the failure surfaces still extend to the bottom of the model, the development of them become more complete. In addition, as shown in Table 4.1, the safety factor obtained from the thickened model is lower than that of the original model. This indicates that model thickness has a direct influence on the calculated safety factor, and a thinner model may lead to an overestimation of slope stability.

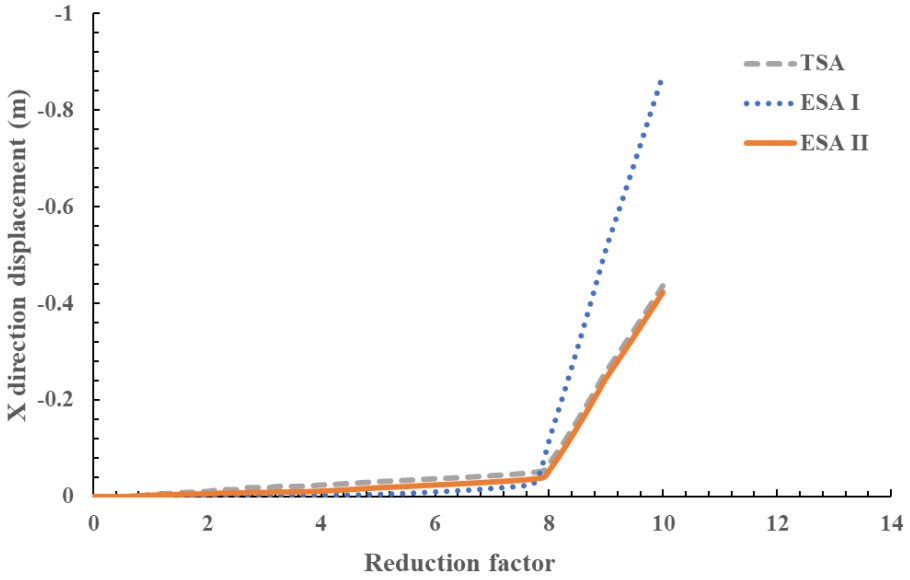

Figure 4.16 Reduction factor vs. x-direction displacement in thick model.

doi:10.6342/NTU202503752

Table 4.1 Difference between original and thicker model in factor of safety.

Models / Factor of safety	TSA	ESA I	ESA II
Original models	8.52	8.56	8.81
Thicker models	7.93	7.83	8.02

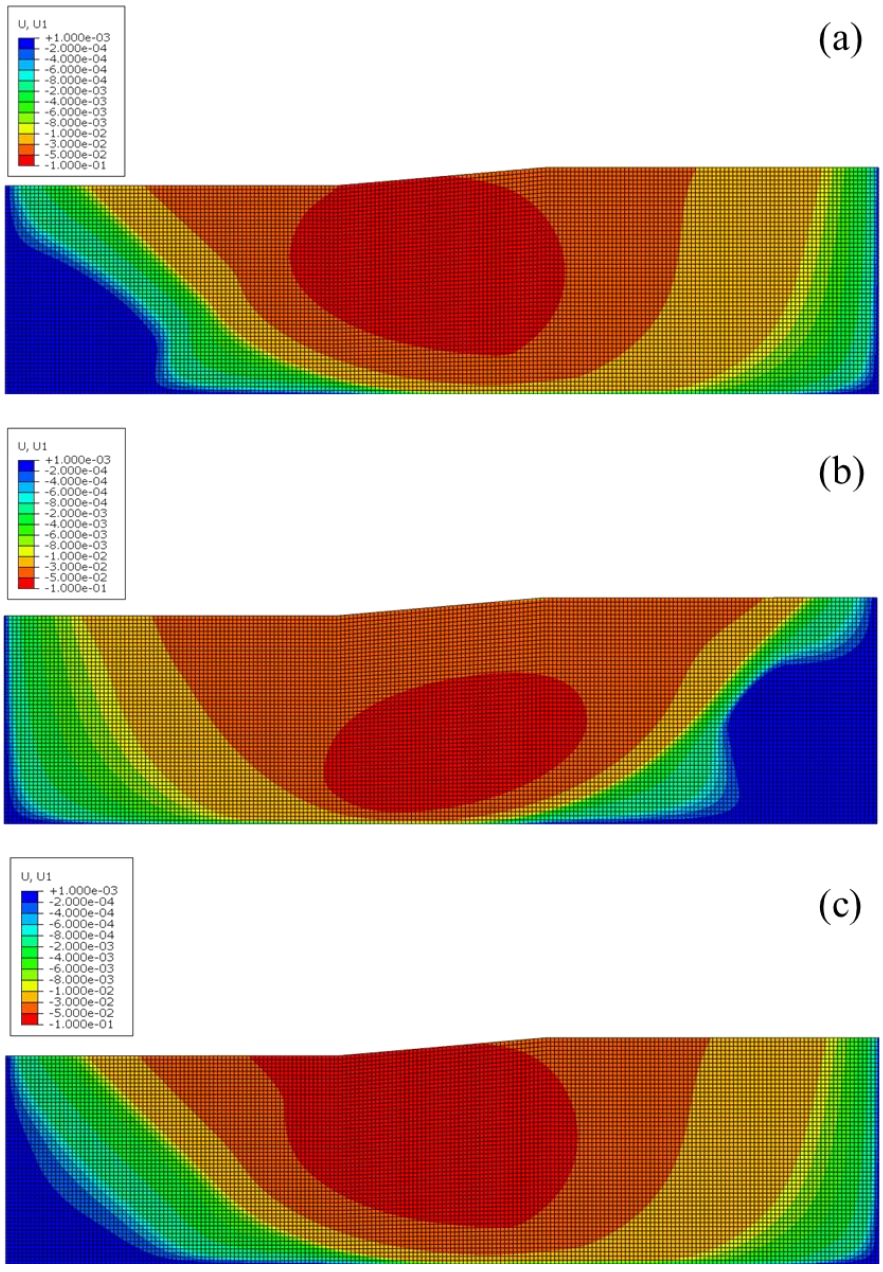

Figure 4.17 X-direction displacement contour of (a) TSA; (b) ESA(I) and (c) ESA(II) model.

doi:10.6342/NTU202503752

4.2 Seismic Analysis

Sections 4.2.1 to 4.2.5 present the validation, analysis results, and comparisons of the two-dimensional submarine slope SNKH model. In section 4.2.2 to 4.2.5, the analyses consider rigid and elastic half space conditions, two sets of undrained shear strengths, three earthquake records, and three slope angles. For the analyses of the Kobe earthquake, two different seawater depths are also considered. In total, 48 total stress analysis cases were performed, as summarized in

Table 4.2. For each output, six different points along the slope were selected, as shown in Figure 4.18, and their respective X-direction displacements, plastic strain histories, and ground motion amplification profiles were extracted. The influence of different variables on slope failure behavior is then discussed and examined.

Table 4.2 Cases summary in earthquake analysis.

Slope angle (°)	Bedrock	Earthquake and station	Undrained shear strength (kPa)	Depth of water (m)
5	rigid	Kobe KJMA	40 and 100	25 and 50
	elastic	San Fernando Pearblossom Pump		50
		Kocaeli Gebze		
10	rigid	Kobe KJMA	40 and 100	25 and 50
	elastic	San Fernando Pearblossom Pump		50
		Kocaeli Gebze		
20	rigid	Kobe KJMA	40 and 100	25 and 50
	elastic	San Fernando Pearblossom Pump		50
		Kocaeli Gebze		

doi:10.6342/NTU202503752

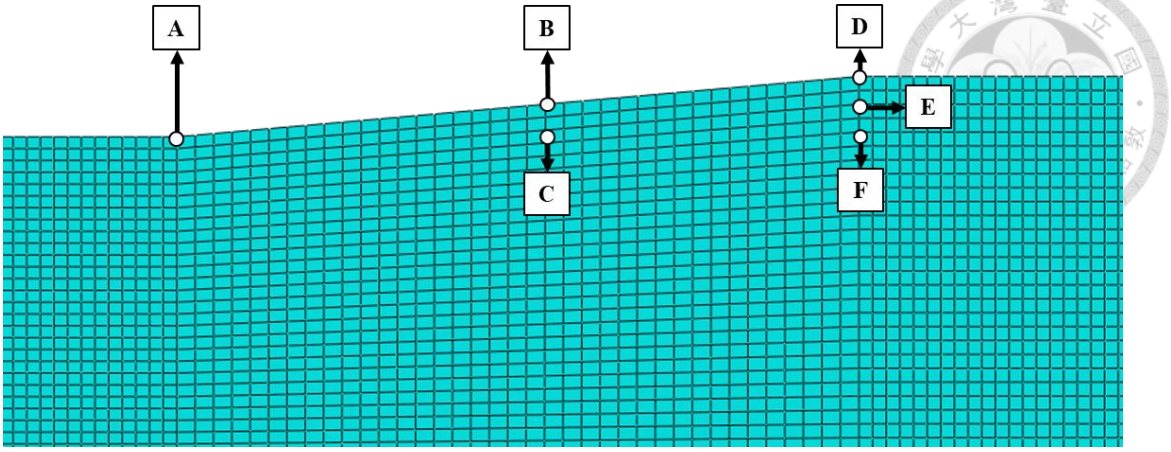

Figure 4.18 Selected points for section 4.2.2 to 4.2.5 outputs.

4.2.1 2-D SNKH Model Verification with 1-D DEEPSOIL Nonlinear Analysis

The SNKH model for a 20-degree submarine slope was used for comparison and validation against the nonlinear DEEPSOIL model, at the profiles located at x = 150 m and x = 400 m, the closer the observation point is to the base of the slope, the greater the discrepancy observed when compared to the DEEPSOIL results. This difference may be attributed to material yielding during seismic wave propagation as well as irregular reflections caused by the asymmetrical geometry of the slope. Nevertheless, across all these cases, the maximum strain difference between the two models is approximately 0.05%, which is considered acceptable. As for the profile at x = 275 m within the slope region, due to the combined effects of geometric asymmetry and plastic sliding, significant plastic strains were observed around the seventh second of shaking. This behavior is consistent with slope sliding under seismic loading. Although the precise magnitude and spatial extent of the sliding cannot be directly validated, the overall agreement observed in the results at x = 150 m and x = 400 m supports the applicability of the SKNH model. Thus, the model can be considered reliable for use in the present study.

doi:10.6342/NTU202503752

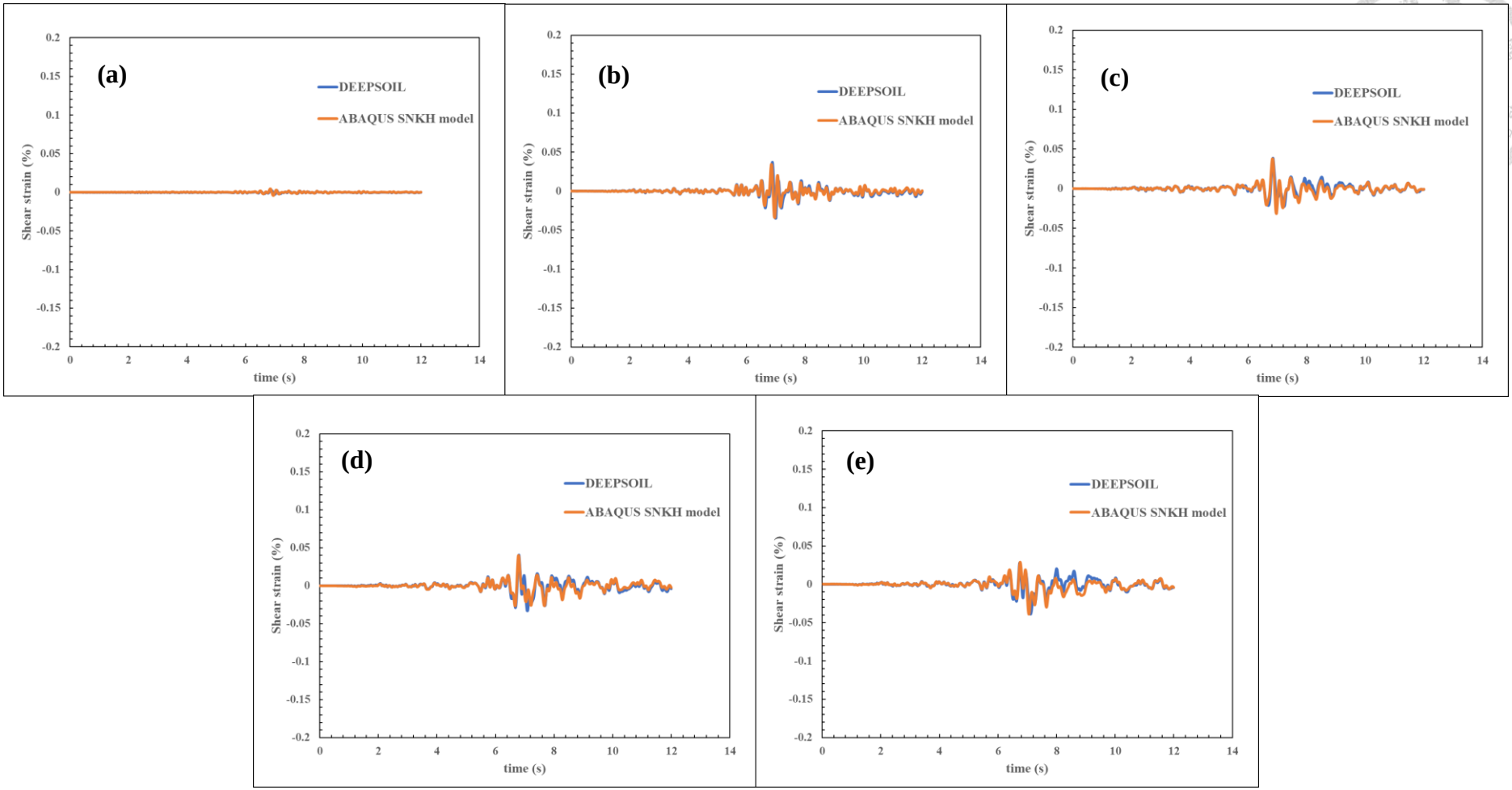

Figure 4.19 Shear strain comparison in elastic half space between DEEPSOIL nonlinear model and ABAQUS SNKH model at x = 150 m (lower platform) and at (a) y = 25 m; (b) y = 20 m; (c) y = 15 m; (d) y = 10 m; (e) y = 5 m.

doi:10.6342/NTU202503752

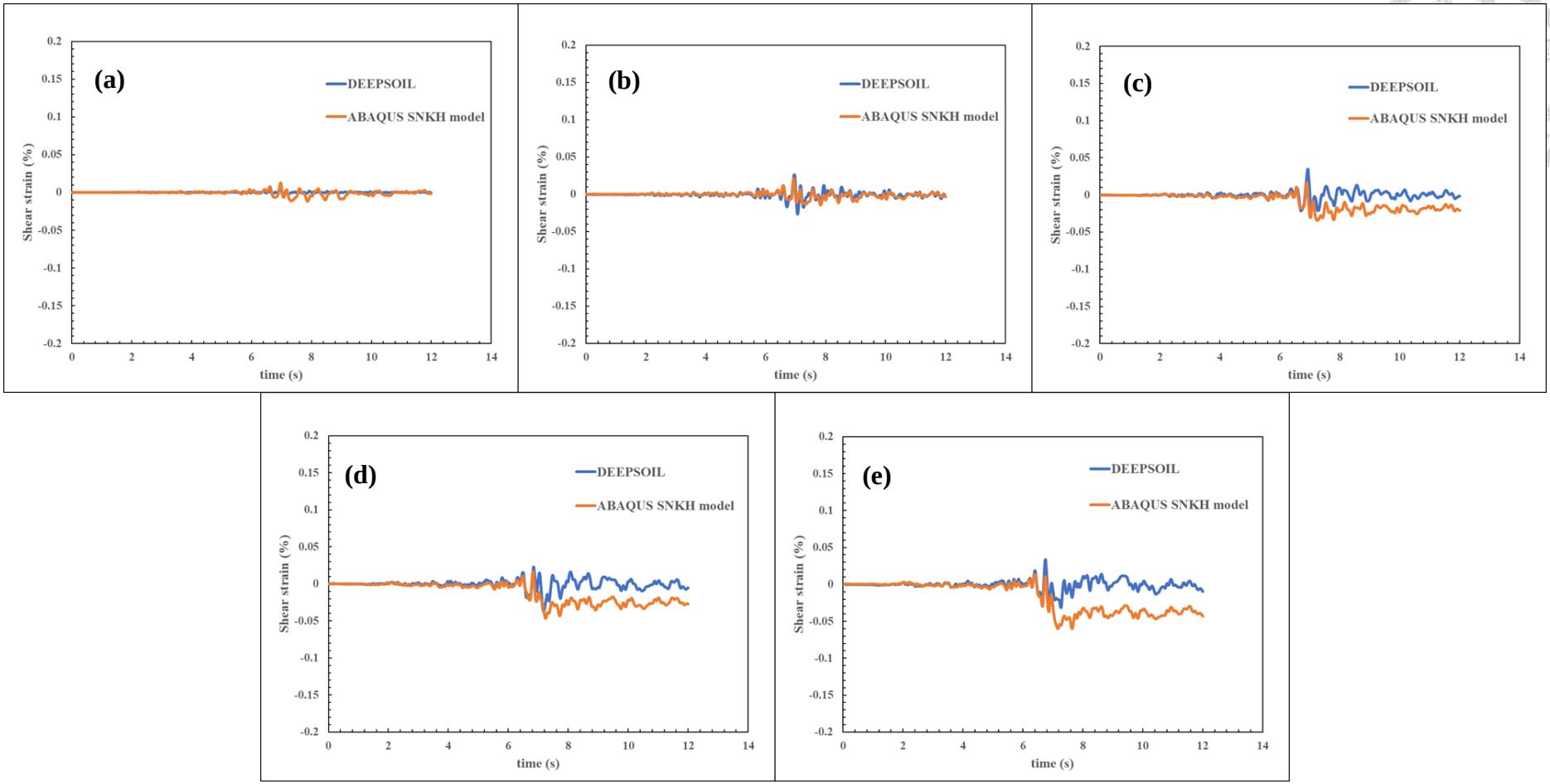

Figure 4.20 Shear strain comparison in elastic half space between DEEPSOIL nonlinear model and ABAQUS SNKH model at x = 275 m (slope area) and at (a) y = 34 m; (b) y = 30 m; (c) y = 25 m; (d) y = 15m; (e) y = 5 m.

doi:10.6342/NTU202503752

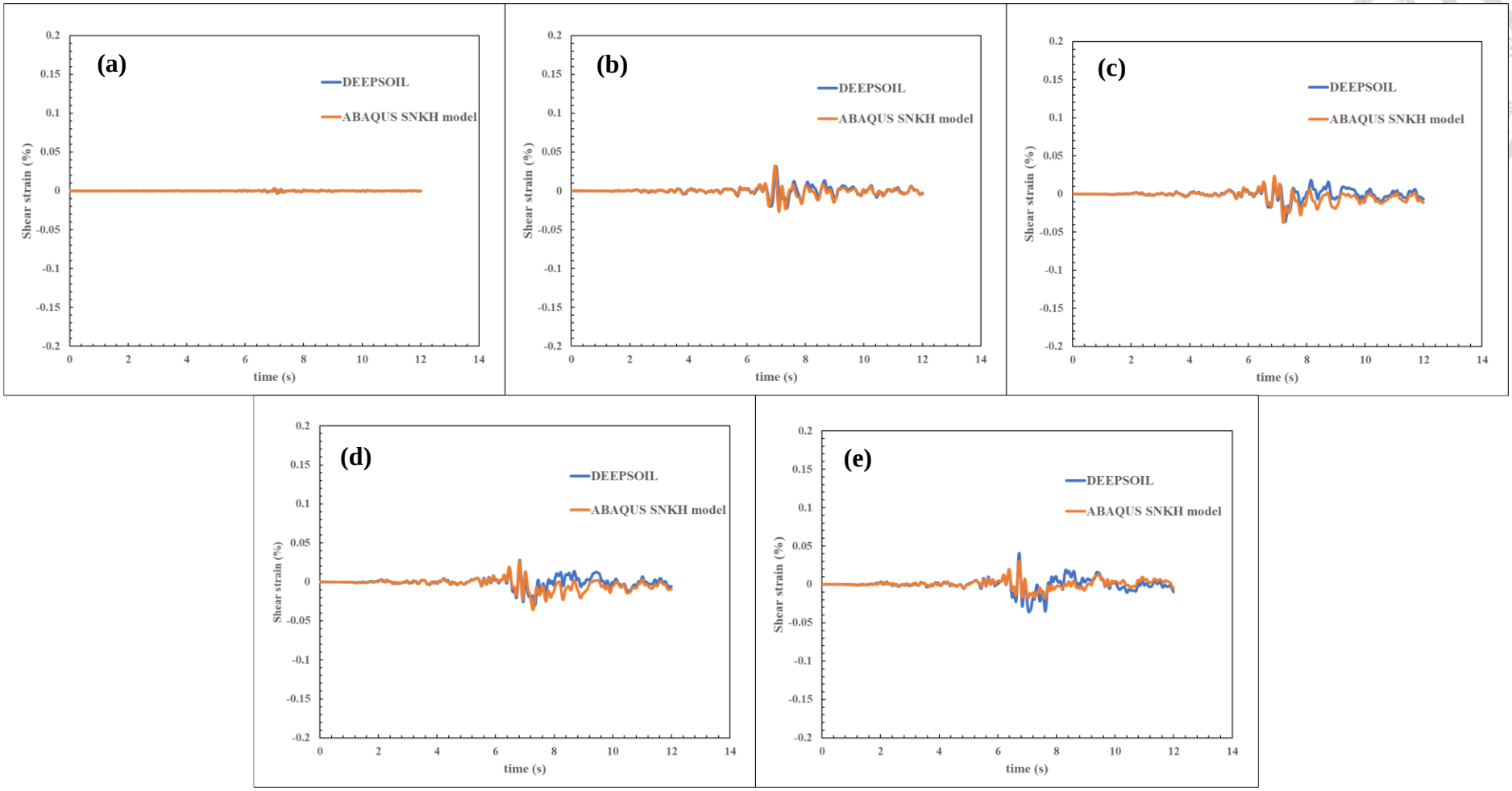

Figure 4.21 Shear strain comparison in elastic half space between DEEPSOIL nonlinear model and ABAQUS SNKH model at x = 400 m (upper platform) and at (a) y = 43 m; (b) y = 33 m; (c) y = 23 m; (d) y = 13m; (e) y = 3 m.

doi:10.6342/NTU202503752

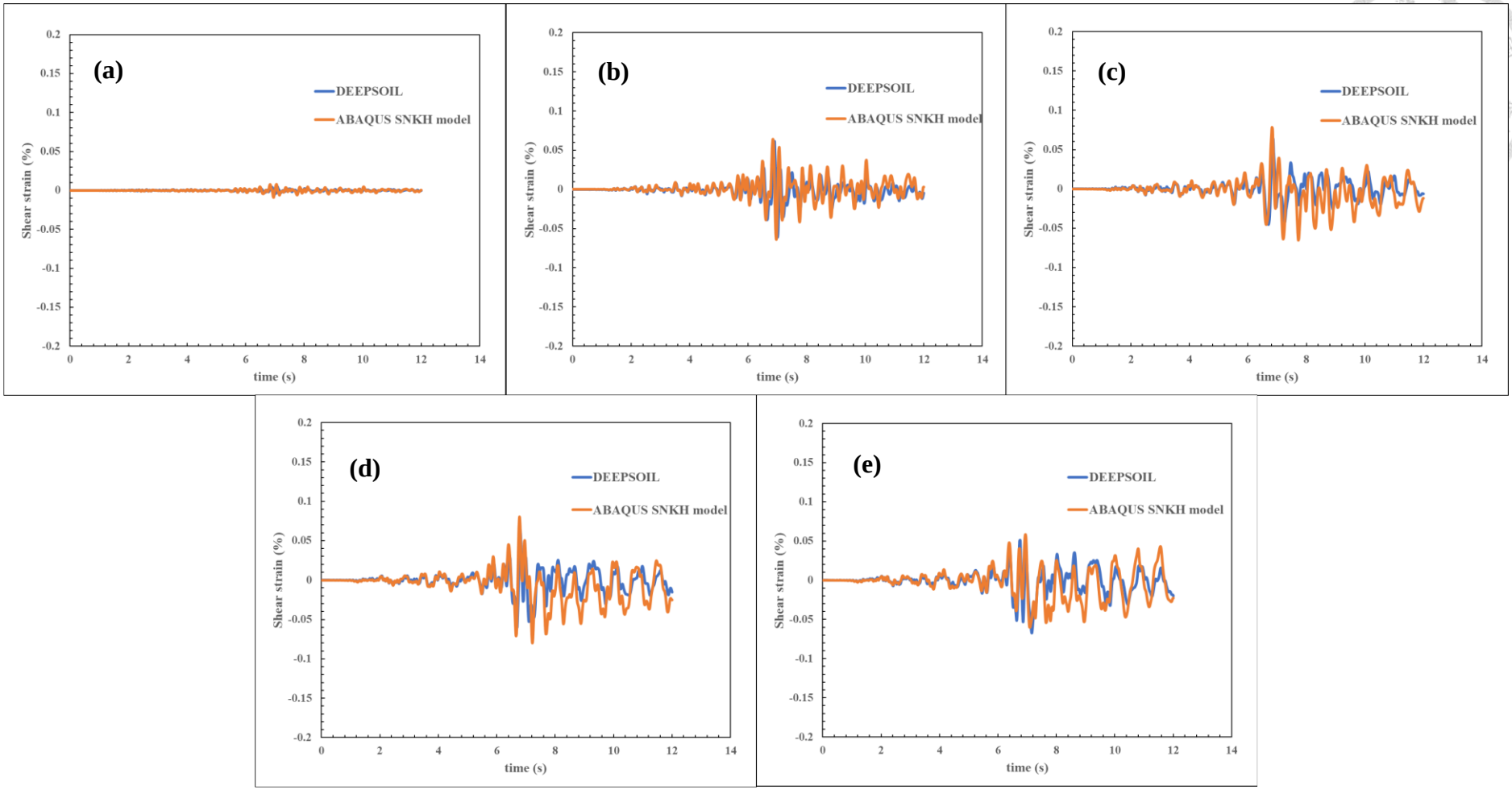

Figure 4.22 Shear strain comparison in rigid half space between DEEPSOIL nonlinear model and ABAQUS SNKH model at x = 150 m (lower platform) and at (a) y = 25 m; (b) y = 20 m; (c) y = 15 m; (d) y = 10 m; (e) y = 5 m.

doi:10.6342/NTU202503752

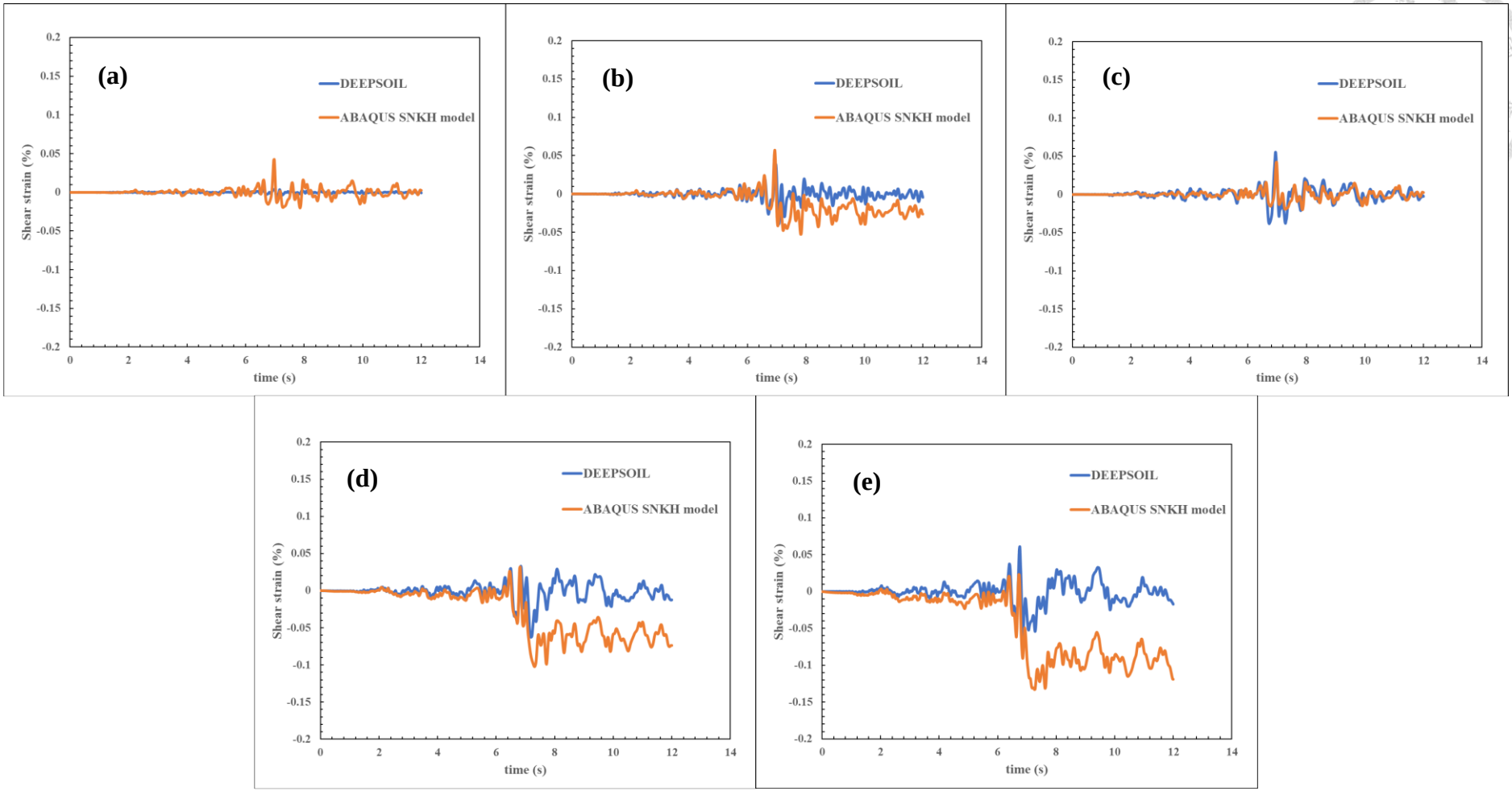

Figure 4.23 Shear strain comparison in rigid half space between DEEPSOIL nonlinear model and ABAQUS SNKH model at x = 275 m (slope area) and at (a) y = 34 m; (b) y = 30 m; (c) y = 25 m; (d) y = 15m; (e) y = 5 m.

doi:10.6342/NTU202503752

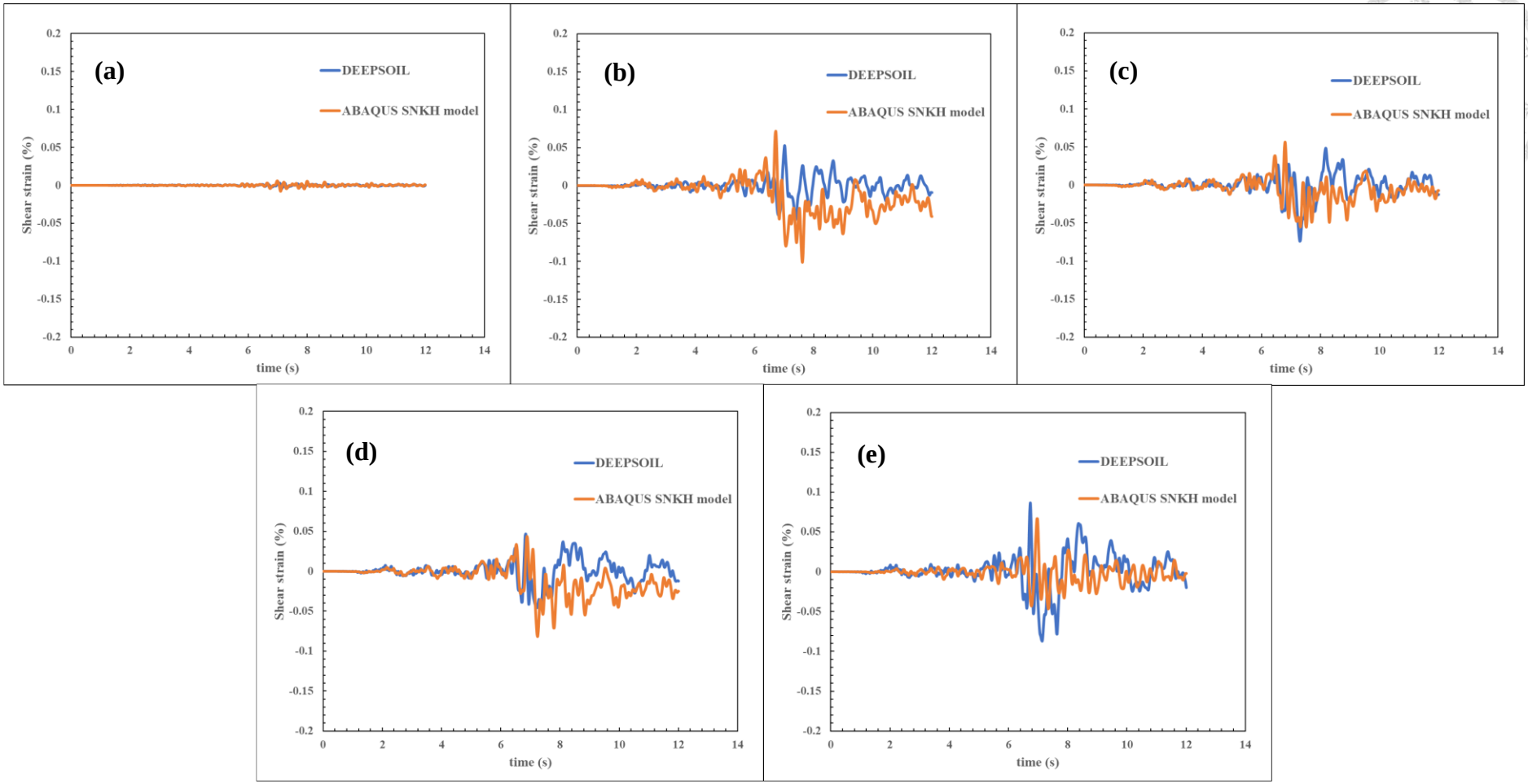

Figure 4.24 Shear strain comparison in rigid half space between DEEPSOIL nonlinear model and ABAQUS SNKH model at x = 400 m (upper platform) and at (a) y = 43 m; (b) y = 33 m; (c) y = 23 m; (d) y = 13m; (e) y = 3

doi:10.6342/NTU202503752

4.2.2 X-Direction Displacement and Shear Strain Histories in Different Earthquake Motions and Slope Angles

Figure 4.25 to 4.25 present the X-direction displacement and shear strain histories at point B in Figure 4.18, which corresponds to the midpoint of the slope surface, under various earthquake inputs and slope angles. In all cases, the undrained shear strength is 40 kPa and the water depth (DW) is 50 meters. The solid lines represent results from the elastic half-space models, while the dashed lines represent those from the rigid half-space models. First, comparing the two bedrock types, the rigid half-space cases consistently produce larger overall displacements and shear strains than the cases of elastic half-space. This indicates that the elastic half-space partially absorbs seismic waves, while the rigid half-space, due to total wave reflection, leads to more significant permanent plastic deformation. Next, it can be observed that as the slope angle increases, both the total displacement and shear strain also increase. In particular, for the 20-degree slope (e.g., the Kobe earthquake with the rigid half-space models), the peak ground displacement (PGD) is 20 cm greater than that of the 10-degree slope, and the maximum shear strain is 8 times larger. In fact, considering the effects of the shear modulus reduction curve, higher shear strain leads to more severe shear modulus degradation. Therefore, the substantial increase in shear strain observed in the steeper slopes (compared to the 5° and 10° cases) is expected. Table 4.4 summarizes the PGD and maximum shear strain values for all cases shown in Figure 4.25 to 4.25.

Interestingly, when examining the displacement histories of the Kobe and Kocaeli earthquakes, it can be observed that in the 5 and 10-degree slope cases, the Kocaeli earthquake resulted in larger peak displacements than the Kobe earthquake. However, the Kobe earthquake input used in this study has a PGA of 0.63 g, which is 4.5 times greater

doi:10.6342/NTU202503752

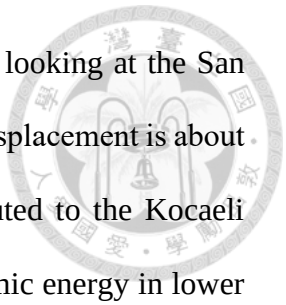

than the 0.14 g PGA of the Kocaeli earthquake. Furthermore, when looking at the San Fernando earthquake, which also has a PGA of 0.14 g, the resulting displacement is about 10 times smaller than that of the Kocaeli case. This can be attributed to the Kocaeli earthquake's longer mean period (1.0681 s), which concentrates seismic energy in lower frequencies that better match the natural period of soft submarine slopes, thus inducing more significant cyclic shear strains and cumulative deformations. The displacement and shear strain data of the remaining points in Figure 4.18 are presented in Appendix A.

doi:10.6342/NTU202503752

Table 4.3 The PGD and the maximum shear strain summary in section 4.2.2.

Slope angle (°)	Motion	Bedrock	PGD (m)	Maximum shear strain (%)
5	Kobe	Elastic	0.17	0.0115
	Kocaeli		0.27	0.0032
	San Fernando		0.01	0.0012
	Kobe	Rigid	0.21	0.0145
	Kocaeli		0.32	0.0069
	San Fernando		0.02	0.0023
10	Kobe	Elastic	0.24	0.0419
	Kocaeli		0.27	0.0082
	San Fernando		0.01	0.0026
	Kobe	Rigid	0.31	0.0758
	Kocaeli		0.33	0.0195
	San Fernando		0.03	0.0046

doi:10.6342/NTU202503752

Slope angle (°)	Motion	Bedrock	PGD (m)	Maximum shear strain (%)
20	Kobe	Elastic	0.33	0.4043
	Kocaeli		0.27	0.0391
	San Fernando		0.02	0.0129
	Kobe	Rigid	0.51	0.6183
	Kocaeli		0.36	0.1312
	San Fernando		0.04	0.0313

doi:10.6342/NTU202503752

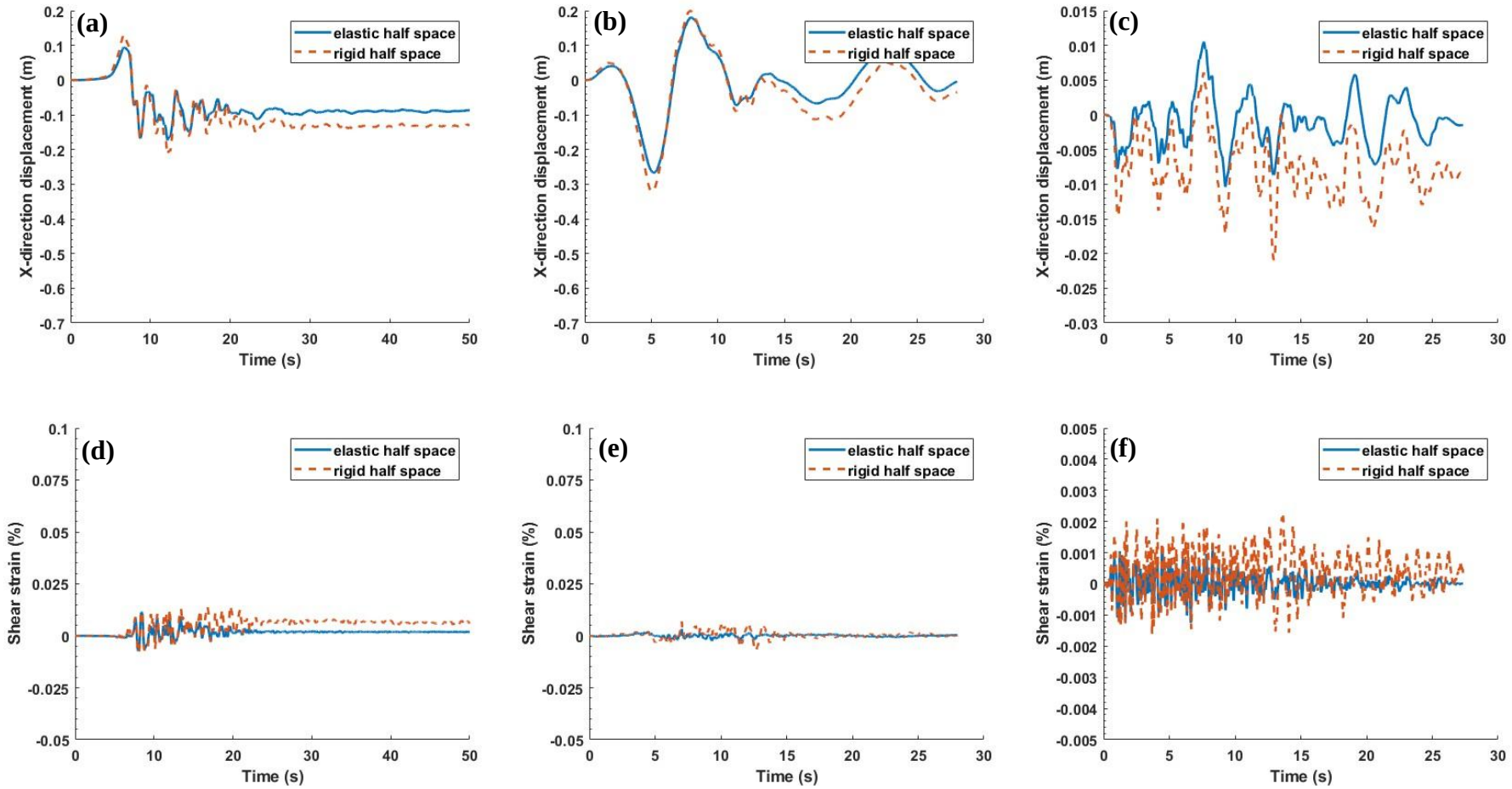

Figure 4.25 X-direction displacement history of (a) Kobe; (b) Kocaeli; (c) San Fernando earthquake and shear strain history of (d) Kobe; (e) Kocaeli; (f) San Fernando earthquake in 5-degree submarine slope with s_u =40 kPa, DW = 50 m.

doi:10.6342/NTU202503752

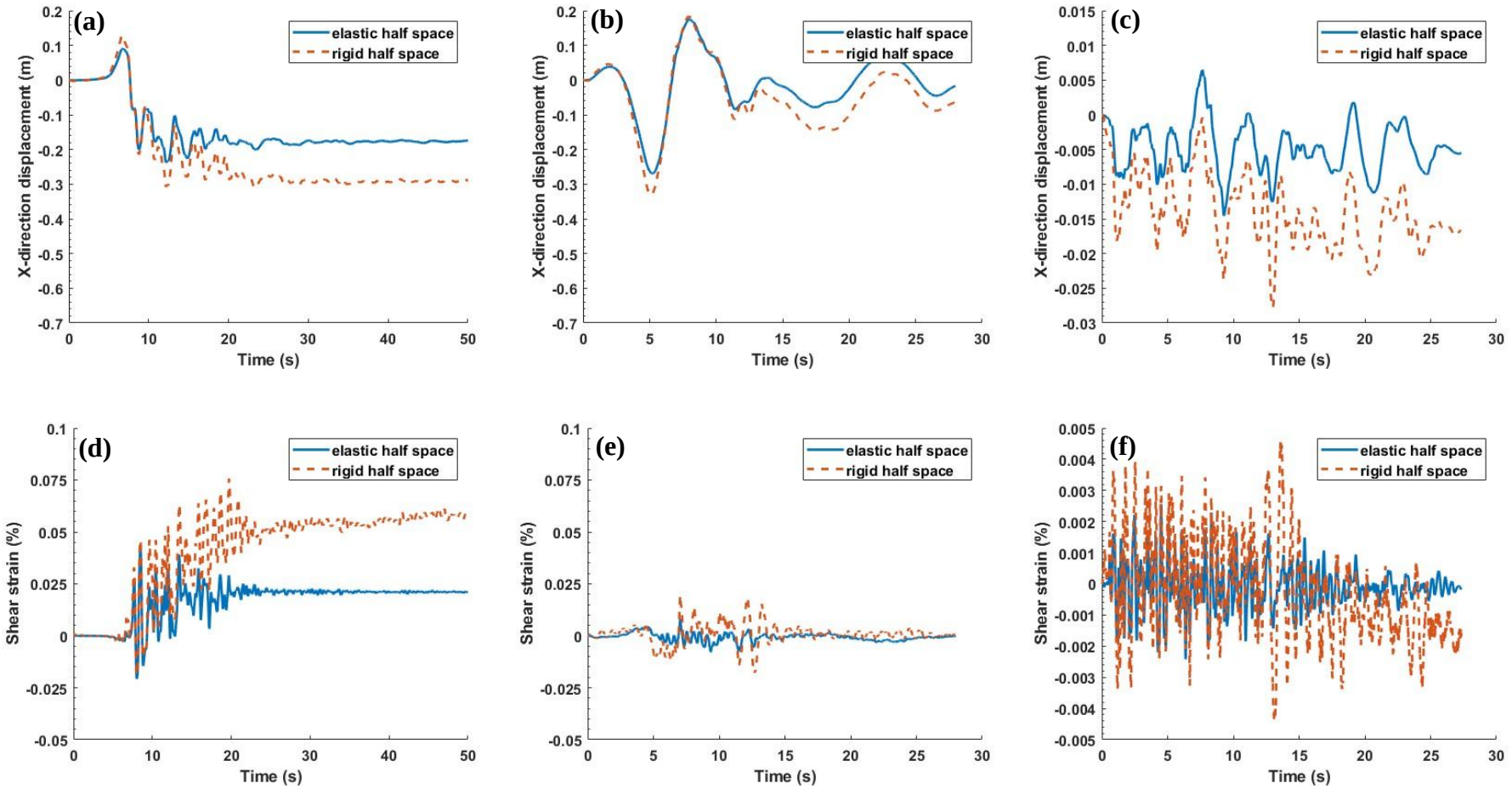

Figure 4.26 X-direction displacement history of (a) Kobe; (b) Kocaeli; (c) San Fernando earthquake and shear strain history of (d) Kobe; (e) Kocaeli; (f) San Fernando earthquake in 10-degree submarine slope with s_u =40 kPa, DW = 50 m.

doi:10.6342/NTU202503752

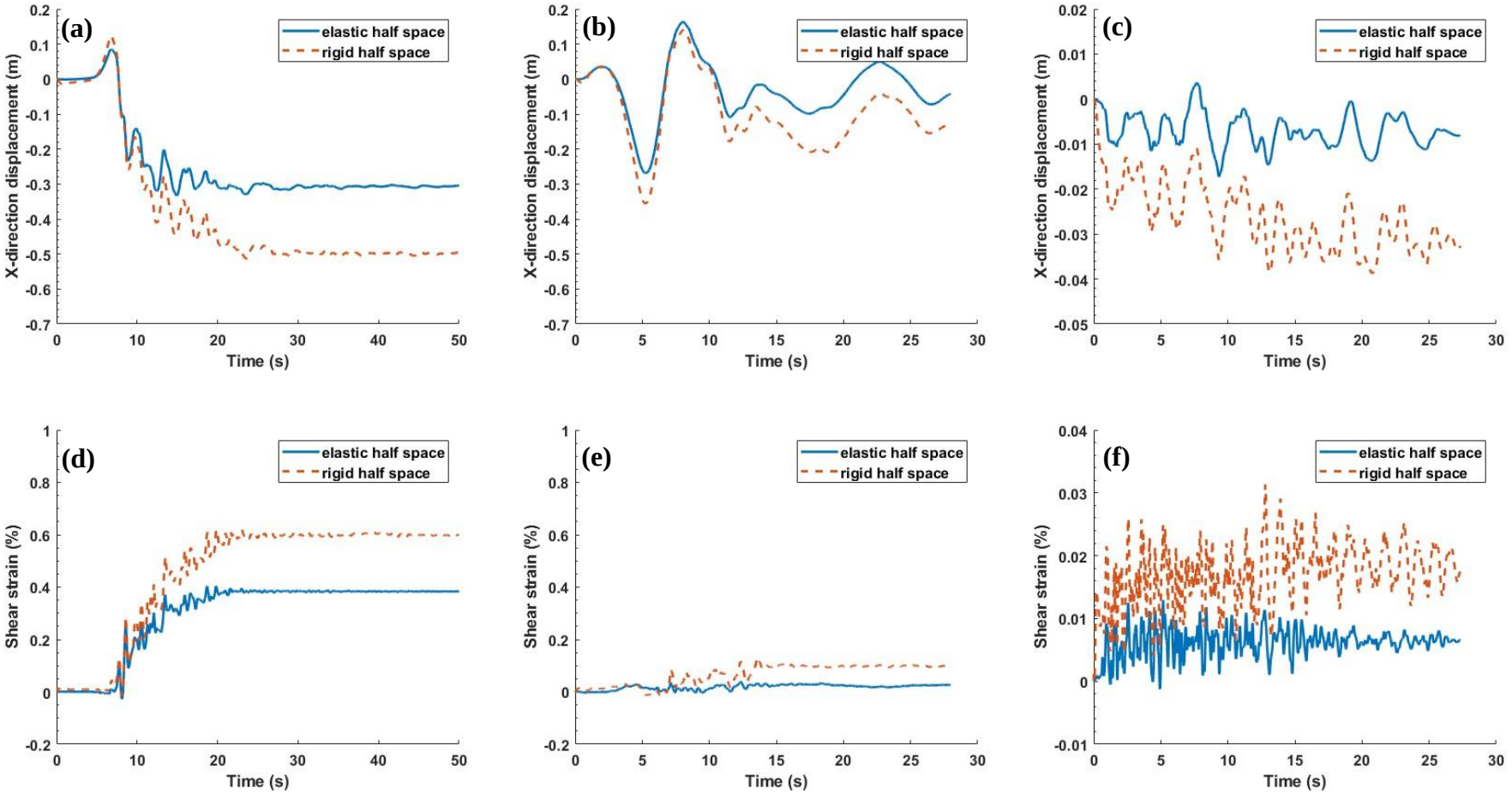

Figure 4.27 X-direction displacement history of (a) Kobe; (b) Kocaeli; (c) San Fernando earthquake and shear strain history of (d) Kobe; (e) Kocaeli; (f) San Fernando earthquake in 20-degree submarine slope with s_u =40 kPa, DW = 50 m.

doi:10.6342/NTU202503752

4.2.3 X-Direction Displacement and Shear Strain Histories in Different Depth of Water

To further investigate the effect of seawater depth on post-earthquake deformation of submarine slopes, the Kobe earthquake was used as the seismic input with s_u fixed at 40 kPa. Two water depths (DW = 25 m and 50 m) and three slope angles (5°, 10°, and 20°) were considered under both elastic and rigid half space bedrock conditions. The comparison between DW = 25m and DW = 50m at point B in Table 4.4, it can be seen that although a deeper water level alters the interaction between the free surface and wave propagation, the results do not show a consistent amplification trend in PGD or maximum shear strain. For instance, under a 10° slope, the elastic bedrock condition yields nearly identical PGDs (0.2369 m vs. 0.2380 m) and shear strains. In the rigid bedrock case, PGD even slightly decreases (from 0.3112 m to 0.3101 m). This indicates that for soft, shallow submarine slopes, the impact of water depth is relatively minor and may be constrained by more dominant factors such as geometry and soil properties. Moreover, time history plots clearly show that rigid half space models consistently produce greater deformation and shear strain compared to elastic ones under the same conditions—especially under the 20° slope. This is attributed to the full reflection of seismic waves in the rigid bedrock model due to the lack of energy dissipation, resulting in more intense shaking and nonlinear soil response near the surface.

In summary, under fixed seismic and undrained shear strength, seawater depth has a limited influence, whereas bedrock type and slope geometry play a more critical role in governing the deformation behavior of submarine slopes. The x-direction displacement and shear strain history plots of DW = 25 m are shown in Figure 4.28, and the plots within s_u = 100 kPa are demonstrated in Appendix B.

doi:10.6342/NTU202503752

Table 4.4 The PGD and the maximum shear strain in Kobe earthquake event under different DW.

Slope angle (°)	DW (m)	Bedrock	PGD (m)	Maximum shear strain (%)
5	25	Elastic	0.1736	0.0115
	50		0.1736	0.0115
	25	Rigid	0.2139	0.0141
	50		0.2136	0.0145
10	25	Elastic	0.2369	0.0417
	50		0.2380	0.0419
	25	Rigid	0.3112	0.0783
	50		0.3101	0.0758
20	25	Elastic	0.3744	0.2827
	50		0.3327	0.4043
	25	Rigid	0.6417	0.4679
	50		0.5137	0.6183

doi:10.6342/NTU202503752

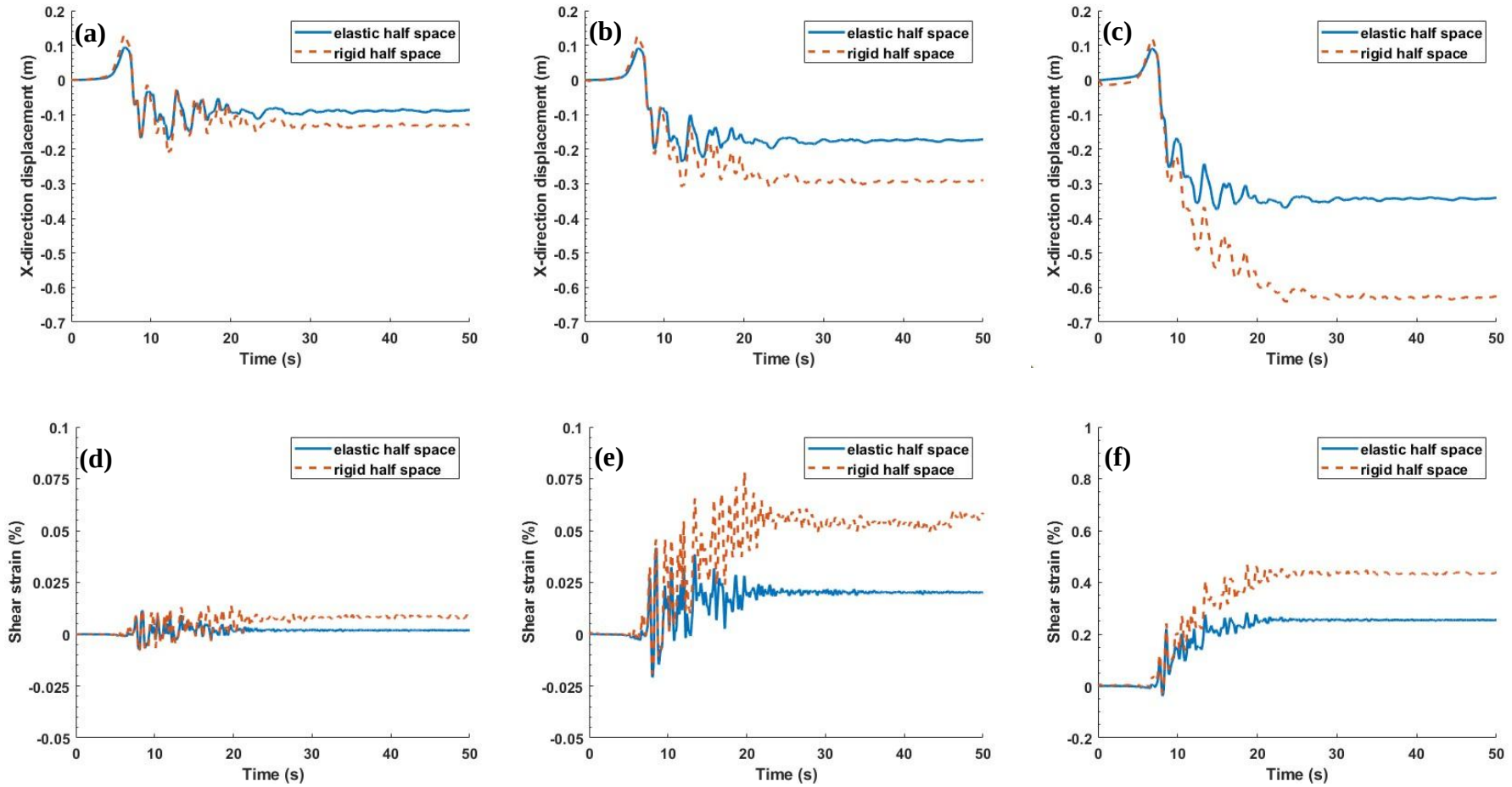

Figure 4.28 X-direction displacement history of Kobe earthquake with DW = 25 m in (a)5°; (b)10°; (c)20° slope and shear strain history in (d)5°; (e)10°; (f)20° slope.

doi:10.6342/NTU202503752

4.2.4 Ground Motion Amplification Profiles

This study employs the Ground Motion Amplification Ratio (GMAR) to evaluate the effectiveness of seismic energy transfer under different slope conditions. GMAR is defined as the ratio of the peak ground acceleration (PGA) observed at a monitoring point within the model to the input PGA at the model base. It reflects the combined effects of soil stiffness, slope geometry, seismic wave frequency, and boundary conditions on seismic response. Table 4.4 to 4.8 and Figure 4.28 to 4.28 present the GMAR distributions for submarine slopes with angles of 5, 10, and 20 degrees under three earthquake records (Kobe, Kocaeli, and San Fernando), and two undrained shear strength conditions (s_u = 40 kPa and 100 kPa). A comparison between elastic and rigid half-space foundations reveals that under identical slope and seismic conditions, GMAR values are consistently higher in elastic half-space models. This indicates that the elastic half-space absorbs part of the incoming wave energy, reducing wave reflection and causing higher surface acceleration compared to rigid models.

Interestingly, GMAR does not increase monotonically with slope angle. In many cases, 10° slopes exhibit the highest amplification, while GMAR values decrease for 20° slopes. This can be explained by the following factors:

1. Steeper slopes cause surface scattering of seismic waves, reducing vertical energy transmission to observation points.
2. At 20°, slope failure mechanisms such as sliding may activate, transforming seismic energy into plastic deformation rather than acceleration.
3. The interaction between incident waves and surface geometry may lead to interference nodes near surface points, reducing GMAR.

doi:10.6342/NTU202503752

Among the three earthquakes, the Kocaeli motion, despite having the same PGA (0.14g) as the San Fernando event, produces significantly higher displacement and GMAR in 5-degree and 10-degree models. This is attributed to its longer mean period (1.0681s), which resonates more strongly with the natural period of soft submarine slopes. In contrast, the San Fernando earthquake, with a shorter period (0.2187s), induces much smaller amplification. In summary, GMAR is governed not only by input intensity (PGA) but also by the interaction of slope geometry, soil strength, and frequency content of the seismic motion. Future studies should emphasize resonance effects and terrain configuration in seismic hazard assessments.

To establish a comparative basis for examining and discussing the variation of GMAR in submarine slopes composed of nonlinear materials under seismic loading, the amplification phenomenon at the crest of elastic soil slopes studied by Ashford et al. (1997) on land is referenced and compared with the results of this study. In Ashford et al.'s analysis, the soil had a shear wave velocity of V_s = 300 m/s, Poisson's ratio of 0.3, and a slope height of H = 30 m. The input motion and slope geometry are illustrated in Figure 4.32. Ashford et al. (1997) simulated the GMAR response for slopes with inclinations of 30°, 45°, 60°, 75°, and 90°, examining how GMAR varies with the slope height-to-wavelength ratio (H/λ). Their results showed that when H/λ < 0.3, the larger the slope angle, the greater the variation in GMAR, as depicted in Figure 4.33. In this study, the 30° slope curve from Ashford et al. is selected for comparison. The comparison results are shown in Figure 4.34, where each earthquake case is marked with a specific symbol:

- Kobe earthquake: triangle
- Kocaeli earthquake: diamond
- San Fernando earthquake: square

doi:10.6342/NTU202503752

The symbols are also colored based on different bedrock conditions and the undrained shear strength of the soil, as summarized in Figure 4.35. The reference curve from Ashford et al. (1997) is shown as a black solid line. Finally, symbol sizes are used to represent different slope angles in this study:

- 5° (smallest symbol)
- 10° (medium)
- 20° (largest)

The results indicate that most GMAR values in this study are lower than those reported by Ashford et al. (1997) for the 30° slope. Moreover, among the three slope angles considered here, there is no consistent trend in terms of magnitude. Only a few data points from the Kocaeli earthquake exceeded Ashford et al. (1997)'s results, further highlighting the importance of dominant frequency of the input motion in triggering resonance phenomena in slope structures.

doi:10.6342/NTU202503752

Table 4.5 Ground motion amplification ratio of 5-degree slope (s_u = 40 kPa).

Motion	Point	GMAR	
		Elastic half space	Rigid half space
Kobe	A	0.572	0.486
	B	0.553	0.461
	C	0.529	0.441
	D	0.594	0.488
	E	0.565	0.465
	F	0.519	0.414
Kocaeli	A	1.059	0.987
	B	1.112	1.100
	C	1.098	1.069
	D	1.188	1.145
	E	1.167	1.130
	F	1.110	1.058
San Fernando	A	1.246	0.879
	B	1.209	0.891
	C	0.982	0.646
	D	1.242	0.853
	E	1.028	0.609
	F	0.642	0.496

doi:10.6342/NTU202503752

Table 4.6 Ground motion amplification ratio of 5-degree slope (s_u = 100 kPa).

Motion	Point	GMAR	
		Elastic half space	Rigid half space
Kobe	A	0.959	0.768
	B	1.016	0.785
	C	1.010	0.765
	D	1.078	0.837
	E	1.055	0.824
	F	1.006	0.780
Kocaeli	A	1.313	1.183
	B	1.298	1.266
	C	1.201	1.117
	D	1.361	1.326
	E	1.307	1.185
	F	1.225	1.145
San Fernando	A	1.246	1.099
	B	1.209	1.108
	C	0.982	1.039
	D	1.242	1.148
	E	1.028	1.082
	F	0.642	0.914

doi:10.6342/NTU202503752

Table 4.7 Ground motion amplification ratio of 10-degree slope (s_u = 40 kPa).

Motion	Point	GMAR	
		Elastic half space	Rigid half space
Kobe	A	0.473	0.431
	B	0.462	0.404
	C	0.373	0.326
	D	0.491	0.432
	E	0.455	0.395
	F	0.363	0.309
Kocaeli	A	0.998	0.961
	B	1.119	1.086
	C	1.073	1.016
	D	1.163	1.093
	E	1.068	1.039
	F	0.904	0.866
San Fernando	A	0.947	0.81
	B	1.003	0.844
	C	0.509	0.472
	D	0.895	0.750
	E	0.598	0.470
	F	0.621	0.555

doi:10.6342/NTU202503752

Table 4.8 Ground motion amplification ratio of 10-degree slope (s_u = 100 kPa).

Motion	Point	GMAR	
		Elastic half space	Rigid half space
Kobe	A	0.933	0.704
	B	0.959	0.687
	C	0.869	0.621
	D	1.064	0.767
	E	1.008	0.738
	F	0.863	0.616
Kocaeli	A	1.183	1.165
	B	1.182	1.227
	C	1.107	0.944
	D	1.318	1.290
	E	1.173	1.153
	F	1.013	0.963
San Fernando	A	0.968	0.891
	B	1.015	1.068
	C	0.544	0.695
	D	0.898	1.069
	E	0.605	0.680
	F	0.607	0.711

doi:10.6342/NTU202503752

Table 4.9 Ground motion amplification ratio of 20-degree slope (s_u = 40 kPa).

Motion	Point	GMAR	
		Elastic half space	Rigid half space
Kobe	A	0.400	0.409
	B	0.370	0.347
	C	0.293	0.266
	D	0.458	0.435
	E	0.292	0.262
	F	0.293	0.242
Kocaeli	A	0.956	1.160
	B	0.958	1.027
	C	0.805	0.899
	D	0.882	1.062
	E	0.782	0.852
	F	0.669	0.647
San Fernando	A	0.904	0.781
	B	0.941	0.801
	C	0.456	0.452
	D	1.022	0.806
	E	0.492	0.381
	F	0.531	0.495

doi:10.6342/NTU202503752

Table 4.10 Ground motion amplification ratio of 20-degree slope (s_u = 100 kPa).

Motion	Point	GMAR	
		Elastic half space	Rigid half space
Kobe	A	0.767	0.697
	B	0.724	0.593
	C	0.515	0.431
	D	0.950	0.805
	E	0.760	0.592
	F	0.456	0.356
Kocaeli	A	1.227	1.185
	B	1.228	1.268
	C	1.015	1.009
	D	1.512	1.415
	E	1.188	0.985
	F	0.828	0.901
San Fernando	A	0.881	0.776
	B	0.891	0.843
	C	0.460	0.470
	D	0.989	0.945
	E	0.547	0.523
	F	0.553	0.641

doi:10.6342/NTU202503752

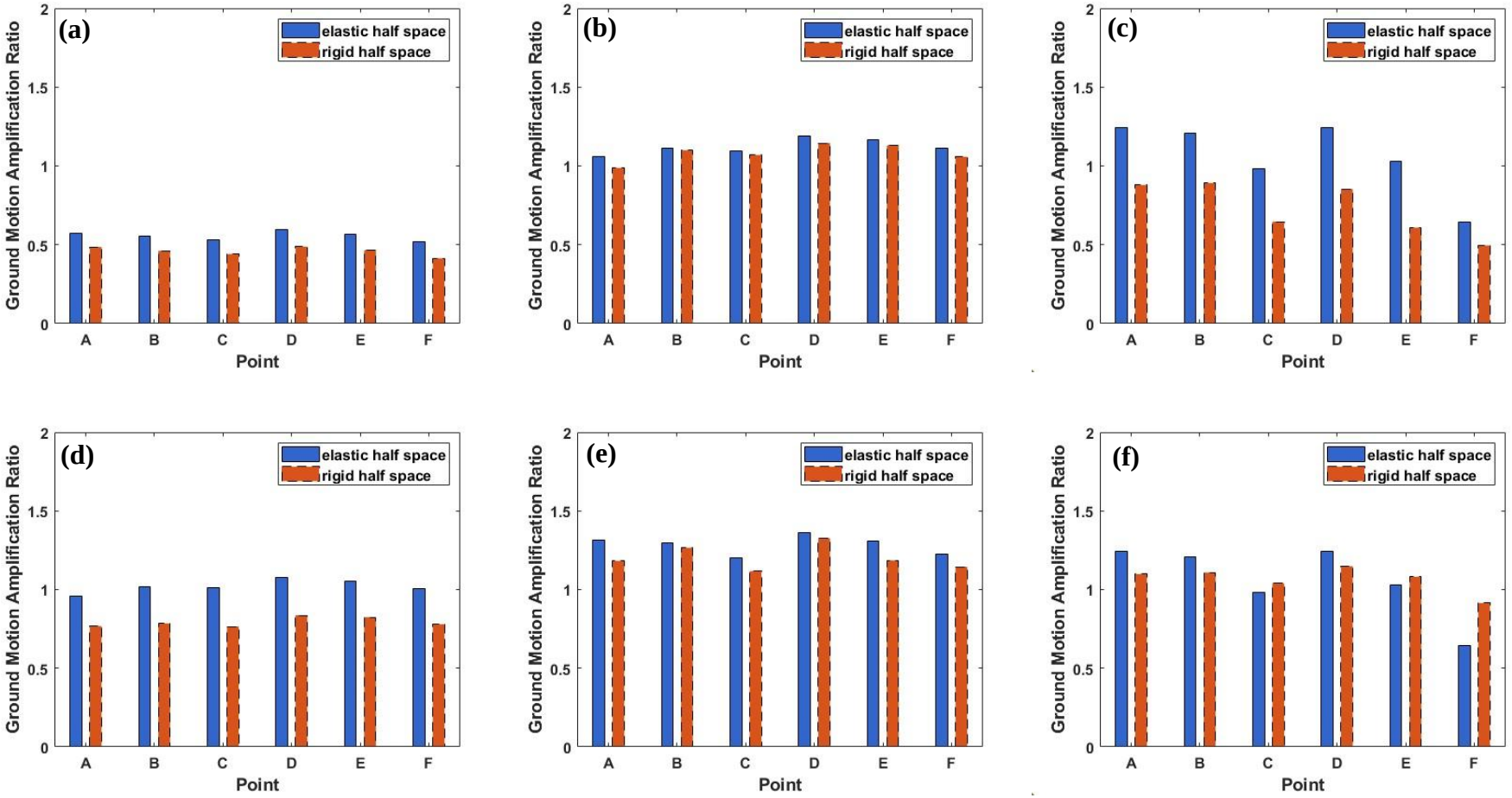

Figure 4.29 Ground motion amplification profiles of 5-degree submarine slope under (a) Kobe; (b) Kocaeli; (c) San Fernando earthquake with s_u = 40 kPa, and (d) Kobe; (e) Kocaeli; (f) San Fernando earthquake with s_u = 100 kPa.

doi:10.6342/NTU202503752

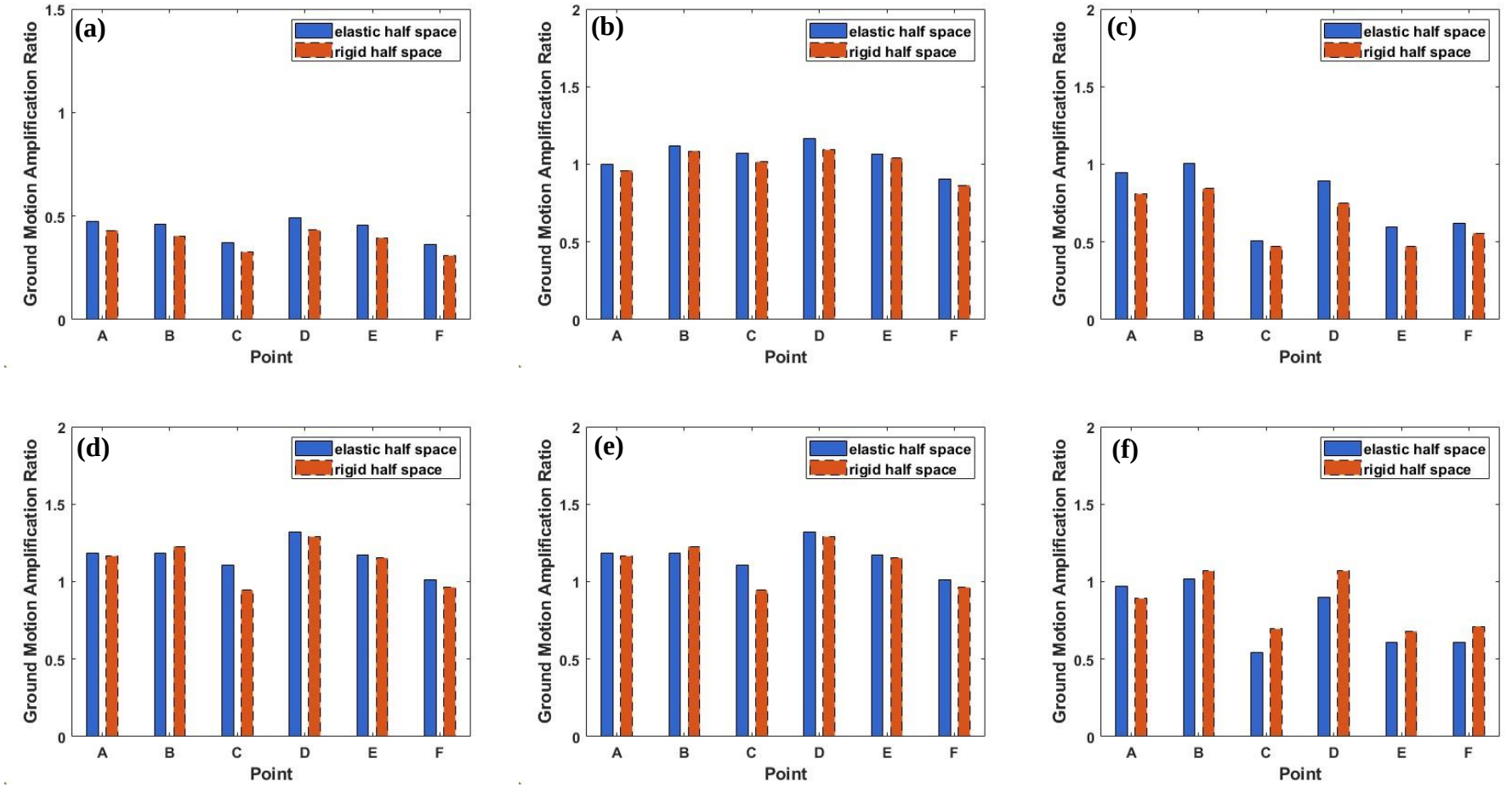

Figure 4.30 Ground motion amplification profiles of 10-degree submarine slope under (a) Kobe; (b) Kocaeli; (c) San Fernando earthquake with s_u = 40 kPa, and (d) Kobe; (e) Kocaeli; (f) San Fernando earthquake with s_u = 100 kPa.

doi:10.6342/NTU202503752

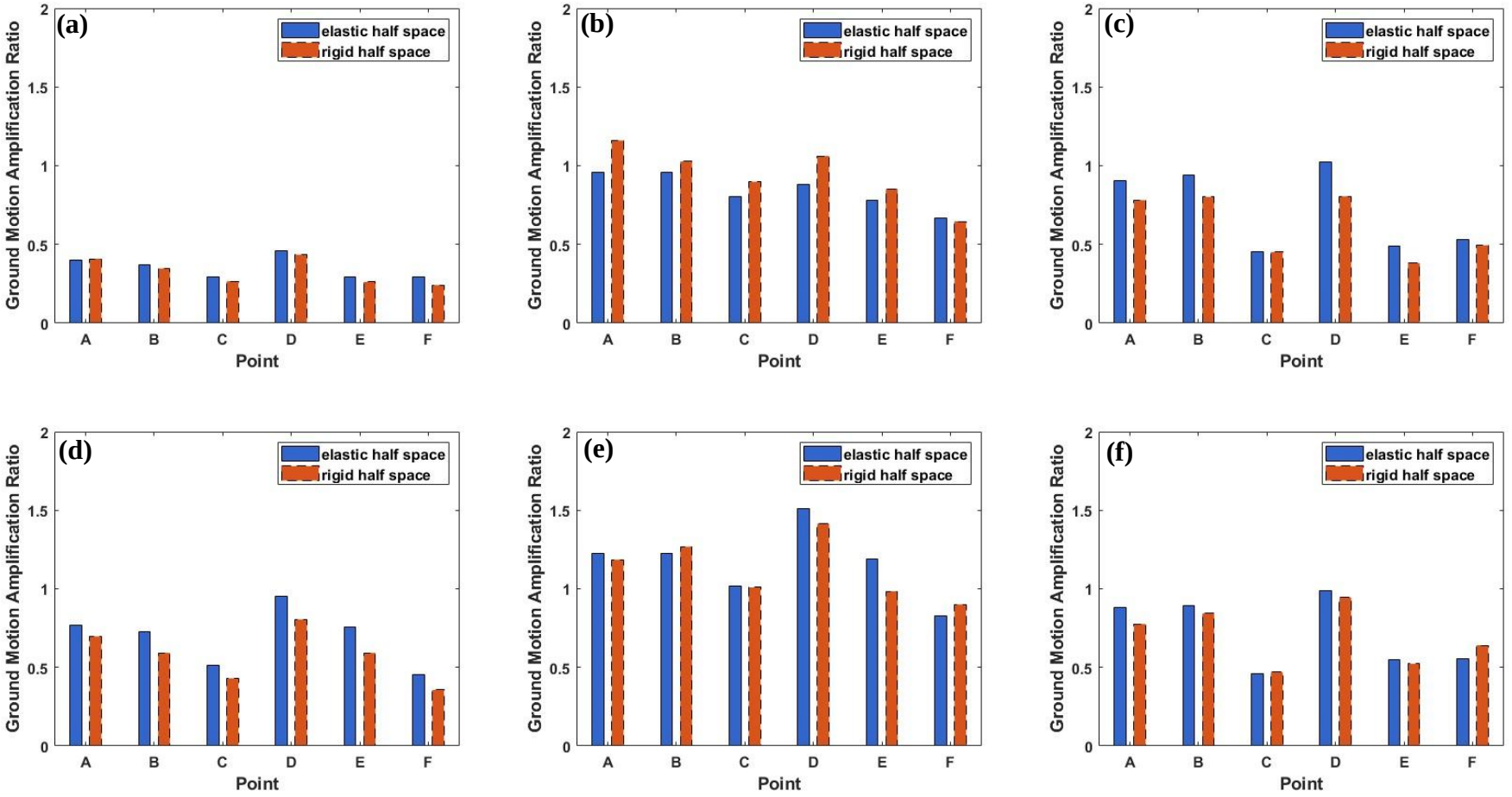

Figure 4.31 Ground motion amplification profiles of 20-degree submarine slope under (a) Kobe; (b) Kocaeli; (c) San Fernando earthquake with s_u = 40 kPa, and (d) Kobe; (e) Kocaeli; (f) San Fernando earthquake with s_u = 100 kPa.

doi:10.6342/NTU202503752

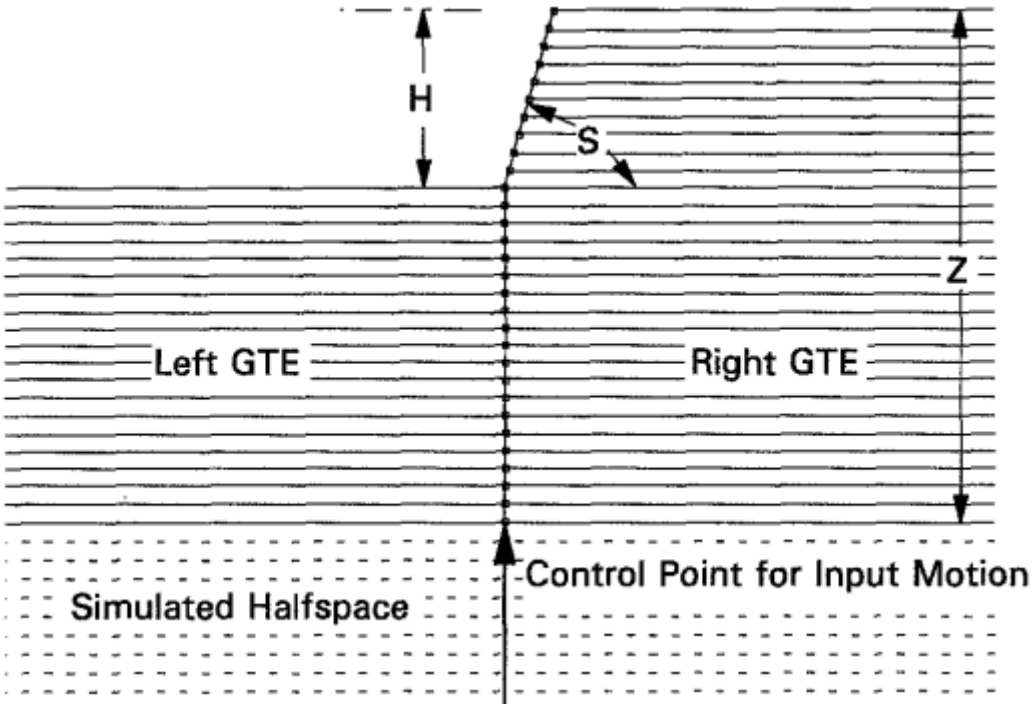

Figure 4.32 Simulated slope geometry and boundary conditions (Ashford et al., 1997)

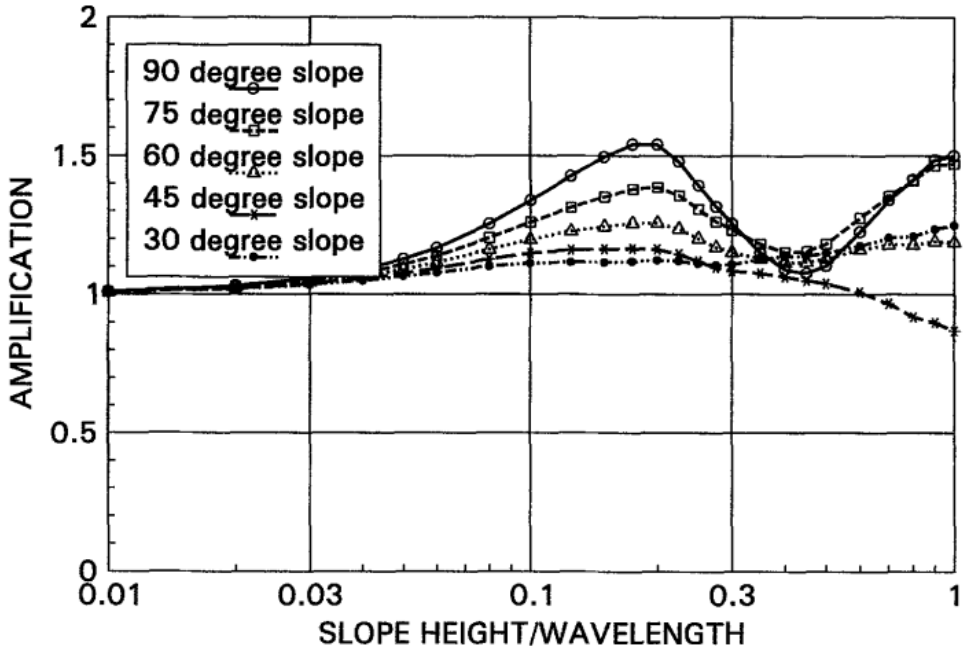

Figure 4.33 Results of GMAR in different slope angles and the slope height-to-wavelength ratio (Ashford et al., 1997)

doi:10.6342/NTU202503752

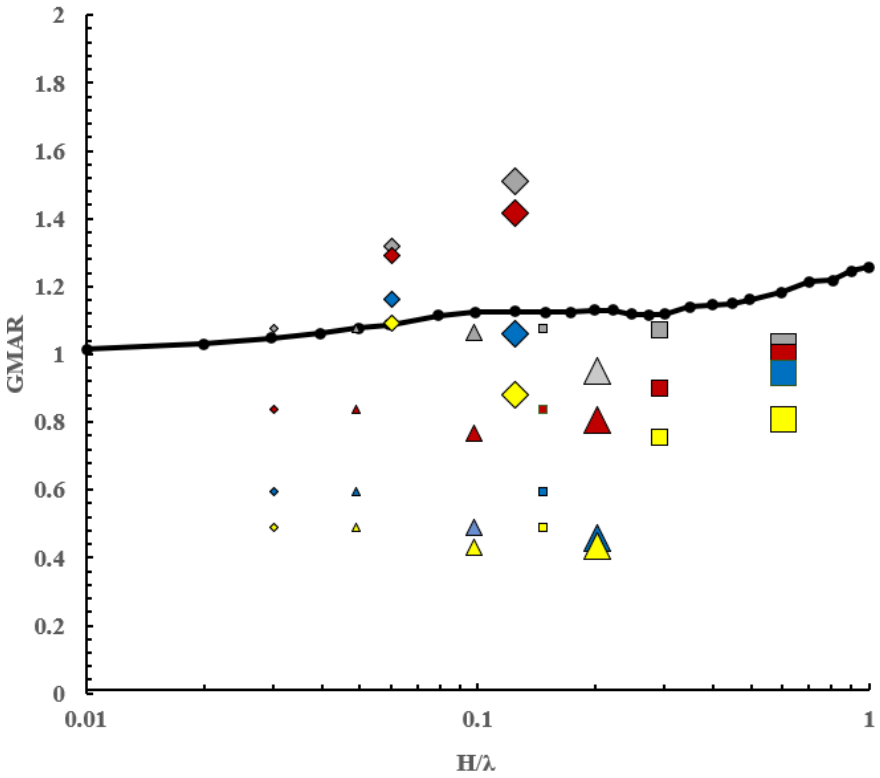

Figure 4.34 Comparisons with Ashford et al. (1997)

Bedrock	s_u (kPa)	Legend		
		Kobe	Kocaeli	San Fernando
Elastic	40	▲	◆	■
	100	▲	◆	■
Rigid	40	▲	◆	■
	100	▲	◆	■
Ashford et al. (1997) 30° line		—●—		

Legend \ β (°)	5	10	20
Symbol size	Small △ ◇ □	Medium △ ◇ □	Big △ ◇ □

Figure 4.35 Legend and symbol size

doi:10.6342/NTU202503752

4.2.5 Slope Failure Observations

In order to characterize the initiation and progression of slope failure, the time history of plastic shear strain at point A (Figure 4.18) was analyzed under the three seismic motions in a 5° submarine slope, as shown in Figure 4.36 (d) to (f). The undrained shear strength and water depth are fixed at 40 kPa and 50 m, respectively. Vertical red dashed lines in Figure 4.36 mark the onset time t_1 and stabilization time t_2 of plastic shear strain, which correspond closely to the evolution of x-direction displacement. Table 4.11 summarizes these key time points for each case. t_1 is defined as the moment when plastic shear strain begins to increase rapidly, indicating the initiation of localized yielding within the slope. t_2 is defined as the point at which plastic shear strain plateaus, signifying the end of progressive plastic deformation. The difference between these two, denoted as $\Delta t = t_2 - t_1$, represents the duration of plastic shear strain development, which is a practical indicator of how long the failure mechanism was actively evolving under seismic loading. Interestingly, the values of t_1 are relatively consistent across the rigid and elastic half space models for Kobe and Kocaeli earthquake, clustering around 7.8 seconds. This consistency implies that the triggering mechanism for failure, such as peak ground acceleration, is not strongly influenced by the bedrock condition. An exception occurs in the San Fernando–elastic case, where no plastic shear strain is generated, suggesting insufficient input energy under that configuration.

In contrast, t_2 vary significantly between rigid and elastic models. For all earthquake motions, the rigid half space results in longer plastic strain durations, which may be attributed to wave reflections and higher cyclic energy retention at the slope base. These prolonged loading conditions lead to greater cumulative deformation, reinforcing the

doi:10.6342/NTU202503752

conclusion that bedrock stiffness not only affects failure magnitude but also prolongs the failure process.

Together, these temporal parameters provide a framework for identifying the critical window of slope destabilization and offer a meaningful way to correlate shear strain evolution with permanent displacement under different seismic and geological conditions.

Table 4.11 Analysis of plastic shear strain initiation (t_1) and stabilization (t_2) times and the duration of plastic shear strain development (Δt).

Motion	**Bedrock**	t_1 **(s)**	t_2 **(s)**	Δt **(s)**
Kobe	**Rigid**	7.8	22.0	14.2
	Elastic	7.8	15.2	7.4
Kocaeli	**Rigid**	7.8	14.1	6.3
	Elastic	7.8	12.6	4.8
San Fernando	**Rigid**	1.3	2.5	1.2
	Elastic	no plastic shear strain generated		

doi:10.6342/NTU202503752

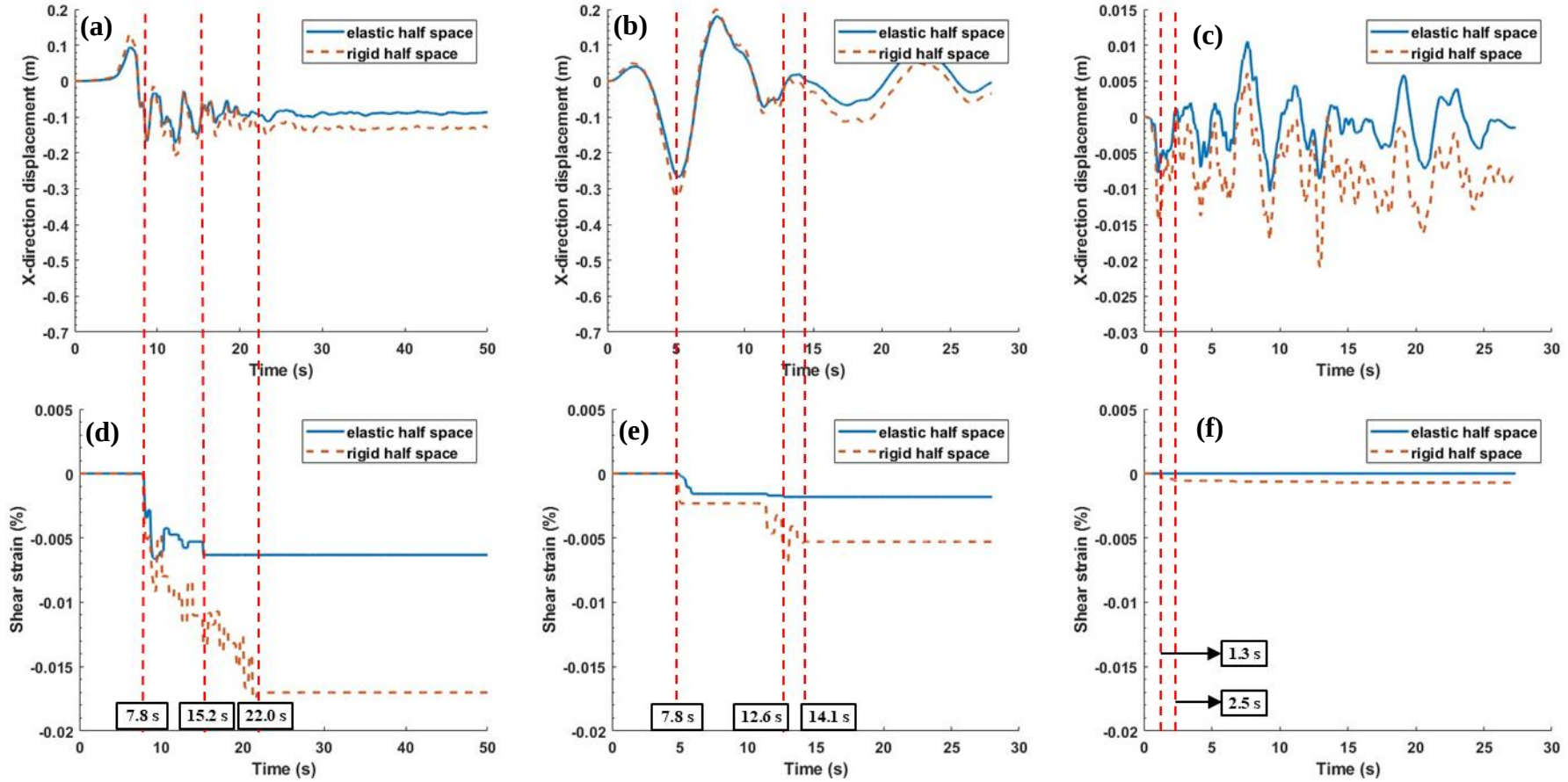

Figure 4.36 X-direction displacement history of (a) Kobe; (b) Kocaeli; (c) San Fernando earthquake and plastic shear strain history of (d) Kobe; (e) Kocaeli; (f) San Fernando earthquake in 5-degree submarine slope with s_u =40 kPa, DW = 50 m.

doi:10.6342/NTU202503752

Chapter 5 Conclusions and Recommendations

5.1 Conclusions

5.1.1 Stability Analyses

The strength reduction analyses conducted in this study offer key insights into the static stability behavior of submarine slopes under both total and effective stress conditions, and across varying seawater depths. The following conclusions can be drawn:

1. **Failure Identification via Displacement Threshold:**

   Across all models, the initiation of failure is characterized by a sharp increase in horizontal displacement beyond a critical reduction factor. This point serves as a reliable indicator for identifying slope failure under static conditions.

2. **Failure Surface Geometry under Total Stress Analysis:**

   When using total stress parameters, failure surfaces consistently extend to the base of the model, indicating global sliding. This behavior is attributed to the uniformity of the cohesive soil and the rapid strength degradation once the critical shear stress is exceeded.

3. **Shallow Failure in Effective Stress Models:**

   In contrast, the effective stress analyses reveal localized, shallow failure surfaces. This is due to increasing effective stress with depth, which raises shear strength at greater depths and shifts failure zones toward the slope surface.

4. **Effect of Analysis Type on Safety Factor:**

   TSA models yield higher factors of safety compared to ESA models under identical input parameters. This discrepancy is due to the higher initial confining

doi:10.6342/NTU202503752

stress considered in total stress analysis (including water pressure), which raises the failure threshold in Mohr-Coulomb terms.

5. **Consistency Between ESA and ESA(II):**

   The effective stress-based results from ESA and ESA with pore pressure (ESAII) show minimal difference, indicating that the impact of the explicitly calculated pore pressure field is minor under static conditions.

6. **Influence of Water Depth on Stability:**

   Varying seawater depth significantly influences slope stability. Results show a non-monotonic trend, where stability improves up to a water depth of 50 m and then gradually deteriorates. This suggests that moderate water depths can have a stabilizing effect due to increased confining pressure on the lower slope, offsetting destabilizing forces near the slope crest.

7. **Numerical Mesh Considerations:**

   The importance of mesh quality is highlighted in the 20-degree slope ESA(II) model, where mesh refinement influenced the stability and convergence of results. Proper mesh aspect ratios are essential for accurately resolving pore pressure and stress fields**.**

In summary, both analysis type and boundary conditions—particularly water depth—play critical roles in submarine slope stability. These findings emphasize the necessity of using appropriate stress frameworks and input parameters for realistic slope failure assessment in offshore environments.

doi:10.6342/NTU202503752

5.1.2 Seismic Analyses

This study systematically investigates the dynamic behavior and failure mechanisms using the SNKH two-dimensional model. A total of 48 cases of total stress analyses were performed, accounting for various combinations of slope geometry, seismic inputs, undrained shear strengths, bedrock types, and seawater depths. The major conclusions are summarized as follows:

1. **Model Validation with DEEPSOIL Confirms Applicability**:

   The 2-D SNKH model was validated against 1-D DEEPSOIL simulations. Although discrepancies are larger near the slope toe due to geometric asymmetry and wave reflections, the maximum strain deviation remains within 0.05%, confirming the model's reliability.

2. **Influence of Bedrock Type on Deformation**:

   Rigid half-space models consistently produce greater permanent displacements and shear strains than elastic models. This is due to the full reflection of seismic energy at the rigid base, which results in more intense cyclic loading and greater plastic deformation near the slope surface.

3. **Effect of Slope Angle on Seismic Response**:

   As slope angle increases, both displacement and shear strain increase significantly. This is due to enhanced stress concentration and shear modulus degradation at steeper angles.

4. **Earthquake Frequency Content Matters More Than PGA**:

   Despite its lower PGA, the Kocaeli earthquake induces larger displacements than the higher-PGA Kobe event in gentle slopes. This is attributed to its longer mean period (1.0681 s), which resonates more effectively with soft submarine slopes.

doi:10.6342/NTU202503752

In contrast, the San Fernando earthquake with a similar PGA but shorter period yields significantly smaller deformation.

5. **Seawater Depth Has Minor Effects**:

   While changes in seawater depth slightly alter free-surface interactions, the overall effects on displacement and shear strain are marginal. Slope geometry and bedrock stiffness are found to play more dominant roles in controlling seismic response.

6. **GMAR Behavior Reflects Complex Interactions**:

   Elastic half-space models exhibit higher GMAR values due to energy absorption and vertical wave transmission. Interestingly, 10° slopes often show the highest GMAR, while 20° slopes show reduced amplification, likely due to wave scattering, interference effects, or plastic deformation absorbing seismic energy.

7. **Temporal Framework of Failure Evolution**:

   Time history analysis of plastic shear strain at point A shows that failure initiation time t_1 is nearly identical across bedrock types, indicating that the onset of failure is controlled more by input motion than bedrock stiffness. However, failure stabilization time t_2 and development duration Δt are notably longer in rigid half-space models. This implies that reflected seismic energy prolongs the failure process and enhances cumulative damage.

In summary, bedrock stiffness, slope geometry, and earthquake frequency content are the most critical factors influencing the seismic behavior of submarine slopes. These findings highlight the importance of considering wave propagation characteristics and geometric nonlinearity in dynamic slope stability assessments. The introduction of

doi:10.6342/NTU202503752

temporal failure metrics such as t_1, t_2, and Δt also provides a valuable tool for identifying critical failure stages in seismic design and hazard mitigation.

5.2 Recommendations for Submarine Slope Studies

In reality, submarine slopes are far more complex than the scenarios examined in this study. This research only considers a two-dimensional, homogeneous clayey slope, whereas actual seabed topography, soil stratification, pore water pressure generation, and other factors play significant roles in determining slope stability. Martel (2003) investigated 3D submarine slope failures and analyzed the relationship between the length-to-width ratio of collapse zones and the orientation of weak planes, offering deeper insight into the terrain and vulnerable zones of real submarine slopes. Rodríguez-Ochoa et al. (2015) considered the increase of undrained shear strength of clays with depth and studied how shallow weak layers influence slope sliding, emphasizing shallow failure mechanisms.

Furthermore, when soil is fully saturated with seawater (100% saturation) under short-term loading, sandy submarine slopes may suffer liquefaction, making dynamic soil-fluid coupling and pore pressure analyses essential. However, since dynamic (implicit/explicit) analyses in ABAQUS currently do not support coupled soil-fluid coupling modeling, other numerical software must be employed to analyze this issue. Alternatively, as proposed by Tsai et al. (2014), the reduction of undrained shear strength due to cyclic loading in clays can be applied in a pseudo-static analysis to approximate the effects of seismic-induced hydro-mechanical interaction.

doi:10.6342/NTU202503752

In fact, pseudo-static slope analysis has already been widely applied in the academic community, as demonstrated in the studies by Karray et al. (2018), Baker et al. (2006), and Macedo et al. (2020). This study has successfully established and validated a method for modeling rigid and elastic half-space conditions and introduced Yang's (2024) SNKH model. We hoped that future research will further explore the aforementioned factors that were not considered in this study, in order to develop more accurate and effective methods for submarine slope analysis.

doi:10.6342/NTU202503752

REFERENCES

1. ABAQUS (2024) Analysis User's Manual (v6.6). Dassault Systems Simulia Inc.
2. Ashford, S. A., Sitar, N., Lysmer, J., & Deng, N. (1997). Topographic effects on the seismic response of steep slopes. *Bulletin of the seismological society of America*, *87*(3), 701-709.
3. Baker, R., Shukha, R., Operstein, V., & Frydman, S. (2006). Stability charts for pseudo-static slope stability analysis. *Soil Dynamics and Earthquake Engineering*, *26(9)*, 813-823.
4. Das, B. M., & Sobhan, K. (2011). Principles of Geotechnical Engineering.
5. Denlinger, R. P., & Iverson, R. M. (1990). Limiting equilibrium and liquefaction potential in infinite submarine slopes. *Marine Georesources & Geotechnology*, *9(4)*, 299-312.
6. Fellenius, W. K. A. (1927). *Erdstatische Berechnungen mit Reibung und Kohäsion (Adhäsion) und unter Annahme kreiszylindrischer Gleitflächen.* W. Ernst & Sohn.
7. FLAC (2024). FLAC3D 7.0 Documentation. Itasca Consulting Group Inc.
8. Joe, W., & Chern, C. S. (1992). in Taiwan Strait during summertime. *La mer*, *30*, 213-221.
9. Karray, M., Hussien, M. N., Delisle, M. C., & Ledoux, C. (2018). Framework to assess pseudo-static approach for seismic stability of clayey slopes. *Canadian Geotechnical Journal*, *55(12)*, 1860-1876.
10. Lysmer, J., & Kuhlemeyer, R. L. (1969). Finite dynamic model for infinite media. *Journal of the engineering mechanics division*, *95(4)*, 859-877.
11. Ma, J. (2015). Numerical modelling of submarine landslides and their impact to underwater infrastructure using the material point method.

doi:10.6342/NTU202503752

12. Macedo, J., & Candia, G. (2020). Performance-based assessment of the seismic pseudo-static coefficient used in slope stability analysis. *Soil Dynamics and Earthquake Engineering*, *133*, 106109.
13. Ngo, V. L., Lee, C., Lee, E. H., & Kim, J. M. (2021). Semi-Automated Procedure to Estimate Nonlinear Kinematic Hardening Model to Simulate the Nonlinear Dynamic Properties of Soil and Rock. *Applied Sciences, 11(18)*, 8611.
14. Nian, T. K., Guo, X. S., Zheng, D. F., Xiu, Z. X., & Jiang, Z. B. (2019). Susceptibility assessment of regional submarine landslides triggered by seismic actions. *Applied Ocean Research*, *93*, 101964.
15. Rodríguez-Ochoa, R., Nadim, F., & Hicks, M. A. (2015). Influence of weak layers on seismic stability of submarine slopes. *Marine and Petroleum Geology*, *65*, 247-268.
16. Safety, I. S. (2004). NEHRP recommended provisions for seismic regulations for new buildings and other structures (FEMA 450). *Building Seismic Safety Council, National Institute of Building Sciences: Washington, DC, USA.*
17. Steward, T., Sivakugan, N., Shukla, S. K., & Das, B. M. (2011). Taylor's slope stability charts revisited. *International Journal of Geomechanics*, 11(4), 348-352.
18. Taylor, D. W. (1937). Stability of earth slopes. *Journal of the Boston Society of Civil Engineers*, *24(3)*, 197-247.
19. Tsai, C.-C., Mejia, L. H., and Meymand, P. (2014). A strain-based procedure to estimate strength softening in saturated clays during earthquakes. *Soil Dynamics and Earthquake Engineering*, *66*, 191–198.
20. Vucetic, M., & Dobry, R. (1991). Effect of soil plasticity on cyclic response. *Journal of geotechnical engineering*, *117(1)*, 89-107.
21. 台灣電力公司 (2018)。離岸風力發電第二期計畫可行性研究。

doi:10.6342/NTU202503752

22. 楊承華 (2024)。海床拖錨承載力之數值研究。國立臺灣大學土木工程學系學位論文，1-131。

doi:10.6342/NTU202503752

Appendix A: X-direction displacement and shear strain histories at DW = 50 m

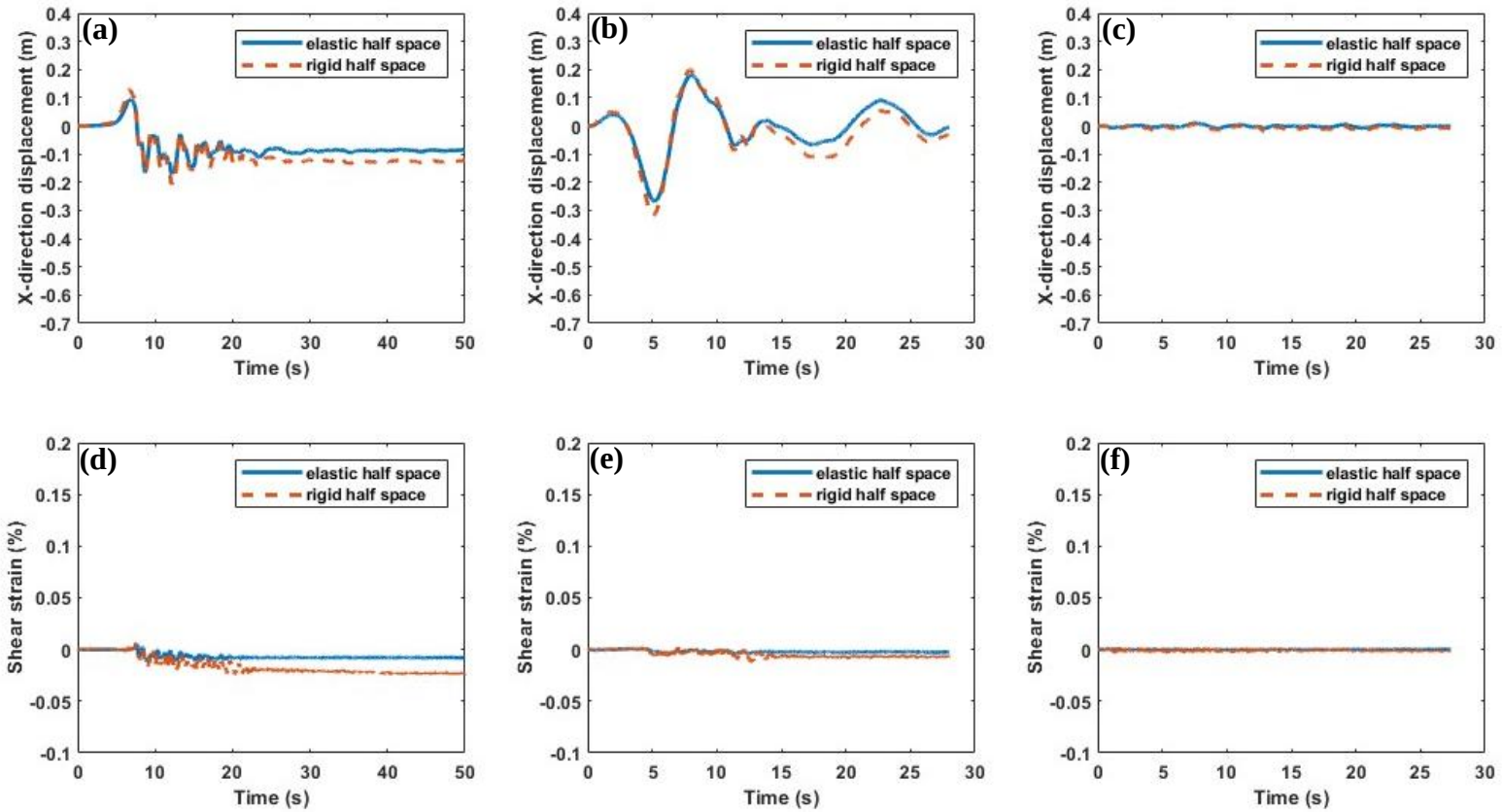

Figure A. 1 Point A x-direction displacement history of (a) Kobe; (b) Kocaeli; (c) San Fernando earthquake and shear strain history of (d) Kobe; (e) Kocaeli; (f) San Fernando earthquake in 5-degree submarine slope with s_u =40 kPa, DW = 50 m.

doi:10.6342/NTU202503752

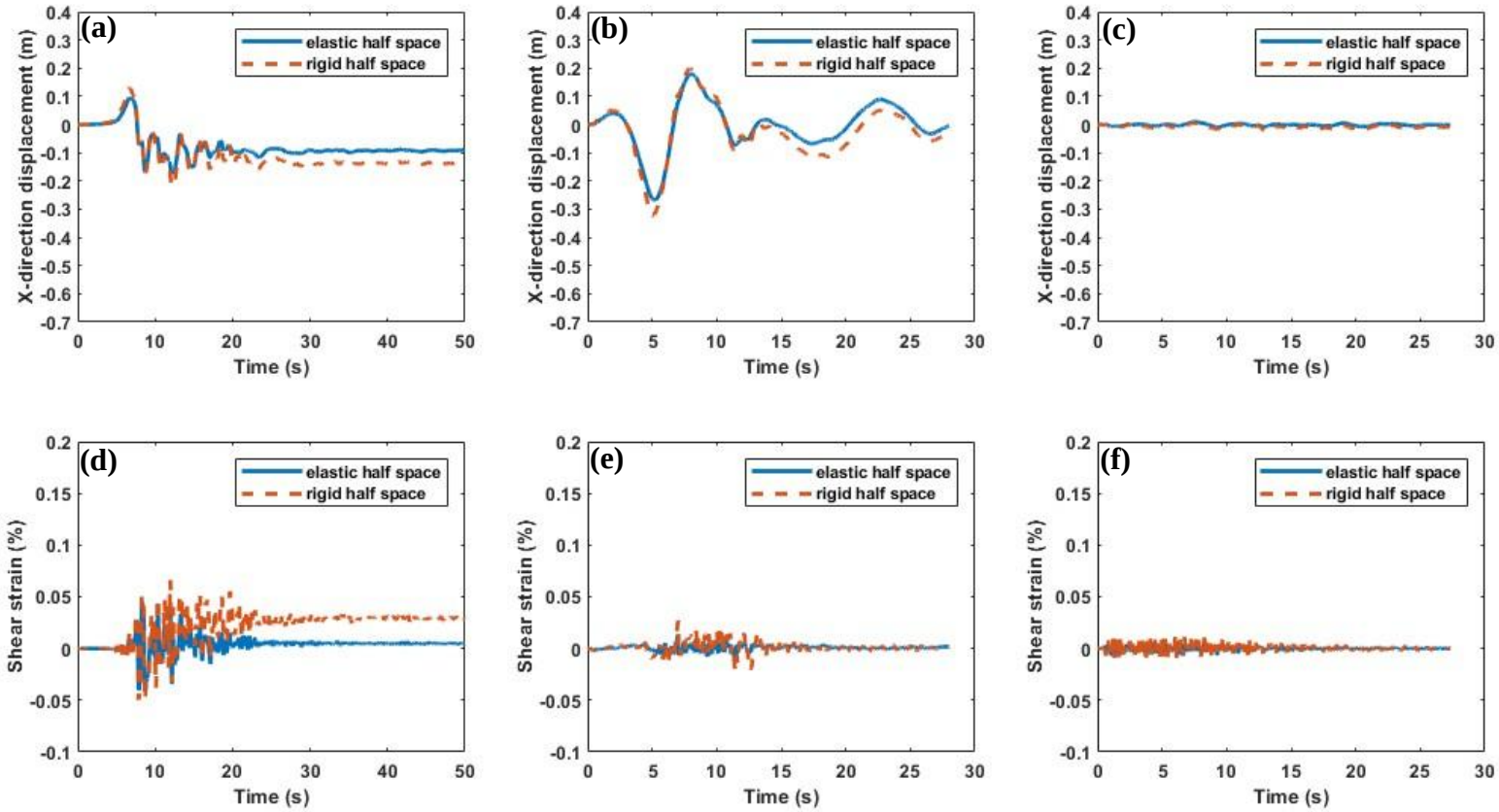

Figure A. 2 Point C x-direction displacement history of (a) Kobe; (b) Kocaeli; (c) San Fernando earthquake and shear strain history of (d) Kobe; (e) Kocaeli; (f) San Fernando earthquake in 5-degree submarine slope with s_u =40 kPa, DW = 50 m.

doi:10.6342/NTU202503752

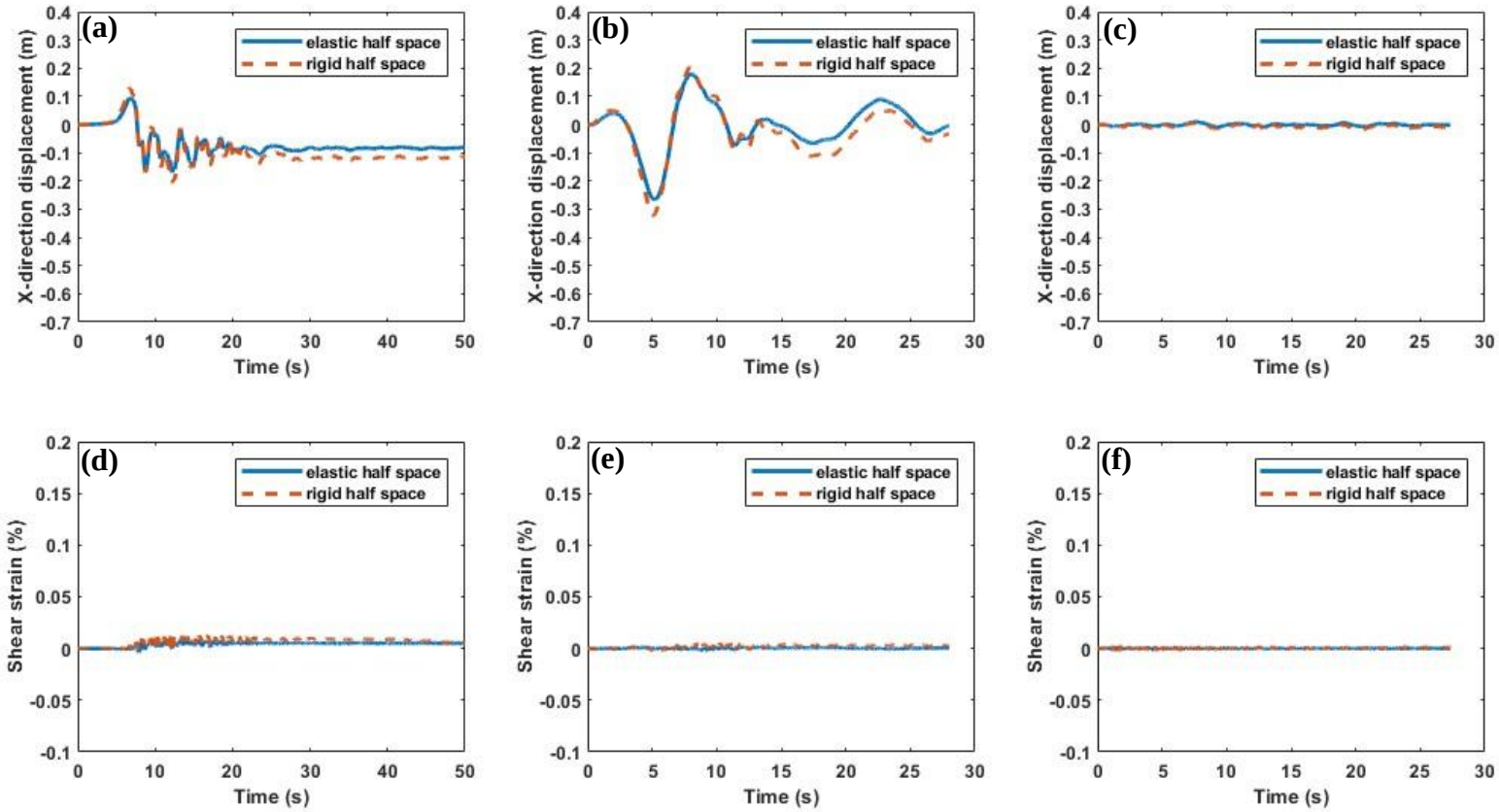

Figure A. 3 Point D x-direction displacement history of (a) Kobe; (b) Kocaeli; (c) San Fernando earthquake and shear strain history of (d) Kobe; (e) Kocaeli; (f) San Fernando earthquake in 5-degree submarine slope with s_u =40 kPa, DW = 50 m.

doi:10.6342/NTU202503752

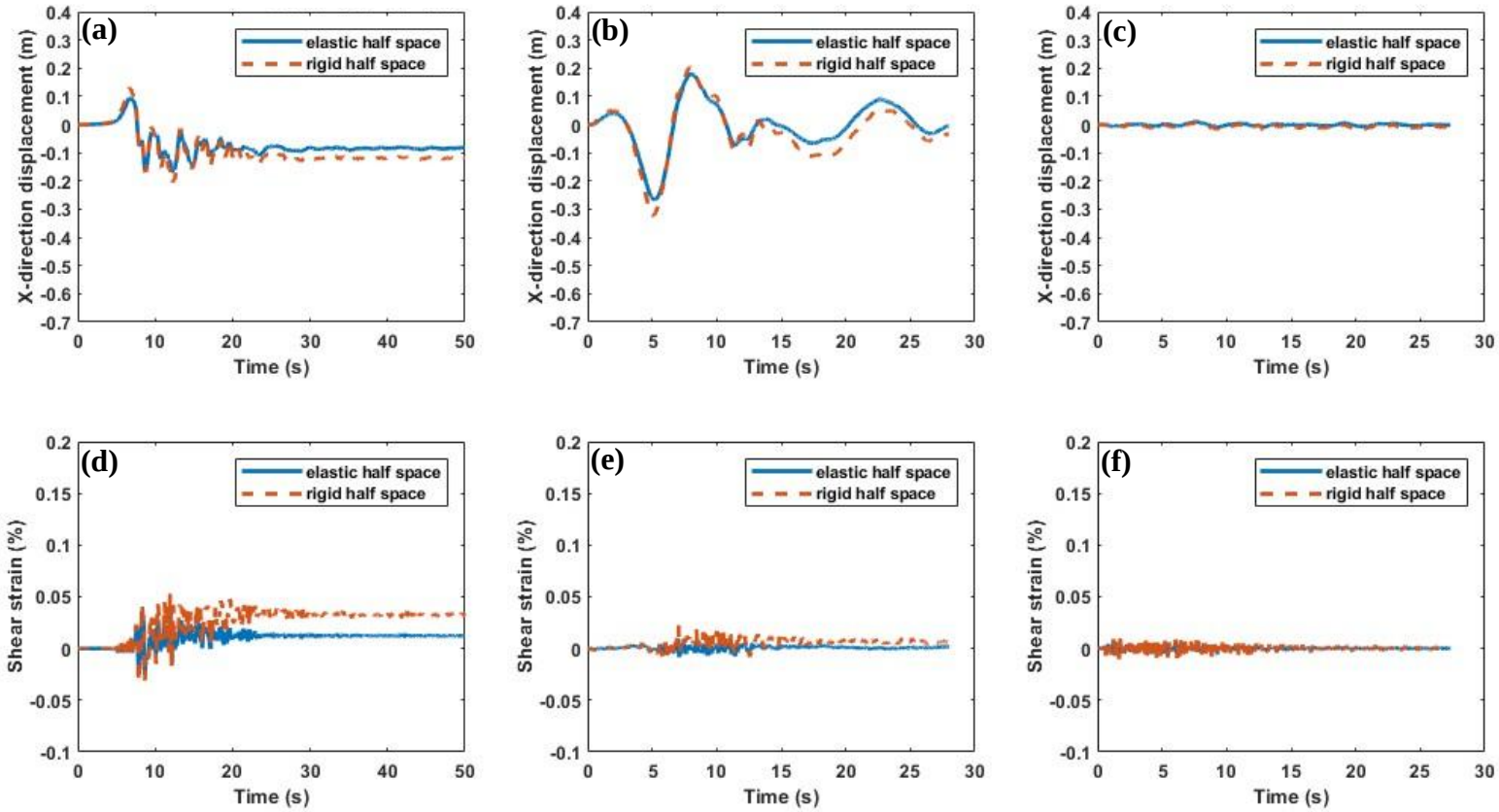

Figure A. 4 Point E x-direction displacement history of (a) Kobe; (b) Kocaeli; (c) San Fernando earthquake and shear strain history of (d) Kobe; (e) Kocaeli; (f) San Fernando earthquake in 5-degree submarine slope with s_u =40 kPa, DW = 50 m.

doi:10.6342/NTU202503752

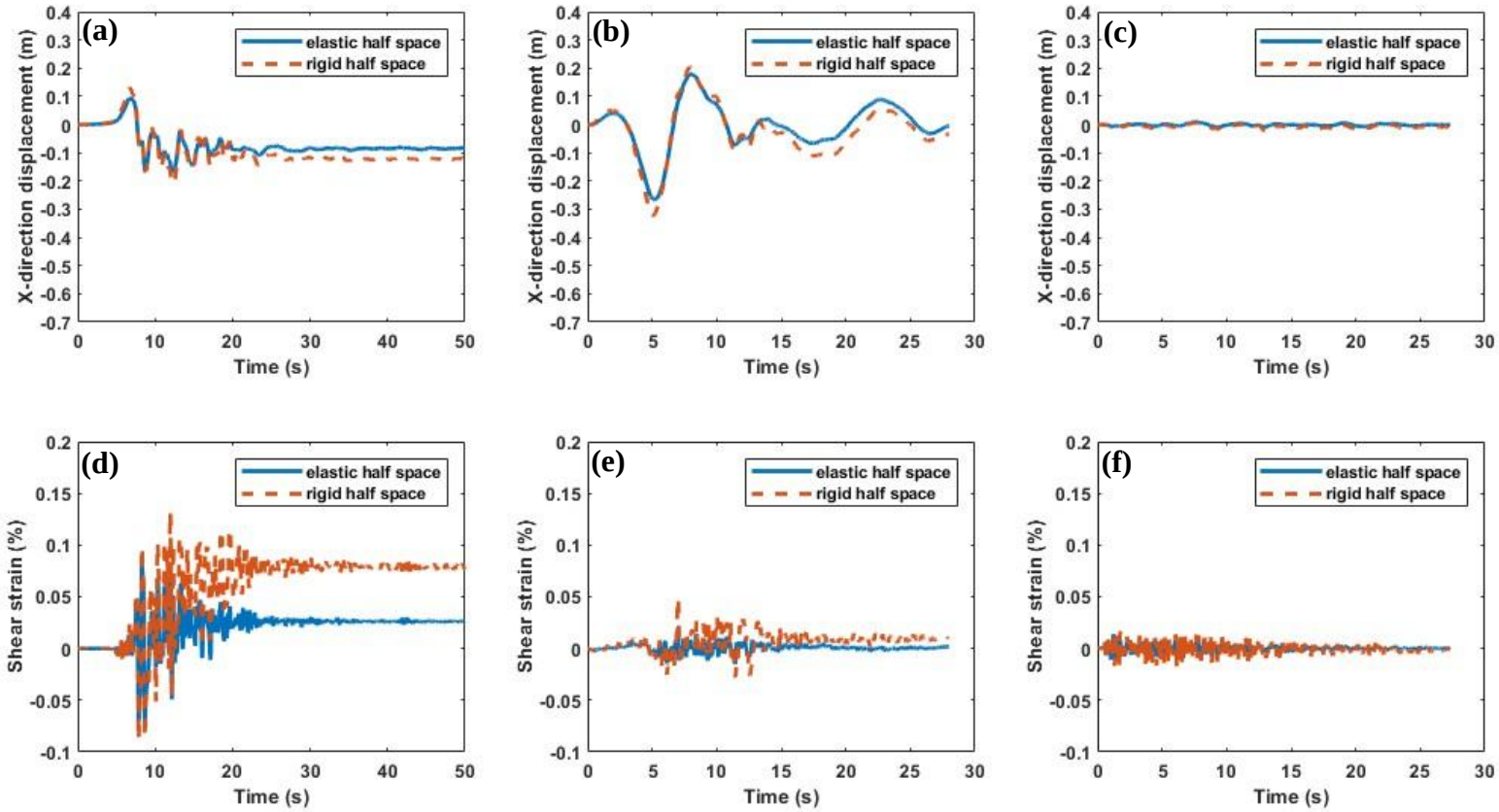

Figure A. 5 Point F x-direction displacement history of (a) Kobe; (b) Kocaeli; (c) San Fernando earthquake and shear strain history of (d) Kobe; (e) Kocaeli; (f) San Fernando earthquake in 5-degree submarine slope with s_u =40 kPa, DW = 50 m.

doi:10.6342/NTU202503752

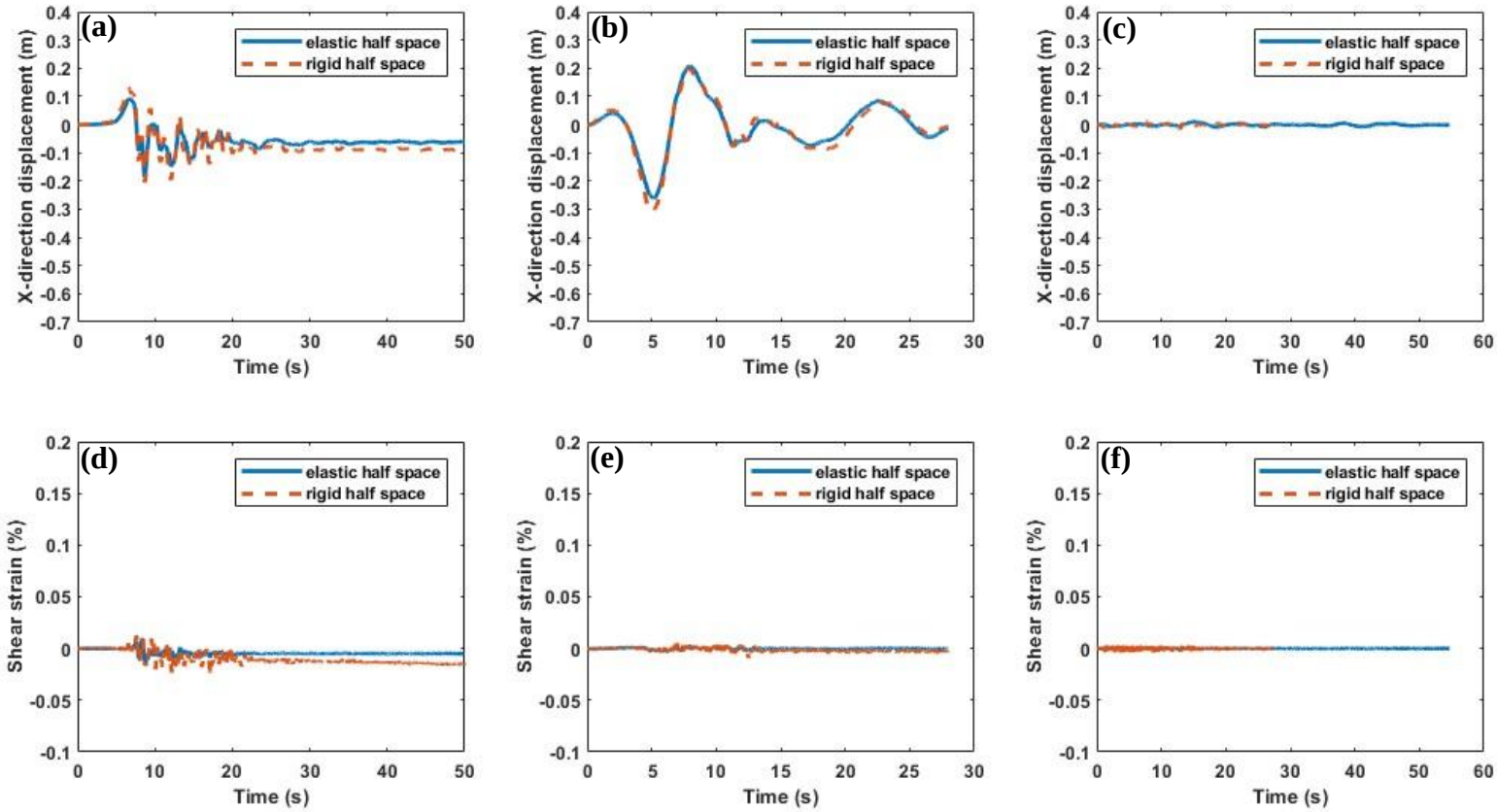

Figure A. 6 Point A x-direction displacement history of (a) Kobe; (b) Kocaeli; (c) San Fernando earthquake and shear strain history of (d) Kobe; (e) Kocaeli; (f) San Fernando earthquake in 5-degree submarine slope with s_u =100 kPa, DW = 50 m.

doi:10.6342/NTU202503752

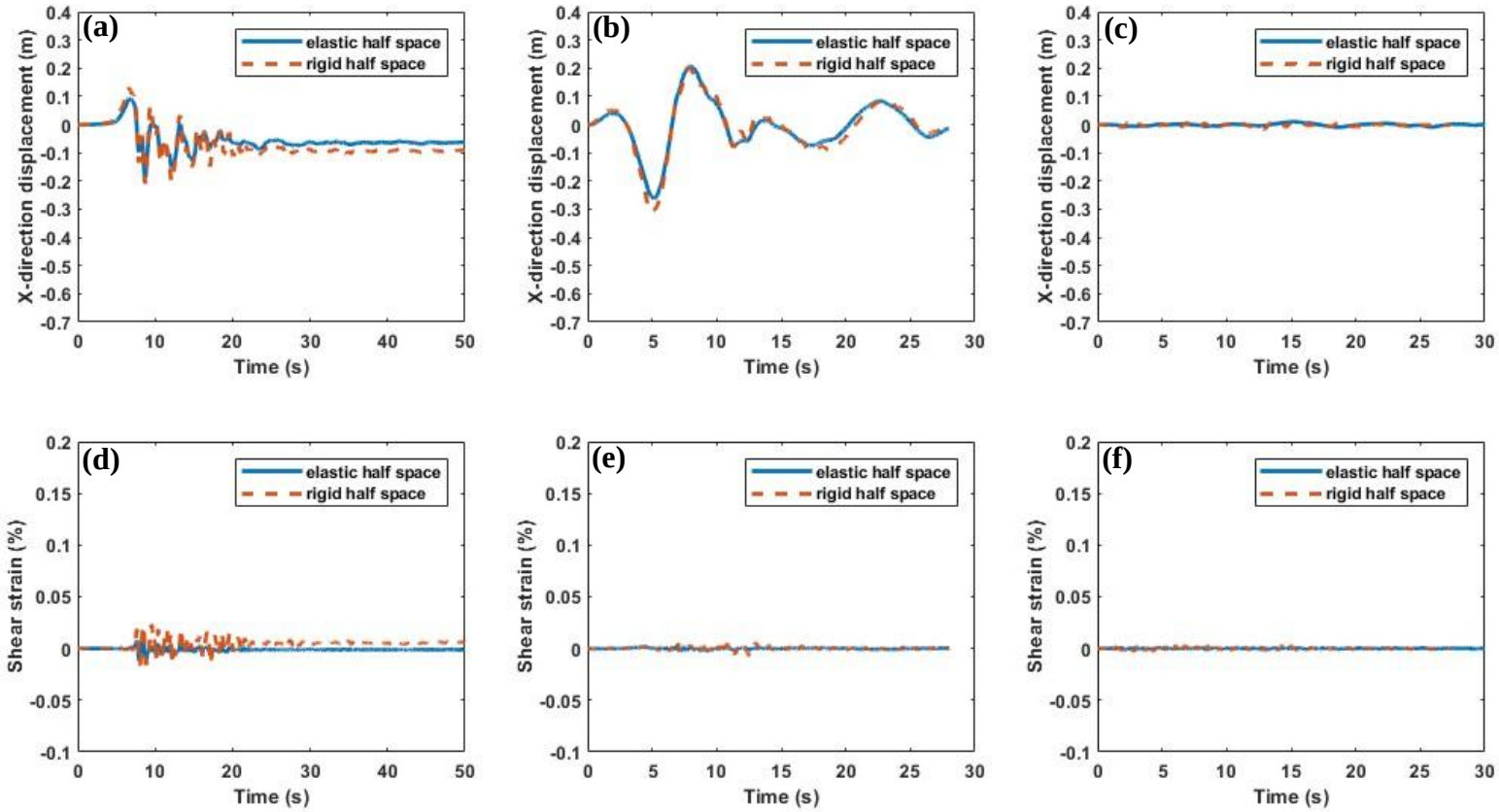

Figure A. 7 Point B x-direction displacement history of (a) Kobe; (b) Kocaeli; (c) San Fernando earthquake and shear strain history of (d) Kobe; (e) Kocaeli; (f) San Fernando earthquake in 5-degree submarine slope with s_u =100 kPa, DW = 50 m.

doi:10.6342/NTU202503752

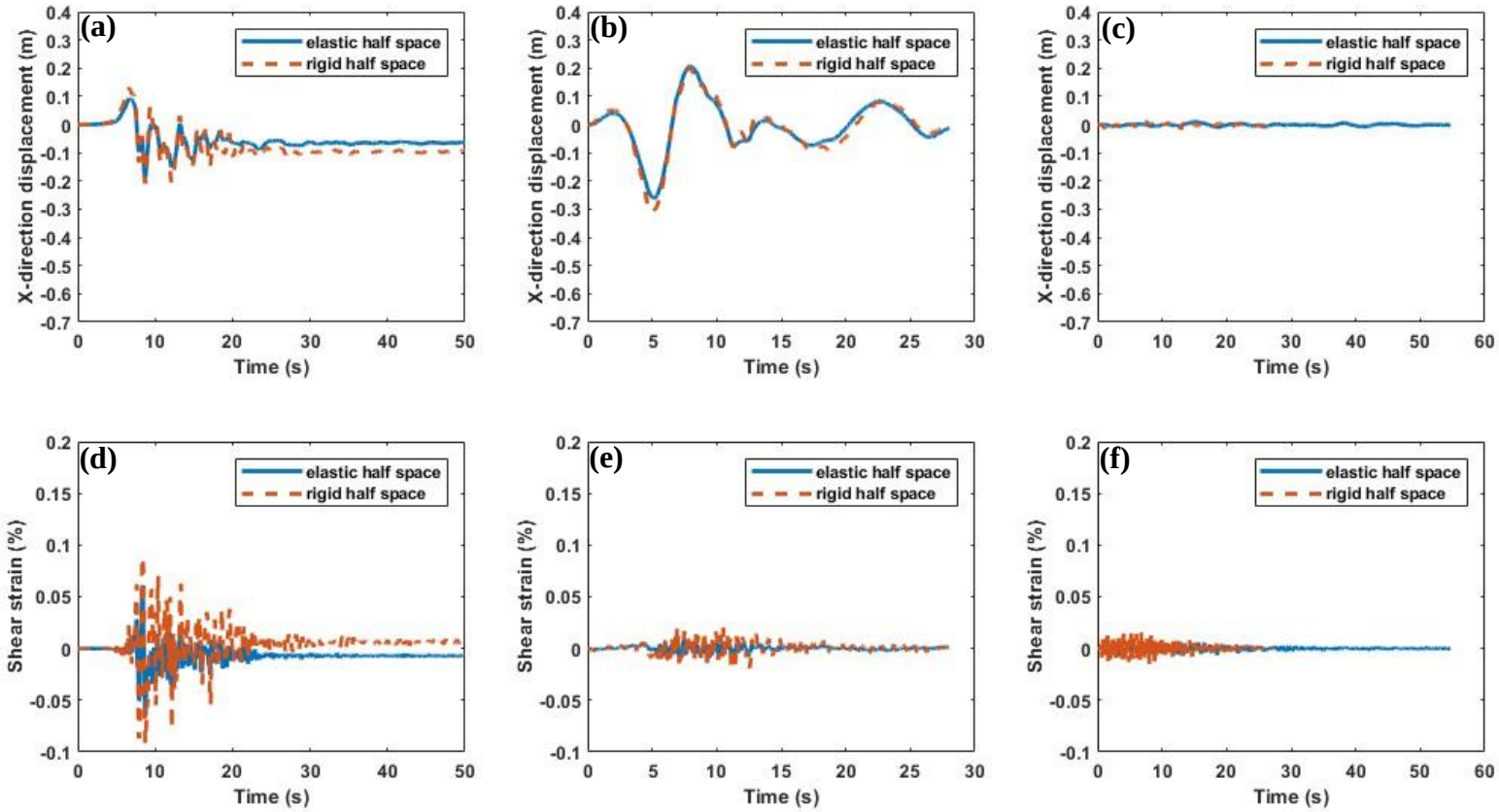

Figure A. 8 Point C x-direction displacement history of (a) Kobe; (b) Kocaeli; (c) San Fernando earthquake and shear strain history of (d) Kobe; (e) Kocaeli; (f) San Fernando earthquake in 5-degree submarine slope with s_u =100 kPa, DW = 50 m.

doi:10.6342/NTU202503752

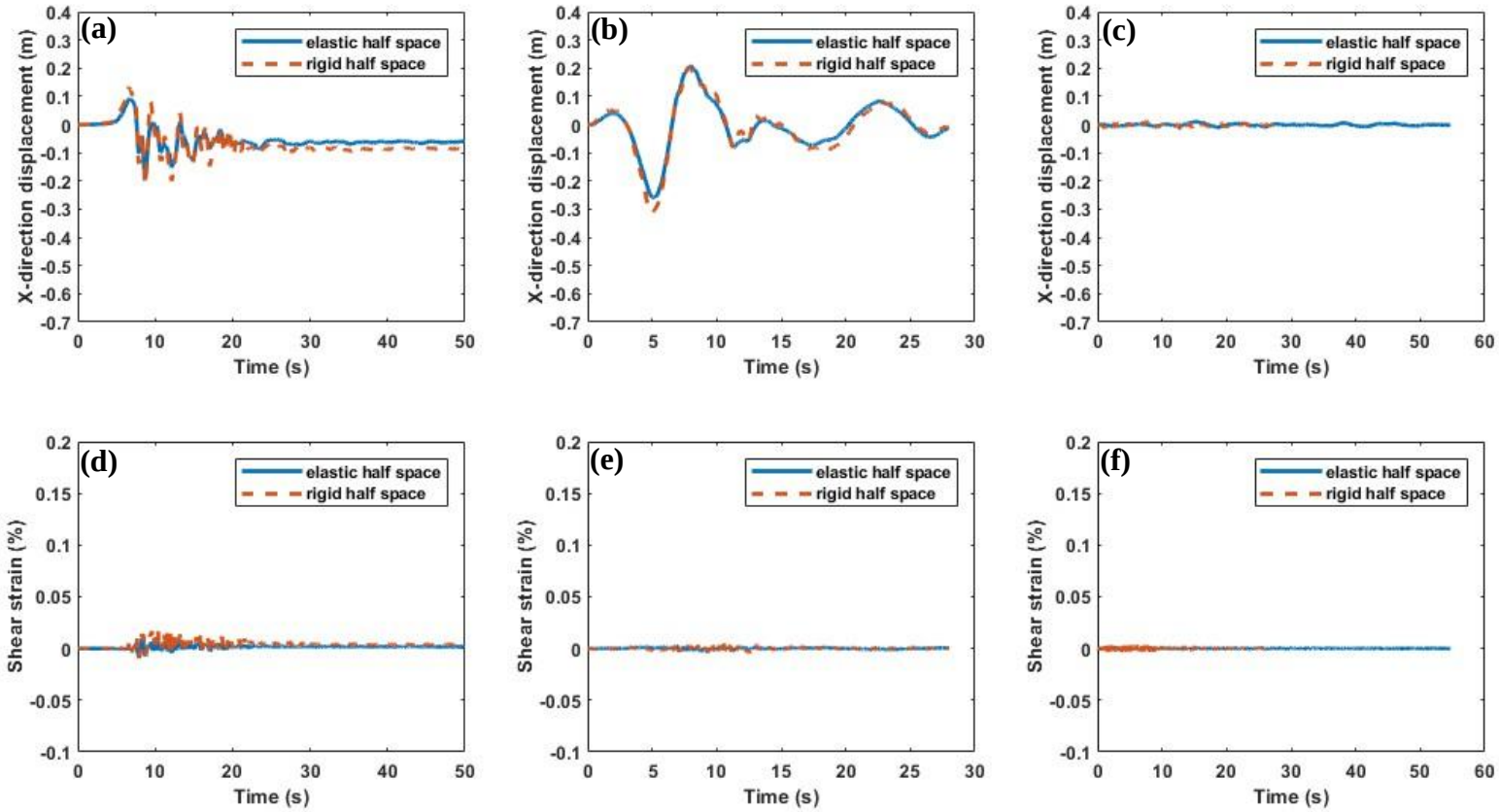

Figure A. 9 Point D x-direction displacement history of (a) Kobe; (b) Kocaeli; (c) San Fernando earthquake and shear strain history of (d) Kobe; (e) Kocaeli; (f) San Fernando earthquake in 5-degree submarine slope with s_u =100 kPa, DW = 50 m.

doi:10.6342/NTU202503752

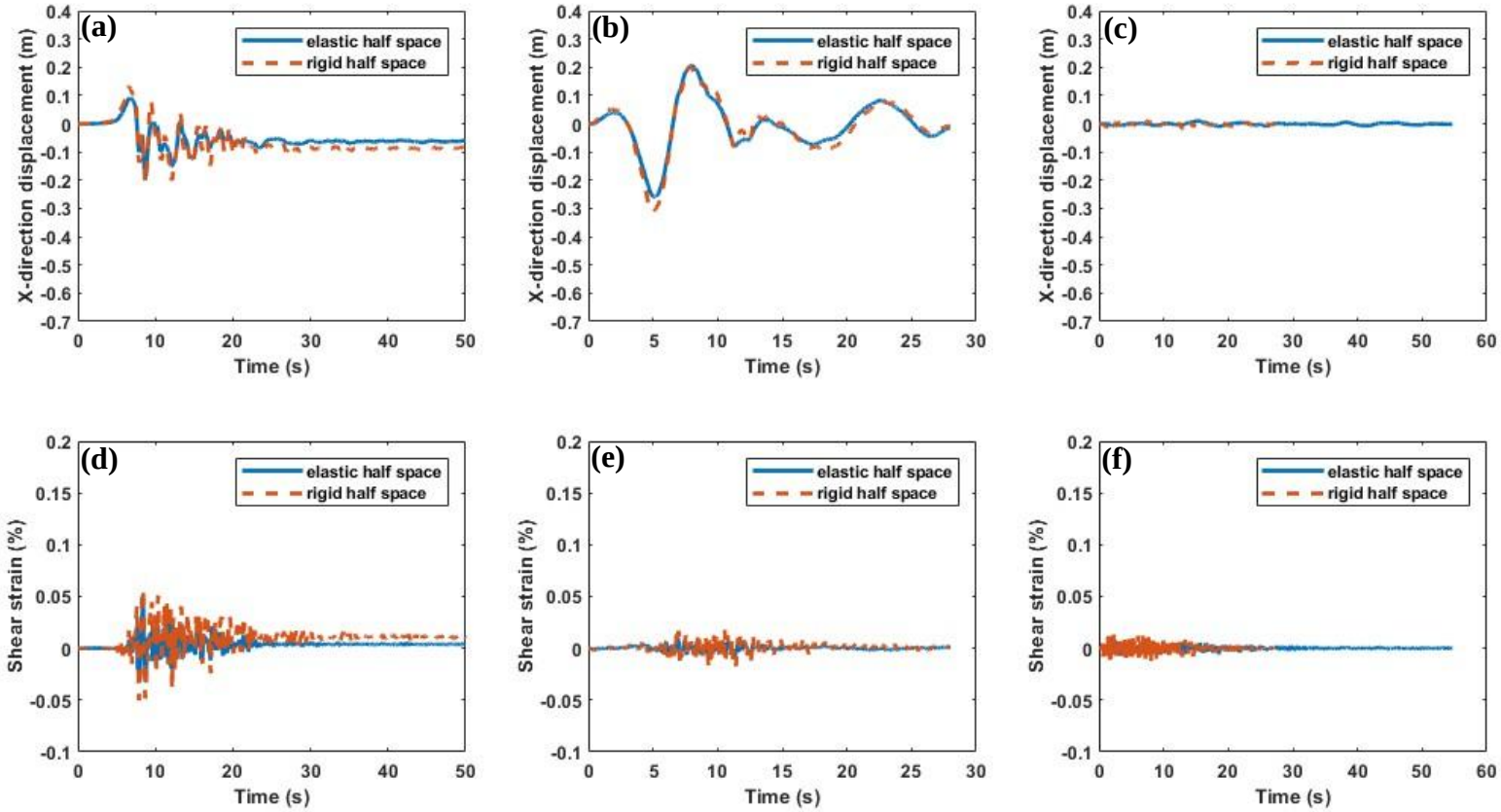

Figure A. 10 Point E x-direction displacement history of (a) Kobe; (b) Kocaeli; (c) San Fernando earthquake and shear strain history of (d) Kobe; (e) Kocaeli; (f) San Fernando earthquake in 5-degree submarine slope with s_u =100 kPa, DW = 50 m.

doi:10.6342/NTU202503752

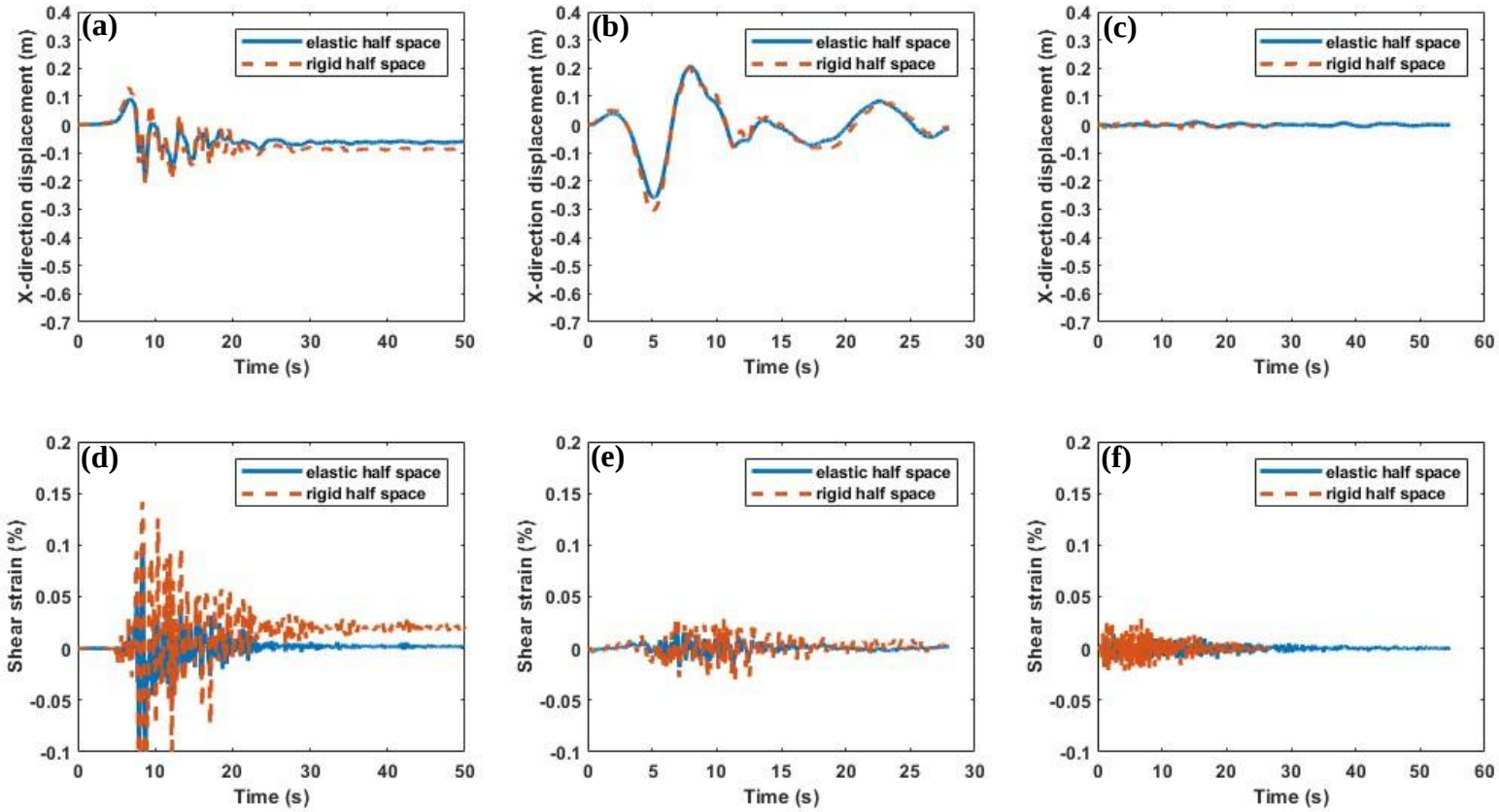

Figure A. 11 Point F x-direction displacement history of (a) Kobe; (b) Kocaeli; (c) San Fernando earthquake and shear strain history of (d) Kobe; (e) Kocaeli; (f) San Fernando earthquake in 5-degree submarine slope with s_u =100 kPa, DW = 50 m.

doi:10.6342/NTU202503752

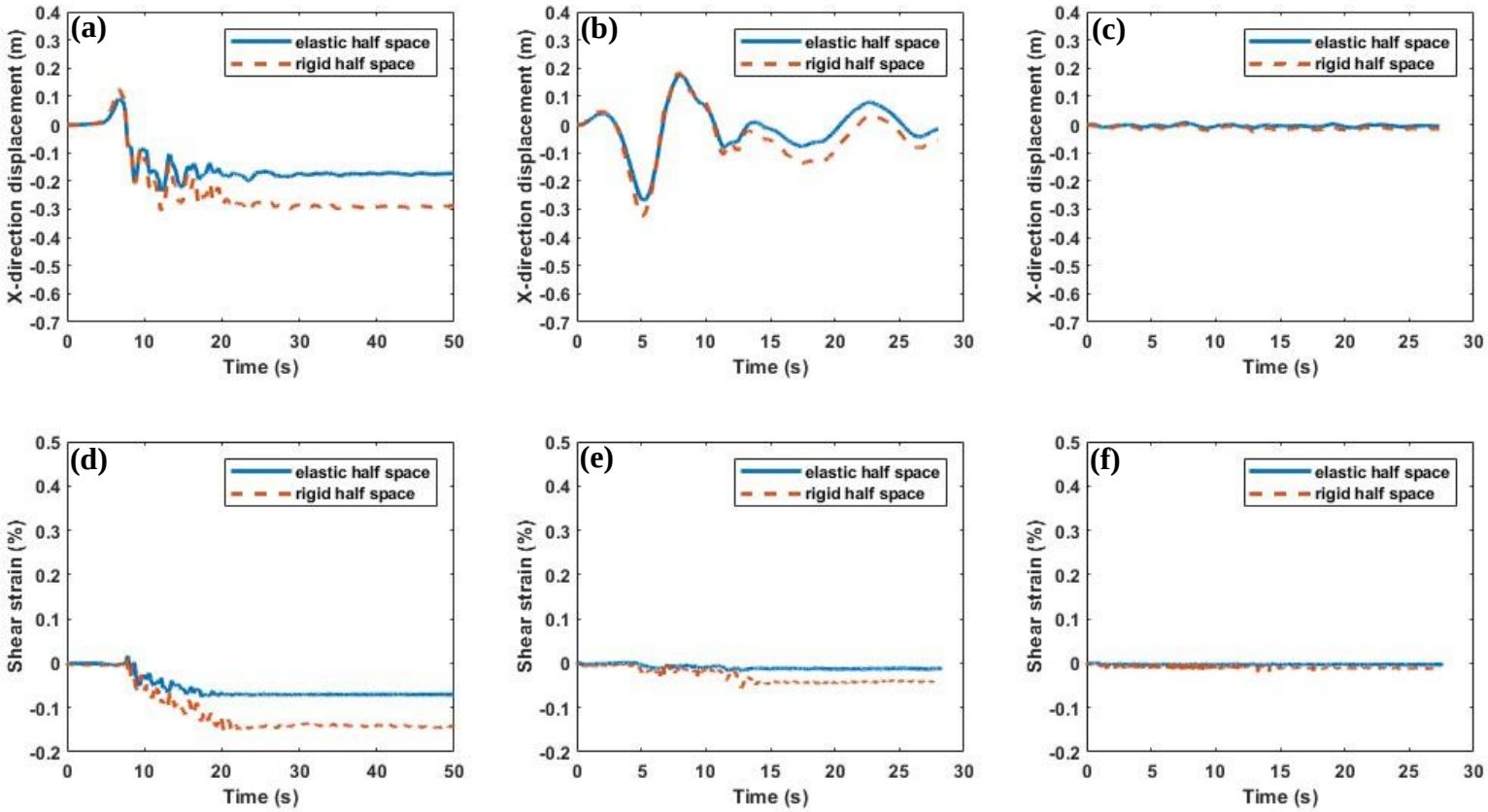

Figure A. 12 Point A x-direction displacement history of (a) Kobe; (b) Kocaeli; (c) San Fernando earthquake and shear strain history of (d) Kobe; (e) Kocaeli; (f) San Fernando earthquake in 10-degree submarine slope with s_u =40 kPa, DW = 50 m.

doi:10.6342/NTU202503752

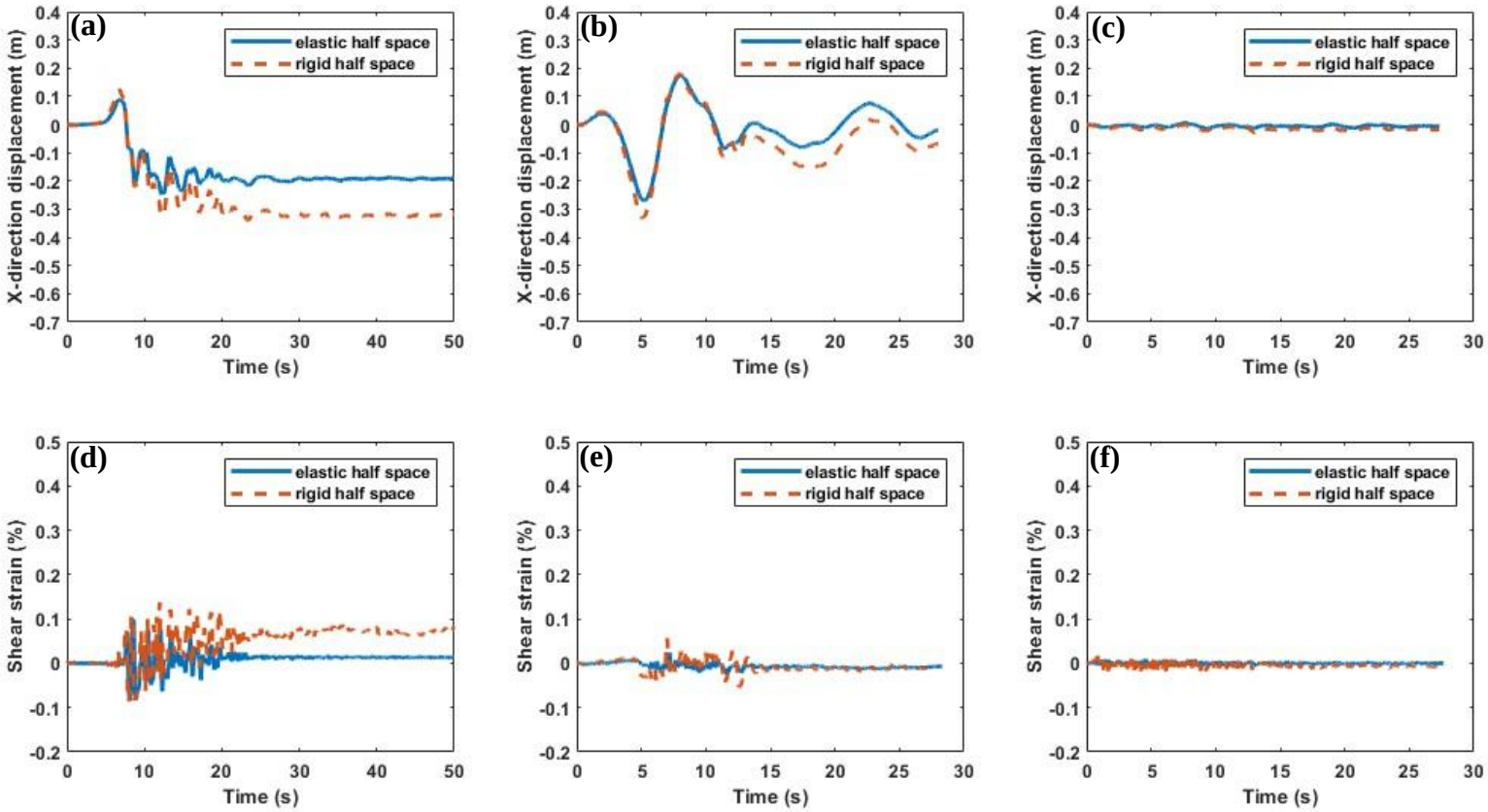

Figure A. 13 Point C x-direction displacement history of (a) Kobe; (b) Kocaeli; (c) San Fernando earthquake and shear strain history of (d) Kobe; (e) Kocaeli; (f) San Fernando earthquake in 10-degree submarine slope with s_u =40 kPa, DW = 50 m.

doi:10.6342/NTU202503752

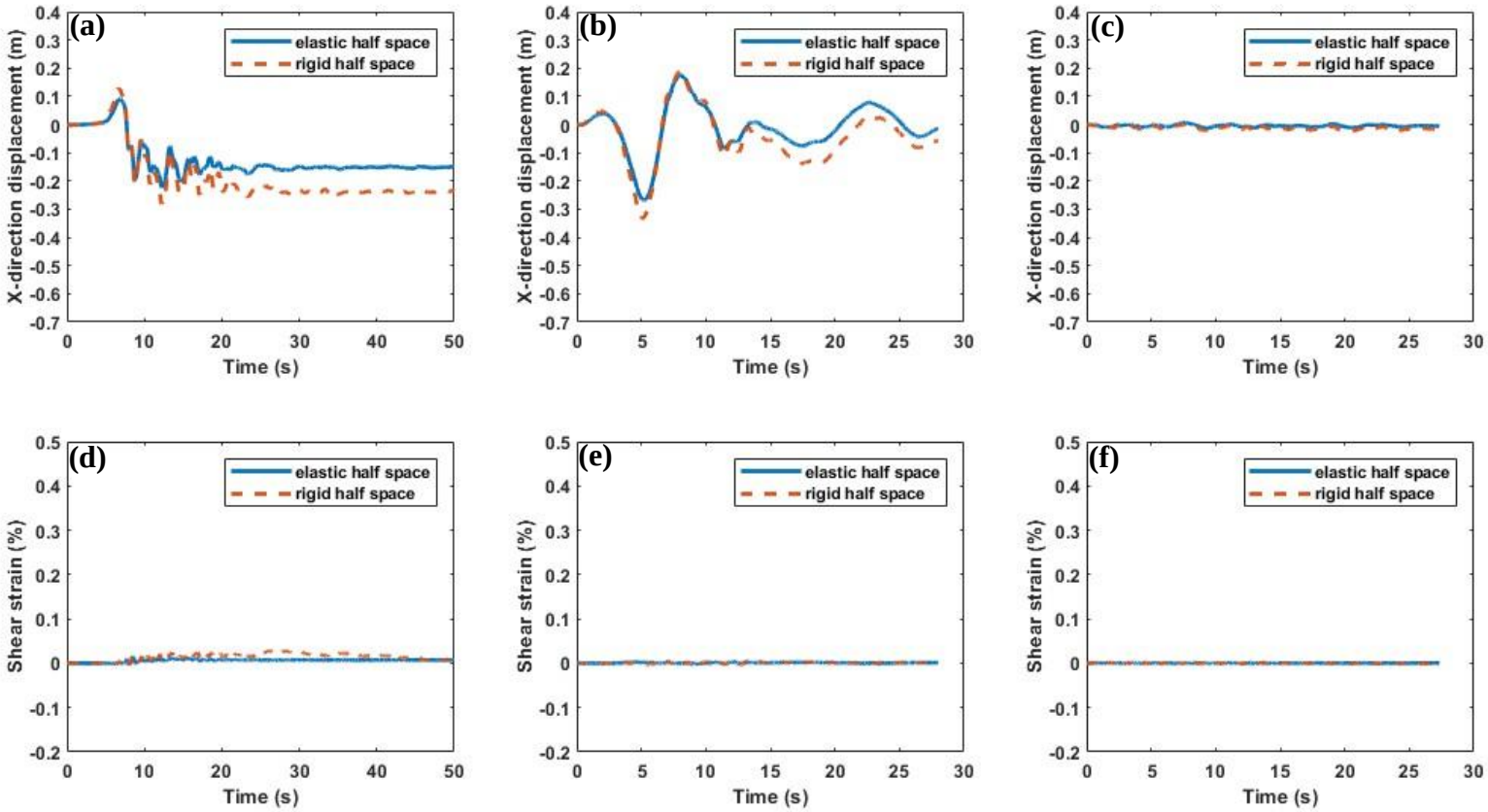

Figure A. 14 Point D x-direction displacement history of (a) Kobe; (b) Kocaeli; (c) San Fernando earthquake and shear strain history of (d) Kobe; (e) Kocaeli; (f) San Fernando earthquake in 10-degree submarine slope with s_u =40 kPa, DW = 50 m.

doi:10.6342/NTU202503752

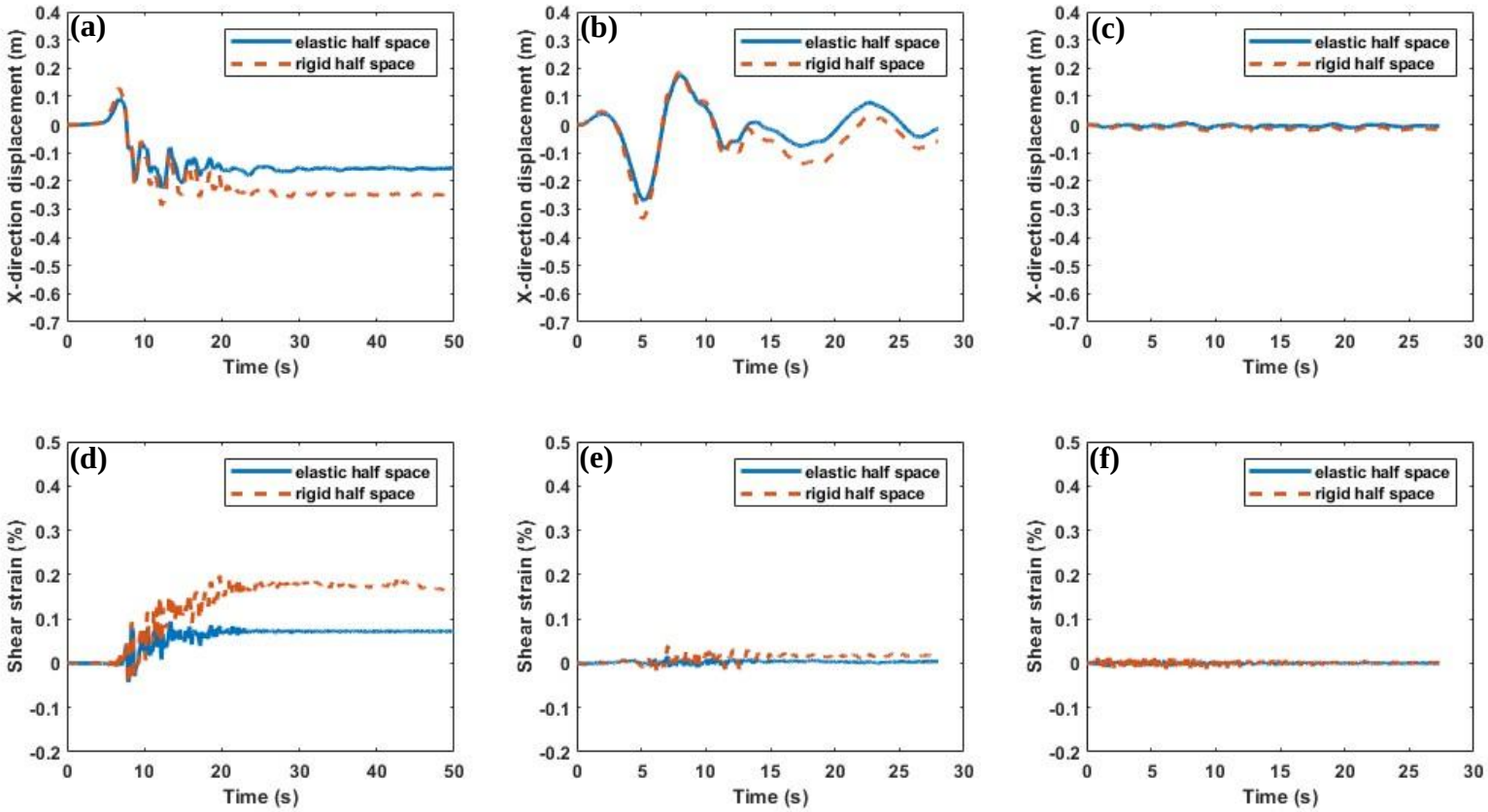

Figure A. 15 Point E x-direction displacement history of (a) Kobe; (b) Kocaeli; (c) San Fernando earthquake and shear strain history of (d) Kobe; (e) Kocaeli; (f) San Fernando earthquake in 10-degree submarine slope with s_u =40 kPa, DW = 50 m.

doi:10.6342/NTU202503752

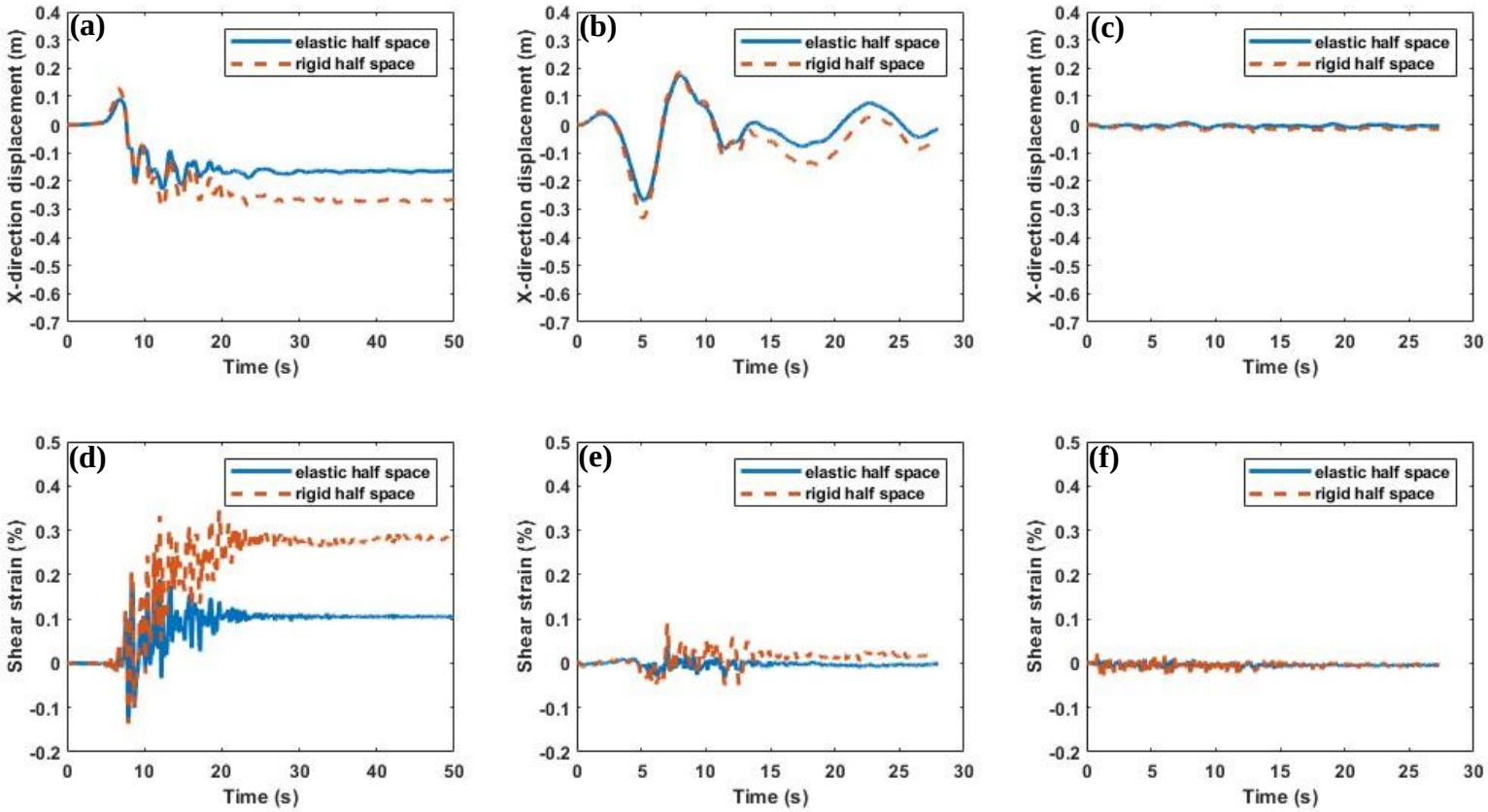

Figure A. 16 Point F x-direction displacement history of (a) Kobe; (b) Kocaeli; (c) San Fernando earthquake and shear strain history of (d) Kobe; (e) Kocaeli; (f) San Fernando earthquake in 10-degree submarine slope with s_u =40 kPa, DW = 50 m.

doi:10.6342/NTU202503752

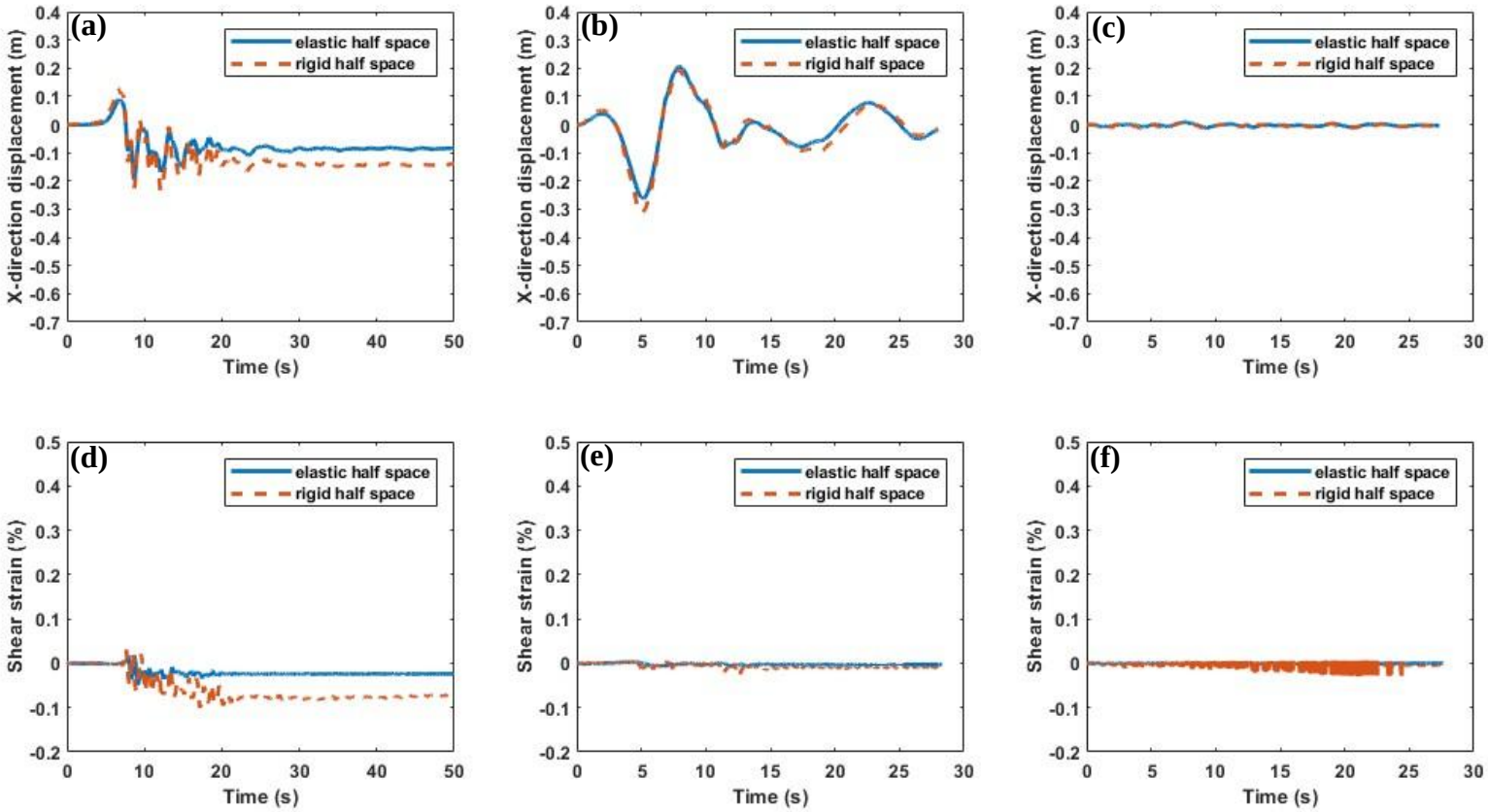

Figure A. 17 Point A x-direction displacement history of (a) Kobe; (b) Kocaeli; (c) San Fernando earthquake and shear strain history of (d) Kobe; (e) Kocaeli; (f) San Fernando earthquake in 10-degree submarine slope with s_u =100 kPa, DW = 50 m.

doi:10.6342/NTU202503752

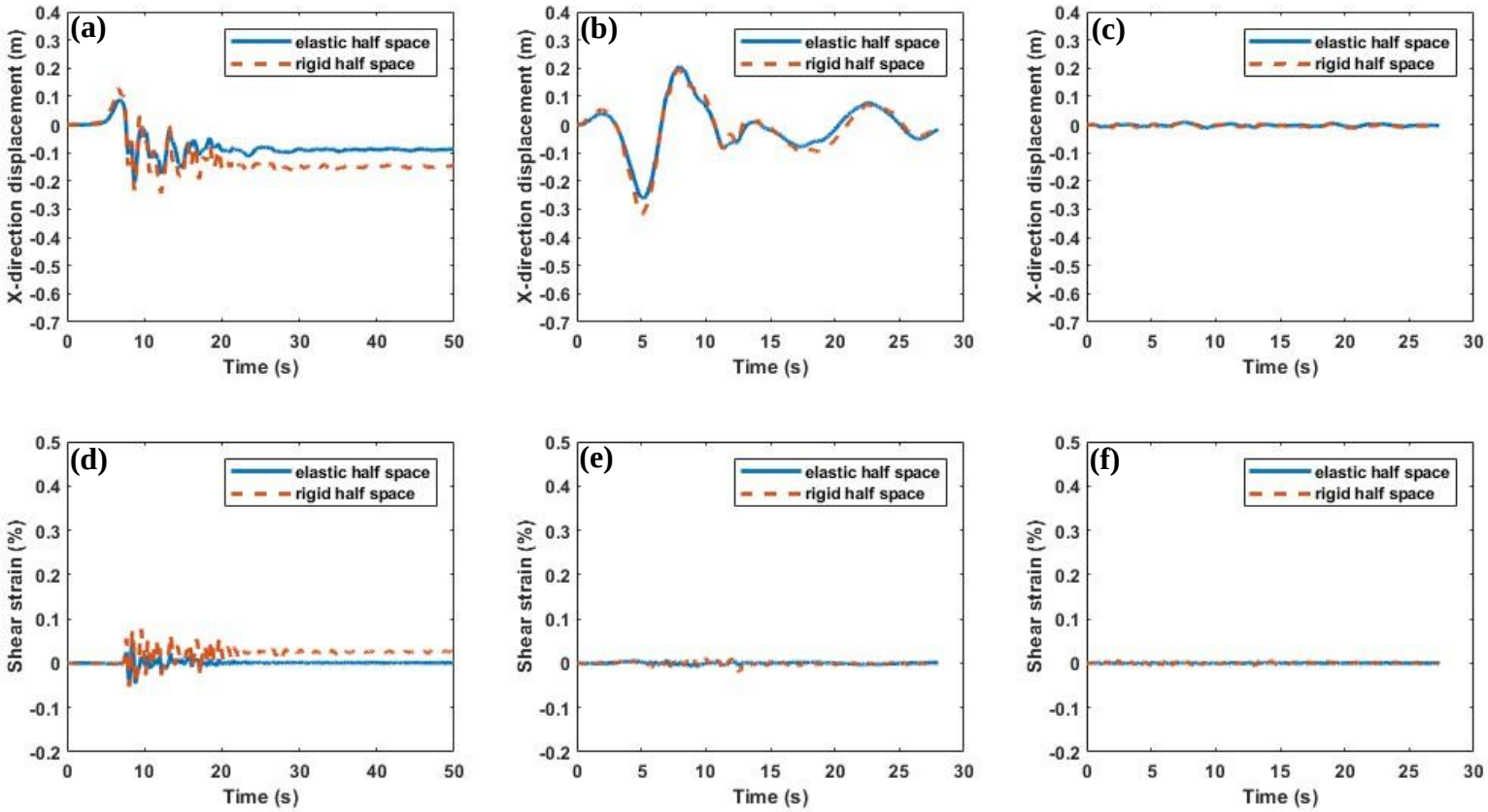

Figure A. 18 Point B x-direction displacement history of (a) Kobe; (b) Kocaeli; (c) San Fernando earthquake and shear strain history of (d) Kobe; (e) Kocaeli; (f) San Fernando earthquake in 10-degree submarine slope with s_u =100 kPa, DW = 50 m.

doi:10.6342/NTU202503752

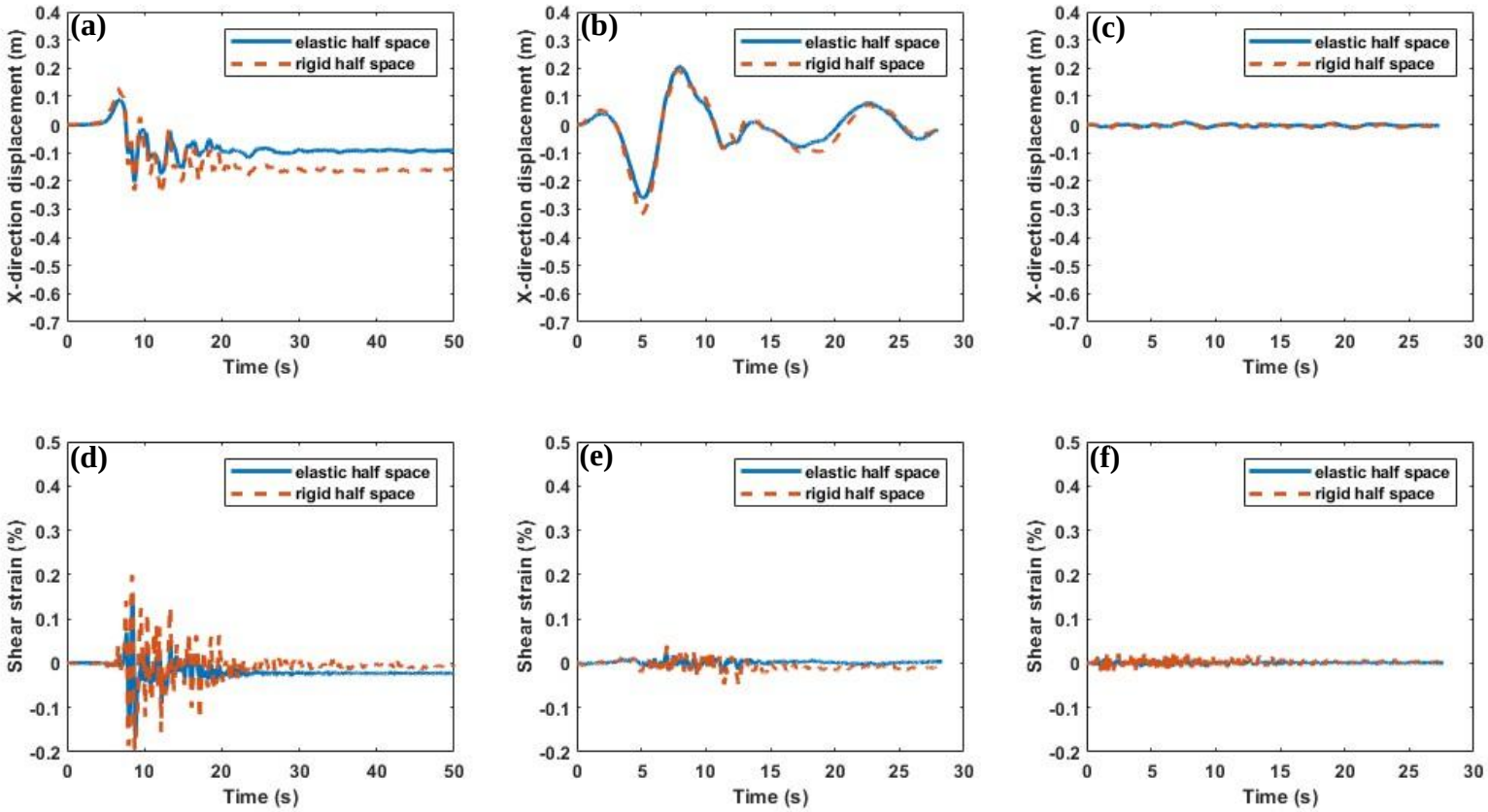

Figure A. 19 Point C x-direction displacement history of (a) Kobe; (b) Kocaeli; (c) San Fernando earthquake and shear strain history of (d) Kobe; (e) Kocaeli; (f) San Fernando earthquake in 10-degree submarine slope with s_u =100 kPa, DW = 50 m.

doi:10.6342/NTU202503752

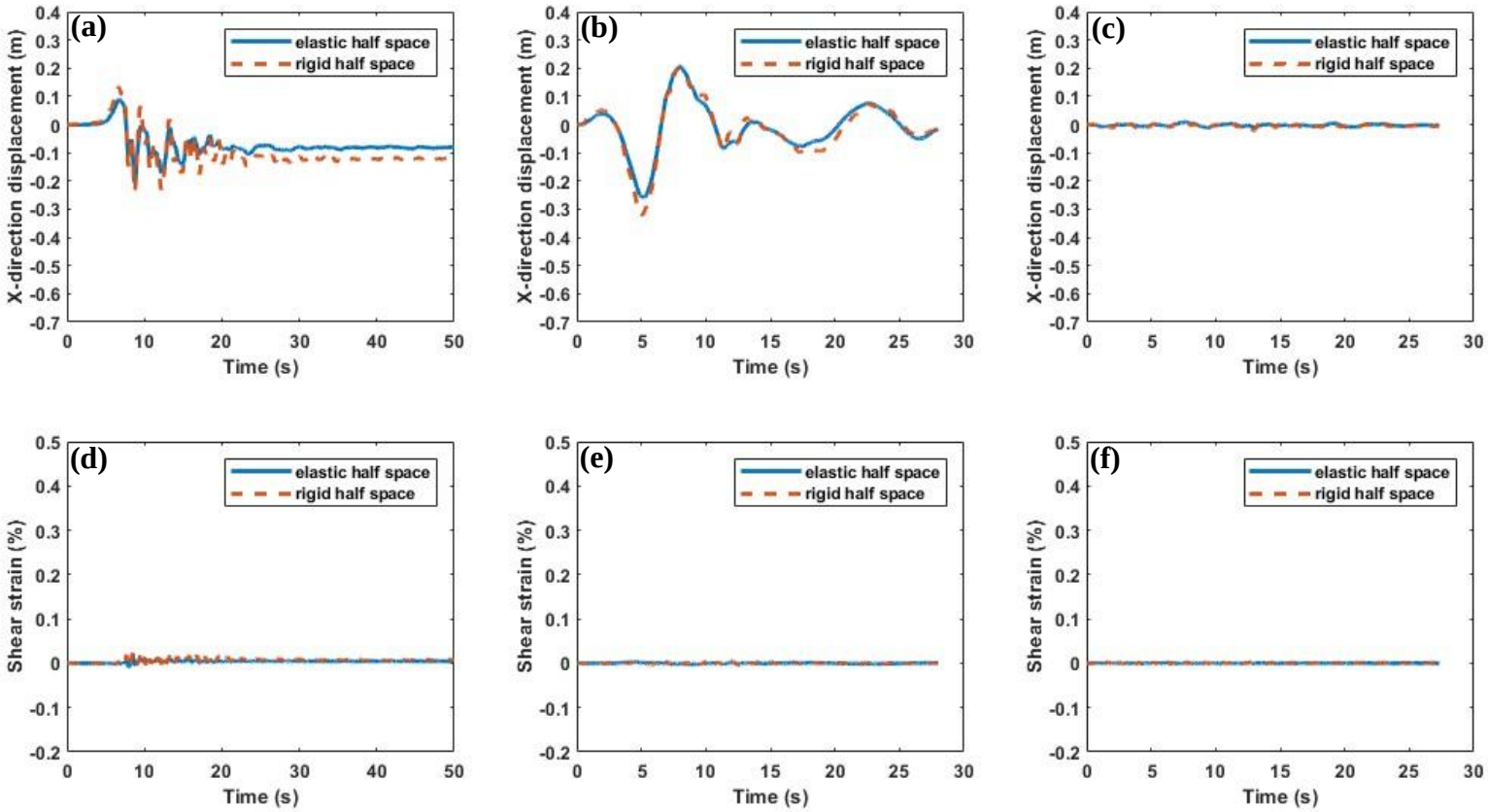

Figure A. 20 Point D x-direction displacement history of (a) Kobe; (b) Kocaeli; (c) San Fernando earthquake and shear strain history of (d) Kobe; (e) Kocaeli; (f) San Fernando earthquake in 10-degree submarine slope with s_u =100 kPa, DW = 50 m.

doi:10.6342/NTU202503752

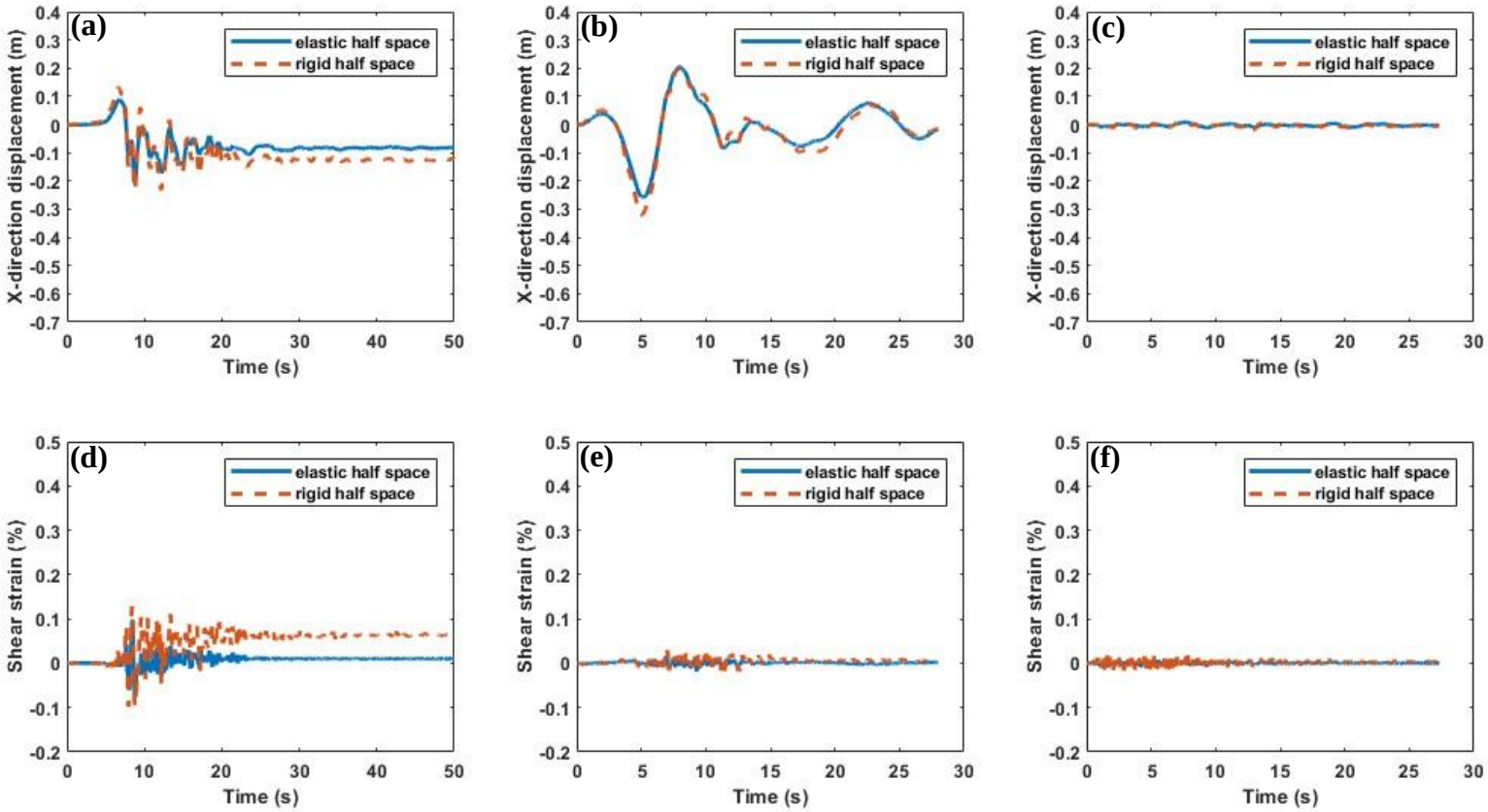

Figure A. 21 Point E x-direction displacement history of (a) Kobe; (b) Kocaeli; (c) San Fernando earthquake and shear strain history of (d) Kobe; (e) Kocaeli; (f) San Fernando earthquake in 10-degree submarine slope with s_u =100 kPa, DW = 50 m.

doi:10.6342/NTU202503752

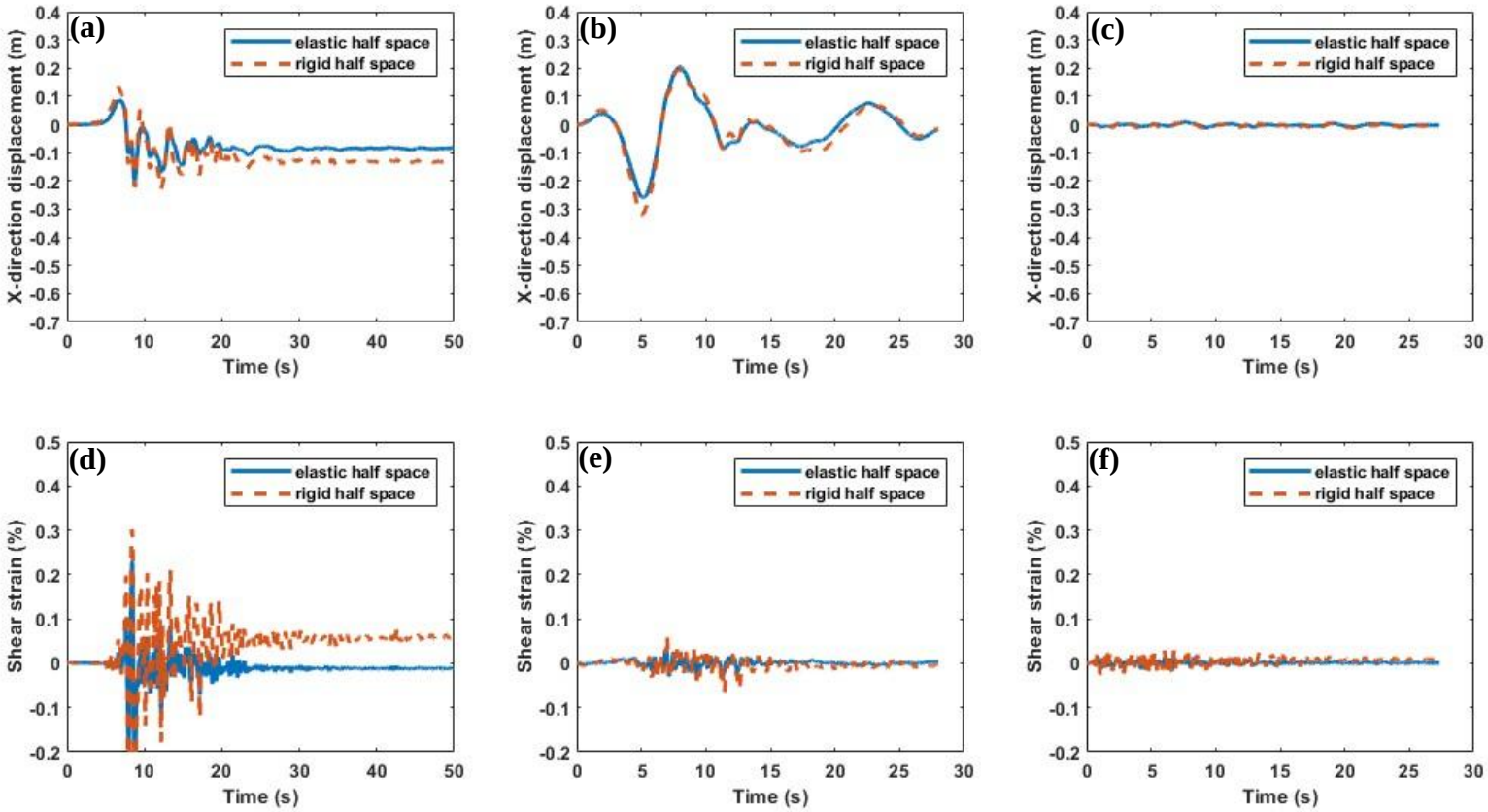

Figure A. 22 Point F x-direction displacement history of (a) Kobe; (b) Kocaeli; (c) San Fernando earthquake and shear strain history of (d) Kobe; (e) Kocaeli; (f) San Fernando earthquake in 10-degree submarine slope with s_u =100 kPa, DW = 50 m.

doi:10.6342/NTU202503752

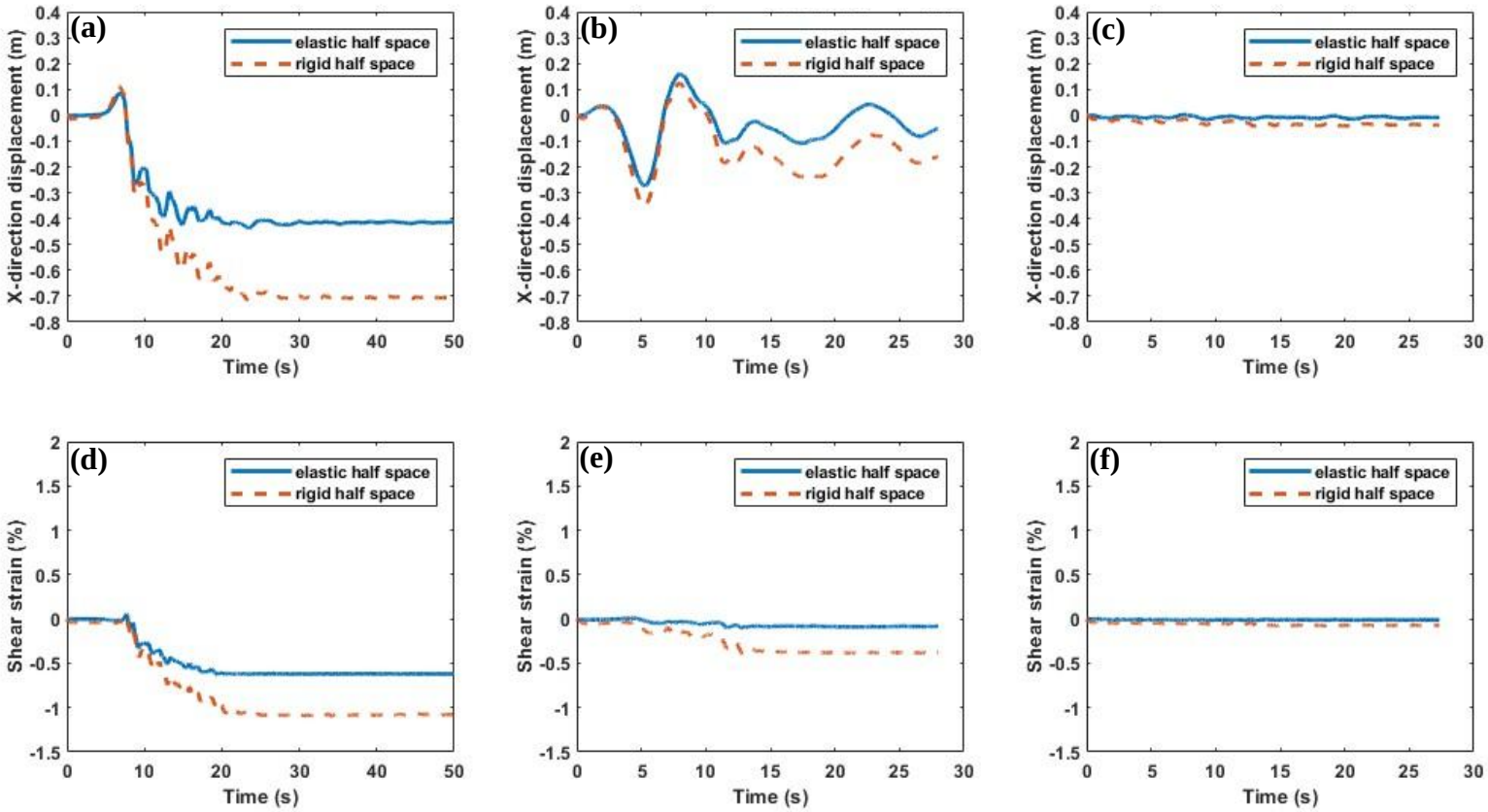

Figure A. 23 Point A x-direction displacement history of (a) Kobe; (b) Kocaeli; (c) San Fernando earthquake and shear strain history of (d) Kobe; (e) Kocaeli; (f) San Fernando earthquake in 20-degree submarine slope with s_u =40 kPa, DW = 50 m.

doi:10.6342/NTU202503752

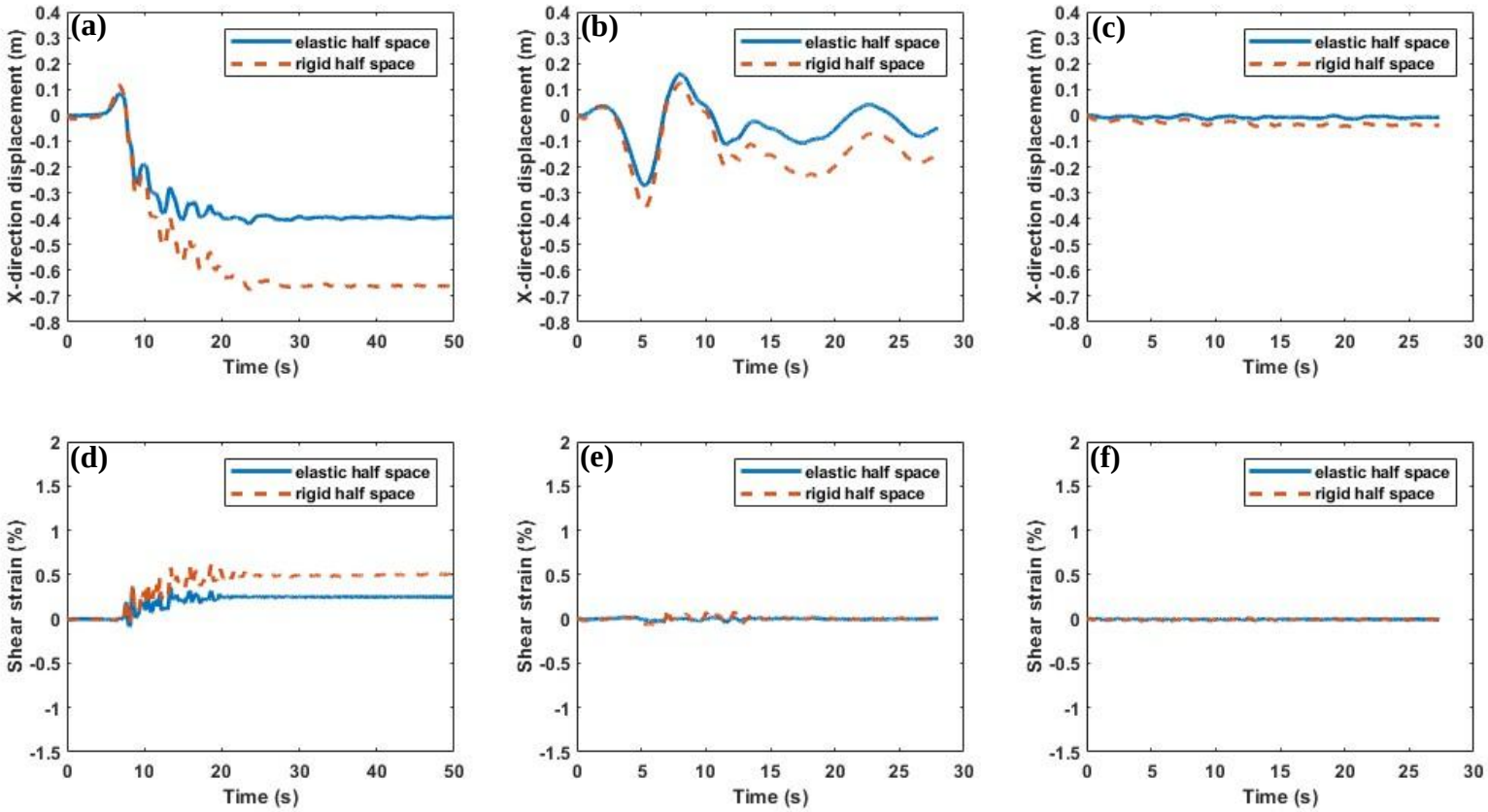

Figure A. 24 Point C x-direction displacement history of (a) Kobe; (b) Kocaeli; (c) San Fernando earthquake and shear strain history of (d) Kobe; (e) Kocaeli; (f) San Fernando earthquake in 20-degree submarine slope with s_u =40 kPa, DW = 50 m.

doi:10.6342/NTU202503752

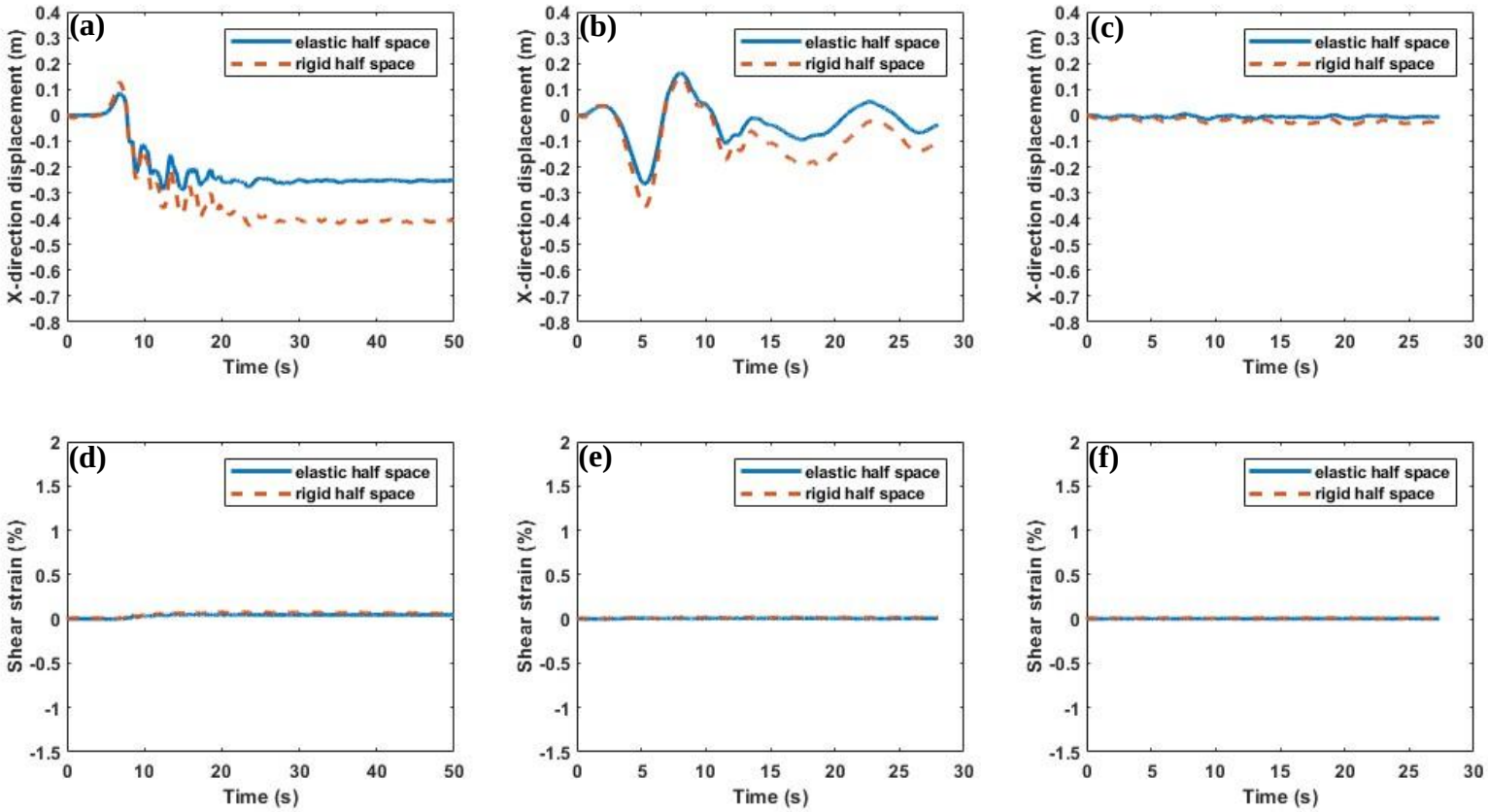

Figure A. 25 Point D x-direction displacement history of (a) Kobe; (b) Kocaeli; (c) San Fernando earthquake and shear strain history of (d) Kobe; (e) Kocaeli; (f) San Fernando earthquake in 20-degree submarine slope with s_u =40 kPa, DW = 50 m.

doi:10.6342/NTU202503752

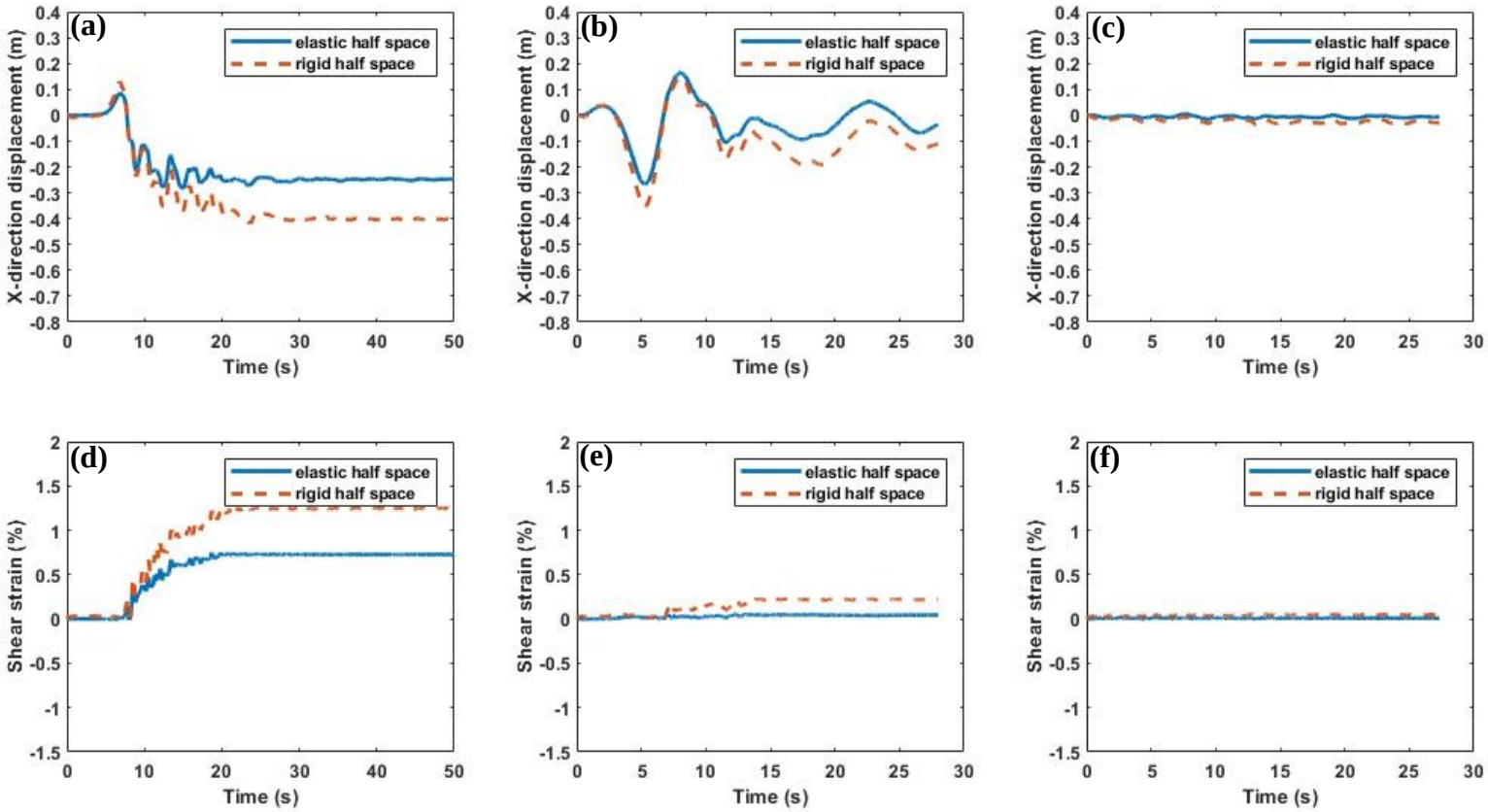

Figure A. 26 Point E x-direction displacement history of (a) Kobe; (b) Kocaeli; (c) San Fernando earthquake and shear strain history of (d) Kobe; (e) Kocaeli; (f) San Fernando earthquake in 20-degree submarine slope with s_u =40 kPa, DW = 50 m.

doi:10.6342/NTU202503752

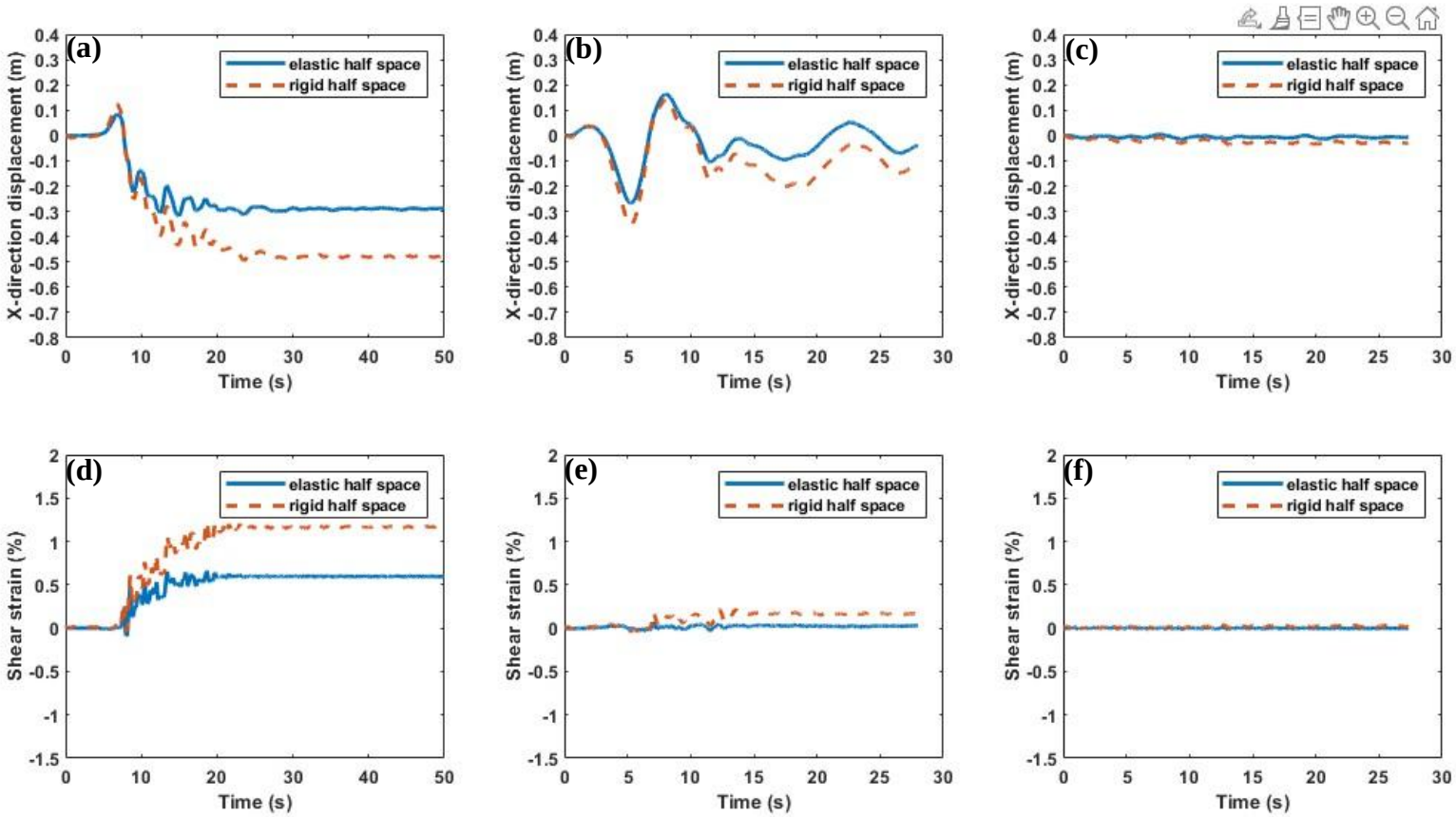

Figure A. 27 Point F x-direction displacement history of (a) Kobe; (b) Kocaeli; (c) San Fernando earthquake and shear strain history of (d) Kobe; (e) Kocaeli; (f) San Fernando earthquake in 20-degree submarine slope with s_u =40 kPa, DW = 50 m.

doi:10.6342/NTU202503752

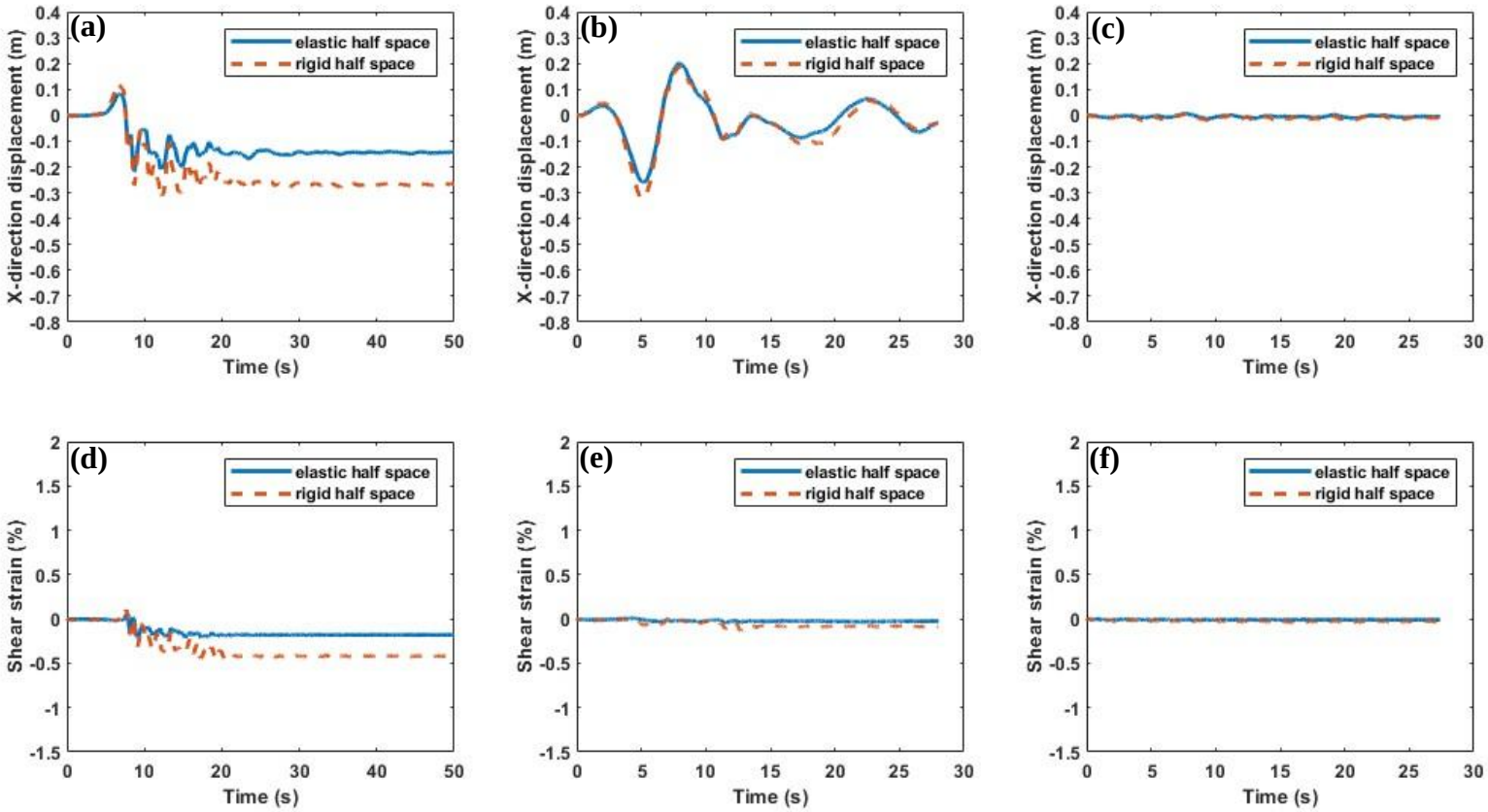

Figure A. 28 Point A x-direction displacement history of (a) Kobe; (b) Kocaeli; (c) San Fernando earthquake and shear strain history of (d) Kobe; (e) Kocaeli; (f) San Fernando earthquake in 20-degree submarine slope with s_u =100 kPa, DW = 50 m.

doi:10.6342/NTU202503752

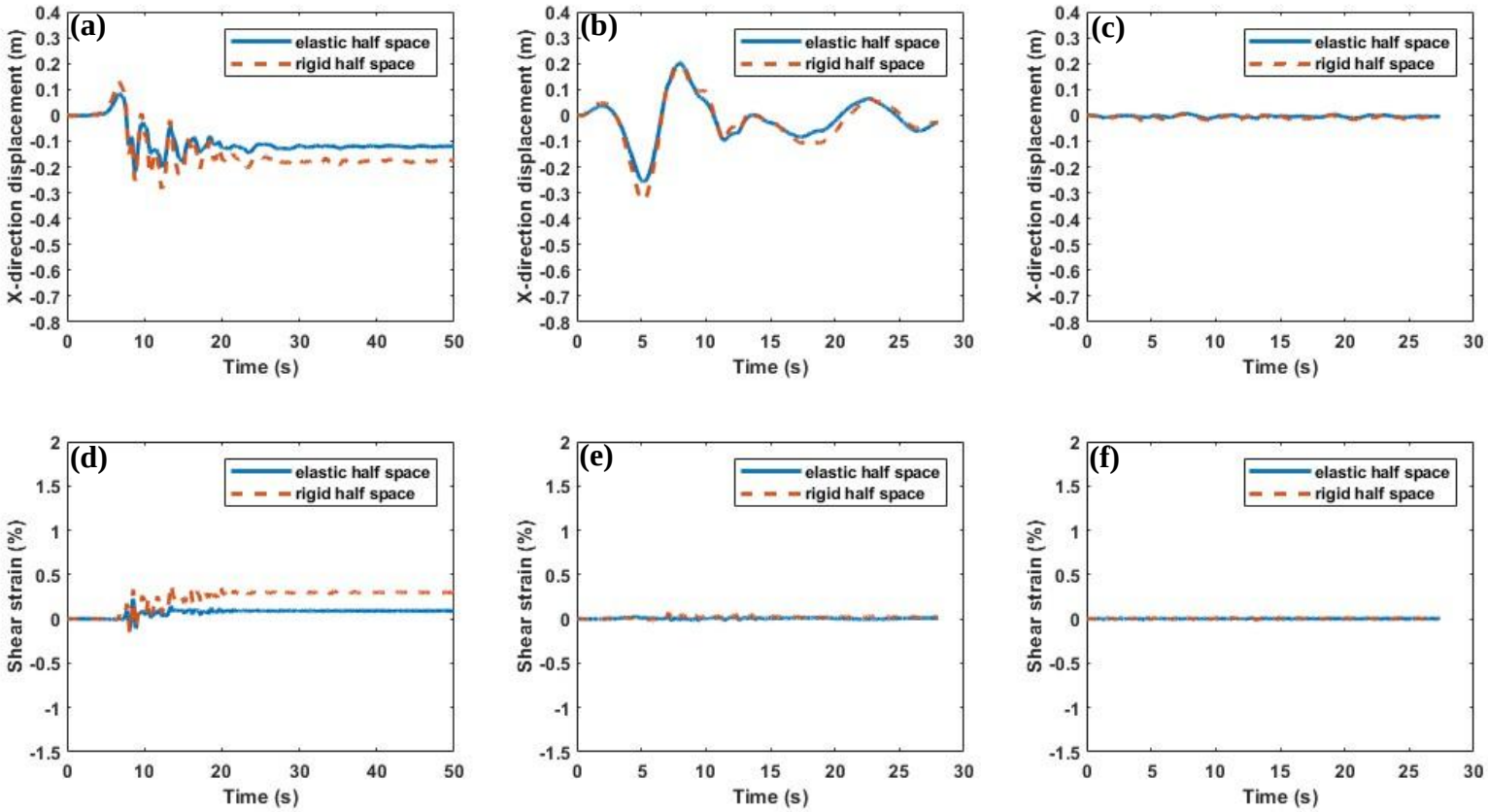

Figure A. 29 Point B x-direction displacement history of (a) Kobe; (b) Kocaeli; (c) San Fernando earthquake and shear strain history of (d) Kobe; (e) Kocaeli; (f) San Fernando earthquake in 20-degree submarine slope with s_u =100 kPa, DW = 50 m.

doi:10.6342/NTU202503752

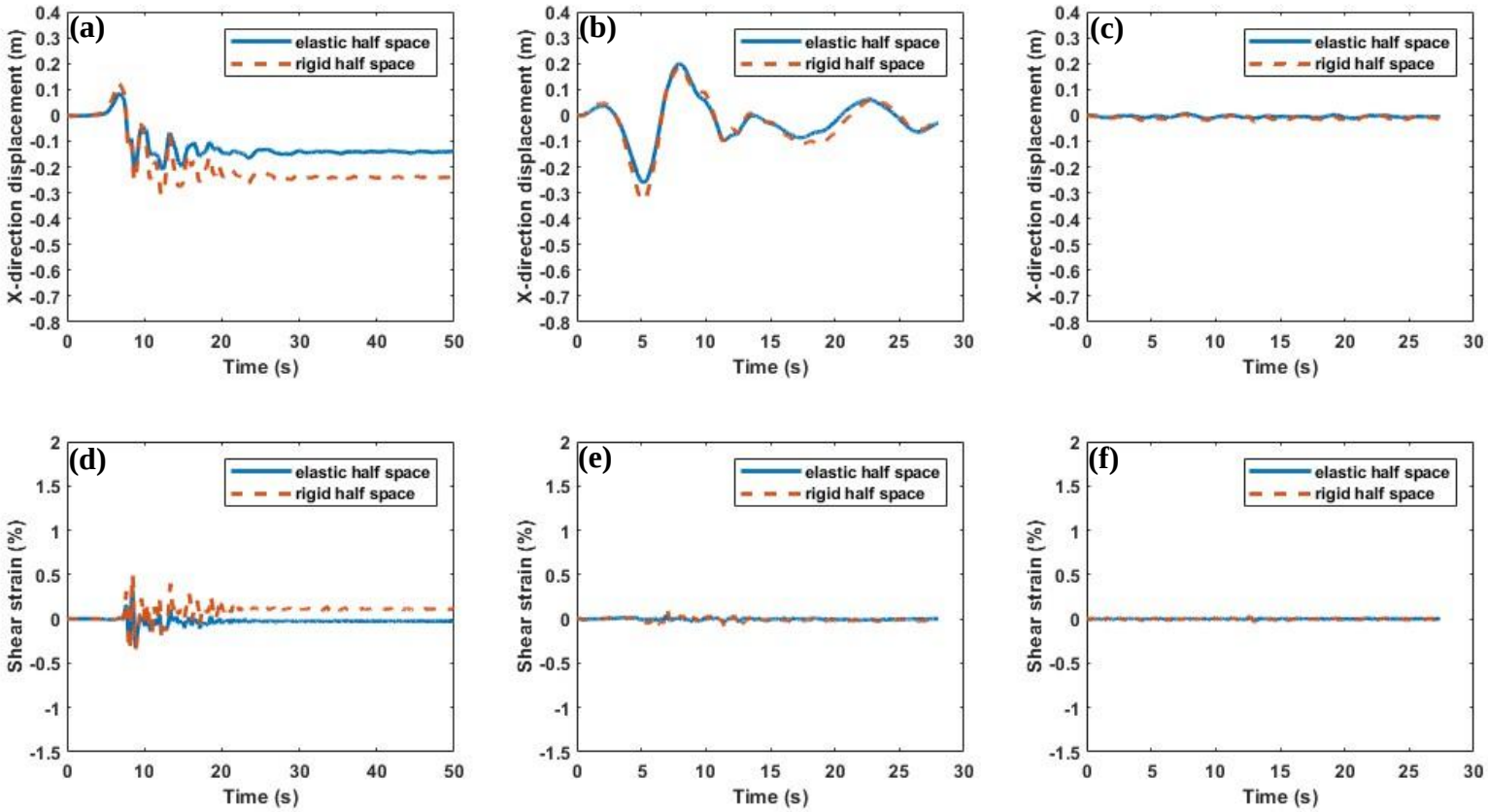

Figure A. 30 Point C x-direction displacement history of (a) Kobe; (b) Kocaeli; (c) San Fernando earthquake and shear strain history of (d) Kobe; (e) Kocaeli; (f) San Fernando earthquake in 20-degree submarine slope with s_u =100 kPa, DW = 50 m.

doi:10.6342/NTU202503752

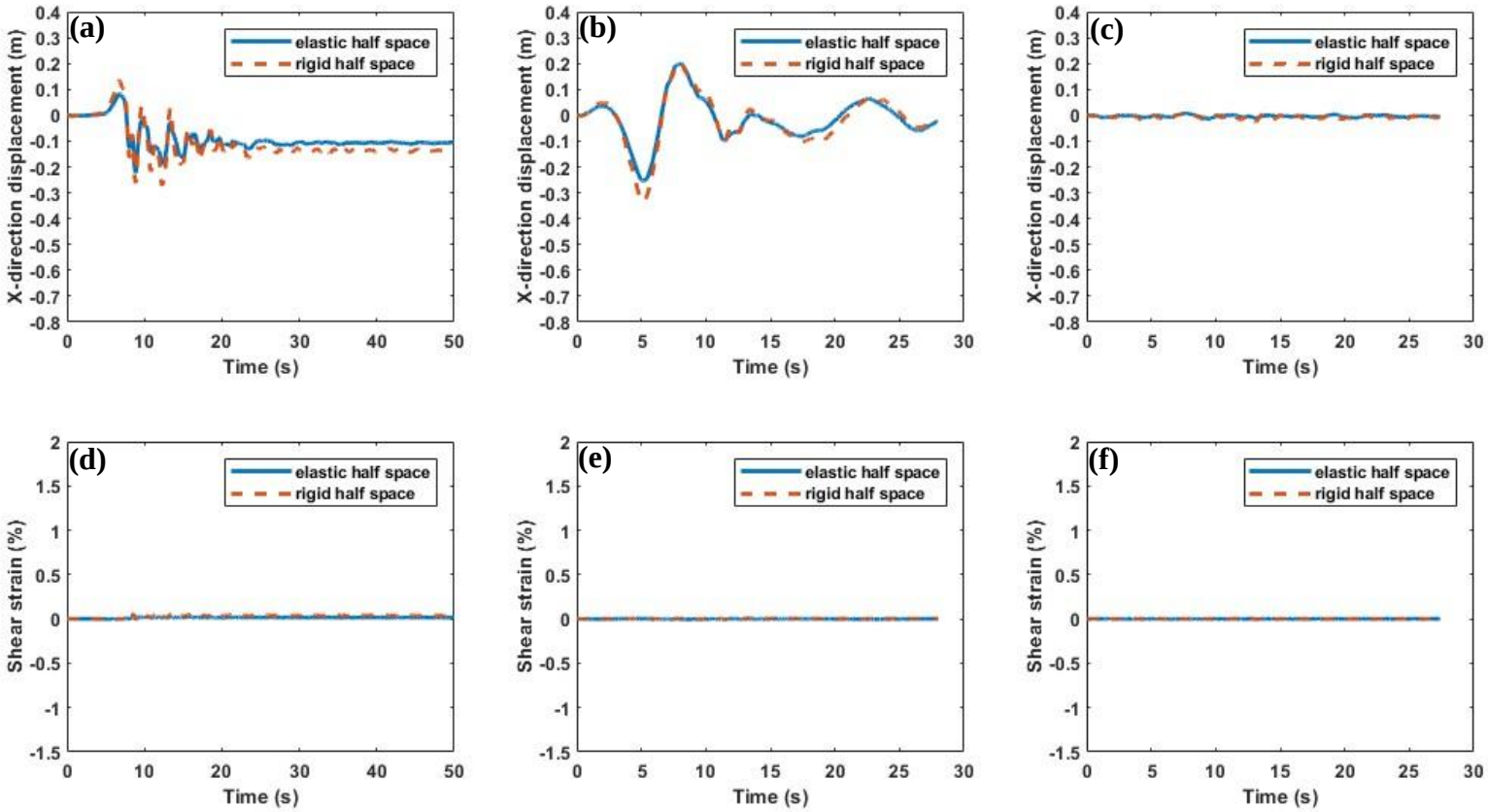

Figure A. 31 Point D x-direction displacement history of (a) Kobe; (b) Kocaeli; (c) San Fernando earthquake and shear strain history of (d) Kobe; (e) Kocaeli; (f) San Fernando earthquake in 20-degree submarine slope with s_u =100 kPa, DW = 50 m.

doi:10.6342/NTU202503752

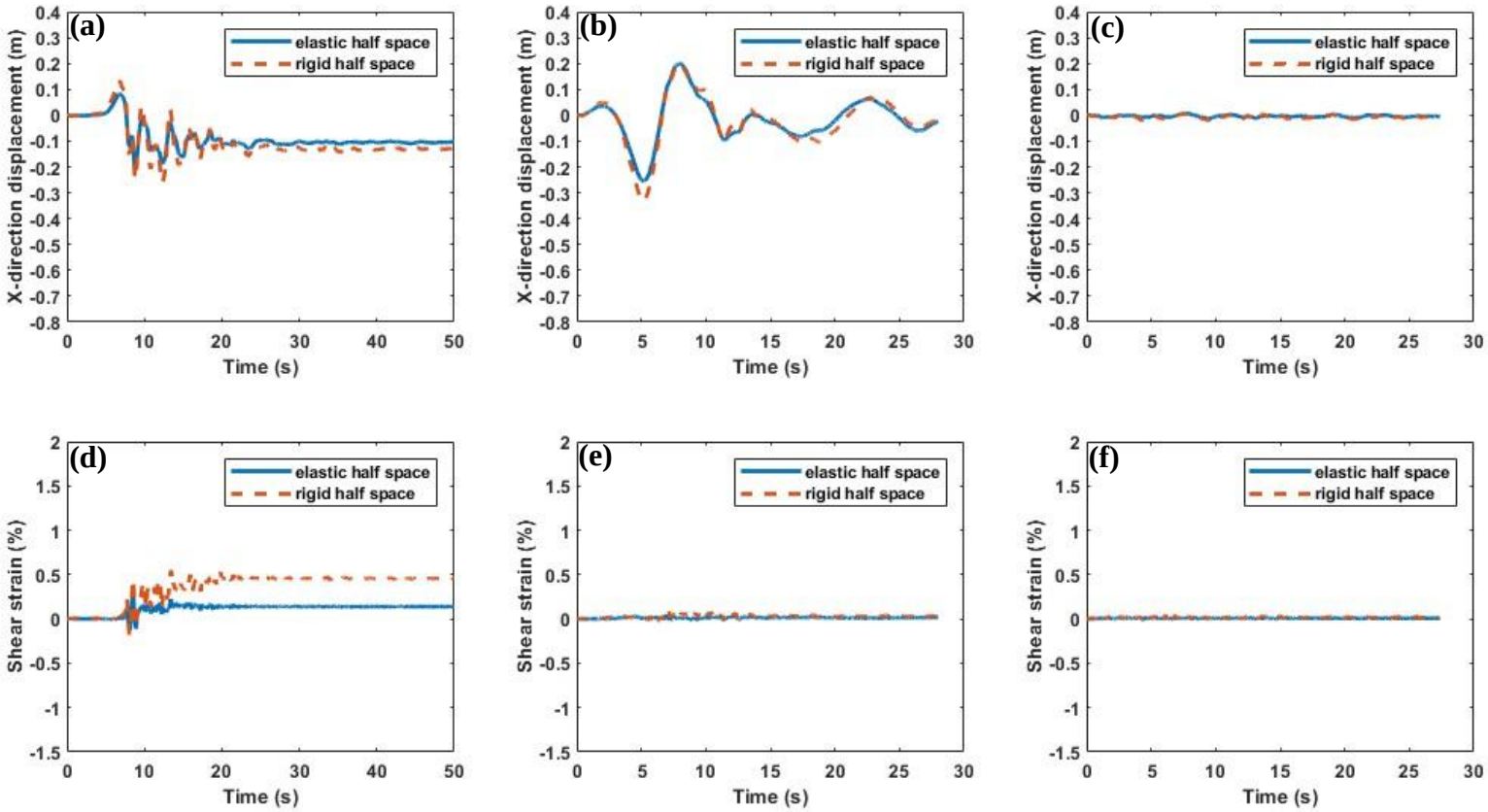

Figure A. 32 Point E x-direction displacement history of (a) Kobe; (b) Kocaeli; (c) San Fernando earthquake and shear strain history of (d) Kobe; (e) Kocaeli; (f) San Fernando earthquake in 20-degree submarine slope with s_u =100 kPa, DW = 50 m.

doi:10.6342/NTU202503752

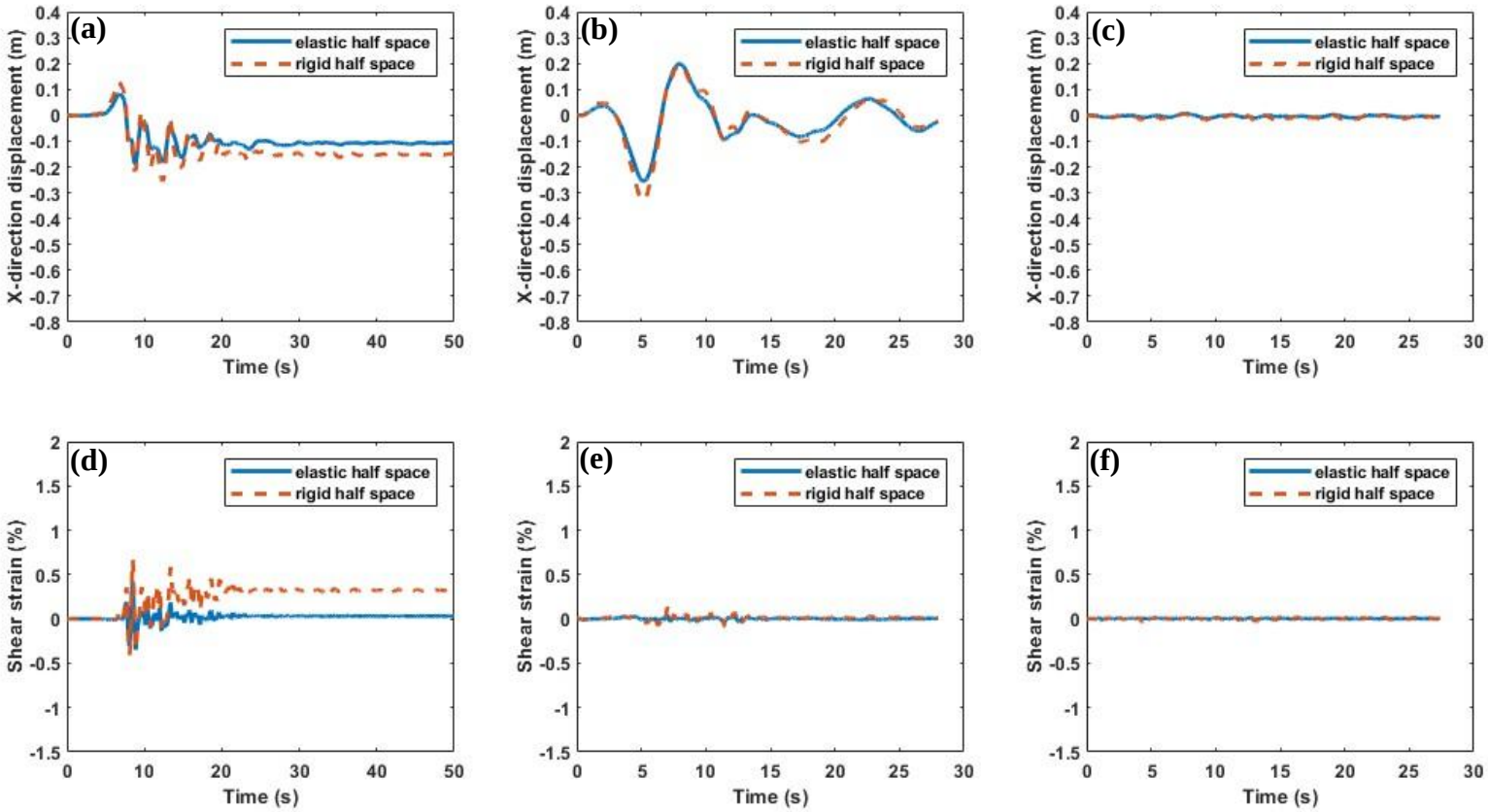

Figure A. 33 Point F x-direction displacement history of (a) Kobe; (b) Kocaeli; (c) San Fernando earthquake and shear strain history of (d) Kobe; (e) Kocaeli; (f) San Fernando earthquake in 20-degree submarine slope with s_u =100 kPa, DW = 50 m.

doi:10.6342/NTU202503752

Appendix B: X-direction displacement and shear strain histories at DW = 25 m

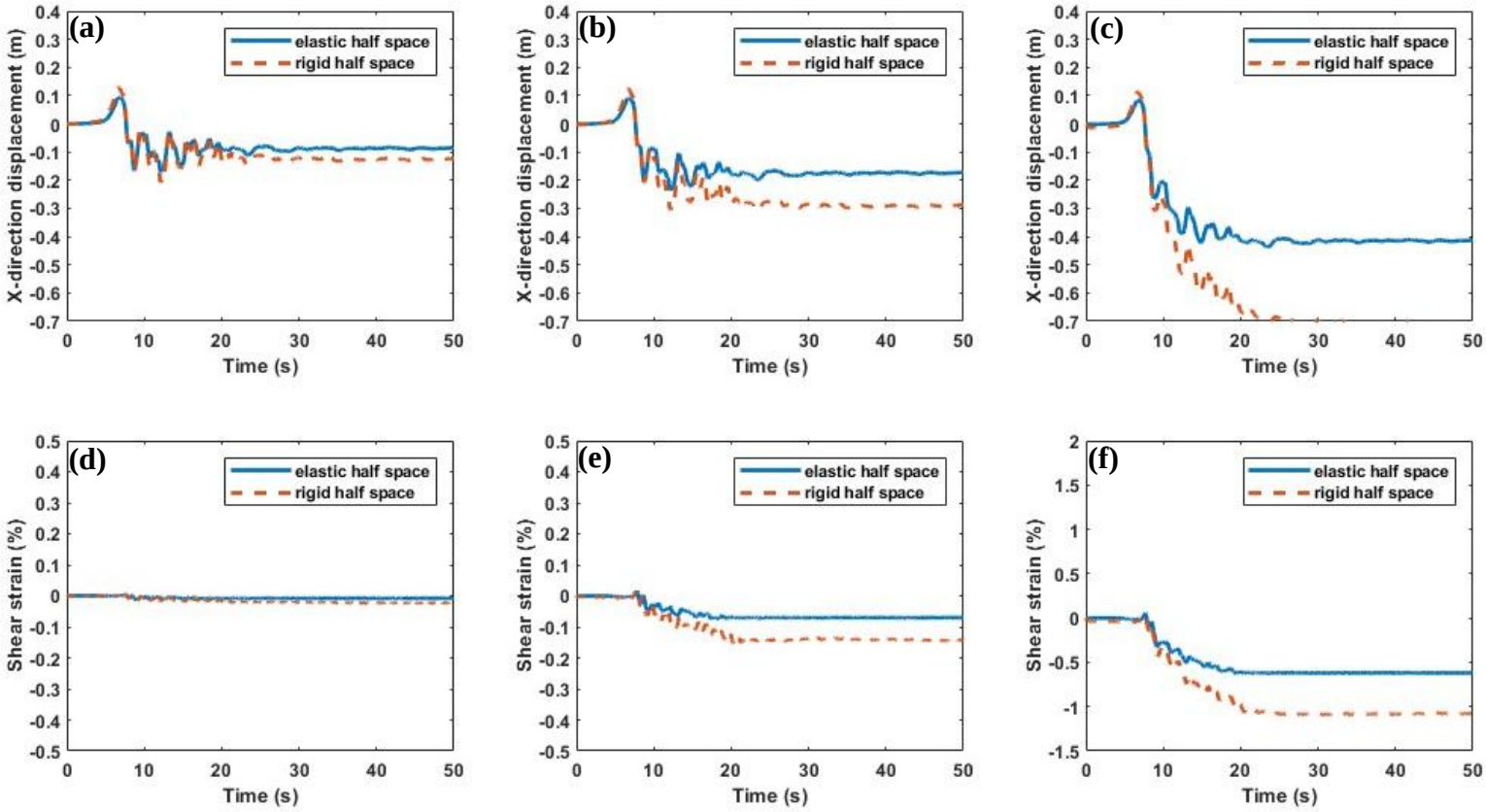

Figure B. 1 Point A x-direction displacement history of Kobe earthquake with s_u =40 kPa, DW = 25 m in (a)5°; (b)10°; (c)20° slope and shear strain history in (d)5°; (e)10°; (f)20° slope.

doi:10.6342/NTU202503752

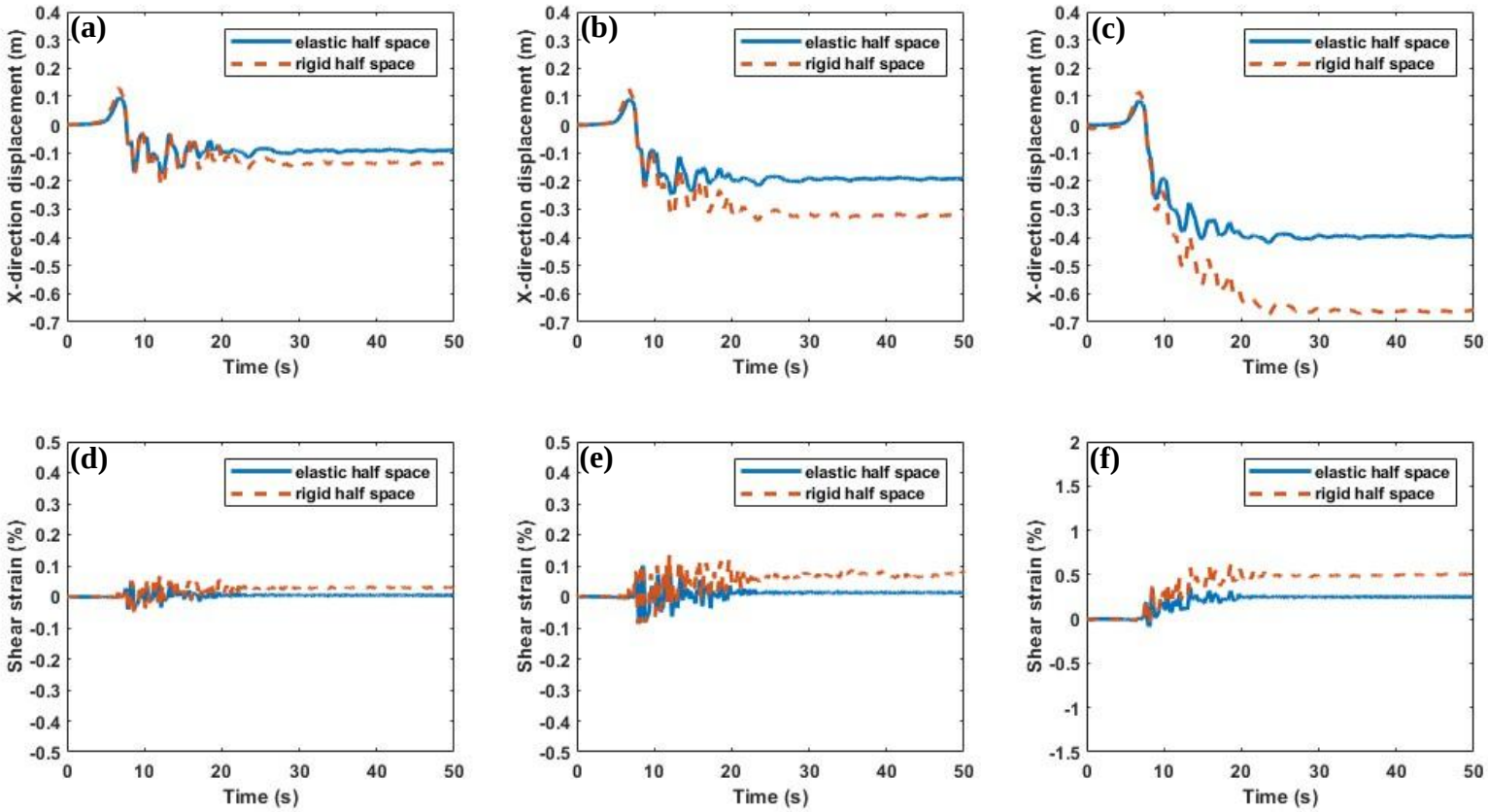

Figure B. 2 Point C x-direction displacement history of Kobe earthquake with s_u =40 kPa, DW = 25 m in (a)5°; (b)10°; (c)20° slope and shear strain history in (d)5°; (e)10°; (f)20° slope.

doi:10.6342/NTU202503752

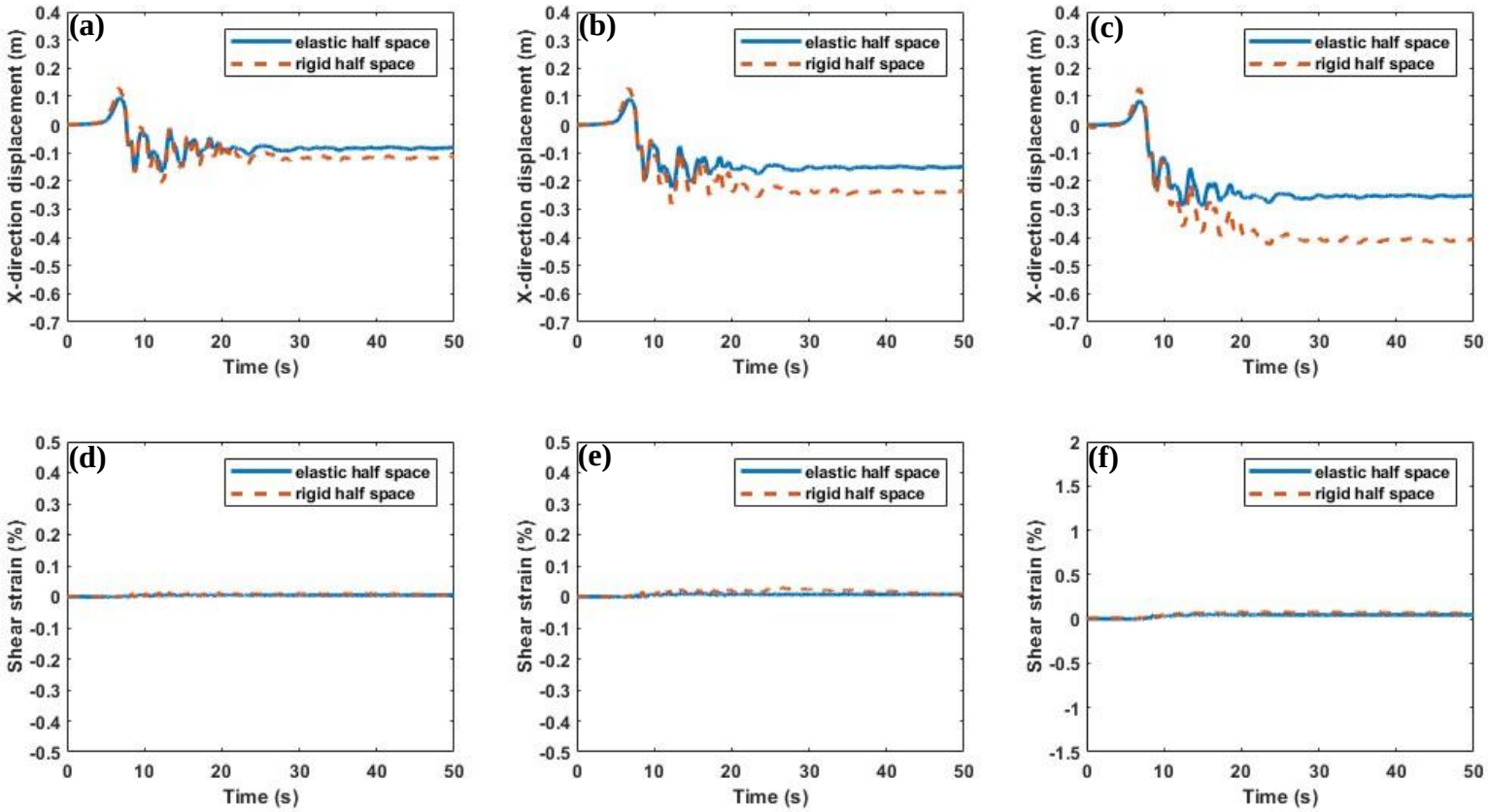

Figure B. 3 Point D x-direction displacement history of Kobe earthquake with s_u =40 kPa, DW = 25 m in (a)5°; (b)10°; (c)20° slope and shear strain history in (d)5°; (e)10°; (f)20° slope.

doi:10.6342/NTU202503752

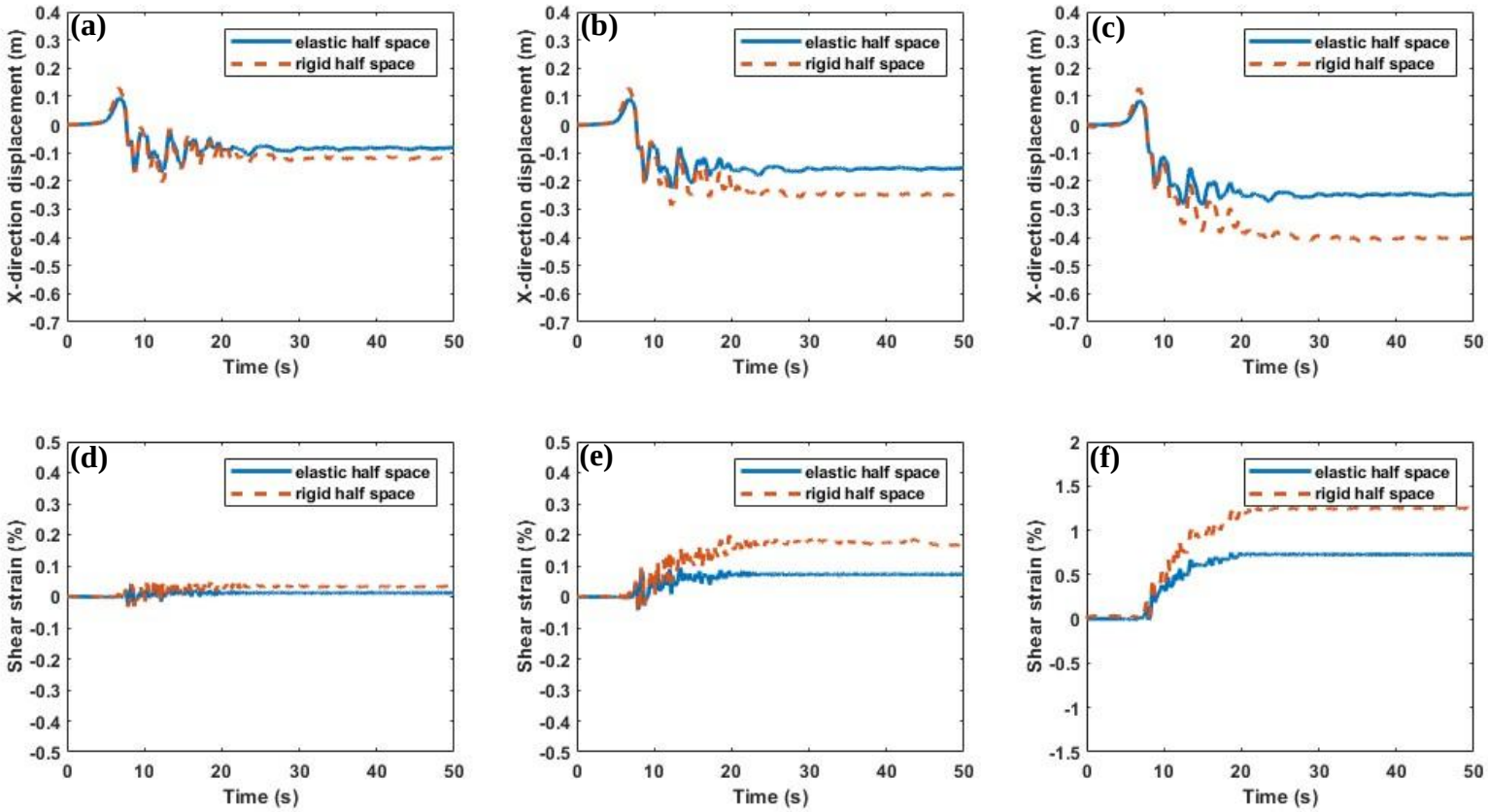

Figure B. 4 Point E x-direction displacement history of Kobe earthquake with s_u =40 kPa, DW = 25 m in (a)5°; (b)10°; (c)20° slope and shear strain history in (d)5°; (e)10°; (f)20° slope.

doi:10.6342/NTU202503752

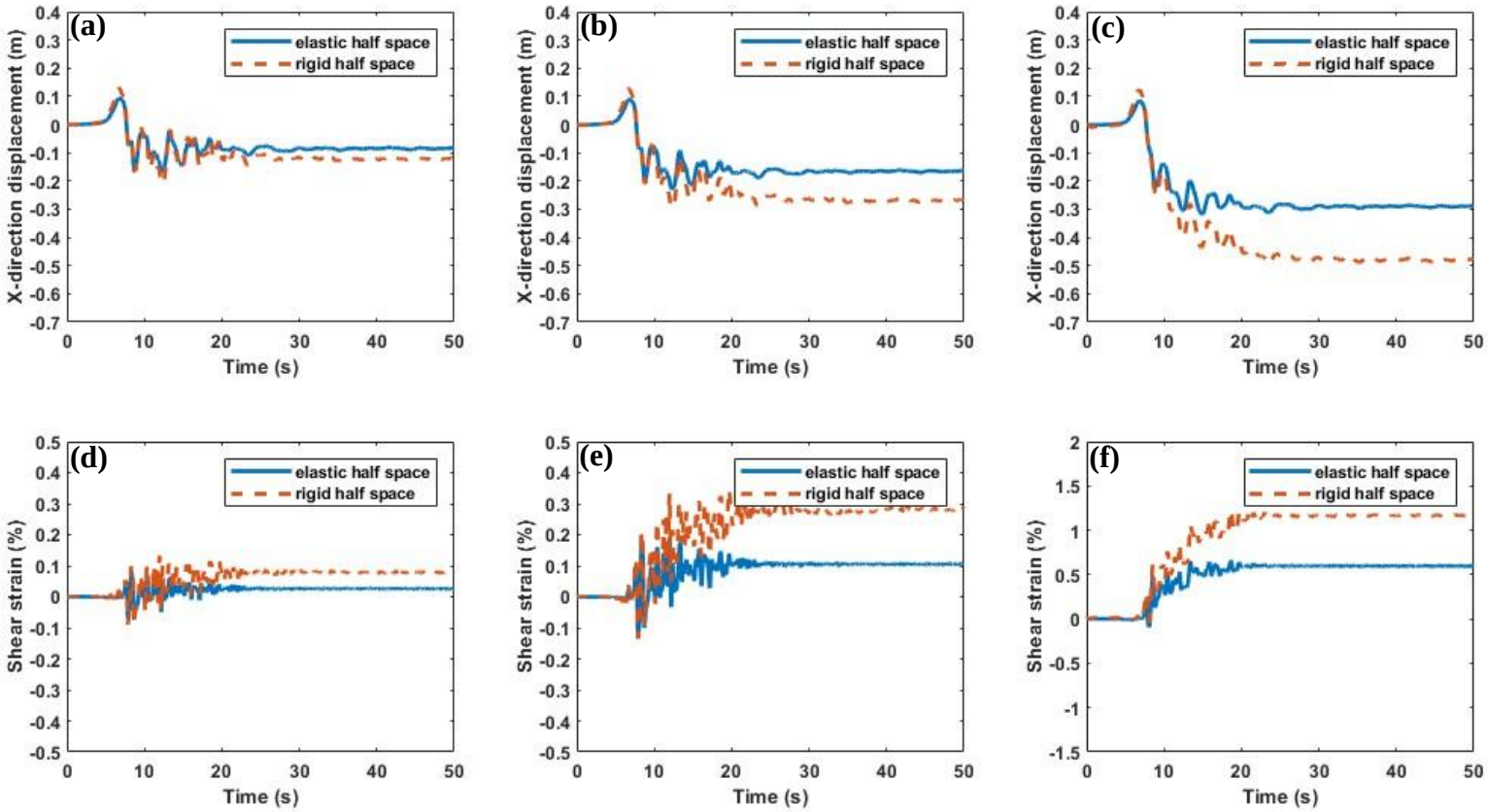

Figure B. 5 Point F x-direction displacement history of Kobe earthquake with s_u =40 kPa, DW = 25 m in (a)5°; (b)10°; (c)20° slope and shear strain history in (d)5°; (e)10°; (f)20° slope.

doi:10.6342/NTU202503752

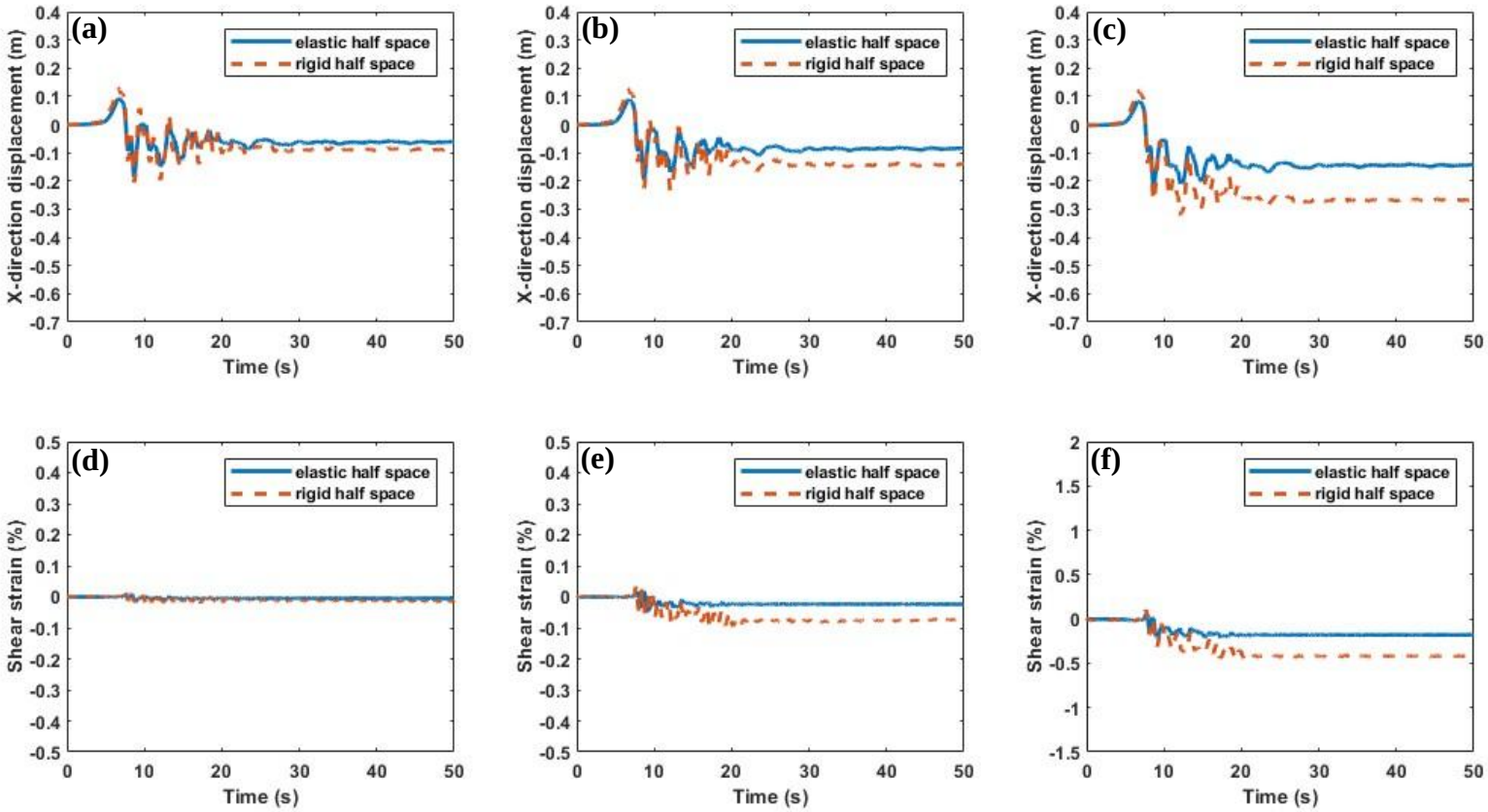

Figure B. 6 Point A x-direction displacement history of Kobe earthquake with s_u =100 kPa, DW = 25 m in (a)5°; (b)10°; (c)20° slope and shear strain history in (d)5°; (e)10°; (f)20° slope.

doi:10.6342/NTU202503752

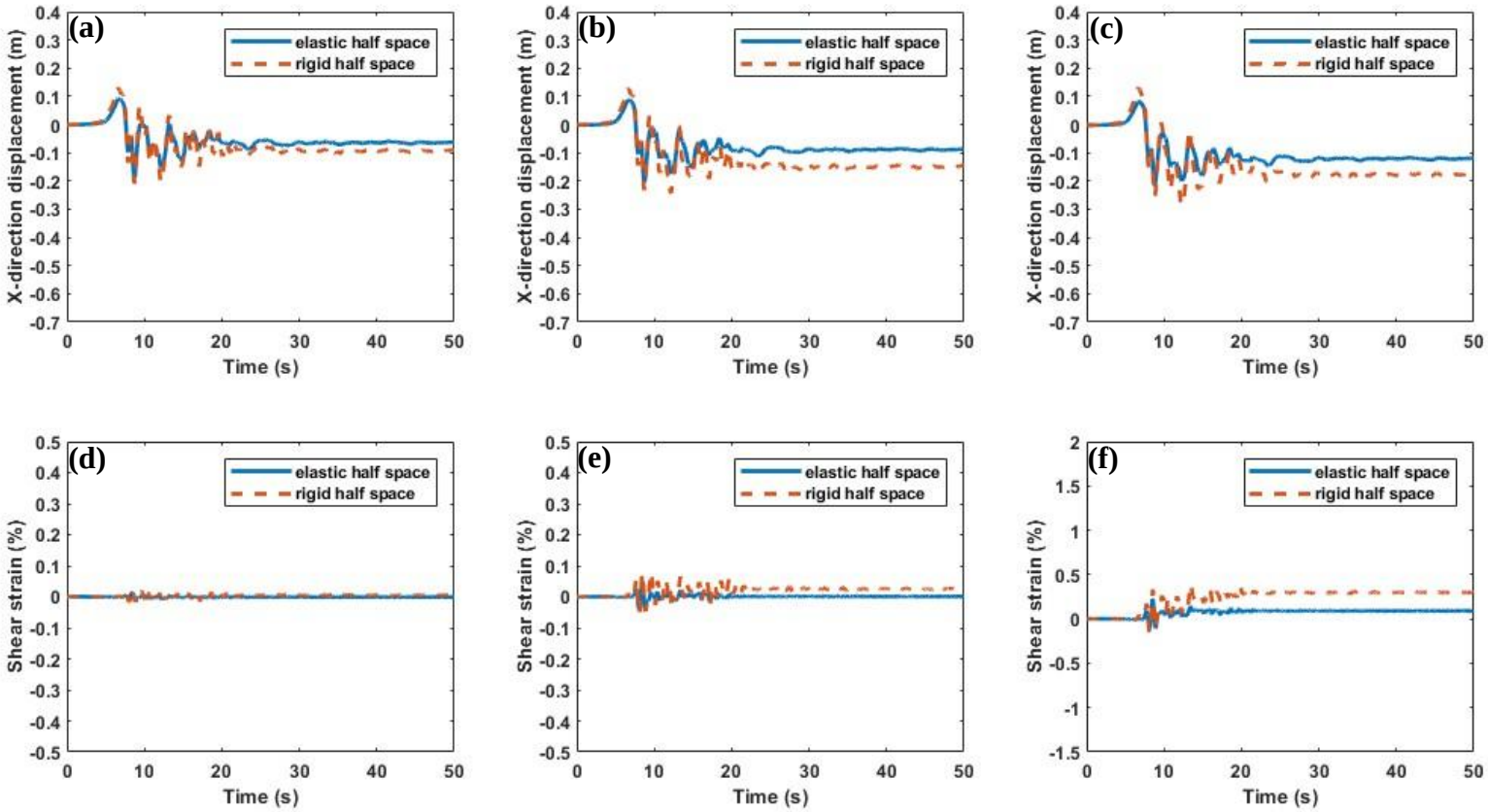

Figure B. 7 Point B x-direction displacement history of Kobe earthquake with s_u =100 kPa, DW = 25 m in (a)5°; (b)10°; (c)20° slope and shear strain history in (d)5°; (e)10°; (f)20° slope.

doi:10.6342/NTU202503752

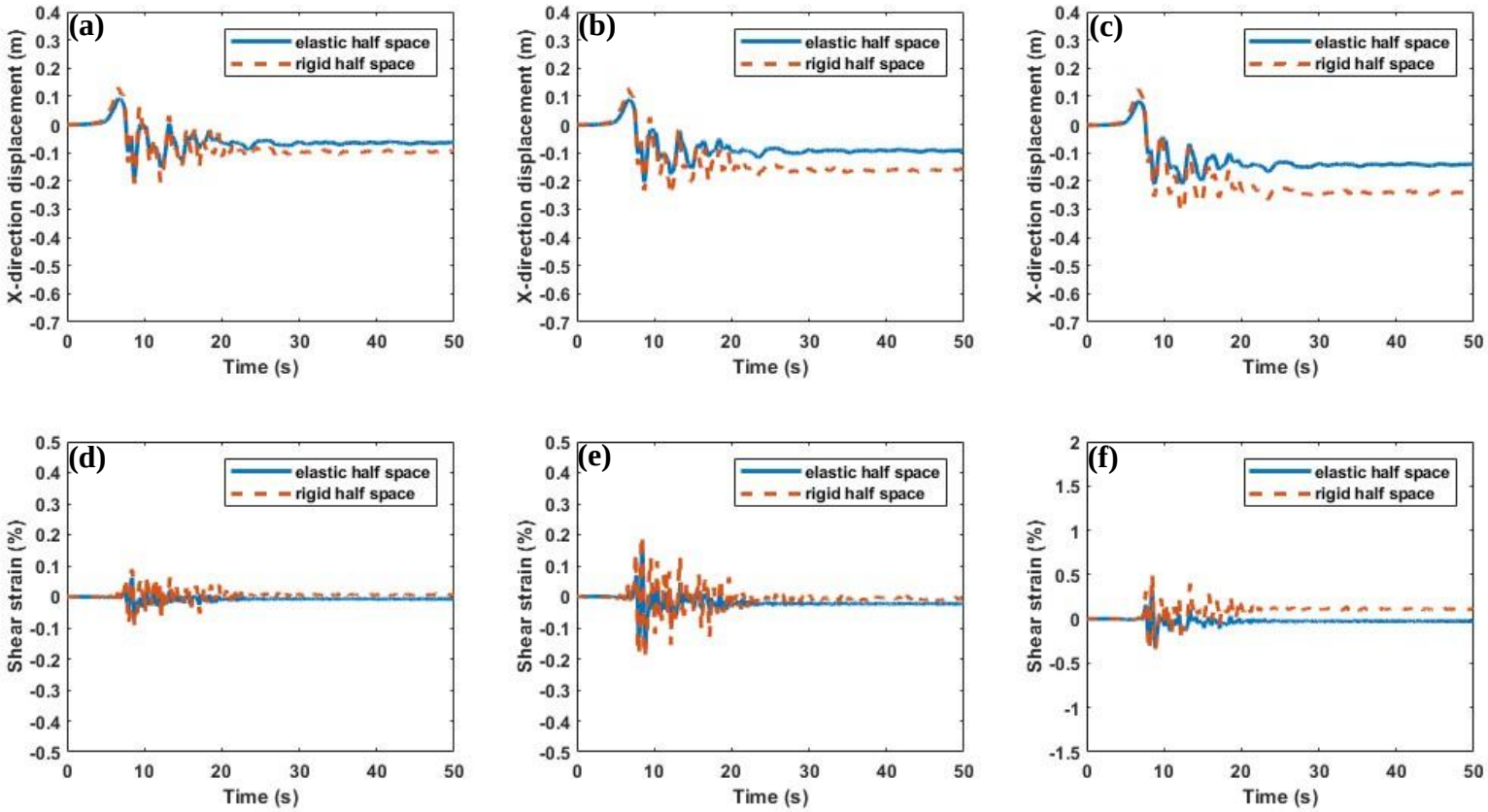

Figure B. 8 Point C x-direction displacement history of Kobe earthquake with s_u =100 kPa, DW = 25 m in (a)5°; (b)10°; (c)20° slope and shear strain history in (d)5°; (e)10°; (f)20° slope.

doi:10.6342/NTU202503752

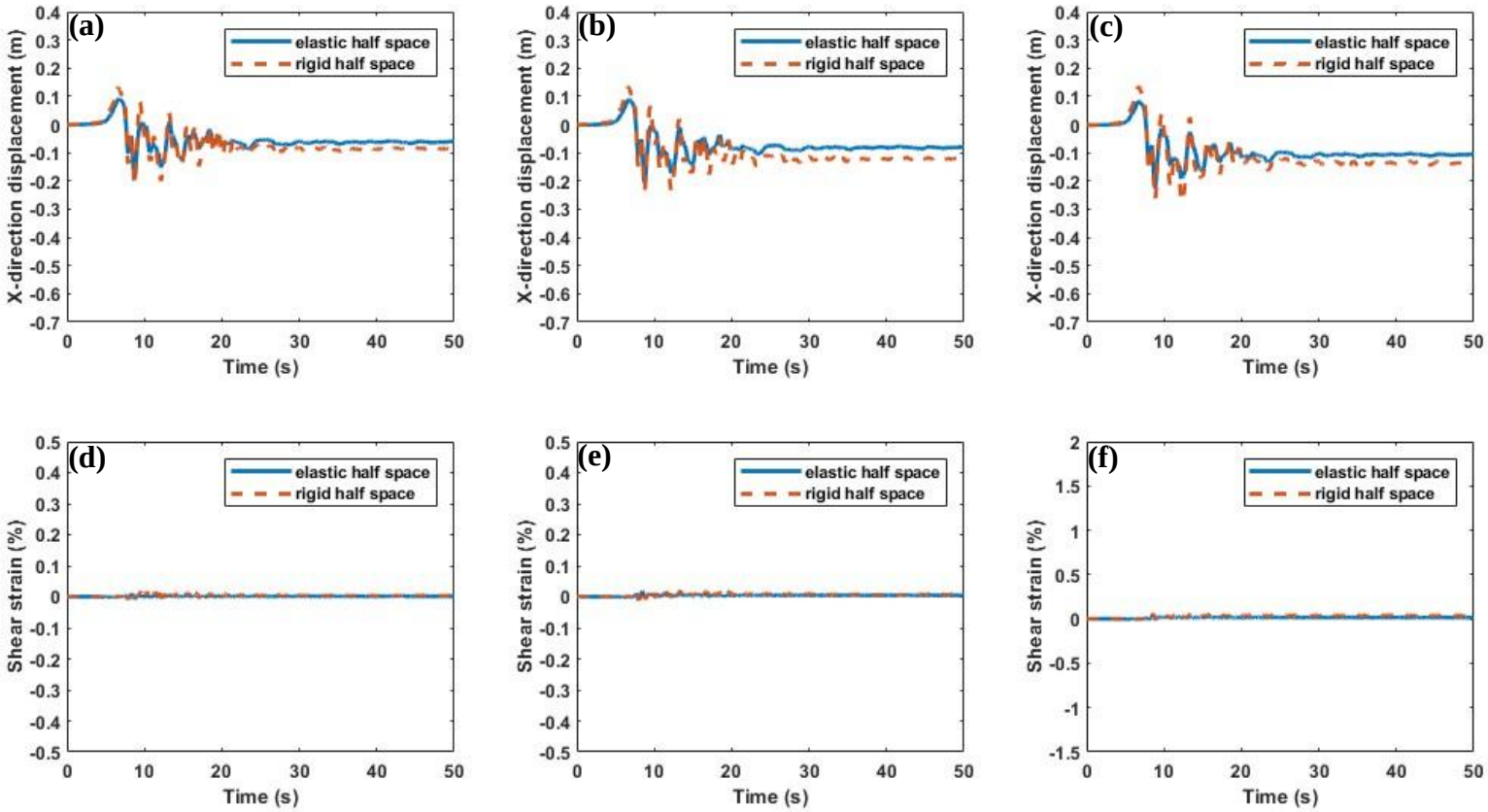

Figure B. 9 Point D x-direction displacement history of Kobe earthquake with s_u =100 kPa, DW = 25 m in (a)5°; (b)10°; (c)20° slope and shear strain history in (d)5°; (e)10°; (f)20° slope.

doi:10.6342/NTU202503752

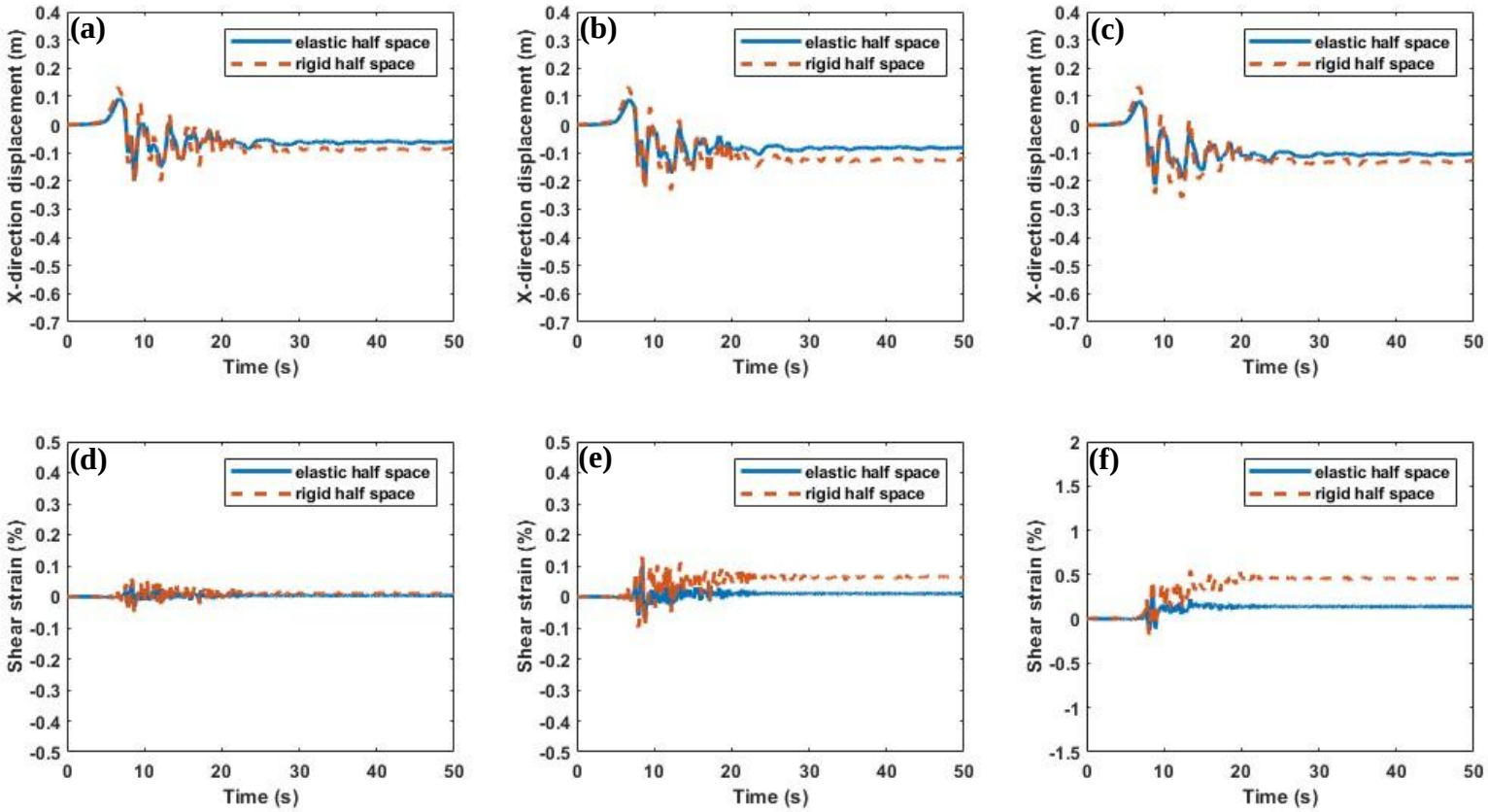

Figure B. 10 Point E x-direction displacement history of Kobe earthquake with s_u =100 kPa, DW = 25 m in (a)5°; (b)10°; (c)20° slope and shear strain history in (d)5°; (e)10°; (f)20° slope.

doi:10.6342/NTU202503752

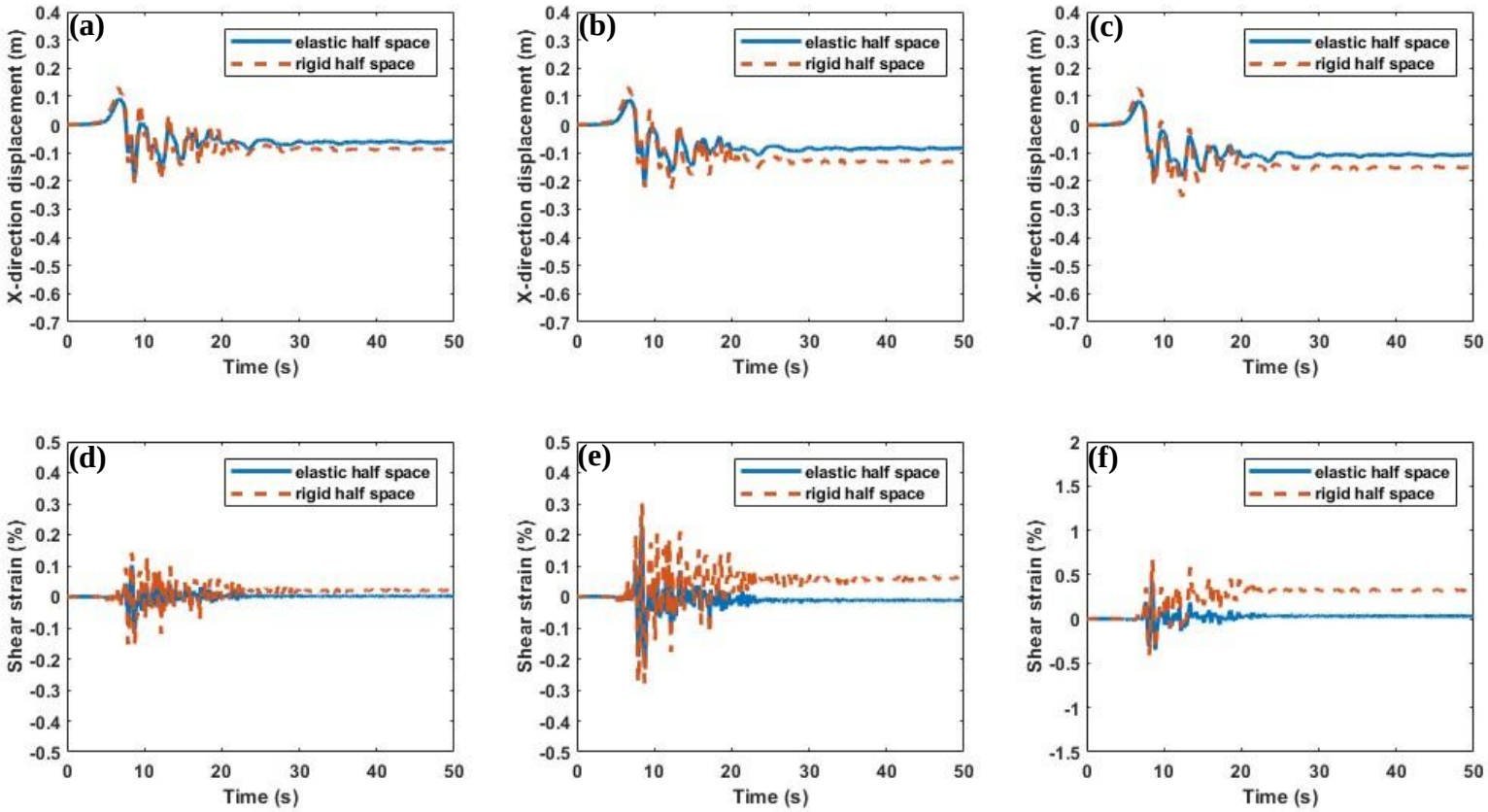

Figure B. 11 Point F x-direction displacement history of Kobe earthquake with s_u =100 kPa, DW = 25 m in (a)5˚; (b)10˚; (c)20˚ slope and shear strain history in (d)5˚; (e)10˚; (f)20˚ slope.

doi:10.6342/NTU202503752